DOI: 10.14750/ME.2016.008

Institute of Applied Mechanics
Faculty of Mechanical Engineering and Informatics
University of Miskolc

László Péter Kiss

Vibrations and Stability of Heterogeneous Curved Beams

PhD thesis

István Sályi Doctoral School
Main Topic Group: Fundamental Sciences in Mechanical Engineering
Topic Group: Mechanics of Solid Bodies

Head of Doctoral School:
Miklós Tisza
Doctor of Science, Full Professor

Head of the Main Topic Group:
István Páczelt
Member of the Hungarian Academy of Sciences, Professor Emeritus

Head of the Topic Group:
Imre Kozák
Member of the Hungarian Academy of Sciences, Professor Emeritus

Scientific Supervisor:
György Szeidl
Doctor of Science, Professor Emeritus

Miskolc
2015

DOI: 10.14750/ME.2016.008

Declaration

The author hereby declares that the work in this thesis contains no material previously published or written by another person and no part of the thesis has been submitted, either in the same or different form to any other university for a PhD degree.

The author confirms that the work presented in this thesis is his own and appropriate credit is given in the text when (and where) reference is made to the work of others.

Miskolc, 27 April 2015

László Péter Kiss

DOI: 10.14750/ME.2016.008

Recommendation of the supervisor to the PhD thesis

Vibrations and Stability of Heterogeneous Curved Beams

by László Péter Kiss

As is well known curved structural elements have been used successfully in various engineering applications for their favorable load carrying capabilities. One can mention, without striving for completeness, arch bridges or stiffeners in roof- and shell structures etc. With technology developing and production volumes increasing it is gradually getting cheaper to manufacture heterogeneous or inhomogeneous curved beams, such as composites, laminates, sandwich structures. The thesis by László Péter Kiss is aimed to solve some (altogether three) fundamental problems concerning the mechanical behavior of heterogeneous curved beams.

The first objective is a generalization of some classical results valid for homogeneous materials. These investigations have yielded some elementary relationships that can be used to determine the stress state in the heterogeneous curved beam by hand made calculations. The second objective is to develop a new nonlinear model for non-strictly shallow curved beams from the principle of virtual work. This model makes it possible to determine the critical load both for symmetric snap-through and antisymmetric bifurcation buckling if the heterogeneous curved beam is subjected to a central load at the crown point. Pinned-pinned, fixed-fixed and elastically restrained beams are considered. The third objective is to clarify what effect the central load has on the frequency spectrum of the heterogeneous curved beam. The solution is based on reducing the corresponding eigenvalue problems to those governed by Fredholm integral equation systems.

The thesis systematically deals with the three problems and does its best to find appropriate solutions. The numerical results were determined by developing and successfully running three programs which were coded in Fortan 90. This work needed a great care but László Péter Kiss solved this issue successfully.

As a scientific supervisor I should emphasize that László Péter Kiss is a hard working and diligent young man who did his work paying careful attention to every detail. The results achieved have been published regularly (four papers have come out and one paper is accepted) by fulfilling the requirements of the István Sályi Doctoral School for publications in this way.

The thesis presents the research work an its results in a clear and well-arranged manner: the numerous figures provide a further help for the reader to understand what effect the various parameters have on the results (critical loads and natural frequencies). In accordance with the three objectives the three statements in the summary can be regarded as a short synopsis of the most important results.

Bükkszentkereszt, 27 April 2015

György Szeidl, DSc
Professor Emeritus

DOI: 10.14750/ME.2016.008

Contents

DOI: 10.14750/ME.2016.008

DOI: 10.14750/ME.2016.008

DOI: 10.14750/ME.2016.008

Nomenclature

Here the most important and most commonly used notations are gathered in alphabetical order. Although each notation is described in the text when first used, this Nomenclature might come handy at times.

Latin symbols:

$A\ , A^{'}$	cross-sectional area, segment area (see Figure 2.3),
$A_e,\ A_e^{'}$	E-weighted areas,
A_{eR}	E-weighted reduced area,
$\mathbf{A}_j, \mathbf{B}_j$	matrices in the representation of the Green function matrix ($j = 1, 2, 3, 4$),
C_e	E-weighted centroid of the cross-section,
$\mathbf{e}_\xi, \mathbf{e}_\eta, \mathbf{e}_\zeta$	orthogonal unit vectors,
$E(\eta, \zeta)$	Young's modulus,
$\mathbf{E}$	Green-Lagrange strain tensor,
$\mathbf{E}^N$	nonlinear part of the Green-Lagrange strain tensor,
$\mathbf{E}^L$	linear part of the Green-Lagrange strain tensor,
$f_n,\ f_t$	distributed forces in the directions ζ, ξ,
G	shear modulus of elasticity,
$\mathbf{G}$	Green function matrix,
G_{ij}	the ij-th element of the Green function matrix ($i, j = 1, 2$),
H	Heaviside function,
i_e	E-weighted radius of gyration,
I_{eR}	E-weighted reduced moment of inertia,
$I_{e\eta}$	E-weighted moment of inertia with respect to the axis η,
I_η	moment of inertia with respect to the axis η,
$k_{\gamma l},\ k_{\gamma r},\ k_\gamma$	each one is a torsional spring stiffness,
κ_γ	shear correction factor,
$\ell_b,\ \ell_r$	lengths of a straight beam, rod,
$m,\ \tilde{m}$	geometric-material parameters, $m = \frac{A_e \rho_o^2}{I_{e\eta}} = \tilde{m} + 1$,
$m_{het},\ m_{\mathrm{hom}}$	parameters for heterogeneous and homogeneous beams,
M	bending moment,
N	axial force,
$P_\zeta,\ P_\xi$	concentrated vertical and horizontal external forces,
$P_{\zeta\ het},\ P_{\zeta\ \mathrm{hom}}$	critical loads for heterogeneous and homogeneous curved beams,
$\mathcal{P}$	critical dimensionless load,
$\hat{\mathcal{P}}$	dimensionless load,
$\overset{i}{\mathbf{P}}$	coefficient matrix ($i = 1, 2, 3, 4$),
Q_{eR}	E-weighted reduced first moment,
$Q_{e\eta},\ Q_{e\eta}^{'}$	E-weighted first moment of the cross-section or its segment A',
s	arc coordinate,
$\mathcal{S}$	dimensionless spring stiffness,
$\mathbf{S}$	the second Piola-Kirchhoff stress tensor,
t	time,
$\mathbf{u}$	displacement vector,
$u_o,\ v_o,\ w_o$	displacements of the centerline in the directions ξ, η, ζ,
U	total strain energy,

DOI: 10.14750/ME.2016.008

U_T	total strain energy from shearing,
U_τ	strain energy from shearing per unit length,
$U_o,\ W_o$	dimensionless displacements in the directions ξ, ζ,
$\hat{U}_{ob},\ \hat{W}_{ob}$	dimensionless displacement increment amplitudes,
V_ζ	shear force,
W_{oC}	dimensionless displacement of the crown point,
$\mathbf{y}$	the column vector that contains the displacement amplitudes.

Greek symbols:

α	eigenfrequency,
α_i^*	the i-th natural frequency of straight beams,
$\alpha_{i\ free}$	the i-th natural frequency of heterogeneous curved beams,
α_i	the i-th eigenfrequency of loaded heterogeneous curved beams,
$\gamma_{\xi\zeta}$	angle distortion,
ε_ξ	axial strain,
$\varepsilon_{o\xi}$	linearized axial strain on the (E-weighted) centerline,
ε_m	nonlinear axial strain on the (E-weighted) centerline,
$\varepsilon_{o\xi\,crit}$	critical axial strain,
$\zeta_o = -e$	ζ coordinate of the neutral axis,
$\hat{\zeta}$	ζ coordinate of the cross-section segment A',
ϑ	semi-vertex angle of the curved beam,
$\bar{\vartheta}$	included angle of the curved beam,
κ_o	curvature change on the centerline,
λ	modified slenderness,
Λ	eigenvalue, proportional to the square of the eigenfrequencies,
ν	Poisson ratio,
ξ, η, ζ	coordinate axes of the applied curvilinear coordinate-system,
ρ_a	average density of the cross-section,
ρ_o	initial radius of the (E weighted) centerline,
$\bar{\rho}_o$	radius of the neutral axis,
σ_ξ	normal stress,
$\tau_{\eta\xi}, \tau_{\zeta\xi}$	shear stresses,
φ	angle coordinate,
χ^2	parameter, $\chi^2 = 1 - m\varepsilon_m$ if $m\varepsilon < 1$, otherwise $\chi^2 = m\varepsilon_m - 1$
$\mathbf{\Psi}$	tensor of infinitesimal rotations,
$\psi_{o\eta}$	rigid body rotation on the centerline about the axis η,
ψ	angle coordinate.

Further notational conventions:

$(...)^{(i)}$	the i-th derivative with respect to the angle coordinate,
$(...)_b$	denotes the increments of some physical quantities,
$(...)^*$	denotes the quantities that belong to the buckled equilibrium,
$\delta\,(...)$	denotes virtual quantities,
∇	Hamilton operator.

DOI: 10.14750/ME.2016.008

CHAPTER 1

Preliminaries & Aims

1.1. Heterogeneous curved beams

Curved (circular, parabolic, sinusoidal, shallow, deep, etc.) beams are widespread used in various practical engineering applications for their favourable load carrying capabilities. We mention, for instance, arch bridges and their role as stiffeners in roof- and shell structures. Moreover, they can have vital functions as machine parts: like crane hooks or clampers.

Beams are said to be curved when the so-called centerline (or centroidal axis) has an initial curvature. For circular beams this curvature is apparently constant.

In many applications, for geometrical reasons, curved beams are more suitable than straight ones. Let us see a simple example. If we consider a straight and a curved beam – both loaded in the middle – then the straight member is subject to shear and bending while the curved beam is besides under compression. This latter kind of stress is generally the most preferred one and, for this property, the load carrying capabilities improve with less deformations. Therefore, in many cases, curved beams better withstand loads.

With technology developing and production volumes increasing it is gradually getting cheaper and cheaper to manufacture nonhomogeneous (heterogeneous or inhomogeneous) curved beams, such as composites, laminates, sandwich structures, etc. The benefits of such structural members can be the reduced weight, improved corrosion, fatigue and chemicals resistance and higher strength. Thus, there is a continuous need to develop appropriate mechanical models predicting the behavior of these members under loading.

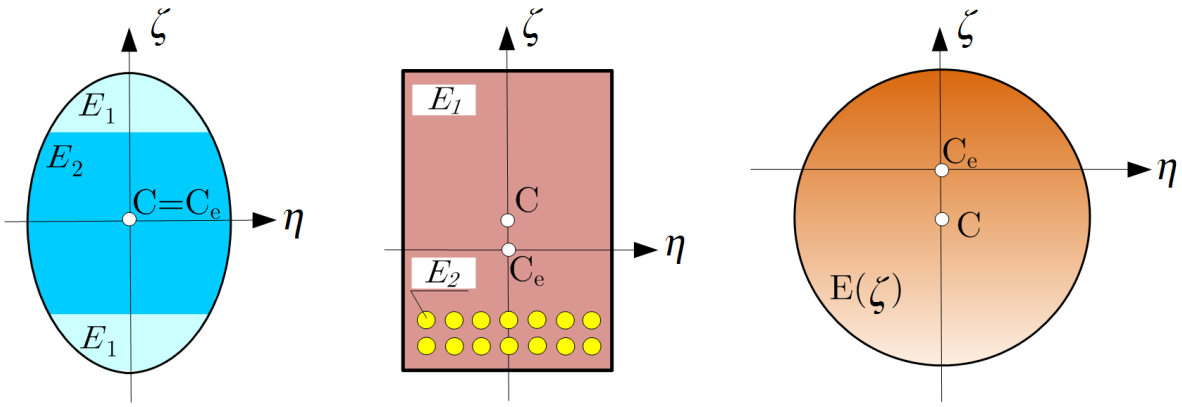

FIGURE 1.1. Some possible nonhomogeneous symmetric cross-sections.

A class of inhomogeneity (heterogeneity) this thesis aims to deal with is called cross-sectional inhomogeneity. It means that the material parameters, like Young's modulus E and the Poisson ratio ν can be functions of the cross-sectional coordinates η, ζ assuming that the symmetry relations $E(\eta,\zeta) = E(-\eta,\zeta)$ and $\nu(\eta,\zeta) = \nu(-\eta,\zeta)$ are satisfied. The material distribution can be continuous, or constant over each segment of the cross-section. In Figure 1.1 point C denotes the geometrical center, and C_e is the E-weighted centroid. For circular beams with cross-sectional inhomogeneity, I intend to deal with three mechanical issues as detailed in the forthcoming.

DOI: 10.14750/ME.2016.008

1.2. Stresses in curved beams

The mechanical behaviour of curved beams has been a topic of interest since the 19^{th} century. The very first related source – found by the author – is a book by Bresse [**1**]. He managed to establish relations between the displacement field and the axial force and bending moment. Winkler [**2**] was the first to propose a formula for the normal stress distribution in curved beams. Meanwhile, Grashof is known for introducing an equilibrium method for the calculation of the shear stress [**3**]. The early results and many additional citations are well collected in the scientific works [**4**, **5**, **6**, **7**].

Curved beams are still subject to intense interest by scientist. On the one hand because of their important role and advantageous properties in various structures and on the other hand due to the spread of nonhomogeneous members.

Well-known formulae for the stress distributions, the deflections of homogeneous straight and curved beams under concentrated and distributed loads can nowadays be found in a bunch of scientific works (books, articles, lecture notes) – see, e.g. [**8**,**9**,**10**,**11**,**12**,**13**,**14**,**15**]. Interestingly, it seems that the relation for the normal stress distribution by Winkler is attributed to Grashof in Hungarian textbooks – see, for instance, [**8**, **12**, **13**] on contrary to [**16**] by Timoshenko. The reason for this misuse might be due to the results achieved by Grashof for cylindrical shells.

There are also some recent and at the same time relevant results which are worthy of mentioning here. A common thing of these is the assumption of a linearly elastic, isotropic constitutive equation.

Tolf [**17**] analytically investigates stresses in bent curved beams made of fibre-reinforced plastic. He finds that the homogeneous model approximates the stresses quite well indeed. Ascione and Fraternali [**18**] use a penalty-technique for curved laminated Timoshenko beams, including warping effects. They have developed a finite element technique to obtain the stresses. Segura and Armengaud [**19**] propose simple analytical formulae for the normal and shearing stresses under bending loads. The normal stress distribution due to the bending moment and axial force is hyperbolic over the cross-section. In addition, the authors have extended Bredt's formula for composite curved beams in order to obtain the shear stresses. Venkatarman and Sankar [**20**] contribute to the static analysis of straight sandwich beams with functionally graded core using the Euler-Bernoulli hypothesis. Young's modulus varies exponentially over the beam thickness. Aimin [**21**] determines the shear stresses in curved composite beams after deriving the governing integral equations. In this way not only the equilibrium equations but also the boundary conditions are satisfied. Ecsedi and Dluhi [**22**] analyse the static bending problem of nonhomogeneous non-shear deformable circular beams and rings. Daouadji et al. [**23**] investigate functionally graded straight cantilever beams (Young's modulus varies continuously through the thickness) from the aspect of a stress function approach. Ecsedi and Lengyel [**24**] consider two-layered elastic circular Euler-Bernoulli beams with weak shear connection (interlayer slip) and provide exact solutions to the displacement and stress fields.

Using the core idea of cross-sectional inhomogeneity [**8**, **25**] it is my

Objective 1 to generalize some classical results valid for homogeneous materials in simple closed-form. These investigations would lead to the following results:

- Generalization of two elementary relationships (valid for homogeneous curved beams), that provide the normal stress caused by an axial force and a bending moment, for curved beams with cross-sectional inhomogeneity.
- Setting up a further formula for computing the shearing stress.
- In addition, a formula for the shear correction factor should also be derived.

DOI: 10.14750/ME.2016.008

– The new results for the stresses should be compared with finite element (FE) computations.

1.3. Stability issues of curved beams

As buckling of beams is a common way of failure in engineering applications, it has been an important subject to investigations for quite a while. The pioneer of this field is Euler who, in 1757, published his well-known formula for the critical (buckling) load of straight bars under compression [**26**]. Since then, a vast amount of novel models have been established. These analytical/numerical investigations include in-plane/out-of-plane, static/dynamic, elastic/elasto-plastic stability of shear-deformable/non-shear-deformable shallow/deep circular/sinusoidal/ parabolic homogeneous/heterogeneous isotropic/anisotropic 1D/3D curved beams/arches with stiff/elastic supports under concentrated/distributed time-independent/dependent loads. A suitable collection of some relevant results can be found in recent textbooks [**27**, **28**, **29**, **30**].

The foremost models concerning the static elastic stability of curved beams were based on the inextensibility of the centerline – see, e.g. article [**31**] by Hurlbrink, who managed to determine the critical pressure of clamped beams. Then Chwalla and Kollbrunner made a huge progress [**32**] as they showed that the extensibility of the centerline should be accounted, otherwise the mechanical models can significantly overestimate the critical load. An extract of the most important results achieved before the 1960s is gathered in book [**33**] by Timoshenko.

Stability issues got in the spotlight during the 1960s. Book [**34**] by Bolotin, among many other topics, is devoted to the dynamic stability of elastic systems involving, e.g. (curved) beams. In [**35**], Schreyer and Masur provide exact analytical solution for a fixed-fixed shallow arch with rectangular cross-section. Papers [**36**, **37**] by DaDeppo are devoted to the determination of the critical load of deep circular beams, which are subjected to a vertical force. Assuming an inextensible centerline, it is shown that quadratic terms should be accounted in the analysis. Papers [**38**, **39**] by Dym are concerned with the buckling and post-buckling behaviour of pinned shallow arches under dead pressure using a continuum model. A summary of these results is also published in book [**40**]. Thesis [**41**] by Szeidl uses analytical methods to determine the Green function matrices of extensible pinned and fixed circular beams and, moreover, determines not only the natural frequencies but also the critical loads if the beams are subjected to a radial dead load whose Fourier series is known. As regards the dynamic behaviour of curved beams survey papers [**6**, **7**, **42**] provide an adequate collection.

There have also been many attempts to tackle the stability problem using a finite element (FE) algorithm under various assumptions – see, e.g. [**43**, **44**, **45**, **46**]. Although higher-order curvature terms are not included into these models, the authors assume that the membrane strain is a quadratic function of the rotation field, while the bending moment is linear in terms of the generalized displacements. Dawe [**47**] approximates deep and shallow arches using the theory of shallow members. More strain-displacement hypotheses are tested (Vlasov, Marguerre) as well as multiple curved elements. A conclusion is that the use of shallow elements for deep arches might result in substantial errors. Fifth-order polynomials seem to provide excellent results even for a sole element. His subsequent work [**48**] is based on the deep-arch theory for the approximation. Loula et al. [**49**] use the Hellinger-Reissner variational principle and introduce the so-called mixed Petrov-Galjorkin FEM for shear-deformable circular beams. A benefit of this technique is that there is no membrane or shear locking. Flores and Godoy [**50**] discretise 3D continuums to determine the critical load both for limit point and bifurcation buckling. Pi et al. [**51**] develop a nonlinear model which is

DOI: 10.14750/ME.2016.008

based on finite rotations. They account for the pre-buckling deformations which – according to the authors – happen to be significant.

Palazotto et al. [**52**, **53**] assume large displacements and rotations and compare five models for the stability of straight and curved beams. Paper [**54**] by Szabó is devoted, among others, to the issue of how to incorporate the fact that the body considered (a circular ring) can have a rigid body motion into the stability investigations. Rajasekaran [**55**] deals with the stability and vibrations of curved beams with a new differential transformation element method: instead of one sixth-order differential equation the author solves six first-order equations.

In the open literature from the recent past, interestingly, there can scarcely be found account for elastic supports. However, as structural members are often connected to each other and they provide elastic restraints, it is worth including these effects. The rotational restraints or those obstructing the displacements can hugely affect the critical load [**56**, **57**]. Plaut accounts for stiffening elastic supports in [**58**]. Yang and Tong [**59**] consider horizontal elastic supports and a vertically distributed uniform load when investigating arches with a linear model.

Nowadays, Pi, Bradford and their co-authors have been contributing to the stability of homogeneous (mainly shallow) arches through thoroughly investigating their new geometrically nonlinear model. Pi et al. have evaluated it for various loads (distributed, concentrated) and boundary conditions (pinned, fixed, elastic supports, mixed supports, etc.) – see [**56**,**57**,**60**,**61**,**62**,**63**,**64**]. Some of these articles also involve investigations concerning the post-buckling behaviour. The authors have drawn the conclusion that both the pre-buckling deformations and the nonlinearities have substantial effect on the permissible load. Progress has also been made in the dynamic stability of shallow arches [**65**, **66**, **67**]. In the previous articles the loading is a sudden concentrated or distributed force. The core idea is based on the method of conservation of energy. It has turned out that the dynamic critical load is always lower than the static.

A common thing of the previously cited works is the assumption of a homogeneous material. Shafiee et al. [**68**], among other topics, study functionally graded (FGM) curved beams from the aspect of in- and out-of-plane buckling behaviour. The linear model leads to an eigenvalue problem. Kim and Chaudhuri [**69**] consider the post-buckling behaviour of laminated thin shallow arches under a concentrated load at the crown point with the aid of the Rayleigh-Ritz method. The infinitesimal rotations are nonlinear as in most of the formerly mentioned articles. Xi et al. [**70**] assume FGM arches (the material composition can vary in the direction of the thickness) under uniformly distributed radial follower load and geometric nonlinearities to tackle the stability issue. Article [**71**] by Vo and Thai is devoted to the stability and vibrations of composite beams using a refined shear deformation theory. Parabolic variation of shear strains through the depth of the beam is assumed. Fraternali et al. [**72**] have developed a geometrically nonlinear FE model to investigate the stability and post-buckling behaviour of composite curved beams. The rotations and shear strains are moderately large and the material is bimodular. Bateni and Eslami [**73**] use the same kinematical hypotheses as in [**61**] but the arch is made of FGM – the material composition follows the Voight-rule of mixture.

On the basis of this overview, no examinations have been carried out concerning the stability problem of circular beams under the assumption of cross-sectional inhomogeneity.

Within the frames of what has been written above my

Objective 2 is summarized in the following two items.

- I intend develop a new nonlinear model for non-strictly shallow curved beams from the principle of virtual work. It is aimed to be more accurate than, e.g. [**61**, **74**] and should be applicable to cross-sectional inhomogeneity as well.

DOI: 10.14750/ME.2016.008

– I aim to evaluate the new model for pinned-pinned, fixed-fixed and rotationally restrained supports provided that the beam is subjected to a central concentrated load at the crown point. This would involve the determination of the critical loads both for symmetric snap-through and antisymmetric bifurcation buckling. At the same time the typical buckling ranges and its endpoints are also sought. Comparison of the results with those available in the literature and with the Abaqus commercial FE software is also an objective.

1.4. Vibrations of curved beams

The first source (found by the author) in relation with the free vibrations of curved beams is article [**75**] by Den Hartog, published in 1928. Further notable contributions in the middle of the last century were devoted to this topic in [**76**, **77**, **78**, **79**]. All these works assume the inextensibility of the centerline.

Szeidl in his PhD thesis [**41**] investigates how the extensibility of the centerline can affect the free vibrations of planar circular beams under a constant radial load. The applied theory is linear. The author obtains solutions using numerical procedures. One of these is based on the Green function matrix. With this in hand, the related boundary value problem is transformed to a problem governed by Fredholm integral equations. Three important survey papers were devoted to the vibrations of curved beams during the 1980-90s: [**6**] by Márkus and Nánási, [**42**] by Laura and Maurizi, and [**7**] by Chidamparam and Leissa.

Qatu and Elsharkawy provide exact solutions to the free vibrations of laminated deep arches in [**80**]. Kang et al. [**81**] determine the frequencies (eigenvalues) for the in-plane and out-of-plane vibrations of circular Timoshenko arches. Both rotatory inertia and shear deformations are accounted. The differential quadrature method is used to get the solutions. Tüfekçi and Arpaci [**82**] managed to gain exact analytical solutions for the in-plane free harmonic vibrations of circular arches. The authors account for the extensibility of the centerline and also for the transverse shear and rotatory inertia effects. Krishnan and Suresh [**83**] developed a shear-deformable FE model to tackle the problem. When there is a constant vertical distributed load, article [**84**] by Huang presents some solutions. Paper [**85**] by Kanga et al. takes point discontinuities, like elastic supports and masses, into account when dealing with the free vibrations. Ecsedi and Dluhi [**22**] analyse some dynamic features of non-homogeneous simply supported curved beams and closed rings. Here the kinematical hypothesis is formally different but mathematically equivalent to that I use in the forthcoming investigations.

Article [**86**] by Lawther is also worthy of mentioning as it tackles the problem of how a pre-stressed state of a body can influence its natural frequencies. He concludes that for multi-parameter problems the eigenvalue of the related solution is described by interaction curves in an eigenvalue space and every such eigenvalue solution has an associated eigenvector. If all points on a curve have the same eigenvector it means that the curve is actually a straight line. Ozturk [**87**] presents a FE model for the free planar vibrations of curved beams. The model is derived from cantilever beams, which are under a vertical force at the free end by fixing it after the deformations. Elastic foundations are taken into account by Çalim [**88**]. Hajianmaleki and Qatu [**89**] consider laminated curved beams. Survey paper [**90**] by the previous two authors reviews the recent past with many citations included. Kovács [**91**] deals with the vibrations of layered arches assuming the possibility of both perfect and even imperfect bonding between any two nearby layers. Wu et al. [**92**] obtain exact solutions (determine the zeros of the frequency determinant) when the curved element carries concentrated elements, including mass moments and inertias. Article [**93**] by Juna et al. is devoted to the free vibrations of laminated curved beams using the trigonometric shear deformation theory. The dynamic stiffness matrix is obtained from the exact solutions

DOI: 10.14750/ME.2016.008

of the related differential equations. This paper is in fact the sequel of [**94**] which deals with straight beams. Nowadays, the dynamic behaviour of FGM straight and curved beams are also of increasing interest – see, e.g. [**95**, **96**, **97**, **98**, **99**].

Overall, in the open literature there are few solutions devoted to the vibrations of beams using the Green function. Here we mention some of these. Szeidl et al. [**100**] determine the natural frequencies of pinned and fixed circular arches under a distributed load using this technique. Kelemen [**101**] extends the former investigations. She provides the natural frequencies as a function of a constant distributed load. Abu-Hilal [**102**] investigates the dynamic response of prismatic damped straight Euler-Bernoulli beams subjected to distributed and concentrated loads. The author obtains exact solutions. Li et al. [**103**] investigate the forced vibrations of straight (Timoshenko) beams. The beam is under a time harmonic concentrated load. Damping effects at the ends are taken into account. There are also some further attempts to investigate the dynamic behaviour of structures (response under periodic loads, displacements, etc.). Lueschen and Bergman [**104**] investigate uniform Timoshenko beams after providing the exact expression of the corresponding Green function. Foda and Abduljabbar [**105**] and Mehri et al. [**106**] determine the deflections and present parametric studies of a straight beam under the effect of a moving mass. Kukla and Zamojska [**107**] deal with the free vibrations of stepped beams. It seems, however, to be an open issue how a central concentrated load affects the in-plane vibrations of heterogeneous circular beams if they are pinned-pinned or fixed-fixed at the endpoints.

Within the frames of what has been mentioned above

Objective 3 is related to the in-plane vibrations of loaded circular beams with cross-sectional inhomogeneity. In details, my goals are

- to derive those boundary value problems which can make it clear how a radial load affects the natural frequencies of pinned and fixed beams,
- to construct the Green function matrix for pinned-pinned and fixed-fixed beams by taking into account that the central load at the crown point can either be compressive or tensile (four Green function matrices are to be determined),
- to reduce the eigenvalue problems set up for the natural frequencies (which depend on the load) to eigenvalue problems governed by homogeneous Fredholm integral equation systems (four integral equation systems should be established),
- to replace these eigenvalue problems with algebraic ones and to solve them numerically,
- to clarify how the vertical force at the crown point affects the frequencies of the vibrations (if there is no concentrated force, it is expected to get back the results valid for the free vibrations),
- to verify some results by FEM or by experimental studies.

DOI: 10.14750/ME.2016.008

CHAPTER 2

Stresses in heterogeneous circular beams

2.1. Kinematical hypothesis

The investigations are carried out in the orthogonal curvilinear coordinate system that is shown in Figure 2.1. Lagrangian description is applied throughout this thesis. It is assumed that (a) each cross-section is uniform and symmetric with respect to the axis ζ [consequently, the beam is symmetric to the coordinate plane $(\xi = s, \zeta)$]; (b) the E-weighted first moment of the cross-section with respect to the axis η – this quantity is denoted by $Q_{e\eta}$ – is equal to zero:

$$Q_{e\eta} = \int_A E(\eta, \zeta)\, \zeta \, \mathrm{d}A = 0 \tag{2.1.1}$$

and (c) Young's modulus E and the Poisson ratio ν are functions of the coordinates η, ζ in such a way that $E = E(\eta, \zeta) = E(-\eta, \zeta)$ and $\nu = \nu(\eta, \zeta) = \nu(-\eta, \zeta)$ – this distribution is called cross-sectional inhomogeneity [**25**]. The axis $\xi = s$ intersects the plane of the cross-section in the point C_e, which is referred to as the E-weighted center of the cross-section (in contrast to the point C, which is the geometrical center of the cross-section).

The coordinate line $\xi = s$ is the E-weighted centerline (or centerline in short) of the curved beam and s is the arc coordinate.

For the sake of later considerations we shall introduce the concepts of the E-weighted area (tensile stiffness) and moment of inertia (bending stiffness) with respect to the axis η:

$$A_e = \int_A E(\eta, \zeta)\, \mathrm{d}A\,, \qquad I_{e\eta} = \int_A E(\eta, \zeta)\, \zeta^2 \mathrm{d}A\,. \tag{2.1.2}$$

These notions have previously been introduced for straight beams in paper [**25**] by Baksa and Ecsedi.

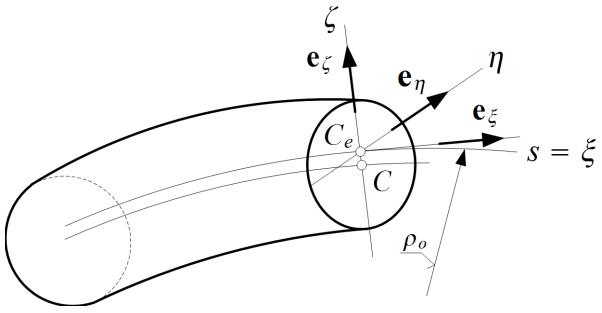

FIGURE 2.1. The coordinate system and the E-weighted centerline.

The orthogonal unit vectors $\mathbf{e}_\xi(s)$, $\mathbf{e}_\eta$ and $\mathbf{e}_\zeta(s)$ of the coordinate lines ξ, η and ζ are shown in Figure 2.1. Let ρ_o be the constant radius of the E-weighted centerline in the initial configuration. It is easy to check that $\mathbf{e}_\xi(s)$, and $\mathbf{e}_\zeta(s)$ satisfy the relations

$$\frac{\mathrm{d}\mathbf{e}_\xi}{\mathrm{d}s} = -\frac{1}{\rho_o}\mathbf{e}_\zeta\,, \qquad \frac{\mathrm{d}\mathbf{e}_\zeta}{\mathrm{d}s} = \frac{1}{\rho_o}\mathbf{e}_\xi \quad \text{and} \quad \mathbf{e}_\zeta \times \mathbf{e}_\xi = \mathbf{e}_\eta = \text{constant}\,. \tag{2.1.3}$$

DOI: 10.14750/ME.2016.008

The symbol $\times$ denotes the vector product, while the Hamilton operator ∇ assumes the form

$$\nabla = \frac{\rho_o}{\rho_o + \zeta}\frac{\partial}{\partial s}\mathbf{e}_\xi + \frac{\partial}{\partial \eta}\mathbf{e}_\eta + \frac{\partial}{\partial \zeta}\mathbf{e}_\zeta \,. \tag{2.1.4}$$

We further assume that (a) the cross-section has a translation and a rigid body rotation about the axis η, i.e. it remains a plane surface during the deformations and (b) the deformed centerline remains perpendicular to the cross-section (Euler-Bernoulli theory). Under these conditions

$$\mathbf{u} = \mathbf{u}_o + \psi_{o\eta}\zeta\mathbf{e}_\xi = w_o\mathbf{e}_\zeta + (u_o + \psi_{o\eta}\zeta)\mathbf{e}_\xi \tag{2.1.5}$$

is the displacement field of the cross-section, in which $\mathbf{u}_o = u_o\mathbf{e}_\xi + w_o\mathbf{e}_\zeta$ and $\boldsymbol{\psi} = \psi_{o\eta}\mathbf{e}_\eta$ are the displacement vector and the rotation on the E-weighted centerline, respectively. As is well-known the cross-product

$$\boldsymbol{\psi} = -\frac{1}{2}(\mathbf{u} \times \nabla) \tag{2.1.6}$$

yields the rigid body rotation. Thus

$$\boldsymbol{\psi}|_{\zeta=0} = \psi_{o\eta}\mathbf{e}_\eta = -\frac{1}{2}\left(w_o\mathbf{e}_\zeta + (u_o + \psi_{o\eta}\zeta)\mathbf{e}_\xi\right) \times \left(\frac{\rho_o}{\rho_o + \zeta}\frac{\partial}{\partial s}\mathbf{e}_\xi + \frac{\partial}{\partial \eta}\mathbf{e}_\eta + \frac{\partial}{\partial \zeta}\mathbf{e}_\zeta\right)\Bigg|_{\zeta=0} = \\ = \frac{1}{2}\left[\left(\frac{u_o}{\rho_o} - \frac{\mathrm{d}w_o}{\mathrm{d}s}\right) + \psi_{o\eta}\right]\mathbf{e}_\eta \tag{2.1.7}$$

is the rotation on the centerline, that is

$$\psi_{o\eta} = \frac{u_o}{\rho_o} - \frac{\mathrm{d}w_o}{\mathrm{d}s}. \tag{2.1.8a}$$

It is the only nonzero coordinate in the antisymmetric tensor of infinitesimal rotations $\boldsymbol{\Psi}$:

$$\boldsymbol{\Psi} = \frac{1}{2}\left(\mathbf{u} \circ \nabla - \nabla \circ \mathbf{u}\right) \,, \quad \psi_\eta = \psi_\eta|_{\zeta=0} = \psi_{o\eta} = \mathbf{e}_\xi \cdot \boldsymbol{\Psi} \cdot \mathbf{e}_\eta \,, \quad \psi_\xi = \psi_{o\xi} = \psi_\zeta = \psi_{o\zeta} = 0. \tag{2.1.8b}$$

Further, we have the curvature change in the form

$$\frac{\mathrm{d}\psi_{o\eta}}{\mathrm{d}s} = \kappa_o = -\frac{\mathrm{d}}{\mathrm{d}s}\left(\frac{\mathrm{d}w_o}{\mathrm{d}s} - \frac{u_o}{\rho_o}\right). \tag{2.1.8c}$$

With the diadic product

$$\mathbf{u} \circ \nabla = \left[w_o\mathbf{e}_\zeta + (u_o + \psi_{o\eta}\zeta)\,\mathbf{e}_\xi\right] \circ \left(\frac{\rho_o}{\rho_o + \zeta}\frac{\partial}{\partial s}\mathbf{e}_\xi + \frac{\partial}{\partial \eta}\mathbf{e}_\eta + \frac{\partial}{\partial \zeta}\mathbf{e}_\zeta\right) = \\ = \frac{\rho_o}{\rho_o + \zeta}\left(\frac{\mathrm{d}u_o}{\mathrm{d}s} + \frac{w_o}{\rho_o} + \zeta\frac{\mathrm{d}\psi_{o\eta}}{\mathrm{d}s}\right)\mathbf{e}_\xi \circ \mathbf{e}_\xi + \\ + \psi_{o\eta}\mathbf{e}_\xi \circ \mathbf{e}_\zeta + \left(\frac{\rho_o}{\rho_o + \zeta}\frac{\mathrm{d}w_o}{\mathrm{d}s} - \frac{u_o + \zeta\psi_{o\eta}}{\rho_o + \zeta}\right)\mathbf{e}_\zeta \circ \mathbf{e}_\xi + ((...)) \tag{2.1.9}$$

in hand we get the axial strain in the linearized Green-Lagrange strain tensor $\boldsymbol{E}^L$ as

$$\varepsilon_\xi = \mathbf{e}_\xi \cdot \boldsymbol{E}^L \cdot \mathbf{e}_\xi = \mathbf{e}_\xi \cdot \frac{1}{2}\left(\mathbf{u} \circ \nabla + \nabla \circ \mathbf{u}\right) \cdot \mathbf{e}_\xi = \\ = \frac{\rho_o}{\rho_o + \zeta}\left(\frac{\mathrm{d}u_o}{\mathrm{d}s} + \frac{w_o}{\rho_o} + \frac{\mathrm{d}\psi_{o\eta}}{\mathrm{d}s}\zeta\right) = \frac{\rho_o}{\rho_o + \zeta}\left(\varepsilon_{o\xi} + \zeta\kappa_o\right) \,. \tag{2.1.10}$$

Here

$$\varepsilon_{o\xi} = \varepsilon_\xi|_{\zeta=0} = \frac{\mathrm{d}u_o}{\mathrm{d}s} + \frac{w_o}{\rho_o} \tag{2.1.11}$$

is the axial strain on the E-weighted centerline.

DOI: 10.14750/ME.2016.008

Some so-called E-weighted reduced quantities like the reduced area, first moment and moment of inertia are defined by the following relations

$$A_{eR} = \int_A \frac{\rho_o}{\rho_o + \zeta} E(\eta,\zeta)\mathrm{d}A \ , \ Q_{eR} = \int_A \frac{\rho_o}{\rho_o + \zeta} E(\eta,\zeta)\zeta\mathrm{d}A \ , \ I_{eR} = \int_A \frac{\rho_o}{\rho_o + \zeta} E(\eta,\zeta)\zeta^2\mathrm{d}A. \tag{2.1.12}$$

We shall now clarify how these are related to A_e, $Q_{e\eta}$ and $I_{e\eta}$. Using the power series of the fraction $\rho_o/\left(\rho_o + \zeta\right)$ we have

$$A_{eR} = \int_A \left(1 - \frac{\zeta}{\rho_o} + \frac{\zeta^2}{\rho_o^2} - ...\right) E(\eta,\zeta)\mathrm{d}A \cong \underbrace{\int_A E(\eta,\zeta)\mathrm{d}A}_{A_e} - \frac{1}{\rho_o}\underbrace{\int_A E(\eta,\zeta)\zeta\mathrm{d}A}_{Q_{e\eta}} =$$

$$= A_e - \frac{Q_{e\eta}}{\rho_o} = A_e \, , \tag{2.1.13a}$$

$$Q_{eR} = \int_A \left(1 - \frac{\zeta}{\rho_o} + \frac{\zeta^2}{\rho_o^2} - ...\right) \zeta E(\eta,\zeta)\mathrm{d}A \cong$$

$$\cong \underbrace{\int_A \zeta E(\eta,\zeta)\mathrm{d}A}_{Q_{e\eta}} - \frac{1}{\rho_o}\underbrace{\int_A \zeta^2 E(\eta,\zeta)\mathrm{d}A}_{I_{e\eta}} = Q_{e\eta} - \frac{I_{e\eta}}{\rho_o} = -\frac{I_{e\eta}}{\rho_o} \tag{2.1.13b}$$

and

$$I_{eR} = \int_A \left(1 - \frac{\zeta}{\rho_o} + \frac{\zeta^2}{\rho_o^2} - ...\right) \zeta^2 E(\eta,\zeta)\mathrm{d}A \cong I_{e\eta} \tag{2.1.13c}$$

because $Q_{e\eta} = 0$ – see (2.1.1). For homogeneous beams we shall use the notations AE, $Q_\eta E$ and $I_\eta E$ instead of A_e, $Q_{e\eta}$ and $I_{e\eta}$.

2.2. Formulae for the normal stress distribution

2.2.1. Generalization of the Grashof formula. It is clear that the axial force and the bending moment are

$$N = \int_A \sigma_\xi \mathrm{d}A \, , \qquad M = \int_A \zeta\sigma_\xi \mathrm{d}A \, . \tag{2.2.1}$$

In the sequel we shall assume that the inequality $\sigma_\xi \gg \sigma_\eta, \sigma_\zeta$ concerning the normal stresses in the second Piola-Kirchhoff stress tensor $\boldsymbol{S}$ holds. Thus, equation $\sigma_\xi = E(\eta,\zeta)\varepsilon_\xi$ is Hooke's law. Upon substitution of Hooke's law and then equation (2.1.10) into $(2.2.1)_1$ we have

$$N = \varepsilon_{o\xi} \int_A \frac{\rho_o}{\rho_o + \zeta} E(\eta,\zeta)\mathrm{d}A + \kappa_o \int_A \frac{\rho_o}{\rho_o + \zeta} E(\eta,\zeta)\zeta\mathrm{d}A = \varepsilon_{o\xi} A_{eR} + \kappa_o Q_{eR} \, . \tag{2.2.2a}$$

As for the bending moment, in a similar way, we obtain

$$M = \varepsilon_{o\xi} \int_A \frac{\rho_o}{\rho_o + \zeta} E(\eta,\zeta)\zeta\mathrm{d}A + \kappa_o \int_A \frac{\rho_o}{\rho_o + \zeta} E(\eta,\zeta)\zeta^2\mathrm{d}A = \varepsilon_{o\xi} Q_{eR} + \kappa_o I_{eR} \, . \tag{2.2.2b}$$

After solving equation system (2.2.2) we get $\varepsilon_{o\xi}$ and κ_o in terms of the inner axial force N and bending moment M:

$$\varepsilon_{o\xi} = \frac{1}{Q_{eR}^2 - A_{eR} I_{eR}} \left(M Q_{eR} - N I_{eR}\right) \ , \quad \kappa_o = \frac{1}{Q_{eR}^2 - A_{eR} I_{eR}} \left(N Q_{eR} - M A_{eR}\right) \, . \tag{2.2.3}$$

Let us now insert these solutions into equation (2.1.10). In this way we get the 'exact' axial strain as a function of N and M in such a way that

$$\varepsilon_\xi = \frac{\rho_o}{\rho_o + \zeta} \ \frac{1}{A_{eR} I_{eR} - Q_{eR}^2} \left[\left(I_{eR} - \zeta Q_{eR}\right) N - M \left(Q_{eR} - \zeta A_{eR}\right)\right] \, . \tag{2.2.4}$$

DOI: 10.14750/ME.2016.008

With the former expression in hand we can rewrite the formula for the normal stress:

$$\sigma_\xi = E(\eta,\zeta)\varepsilon_\xi = E(\eta,\zeta)\,\frac{\rho_o}{\rho_o+\zeta}\,\frac{1}{A_{eR}I_{eR}-Q_{eR}^2}\left[\left(I_{eR}-\zeta Q_{eR}\right)N - M\left(Q_{eR}-\zeta A_{eR}\right)\right]\,. \tag{2.2.5}$$

In the sequel an attempt is made to simplify (2.2.5). Concerning the denominator, the following approximation holds

$$A_{eR}I_{eR}\left(1-\frac{Q_{eR}^2}{I_{eR}A_{eR}}\right) \simeq A_{eR}I_{eR}\left(1-\frac{1}{\rho_o^2}\frac{I_{e\eta}^2}{A_{eR}I_{eR}}\right) = A_{eR}I_{eR}\left(1-\frac{1}{\rho_o^2}\frac{I_{e\eta}}{A_{eR}}\right) \simeq A_{eR}I_{eR} \tag{2.2.6}$$

since

$$1 \gg \frac{1}{\rho_o^2}\frac{I_{e\eta}}{A_{eR}}\,.$$

Owing to this result we can equivalently rewrite formula (2.2.4) in the form

$$\begin{aligned}\varepsilon_\xi &\approx \frac{\rho_o}{\rho_o+\zeta}\,\frac{1}{A_{eR}I_{eR}}\left[\left(I_{eR}-\zeta Q_{eR}\right)N - M\left(Q_{eR}-\zeta A_{eR}\right)\right] = \\ &= \left(1-\zeta\frac{Q_{eR}}{I_{eR}}\right)\frac{\rho_o}{\rho_o+\zeta}\frac{N}{A_{eR}} + \left(-\frac{Q_{eR}}{A_{eR}I_{eR}}+\frac{\zeta}{I_{eR}}\right)\frac{\rho_o}{\rho_o+\zeta}M\,.\end{aligned} \tag{2.2.7}$$

Recalling approximations (2.1.13) one can easily accept the validity of equations

$$\frac{Q_{eR}}{I_{eR}} \simeq -\frac{1}{\rho_o}\frac{I_{e\eta}}{I_{eR}} \simeq -\frac{1}{\rho_o}\,, \qquad \frac{1}{\rho_o}\frac{\rho_o}{\rho_o+\zeta}\frac{M}{A_{eR}} \simeq \frac{M}{\rho_o A_{eR}}\,. \tag{2.2.8}$$

Substituting now the last two expressions into (2.2.7) and then the strain into Hooke's law, we arrive at

$$\sigma_\xi = E(\eta,\zeta)\left(\frac{N}{A_{eR}}+\frac{M}{\rho_o A_{eR}}+\frac{M}{I_{eR}}\frac{\rho_o}{\rho_o+\zeta}\zeta\right)\,. \tag{2.2.9}$$

This equation can be considered as the generalization of the Grashof (Winkler) formula, which is valid only for homogeneous curved beams. It can be compared with, e.g. (10.10) in [**13**]:

$$\sigma_\xi = \left(\frac{N}{A}+\frac{M}{\rho_o A}+\frac{M}{I_R}\frac{\rho_o}{\rho_o+\zeta}\zeta\right)\,. \tag{2.2.10}$$

2.2.2. The normal stress under pure bending. English textbooks often contain a formula for the normal stress under the assumption of pure bending – see, for instance, equation (4.71) p. 224 in [**11**]. Our aim is to generalize the cited equation for heterogeneous circular beams. Figure 2.2 displays the cross-section and the geometrical meaning of some notational conventions: ζ_o is the coordinate of the neutral axis with radius $\overline{\rho}_o$, and the radius of an arbitrary point P on the cross-section with coordinate ζ is r ($r=\rho_o+\zeta$). For pure bending – based on the exact equation (2.2.5) –

$$\sigma_\xi = E(\eta,\zeta)\frac{\rho_o}{\rho_o+\zeta}\frac{1}{A_{eR}I_{eR}-Q_{eR}^2}\left(\zeta A_{eR}-Q_{eR}\right)M \tag{2.2.11}$$

is the stress distribution. We intend to manipulate it into a similar form as published in [**11**]. The comparison will be carried out on page 12.

As a first step we shall determine the location of the neutral axis, where $\sigma_\xi = 0$. Based on (2.2.11) its location can be obtained from

$$Q_{eR} = \zeta_o\, A_{eR}\,, \tag{2.2.12}$$

DOI: 10.14750/ME.2016.008

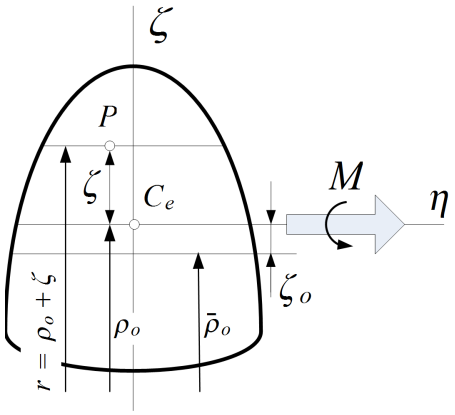

FIGURE 2.2. Some geometrical notations over the cross-section.

or which is the same from equation

$$Q_{eR} = (\rho_o + \zeta_o - \rho_o)\, A_{eR} = (\overline{\rho}_o - \rho_o)\, A_{eR} = \overline{\rho}_o A_{eR} - \rho_o A_{eR} \quad . \tag{2.2.13}$$

Therefore

$$\overline{\rho}_o = \frac{Q_{eR}}{A_{eR}} + \rho_o \tag{2.2.14}$$

is the radius sought. Upon substitution of A_{eR} and Q_{eR} from (2.1.12) this radius assumes the form

$$\begin{aligned}
\overline{\rho}_o = \rho_o + \frac{\int_A E(\eta,\zeta)\zeta\frac{\rho_o}{r}\mathrm{d}A}{\int_A \frac{\rho_o}{r}E(\eta,\zeta)\mathrm{d}A} = \frac{\int_A E(\eta,\zeta)\zeta\frac{\rho_o}{r}\mathrm{d}A + \rho_o^2\int_A \frac{E(\eta,\zeta)}{r}\mathrm{d}A}{\rho_o\int_A \frac{E(\eta,\zeta)}{r}\mathrm{d}A} = \\
= \frac{\frac{1}{\rho_o}\int_A E(\eta,\zeta)\zeta\frac{\rho_o}{r}\mathrm{d}A + \rho_o\int_A \frac{E(\eta,\zeta)}{r}\mathrm{d}A}{\int_A \frac{E(\eta,\zeta)}{r}\mathrm{d}A} = \\
= \frac{\int_A \frac{E(\eta,\zeta)\zeta}{r}\mathrm{d}A + \rho_o\int_A \frac{E(\eta,\zeta)}{r}\mathrm{d}A}{\int_A \frac{E(\eta,\zeta)}{r}\mathrm{d}A} = \frac{\int_A \left[\frac{E(\eta,\zeta)\zeta}{r} + \rho_o\frac{E(\eta,\zeta)}{r}\right]\mathrm{d}A}{\int_A \frac{E(\eta,\zeta)}{r}\mathrm{d}A} = \\
= \frac{\int_A E(\eta,\zeta)\left[\frac{\zeta}{r} + \frac{\rho_o}{r}\right]\mathrm{d}A}{\int_A \frac{E(\eta,\zeta)}{r}\mathrm{d}A} = \frac{\int_A E(\eta,\zeta)\left[\frac{\zeta+\rho_o}{\rho_o+\zeta}\right]\mathrm{d}A}{\int_A \frac{E(\eta,\zeta)}{r}\mathrm{d}A} = \frac{\int_A E(\eta,\zeta)\mathrm{d}A}{\int_A \frac{E(\eta,\zeta)}{r}\mathrm{d}A}.
\end{aligned}$$

If the modulus E is constant the above equation coincides with formula (4.66) in [**11**].

We proceed with the determination of the normal stress. With equation (2.2.14), the term in parentheses in (2.2.11) can be rewritten:

$$\zeta A_{eR} - Q_{eR} = (r - \rho_o)\, A_{eR} + \rho_o A_{eR} - \overline{\rho}_o A_{eR} = (r - \overline{\rho}_o)\, A_{eR}\,. \tag{2.2.15}$$

Taking the inequality $A_{eR}I_{eR} \gg Q_{eR}^2$ into consideration and substituting back the previous term into equation (2.2.11) we obtain

$$\sigma_\xi = E(\eta,\zeta)\frac{1}{r}M\frac{\rho_o}{I_{eR}}\,(r - \overline{\rho}_o) \quad . \tag{2.2.16}$$

One ultimate question is how to transform the quotient ρ_o/I_{eR} into a more favourable form. All the necessary transformation steps are detailed hereinafter

$$\begin{aligned}
I_{eR} = \int_A E(\eta,\zeta)\frac{\rho_o}{r}\zeta^2\mathrm{d}A = \int_A E(\eta,\zeta)\rho_o\frac{\rho_o+\zeta-\rho_o}{r}\zeta\mathrm{d}A = \\
= \int_A E(\eta,\zeta)\rho_o\frac{r-\rho_o}{r}\zeta\mathrm{d}A = \rho_o\int_A E(\eta,\zeta)\zeta\mathrm{d}A - \int_A E(\eta,\zeta)\rho_o^2\frac{1}{r}(r-\rho_o)\mathrm{d}A =
\end{aligned}$$

DOI: 10.14750/ME.2016.008

$$= \underbrace{\rho_o Q_{e\eta}}_{0} - \int_A E(\eta,\zeta)\rho_o^2 \frac{1}{r}(r-\rho_o)\mathrm{d}A = -\rho_o^2 \int_A E(\eta,\zeta)\mathrm{d}A + \rho_o^3 \int_A \frac{E(\eta,\zeta)}{r}\mathrm{d}A =$$

$$= -\rho_o^2 A_e + \rho_o^3 \int_A \frac{E(\eta,\zeta)}{r}\mathrm{d}A = A_e\left(\frac{\rho_o^3}{\overline{\rho}_o} - \rho_o^2\right) =$$

$$= A_e\rho_o^2\left(\frac{\rho_o}{\overline{\rho}_o} - 1\right) = A_e\rho_o^2\left(\frac{\overbrace{\rho_o - \overline{\rho}_o}^{-\zeta_o}}{\overline{\rho}_o}\right) = -A_e\frac{\rho_o^2}{\overline{\rho}_o}\zeta_o\,. \quad (2.2.17)$$

If we introduce the notation $e = -\zeta_o$ and substitute the result obtained into formula (2.2.16) we arrive at the

$$\sigma_\xi = E(\eta,\zeta)\,\frac{M}{r}\,\frac{r-\overline{\rho}_o}{A_e\,e} \quad (2.2.18)$$

final form of the normal stress. This equation is the extension of formula (4.71) p. 224 in [**11**] for beams with cross-sectional inhomogeneity. The formula cited is

$$\sigma_\xi = \frac{M}{r}\,\frac{r-\overline{\rho}_o}{A}\,e \quad (2.2.19)$$

if we use our notations and coordinate system.

2.3. Formula for the shear stress

The next goal is to derive closed-form solution for the calculation of the shear stress. Equilibrium equations will be used for this purpose. This approach results in a relatively simple formula, however, it has the drawback that the kinematical equations are not completely satisfied. The basic concept is well known from the theory of straight beams: we divide a short portion of the beam into two parts and then analyse the equilibrium conditions of one part.

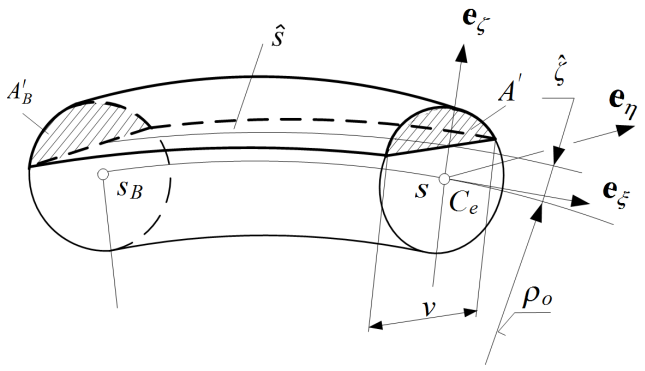

FIGURE 2.3. The investigated portion of the beam.

Consider Figure 2.3 which shows a finite portion of the curved beam with cross-sectional inhomogeneity. The left cross-section with arc coordinate s_B is fixed and the coordinate $s > s_B$ of the right cross-section is regarded as a parameter. We shall use the following assumptions:

(1) the shear stresses $\boldsymbol{\tau}_\xi = \tau_{\eta\xi}\mathbf{e}_\eta + \tau_{\zeta\xi}\mathbf{e}_\zeta$ on the line $\zeta = \hat{\zeta} =$ constant intersect each other in one point which coincides with the intersection point of the tangents to the contour of the cross-section at $\zeta = \hat{\zeta} =$ constant. Consequently, $\tau_{\eta\xi}(\eta) = -\tau_{\eta\xi}(-\eta)$, which means that $\tau_{\eta\xi}(\eta)$ is an odd function of η.
(2) The shear stress $\tau_{\zeta\xi}$ is constant if $\zeta =$ constant.

DOI: 10.14750/ME.2016.008

(3) The bending moment M and the shear force V_ζ are related to each other via equilibrium condition

$$\frac{\mathrm{d}M}{\mathrm{d}s} = -V_\zeta. \tag{2.3.1}$$

(4) The normal stress σ_ξ can be calculated from equation (2.2.9), for which, we assume $N = 0$ – there is no axial force in the cross-section.

For calculating the shear stress $\tau_{\zeta\xi}$ let us consider the part of the beam with outlines drawn in thick in Figure 2.3. It is bounded by the marked endfaces A'_B, A', the cylinder with radius $\rho_o + \hat{\zeta}$ and the lateral surface. By assumption the lateral surface is unloaded.

The equilibrium equation for the considered portion is of the form

$$\int_{A'} (\sigma_\xi \mathbf{e}_\xi(\xi) + \boldsymbol{\tau}_\xi)\,\mathrm{d}A - \int_{A'_B} (\sigma_\xi \mathbf{e}_\xi(\xi) + \boldsymbol{\tau}_\xi)\,\mathrm{d}A - \int_{s_B}^{s} \frac{\rho_o + \hat{\zeta}}{\rho_o} v(\hat{\zeta}) \tau_{\xi\zeta}(\hat{\zeta}) \mathbf{e}_\xi(\xi)\mathrm{d}\xi = \mathbf{0}\,. \tag{2.3.2}$$

If we take into account that the shear stress $-\tau_{\xi\zeta}(\hat{\zeta})\mathbf{e}_\xi(s)$ is constant on the cylindrical surface with radius $\rho_o + \hat{\zeta}$, and the fact that

$$\frac{\rho_o + \hat{\zeta}}{\rho_o} v(\hat{\zeta})\mathrm{d}\xi = \mathrm{d}A$$

is the surface element then it follows that the last integral in (2.3.2) is the resultant of the shear stresses.

Let us differentiate equation (2.3.2) with respect to s. After that (a) substitute (2.1.3) for the derivatives of the unit vectors $\mathbf{e}_\xi$ and $\mathbf{e}_\zeta$; (b) take into account that (i) the integral over A'_B is constant therefore its derivative is zero; (ii) $\tau_{\eta\xi}$ is an odd function of η, therefore its integral is zero; (iii) the derivative of an integral with respect to the upper limit is the integrand itself. The former thoughts lead to

$$\int_{A'} \frac{\mathrm{d}\sigma_\xi}{\mathrm{d}s}\mathbf{e}_\xi \mathrm{d}A - \int_{A'} \frac{\sigma_\xi}{\rho_o}\mathbf{e}_\zeta \mathrm{d}A + \frac{\mathrm{d}}{\mathrm{d}s}\underbrace{\int_{A'} \tau_{\eta\xi}\mathbf{e}_\eta \mathrm{d}A}_{=\mathbf{0}} + \int_{A'} \left(\frac{\mathrm{d}\tau_{\zeta\xi}}{\mathrm{d}s}\mathbf{e}_\zeta + \frac{\tau_{\zeta\xi}}{\rho_o}\mathbf{e}_\xi\right)\mathrm{d}A - \frac{\rho_o + \hat{\zeta}}{\rho_o} v(\hat{\zeta})\tau_{\xi\zeta}(\hat{\zeta})\mathbf{e}_\zeta(s) = \mathbf{0}\,.$$

If we now dot multiply throughout by $\mathbf{e}_\xi$ we obtain

$$\int_{A'} \frac{\mathrm{d}\sigma_\xi}{\mathrm{d}s}\mathrm{d}A + \int_{A'} \frac{\tau_{\zeta\xi}}{\rho_o}\mathrm{d}A - \frac{\rho_o + \hat{\zeta}}{\rho_o} v(\hat{\zeta})\tau_{\xi\zeta}(\hat{\zeta}) = 0\,. \tag{2.3.3}$$

Let $e_{\max}$ be the distance between the top of the cross-section and the point C_e. This is always less than ρ_o for curved beams. The area A' can be given as the product $v(\hat{\zeta})h(\hat{\zeta})$, where $h(\hat{\zeta})$ is less than $e_{\max}$. Consequently,

$$\int_{A'} \frac{\tau_{\zeta\xi}(\eta,\zeta)}{\rho_o}\mathrm{d}A \simeq \frac{1}{\rho_o} h(\hat{\zeta}) v(\hat{\zeta}) \tau_{\xi\zeta}(\hat{\zeta})\,, \qquad \frac{h(\hat{\zeta})}{\rho_o} \ll 1$$

is an upper limit for the second integral in (2.3.3). Really, if we take into account that the shear stress is taken on the line $\hat{\zeta}$ (instead of being taken at inner points of A') we can readily check the validity of the previous statement. On the basis of this estimation, the second term in (2.3.3) can be neglected if we compare it to the third one. Omitting this term results in the equation

$$\int_{A'} \frac{\mathrm{d}\sigma_\xi}{\mathrm{d}s}\,\mathrm{d}A = \frac{\rho_o + \hat{\zeta}}{\rho_o} v(\hat{\zeta})\tau_{\xi\zeta}(\hat{\zeta}) \tag{2.3.4}$$

DOI: 10.14750/ME.2016.008

for the calculation of the shear stress $\tau_{\xi\zeta}(\hat{\zeta})$. After some rearrangements we obtain the average value

$$\tau_{\xi\zeta}(\hat{\zeta}) = \frac{\rho_o}{\rho_o+\hat{\zeta}}\frac{1}{v(\hat{\zeta})}\int_{A'}\frac{\mathrm{d}\sigma_\xi}{\mathrm{d}s}\mathrm{d}A\,. \tag{2.3.5}$$

Upon substitution of the normal stress from (2.2.9) – given that $N=0$ – we have

$$\tau_{\xi\zeta}(\hat{\zeta}) = \frac{\rho_o}{\rho_o+\hat{\zeta}}\frac{1}{v(\hat{\zeta})}\int_{A'}\frac{\mathrm{d}}{\mathrm{d}s}\left[E(\eta,\zeta)\left(\frac{M}{\rho_o A_{eR}}+\frac{M}{I_{eR}}\frac{\rho_o}{\rho_o+\zeta}\zeta\right)\right]\mathrm{d}A\,. \tag{2.3.6}$$

A further transformation yields

$$\begin{aligned}\tau_{\xi\zeta}(\hat{\zeta}) &= \frac{\rho_o}{\rho_o+\hat{\zeta}}\frac{1}{v(\hat{\zeta})}\frac{\mathrm{d}M}{\mathrm{d}s}\int_{A'}\left(\frac{E(\eta,\zeta)}{\rho_o A_{eR}}+\frac{E(\eta,\zeta)}{I_{eR}}\frac{\rho_o}{\rho_o+\zeta}\zeta\right)\mathrm{d}A = \\ &= \frac{\rho_o}{\rho_o+\hat{\zeta}}\frac{1}{v(\hat{\zeta})}\frac{\mathrm{d}M}{\mathrm{d}s}\frac{1}{I_{eR}}\left(\rho_o\frac{I_{eR}}{\rho_o^2 A_{eR}}\int_{A'}E(\eta,\zeta)\mathrm{d}A+\int_{A'}\frac{\rho_o}{\rho_o+\zeta}\zeta E(\eta,\zeta)\mathrm{d}A\right)\,.\end{aligned}$$

Introducing the notations

$$\beta_e = \frac{I_{eR}}{\rho_o^2 A_{eR}};\qquad Q'_{e\eta} = \int_{A'}E(\eta,\zeta)\frac{\rho_o}{\rho_o+\zeta}\zeta\mathrm{d}A,\qquad A'_e = \int_{A'}E(\eta,\zeta)\mathrm{d}A \tag{2.3.7}$$

and recalling (2.3.1) we get the

$$\tau_{\xi\zeta}(\hat{\zeta}) = -\frac{\rho_o}{\rho_o+\hat{\zeta}}\frac{V_\zeta}{I_{eR}\,v(\hat{\zeta})}\left(\rho_o\beta_e A'_e+Q'_{e\eta}\right) \tag{2.3.8}$$

formula for the averaged shear stress. This result is the generalization of the classical formula valid for curved beams made of homogeneous material – see pp. 358-359 in [**13**].

2.3.1. The shear correction factor. If we determine the shear stress distribution over the cross-section using the constitutive equation, then we find it to be constant. However, physically, it is not right: when the shear stress is calculated from equilibrium equations then the distribution is parabolic. The shear correction factor is the ratio of the two energies that belong to the two different stress distributions. We now assume that the material distribution depends on the coordinate ζ only. It is also a hypothesis that the total strain energy from shearing is

$$U_T = \frac{1}{2}\int_V\frac{\tau_{\xi\zeta}(\zeta)^2}{G(\zeta)}\mathrm{d}V = \frac{1}{2}\int_{\mathcal{L}}\int_A\left(1+\frac{\zeta}{\rho_o}\right)\frac{\tau_{\xi\zeta}(\zeta)^2}{G(\zeta)}\mathrm{d}A\mathrm{d}s\,, \tag{2.3.9}$$

where $\mathcal{L}$ is the length of the centerline; $G(\zeta)$ is the shear modulus which can be calculated from the relation $E(\zeta)=2G(\zeta)\left[1+\nu(\zeta)\right]$ and ν denotes the Poisson ratio. The strain energy stored in a unit length is therefore

$$U_\tau = \frac{1}{2}\int_A\left(1+\frac{\zeta}{\rho_o}\right)\frac{\tau_{\xi\zeta}(\zeta)^2}{G(\zeta)}\mathrm{d}A = \frac{1}{2}\left(\frac{V_\zeta}{I_{eR}}\right)^2\int_A\frac{1}{1+\frac{\zeta}{\rho_o}}\frac{1}{G(\zeta)}\frac{\left(\rho_o\beta_e A'_e+Q'_{e\eta}\right)^2}{v(\zeta)^2}\mathrm{d}A \tag{2.3.10}$$

given that $\tau_{\xi\zeta}$ is inserted here from (2.3.8). Moreover, utilizing

$$\gamma_{\xi\zeta}=\gamma_{\zeta\xi}=\left[\frac{\rho_o}{\rho_o+\zeta}\left(\frac{\partial w_o}{\partial\xi}-\frac{u_o}{\rho_o}\right)+\left(1-\frac{\zeta}{\rho_o}\right)\psi_{o\eta}\right]$$

which is the angle distortion on the cross-section, we can rewrite (2.3.10) as

$$U_\tau = \frac{1}{2}\int_A\left(1+\frac{\zeta}{\rho_o}\right)\tau_{\xi\zeta}(\zeta)\gamma_{\xi\zeta}(\zeta)\mathrm{d}A =$$

DOI: 10.14750/ME.2016.008

$$= \frac{1}{2}\int_A \underbrace{\left[\left(\frac{\partial w_o}{\partial \xi} - \frac{u_o}{\rho_o}\right) + \left(1 - \left(\frac{\zeta}{\rho_o}\right)^2\right)\psi_{o\eta}\right]}_{\simeq \gamma_{\xi\zeta}(0)=\gamma_{\xi\zeta\ o}=\text{constant}} \tau_{\xi\zeta}(\hat{\zeta})\mathrm{d}A \approx -\frac{1}{2}V_\zeta \gamma_{\xi\zeta\ o}\,. \quad (2.3.11)$$

This expression shows that we neglect the term $(\zeta/\rho_o)^2$ when it is compared to the unit. Comparison of formulae (2.3.10) and (2.3.11) yields

$$\frac{1}{2}V_\zeta \gamma_{\xi\zeta\ o} = -\frac{1}{2}\left(\frac{V_\zeta}{I_{eR}}\right)^2 \int_A \frac{\rho_o}{\rho_o+\zeta}\frac{1}{G(\zeta)}\frac{\left(\rho_o\beta_e A'_e + Q'_{e\eta}\right)^2}{v(\hat{\zeta})^2}\mathrm{d}A\,,$$

from which we get

$$V_\zeta = -\gamma_{\xi\zeta\ o}\frac{I_{eR}^2}{\int_A \frac{\rho_o}{\rho_o+\zeta}\frac{1}{G(\zeta)}\frac{\left(\rho_o\beta_e A'_e+Q'_{e\eta}\right)^2}{v(\zeta)^2}\mathrm{d}A} = -\gamma_{\xi\zeta\ o}\,h_\gamma\,, \quad (2.3.12)$$

where

$$h_\gamma = \frac{I_{eR}^2}{\int_A \frac{\rho_o}{\rho_o+\zeta}\frac{1}{G(\zeta)}\frac{\left(\rho_o\beta_e A'_e+Q'_{e\eta}\right)^2}{v(\zeta)^2}\mathrm{d}A} \quad \text{and} \quad \kappa_\gamma = \frac{h_\gamma}{\int_A G(\zeta)\,\mathrm{d}A}\,. \quad (2.3.13)$$

Here κ_γ is referred to as the shear correction factor. From $(2.3.13)_2$ after some minor manipulations – E and G are constant, $\rho_o \to \infty$ and β_e is zero – we get the formula

$$\kappa_\gamma = \frac{I_\eta^2}{A\int_A \frac{\left(Q'_\eta\right)^2}{v(\zeta)^2}\mathrm{d}A} \quad (2.3.14)$$

valid for straight beams ($I_\eta = \int_A \zeta^2 \mathrm{d}A$; $Q'_\eta = \int_A \zeta \mathrm{d}A$). It only depends on the cross-sectional properties. Finally, we remark that

$$V_\zeta = -\gamma_{\xi\zeta_o}\int G(\zeta)\mathrm{d}A\kappa_\gamma \quad (2.3.15)$$

is applicable both for homogeneous straight and for heterogeneous curved beams.

2.4. Curvature change and strain energy

In this section [the radius of curvature] {the location of a point} on the E-weighted centerline before and after deformation are denoted by [ρ_o and $\tilde{\rho}_o$] {P_o and $\tilde{P}_o$}. The angle of the tangent of the centerline at P_o and the horizontal axis is noted by ψ_o. Its change during deformation is $\psi_{o\eta}$ – the rigid body rotation. The calculation of the curvature change is based on Figure 2.4 which shows all the quantities mentioned.

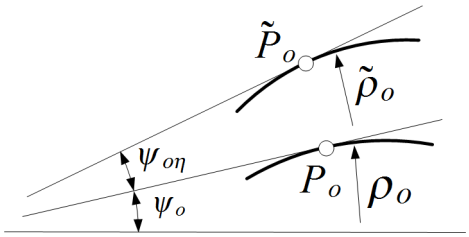

FIGURE 2.4. The curvature change on the centerline.

The infinitesimal arc element $\mathrm{d}s_o$ on the centerline before deformation changes to $\mathrm{d}s$. It is clear that

$$\varepsilon_{o\xi} = \frac{\mathrm{d}s - \mathrm{d}s_o}{\mathrm{d}s_o} \quad (2.4.1)$$

DOI: 10.14750/ME.2016.008

is the axial strain on the centerline. Consequently,

$$\mathrm{d}s_o = \frac{\mathrm{d}s}{1+\varepsilon_{o\xi}} \,. \tag{2.4.2}$$

Using the above equation we can establish a formula for the curvature change:

$$\frac{1}{\tilde{\rho}_o} - \frac{1}{\rho_o} = \frac{\mathrm{d}\left(\psi_o + \psi_{o\eta}\right)}{\mathrm{d}s} - \frac{\mathrm{d}\psi_o}{\mathrm{d}s_o} = \frac{\mathrm{d}(\psi_o + \psi_{o\eta})}{\mathrm{d}s} - \frac{\mathrm{d}\psi_o}{\mathrm{d}s}(1+\varepsilon_{o\xi}) = \frac{\mathrm{d}\psi_{o\eta}}{\mathrm{d}s} - \varepsilon_{o\xi}\frac{\mathrm{d}\psi_o}{\mathrm{d}s} \,. \tag{2.4.3}$$

Here

$$\varepsilon_{o\xi}\frac{\mathrm{d}\psi_o}{\mathrm{d}s} = \varepsilon_{o\xi}\frac{\mathrm{d}\psi_o}{\mathrm{d}s_o}\left(1+\varepsilon_{o\xi}\right) \simeq \varepsilon_{o\xi}\frac{\mathrm{d}\psi_o}{\mathrm{d}s_o} = \varepsilon_{o\xi}\frac{1}{\rho_o} \,. \tag{2.4.4}$$

Comparison of equations (2.1.8), (2.4.3) and (2.4.4) yields

$$\frac{1}{\tilde{\rho}_o} - \frac{1}{\rho_o} = \kappa_o - \varepsilon_{o\xi}\frac{1}{\rho_o} \,. \tag{2.4.5}$$

Substituting κ_o from (2.2.3) and taking into account that in the present case $N = 0$ and $Q_{eR}^2 \ll A_{eR}I_{eR}$, we have

$$\frac{1}{\tilde{\rho}_o} - \frac{1}{\rho_o} = -\frac{M}{Q_{eR}^2 - A_{eR}I_{eR}}\left(A_{eR} + \underbrace{\frac{Q_{eR}}{\tilde{\rho}_o}}_{\approx 0}\right) \simeq \frac{MA_{eR}}{A_{eR}I_{eR} - Q_{eR}^2} \simeq \frac{MA_{eR}}{A_{eR}I_{eR}} = \frac{M}{I_{eR}}$$

that is

$$\frac{1}{\tilde{\rho}_o} - \frac{1}{\rho_o} = \frac{M}{I_{eR}} \,. \tag{2.4.6}$$

Now we proceed with the determination of the strain energy stored in the beam. It is not too difficult to check using equation (2.4.6) that the angle change $\mathrm{d}\psi$ due to the bending moment is

$$\mathrm{d}\psi = \frac{\mathrm{d}s}{\tilde{\rho}_o} - \frac{\mathrm{d}s_o}{\rho_o} \simeq \frac{\mathrm{d}s}{\tilde{\rho}_o} - \frac{\mathrm{d}s}{\rho_o} = \frac{M}{I_{eR}}\mathrm{d}s \,. \tag{2.4.7}$$

As a result

$$\mathrm{d}U = \frac{1}{2}M\mathrm{d}\psi = \frac{1}{2}\frac{M^2}{I_{eR}}\mathrm{d}s \tag{2.4.8}$$

is the work done by the bending moment exerted on an infinitesimal portion of the beam. After integration

$$U = \frac{1}{2}\int_{\mathcal{L}} \frac{M^2}{I_{eR}}\,\mathrm{d}s \tag{2.4.9}$$

is the strain energy stored in the beam. We have derived this formula assuming $\mathrm{d}s = \mathrm{d}s_o$. The parts of the strain energy due to the axial and shear forces were neglected.

2.5. Numerical examples

2.5.1. Example 1. Figure 2.5 shows the cross-section of the circular beam. It is subjected to pure bending by a moment $\mathbf{M} = M\,\mathbf{e}_\eta\,, M = 100$ Nm. The geometric dimensions are all given in Figure 2.5. The lower part of the beam is made of steel and the upper part is made of aluminium. The corresponding material parameters are $E_1 = 2.1 \cdot 10^5$ MPa and $E_2 = 7 \cdot 10^4$ MPa. Our aim is to depict graphically the normal stress distribution as a function of ζ using the three formulae derived in the previous sections. This allows us to compare the various results. It would also be interesting to check the difference between these formulae regarding the radius of the neutral axis.

DOI: 10.14750/ME.2016.008

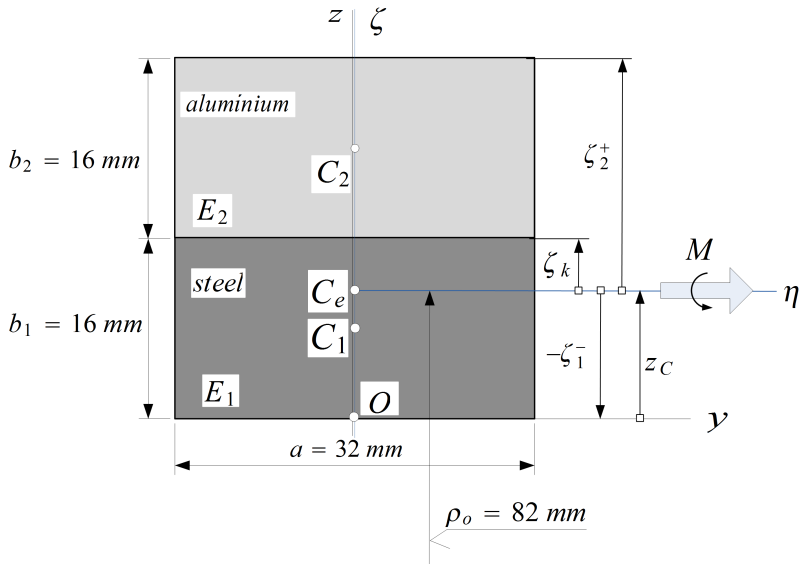

FIGURE 2.5. Cross-section of Example 1.

First, we determine the ordinate z_C of the E-weighted centerline in the coordinate system yz. Since the E-weighted first moment of the cross-section with respect to the axis η is zero, the following equation holds

$$Q_{e\eta} = Q_{ey} - z_C A_e = 0\,. \tag{2.5.1}$$

Here Q_{ey} is the E-weighted first moment of the cross-section to the axis y defined by

$$Q_{ey} = \int_A E(\eta,\zeta) z \mathrm{d}A.$$

Consequently,

$$z_C = \frac{Q_{ey}}{A_e} = \frac{E_1 \frac{b_1}{2} A_1 + E_2 \left(b_1 + \frac{b_1}{2}\right) A_2}{E_1 A_1 + E_2 A_2} = 12\,\mathrm{mm}. \tag{2.5.2}$$

In the knowledge of z_C one can easily read off from Figure 2.5 that

$$\zeta_1^- = -z_C = -12\ \mathrm{mm}, \quad \zeta_k = 4\ \mathrm{mm}, \quad \zeta_2^+ = 20\ \mathrm{mm}. \tag{2.5.3}$$

Before computing the stresses sought, we shall set up appropriate formulae for the E-weighted geometrical quantities A_{eR}, Q_{eR}, $I_{e\eta}$ and I_{eR}. Recalling equation $(2.1.12)_1$ we can write

$$A_{eR} = \int_{\mathcal{L}} \frac{\rho_o + \zeta - \zeta}{\rho_o + \zeta} E(\eta,\zeta) a \mathrm{d}\zeta = \underbrace{\int_A E(\eta,\zeta)\,\mathrm{d}A}_{A_e} - E_1 a \int_{\zeta_1^-}^{\zeta_k} \frac{\zeta}{\rho_o + \zeta}\mathrm{d}\zeta - E_2 a \int_{\zeta_k}^{\zeta_2^+} \frac{\zeta}{\rho_o + \zeta}\mathrm{d}\zeta =$$

$$= A_e - E_1 a \left[\zeta - \rho_o \ln(\zeta + \rho_o)\right]\Big|_{\zeta_1^-}^{\zeta_k} - E_2 a \left[\zeta - \rho_o \ln(\zeta + \rho_o)\right]\Big|_{\zeta_k}^{\zeta_2^+} =$$

$$= A_1 E_1 + A_2 E_2 + a\left[(E_2 - E_1)\zeta_k + E_1 \zeta_1^- - E_2 \zeta_2^+\right] +$$

$$+ a\rho_o \left[(E_1 - E_2)\ln(\zeta_k + \rho_o) - E_1 \ln\left(\zeta_1^- + \rho_o\right) + E_2 \ln\left(\zeta_2^+ + \rho_o\right)\right]\,. \tag{2.5.4}$$

Regarding the E-weighted reduced first moment of the cross-section, equation $(2.1.12)_2$ yields

$$Q_{eR} = \int \frac{\rho_o + \zeta - \zeta}{\rho_o + \zeta} E(\eta,\zeta)\zeta a \mathrm{d}\zeta = \underbrace{Q_{e\eta}}_{=0} - \int \frac{\zeta^2 E(\eta,\zeta)}{\rho_o + \zeta} a \mathrm{d}\zeta = -\int \frac{\zeta^2 E(\eta,\zeta)}{\rho_o + \zeta} a \mathrm{d}\zeta =$$

$$= -E_1 a \left[\frac{1}{2}(\zeta_k)^2 - \zeta_k \rho_o + \rho_o^2 \ln(\rho_o + \zeta_k) - \frac{1}{2}\left(\zeta_1^-\right)^2 + \zeta_1^- \rho_o - \rho_o^2 \ln\left(\rho_o + \zeta_1^-\right)\right] -$$

DOI: 10.14750/ME.2016.008

$$- E_2 a \left[\frac{1}{2} \left(\zeta_2^+ \right)^2 - \zeta_2^+ \rho_o + \rho_o^2 \ln \left(\rho_o + \zeta_2^+ \right) - \frac{1}{2} \left(\zeta_k \right)^2 + \zeta_k \rho_o - \rho_o^2 \ln \left(\rho_o + \zeta_k \right) \right] \quad . \quad (2.5.5)$$

Using the parallel axis theorem, we can determine $I_{e\eta}$ as

$$I_{e\eta} = \int_A E(\eta, \zeta) \zeta^2 \mathrm{d}A = E_1 \int_{A_1} \zeta^2 \mathrm{d}A + E_2 \int_{A_2} \zeta^2 \mathrm{d}A = \\ = E_1 \left[\frac{a b_1^3}{12} + \left(z_C - \frac{b_1}{2} \right)^2 a b_1 \right] + E_2 \left[\frac{a b_2^3}{12} + \left(b_1 - z_C + \frac{b_2}{2} \right)^2 a b_2 \right] \quad . \quad (2.5.6)$$

Therefore, recalling $(2.1.12)_3$ and utilizing equation (2.5.6) we can establish a formula for the E-weighted reduced moment of inertia:

$$I_{eR} = \int_{A_1 \cup A_2} \frac{\rho_o}{\rho_o + \zeta} \zeta^2 E(\eta, \zeta) \mathrm{d}A = \int_{A_1 \cup A_2} \frac{\rho_o + \zeta - \zeta}{\rho_o + \zeta} \zeta^2 E(\eta, \zeta) \mathrm{d}A = I_{e\eta} - \\ - \int_{A_1 \cup A_2} \frac{\zeta^3}{\rho_o + \zeta} E(\eta, \zeta) \mathrm{d}A = I_{e\eta} + a(E_2 - E_1) \left(\zeta_k \rho_o^2 - \frac{1}{2} \left(\zeta_k \right)^2 \rho_o - \rho_o^3 \ln \left(\rho_o + \zeta_k \right) + \frac{1}{3} \left(\zeta_k \right)^3 \right) - \\ - E_1 a \left(- \frac{1}{3} \left(\zeta_1^- \right)^3 + \frac{1}{2} \left(\zeta_1^- \right)^2 \rho_o - \zeta_1^- \rho_o^2 + \rho_o^3 \ln \left(\rho_o + \zeta_1^- \right) \right) - \\ - a E_2 \left(\frac{1}{3} \left(\zeta_2^+ \right)^3 - \frac{1}{2} \left(\zeta_2^+ \right)^2 \rho_o + \zeta_2^+ \rho_o^2 - \rho_o^3 \ln \left(\rho_o + \zeta_2^+ \right) \right) \quad . \quad (2.5.7)$$

Substituting now a, b_1, b_2, ρ_o, A_1, E_1, A_2, E_2, ζ_k, ζ_1^- and ζ_2^+ into equations (2.5.4)-(2.5.7) we obtain the following numerical values:

$$A_e = 1.4336 \cdot 10^8 \text{ N} \,, \;\; A_{eR} = 1.4477 \cdot 10^8 \text{ N} \,, \;\; Q_{eR} = -1.1588 \cdot 10^8 \text{ Nmm} \,, \\ I_{e\eta} = 9.9396 \cdot 10^9 \text{ Nmm}^2 \,, \;\; I_{eR} = 9.5024 \cdot 10^9 \text{ Nmm}^2 . \quad (2.5.8)$$

To illustrate the significant effect of heterogeneity, we now provide the former quantities for a homogeneous steel

$$A_e = 2.150 \cdot 10^8 \text{ N} \,, \;\; A_{eR} = 2.288 \cdot 10^8 \text{ N} \,, \;\; Q_{eR} = -2.179 \cdot 10^8 \text{ Nmm} \,, \\ I_{e\eta} = 1.835 \cdot 10^{10} \text{ Nmm}^2 \,, \;\; I_{eR} = 1.874 \cdot 10^{10} \text{ Nmm}^2$$

and aluminium

$$A_e = 7.168 \cdot 10^7 \text{ N} \,, \;\; A_{eR} = 7.626 \cdot 10^7 \text{ N} \,, \;\; Q_{eR} = -7.264 \cdot 10^7 \text{ Nmm} \,, \\ I_{e\eta} = 6.116 \cdot 10^9 \text{ Nmm}^2 \,, \;\; I_{eR} = 6.247 \cdot 10^9 \text{ Nmm}^2$$

section. These quantities can vary in a rather wide interval.

With these results we can compute the normal stress σ_ξ using the three derived expressions. Eq. (2.2.5) is the 'exact' formula under the applied displacement and stress hypotheses, (2.2.9) is the generalization of the Grashof formula and (2.2.18) is the generalization of the formula that can be found in English textbooks on Strength of Materials. The computational results are presented graphically in Figure 2.6. Finite element computational result is also provided. It was obtained using Abaqus 6.12.

DOI: 10.14750/ME.2016.008

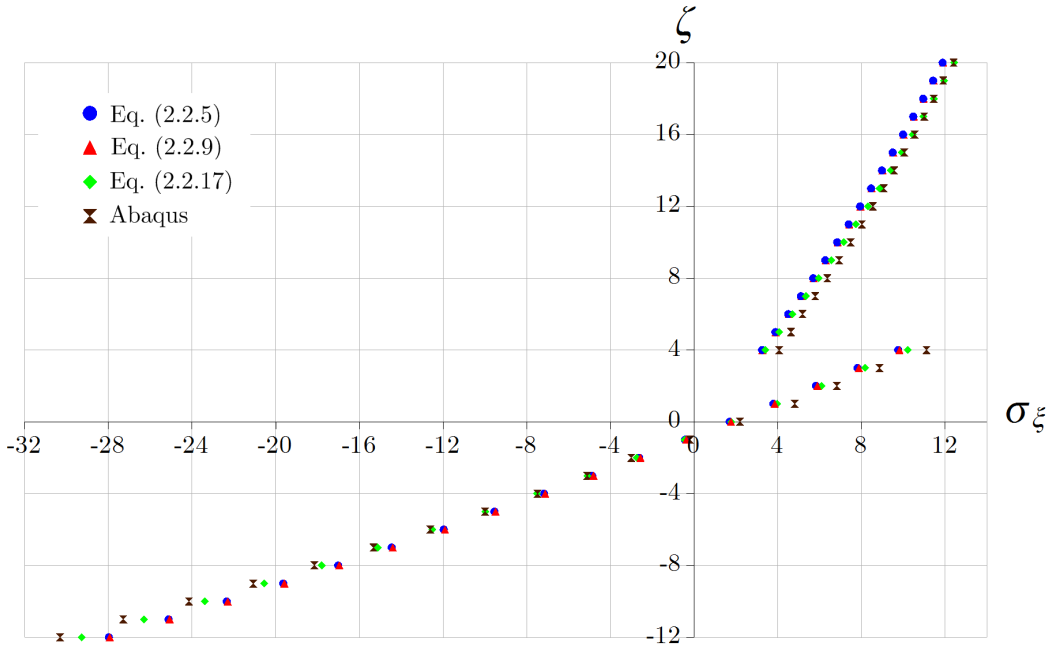

FIGURE 2.6. Normal stress distribution for Example 1.

For the Abaqus models of the two-layered (Example 1) and sandwich beams (Example 2 and 3 – see later), one of the beam endfaces was always fixed and the other was subjected to a [shear force] or a {bending moment} applied at a so-called reference point in the software (it coincides with the E-weighted centroid) using kinematic coupling between the point and the endfaces of the layers. The layers of the beams were perfectly tied together at their overlapping surfaces. The central angle was chosen to be 180°. The [shear stress] {normal stress} distributions were drawn along the axis ζ in a cross-section being [3.6°] {90°} away from the loaded endface. 20-node $3D$ elements were applied and the Static, General Step.

As regards Figure 2.6 the symbols representing the exact solution, the solution obtained from (2.2.9) and the solution calculated with equation (2.2.18) are drawn in blue, red and green, respectively. The Abaqus outcomes are drawn in brown. Overall, the differences are minor between the four models.

As for the ordinate of the neutral axis, by setting $\sigma_\xi(\zeta) = 0$, Eqs. (2.2.5), (2.2.9) and (2.2.18) yield -0.800 mm, -0.777 mm and -0.785 mm, respectively. We note that the last result is exactly the same as the value that can be obtained from (2.2.14).

2.5.2. Example 2. In practise, beams with sandwich structure are commonly used. For this reason we investigate the normal stress distribution in a doubly-symmetric cross-section under pure bending. The faces are made of steel and the core is aluminium – the material parameters are therefore the same as in the previous example. Let the bending moment M be $8 \cdot 10^5$ Nmm – see Figure 2.7 for more data.

Due to the horizontal symmetry in the material distribution, the centroid and the E-weighted centroid coincide – i.e. $z_C = 30$ mm. With this in hand, the following data can be read off from Figure 2.7:

$$\zeta_{1l} = -30\,\text{mm}\,; \quad \zeta_{1u} = -20\,\text{mm}\,; \quad \zeta_{2u} = 20\,\text{mm}\,; \quad \zeta_{3u} = 30\,\text{mm}\,. \tag{2.5.9}$$

DOI: 10.14750/ME.2016.008

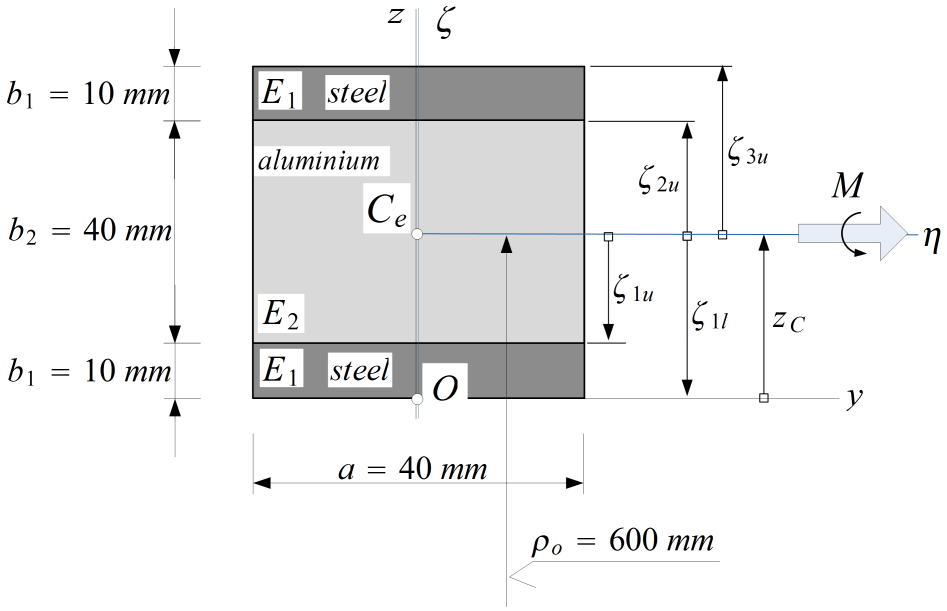

FIGURE 2.7. Cross-section of Example 2.

In the forthcoming, we provide some formulae valid for such sandwich cross-sections. These expressions are originated from equations (2.1.2) and (2.1.12).

The E-weighted area (tensile stiffness) is

$$A_e = 2E_1A_1 + E_2A_2, \tag{2.5.10}$$

while

$$A_{eR} = 2E_1A_1 + E_2A_2 - E_1a\left[-\zeta_{1l} + \rho_o \ln\left(\rho_o + \zeta_{1l}\right)\right] + \left(E_1 - E_2\right)a\left[\rho_o \ln\left(\rho_o + \zeta_{1u}\right) - \zeta_{1u}\right] - \\ - E_1a\left[\zeta_{3u} - \rho_o \ln\left(\rho_o + \zeta_{3u}\right) - \zeta_{2u} + \rho_o \ln\left(\rho_o + \zeta_{2u}\right)\right] - E_2a\left[\zeta_{2u} - \rho_o \ln\left(\rho_o + \zeta_{2u}\right)\right] \tag{2.5.11}$$

yields the E-weighted reduced area. Furthermore, the E-weighted reduced first moment can be obtained upon substitution into the formula

$$Q_{eR} = -aE_1\left(\zeta_{1l}\rho_o - \frac{1}{2}\zeta_{1l}^2 - \rho_o^2 \ln\left(\rho_o + \zeta_{1l}\right)\right) - aE_1\left(-\zeta_{3u}\rho_o + \frac{\zeta_{3u}^2}{2} + \rho_o^2 \ln\left(\rho_o + \zeta_{3u}\right)\right) - \\ - a\left(E_1 - E_2\right)\left(\frac{\zeta_{1u}^2}{2} - \zeta_{1u}\rho_o + \rho_o^2 \ln\left(\rho_o + \zeta_{1u}\right) + \zeta_{2u}\rho_o - \frac{\zeta_{2u}^2}{2} - \rho_o^2 \ln\left(\rho_o + \zeta_{2u}\right)\right). \tag{2.5.12}$$

The E-weighted moment of inertia (bending stiffness) follows from the parallel axis theorem as

$$I_{e\eta} = 2E_1\left[\frac{ab_1^3}{12} + \left(z_C - \frac{b_1}{2}\right)^2 ab_1\right] + E_2\left[\frac{ab_2^3}{12}\right], \tag{2.5.13}$$

and finally

$$I_{eR} = 2E_1\left[\frac{ab_1^3}{12} + \left(z_C - \frac{b_1}{2}\right)^2 ab_1\right] + E_2\left[\frac{ab_2^3}{12}\right] - \\ - aE_1\left[-\zeta_{1l}\rho_o^2 + \frac{\zeta_{1l}^2\rho_o}{2} - \frac{\zeta_{1l}^3}{3} + \rho_o^3 \ln\left(\rho_o + \zeta_{1l}\right) + \zeta_{3u}\rho_o^2 - \frac{\zeta_{3u}^2\rho_o}{2} + \frac{\zeta_{3u}^3}{3} - \rho_o^3 \ln\left(\rho_o + \zeta_{3u}\right)\right] - \\ - a\left(E_1 - E_2\right)\left[\zeta_{1u}\rho_o^2 - \frac{\zeta_{1u}^2\rho_o}{2} + \frac{\zeta_{1u}^3}{3} - \rho_o^3 \ln\left(\rho_o + \zeta_{1u}\right) + \right.$$

DOI: 10.14750/ME.2016.008

$$+\frac{\zeta_{2u}^2\rho_o}{2}-\zeta_{2u}\rho_o^2-\frac{\zeta_{2u}^3}{3}+\rho_o^3\ln\left(\rho_o+\zeta_{2u}\right)\Big] \quad (2.5.14)$$

provides the E-weighted reduced moment of inertia. The numerical values of these quantities for the chosen example are listed below:

$$A_e=2.8\cdot10^8\text{ N},\quad A_{eR}=2.803\,376\cdot10^8\text{ N},\quad Q_{eR}=-2.025\,676\cdot10^8\text{ Nmm},$$
$$I_{e\eta}=1.213\,333\cdot10^{11}\text{ Nmm}^2,\quad I_{eR}=1.215\,406\cdot10^{11}\text{ Nmm}^2. \quad (2.5.15)$$

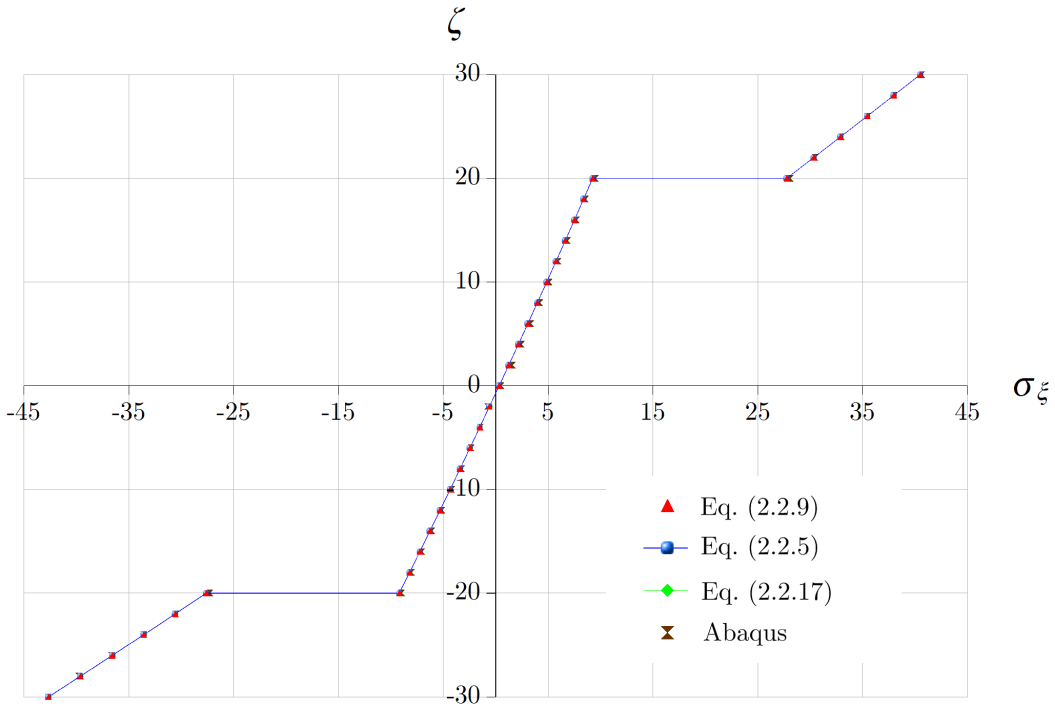

FIGURE 2.8. Normal stress distribution for Example 2.

Based on these formulae the normal stress distribution can be calculated using equations (2.2.5), (2.2.9) and (2.2.18) as shown in Figure 2.8. One can conclude that the correlation between the cited formulae and the commercial finite element software calculations are very good yet again.

The almost identical coordinates of the neutral axis according to the corresponding formulae are $-0.722\,6$; $-0.721\,6$ and $-0.722\,6$ mm, respectively.

2.5.3. Example 3. All the data are the same as in the previous subsection, but this time the beam is under a shear force V_ζ with magnitude $5\cdot10^4\,N$. For more details see Figure 2.9. Let the related Poisson ratios be $\nu_1=\nu_2=0.3$. Upon substitution of ρ_o and $(2.5.15)_{2,5}$ into $(2.3.7)_1$ we have

$$\beta_e=1.204\,307\cdot10^{-3}.$$

DOI: 10.14750/ME.2016.008

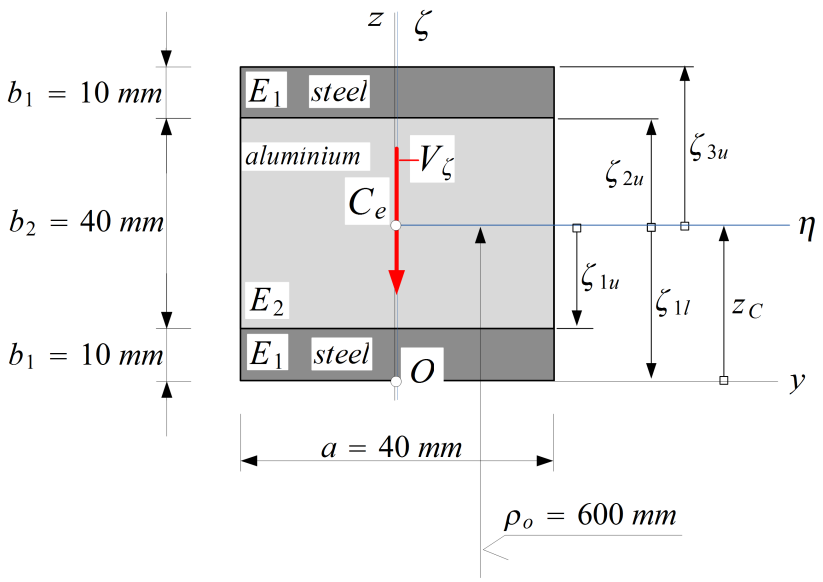

FIGURE 2.9. Cross-section of Example 3.

Moreover, if $\hat{\zeta} \in [-30; -20]$ then

$$A_e' = 210\ 000 \cdot 40 \cdot \int_{-30}^{\hat{\zeta}} \mathrm{d}\zeta = 8\ 400\,000\hat{\zeta} + 252\,000\,000$$

and

$$Q_{e\eta}' = 210\ 000 \cdot 40 \cdot \int_{-30}^{\hat{\zeta}} \frac{600\zeta}{600+\zeta}\mathrm{d}\zeta = \\ = 5.04 \cdot 10^9\hat{\zeta} - 3.024 \cdot 10^{12} \ln\left(600+\hat{\zeta}\right) + 1.934\,040 \cdot 10^{13},$$

therefore the shear stress distribution (2.3.8) in the bottom layer happens to be described by the formula

$$\tau_{\xi\zeta}(\hat{\zeta}) = -\frac{6170.776\,882}{600+\hat{\zeta}} \cdot \left(5.046\,069\hat{\zeta} + 1.934\,058 \cdot 10^4 - 3.024 \cdot 10^3 \ln\left(600+\hat{\zeta}\right)\right). \tag{2.5.16}$$

If $\hat{\zeta} \in [-20, 20]$ then

$$A_e' = 210\,000 \cdot 40 \cdot \int_{20}^{30} \mathrm{d}\zeta + 70000 \cdot 40 \cdot \int_{\hat{\zeta}}^{20} \mathrm{d}\zeta = 140\,000\,000 - 2800\,000\hat{\zeta},$$

in addition to this

$$Q_{e\eta}' = 210\,000 \cdot 40 \cdot \int_{20}^{30} \left(\frac{600\cdot\zeta}{600+\zeta}\right)\mathrm{d}\zeta + 70000 \cdot 40 \cdot \int_{\hat{\zeta}}^{20} \left(\frac{600\cdot\zeta}{600+\zeta}\right)\mathrm{d}\zeta = \\ = -6.445\,542 \cdot 10^{12} - 1.68 \cdot 10^9\hat{\zeta} + 1.008 \cdot 10^{12} \ln\left(600+\hat{\zeta}\right)$$

consequently,

$$\tau_{\xi\zeta}(\hat{\zeta}) = -\frac{6170.776\,882}{600+\hat{\zeta}} \cdot \left[-6.445\,441 \cdot 10^3 - 1.682\,023\hat{\zeta} + 1.008 \cdot 10^3 \ln\left(600+\hat{\zeta}\right)\right] \tag{2.5.17}$$

is the sought function in the aluminium core.

DOI: 10.14750/ME.2016.008

In the uppermost layer $\hat{\zeta} \in [20, 30]$, so we can write

$$A_e' = 210\,000 \cdot 40 \cdot \int_{\hat{\zeta}}^{30} \mathrm{d}\zeta = 252\,000\,000 - 8\,400\,000\hat{\zeta},$$

further

$$Q_{e\eta}' = 210\,000 \cdot 40 \int_{\hat{\zeta}}^{30} \left(\frac{600 \cdot \zeta}{600 + \zeta}\right) \mathrm{d}\zeta =$$
$$= -1.\,934\,065 \cdot 10^{13} - 5.04 \cdot 10^{9}\hat{\zeta} + 3.024 \cdot 10^{12} \ln\left(600 + \hat{\zeta}\right) \text{ Nmm}\,.$$

As a result we have the shear stress as

$$\tau_{\xi\zeta}(\hat{\zeta}) = -\frac{6170.\,776\,882}{600 + \hat{\zeta}} \cdot \left(-1.\,934\,047 \cdot 10^{4} - 5.\,046\,069 \cdot \hat{\zeta} + 3.024 \cdot 10^{3} \ln\left(600 + \hat{\zeta}\right)\right). \tag{2.5.18}$$

The distribution $\tau_{\xi\zeta}(\hat{\zeta})$ over the cross-section is plotted in Figure 2.10. There is quite a good correlation with Abaqus.

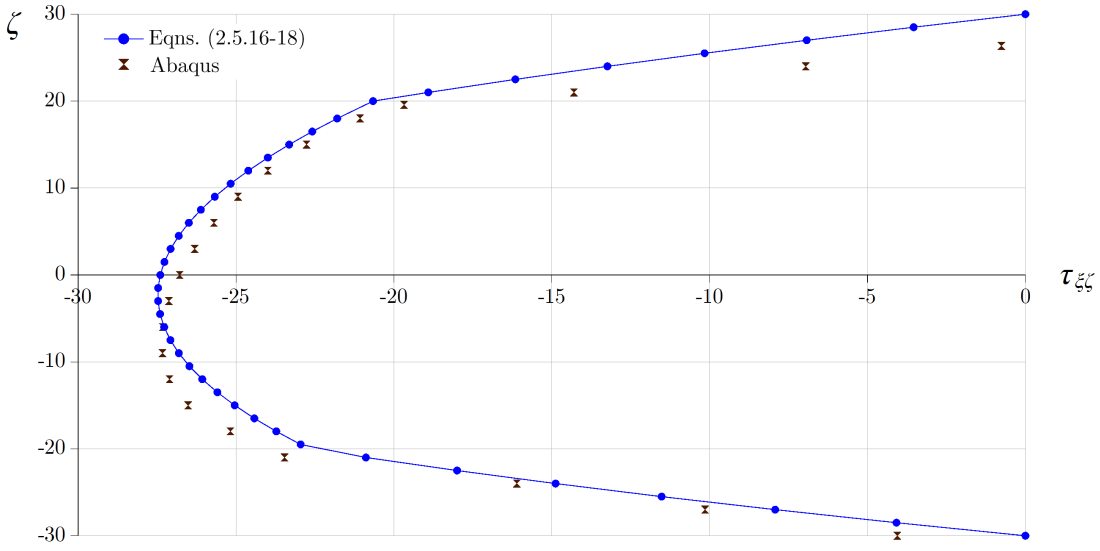

FIGURE 2.10. Shear stress distribution for Example 3.

2.5.3.1. *The shear correction factor.* As a first step, let us substitute the known quantities into formula $(2.3.13)_1$. Here we take the following points into consideration: (a) $v(\zeta)$ is now equal to the a width of the rectangular cross-section; (b) the shear modulus $G(\zeta)$ is constant in each of the intervals $\hat{\zeta} \in [-30; -20]$, $\hat{\zeta} \in [-20; 20]$, and $\hat{\zeta} \in [20; 30]$ and (c) properties A_e', $Q_{e\eta}'$ are continuous in each of the intervals. Thus, it follows that the denominator of $(2.3.13)_1$ is equal to

$$\int \frac{\rho_o}{\rho_o + \zeta} \frac{1}{G} \frac{\left(\rho_o \beta_e A_e' + Q_{e\eta}'\right)^2}{v^2} \mathrm{d}A = \frac{1}{G_1 a} \int_{-30}^{-20} \frac{\rho_o}{\rho_o + \zeta} \left(\rho_o \beta_e A_e' + Q_{e\eta}'\right)^2 \mathrm{d}\zeta +$$
$$+ \frac{1}{G_2 a} \int_{-20}^{20} \frac{\rho_o}{\rho_o + \zeta} \left(\rho_o \beta_e A_e' + Q_{e\eta}'\right)^2 \mathrm{d}\zeta + \frac{1}{G_1 a} \int_{20}^{30} \frac{\rho_o}{\rho_o + \zeta} \left(\rho_o \beta_e A_e' + Q_{e\eta}'\right)^2 \mathrm{d}\zeta =$$
$$= 2.\,392\,438 \cdot 10^{14}. \tag{2.5.19}$$

DOI: 10.14750/ME.2016.008

Inserting it back to $(2.3.13)_1$ yields

$$h_\gamma = \frac{I_{eR}^2}{\int \frac{\rho_o}{\rho_o+\zeta}\frac{1}{G}\frac{\left(\rho_o\beta_e A'_e+Q'_{e\eta}\right)^2}{v^2}\mathrm{d}A} = \frac{\left(1.215\,406\cdot 10^{11}\right)^2}{2.392\,438\cdot 10^{14}} = 6.174\,502\cdot 10^7.$$

The dimensionless (and material dependent) shear correction factor κ_γ can be calculated using the definition $(2.3.13)_2$ therefore, it is now

$$\kappa_\gamma = \frac{h_\gamma}{\int G\mathrm{d}A} = \frac{h_\gamma}{G_1 a\int_{-30}^{-20}\mathrm{d}\zeta + G_2 a\int_{-20}^{20}\mathrm{d}\zeta + G_1 a\int_{20}^{30}\mathrm{d}\zeta} = \frac{6.174\,502\cdot 10^7}{1.076\,923\cdot 10^8} = 0.573\,346.$$

This figure is about the 69% of the solution valid for a homogeneous rectangular cross-section. So, obviously, heterogeneity can have a huge effect on this property as well.

2.6. Summary of the results achieved in Section 2

The first objective was to provide formulae for the determination of the stress state in heterogeneous curved beams by generalizing the formulae valid for homogeneous curved beams. It involves the expressions of the normal stress and shear stress. An expression for the shear correction factor was also provided. The most important results are as follows:

1. I have derived an exact and two approximative relationships that provide the normal stress caused by an axial force and a bending moment in curved beams with cross-sectional inhomogeneity. The latter two are generalizations of well-known relationships valid for homogeneous curved beams. A further formula has been established for computing the shearing stress.
2. In addition, a formula for the shear correction factor has also been derived. The results obtained by the relationships set up for the stresses were compared with the computations. A good agreement was found between the different models.

DOI: 10.14750/ME.2016.008

CHAPTER 3

In-plane elastic stability of heterogeneous shallow circular beams

3.1. Fundamental assumptions

3.1.1. General relations regarding the pre-buckling state. All the geometrical conditions, hypotheses and kinematical relations mentioned previously in Section 2.1 hold. However, some physical quantities will be addressed in a more accurate manner.

For the forthcoming shallow planar circular beam model we maintain the validity of the Euler-Bernoulli beam theory – i.e. the cross-sections remain plane and perpendicular to the deformed centerline. The novelty in this chapter is that the Green-Lagrange strain tensor $\boldsymbol{E}$ is now not linearized, thus

$$\boldsymbol{E} = \boldsymbol{E^L} + \boldsymbol{E^N} \ , \quad \boldsymbol{E^L} = \frac{1}{2}\left(\mathbf{u}\circ\nabla + \nabla\circ\mathbf{u}\right) \ , \qquad \boldsymbol{E^N} = \frac{1}{2}\left(\nabla\circ\mathbf{u}\right)\cdot\left(\mathbf{u}\circ\nabla\right) \ . \tag{3.1.1}$$

Here $\boldsymbol{E^L}$ is the linear part and $\boldsymbol{E^N}$ is the nonlinear part of the strain tensor.

Moreover, we assume that the tensor of infinitesimal rotations $\boldsymbol{\Psi}$ – see (2.1.8b) – is the dominant when that is compared to the linear strains and the strain-rotation product:

$$\begin{aligned}\boldsymbol{E^N} &= \frac{1}{2}\left(\nabla\circ\mathbf{u}\right)\cdot\left(\mathbf{u}\circ\nabla\right) = \frac{1}{2}\left(\boldsymbol{E^L}+\boldsymbol{\Psi}^T\right)\cdot\left(\boldsymbol{E^L}+\boldsymbol{\Psi}\right) = \\ &= \frac{1}{2}\left(\boldsymbol{E^L}\cdot\boldsymbol{E^L} + \boldsymbol{\Psi}^T\cdot\boldsymbol{E^L} + \boldsymbol{E^L}\cdot\boldsymbol{\Psi} + \boldsymbol{\Psi}^T\cdot\boldsymbol{\Psi}\right) \approx \frac{1}{2}\boldsymbol{\Psi}^T\cdot\boldsymbol{\Psi} = \frac{1}{2}\boldsymbol{\Psi}\cdot\boldsymbol{\Psi}^T \ .\end{aligned} \tag{3.1.2}$$

This assumption is generally accepted in the literature when modelling beams – see, e.g. [**73**, **74**, **108**]. The superscript ^{T} stands for the transpose of a tensor (or vector). Based on the former hypothesis

$$\varepsilon_\xi = \mathbf{e}_\xi\cdot\frac{1}{2}\left(\mathbf{u}\circ\nabla+\nabla\circ\mathbf{u}\right)\cdot\mathbf{e}_\xi + \mathbf{e}_\xi\cdot\frac{1}{2}\left(\boldsymbol{\Psi}^T\cdot\boldsymbol{\Psi}\right)\cdot\mathbf{e}_\xi = \frac{1}{1+\frac{\zeta}{\rho_o}}\left(\varepsilon_{o\xi}+\zeta\kappa_o\right) + \frac{1}{2}\psi_{o\eta}^2 \tag{3.1.3}$$

is the axial strain at an arbitrary point on the cross-section while the nonlinear strain on the centerline is

$$\varepsilon_\xi\big|_{\zeta=0} = \varepsilon_m = \varepsilon_{o\xi} + \frac{1}{2}\psi_{o\eta}^2 \, . \tag{3.1.4}$$

Based on equations (2.1.8)-(2.1.11) we remind the reader that ρ_o is the initial radius of the centerline, $\varepsilon_{o\xi}$, $\psi_{o\eta}$ and κ_o are the linearized strain; the rotation and the curvature on the centerline.

Bradford et al. in their model assume that

$$\frac{1}{1+\frac{\zeta}{\rho_o}} \simeq 1; \quad \kappa_o = -\frac{\mathrm{d}^2 w_o}{\mathrm{d}s^2} \tag{3.1.5}$$

thus, with our notations, the strain according to them is

$$\varepsilon_\xi = \varepsilon_{o\xi} + \zeta\kappa_o + \frac{1}{2}\psi_{o\eta}^2 \simeq \frac{\mathrm{d}u_o}{\mathrm{d}s} + \frac{w_o}{\rho_o} - \zeta\frac{\mathrm{d}^2 w_o}{\mathrm{d}s^2} + \frac{1}{2}\left(\frac{\mathrm{d}w_o}{\mathrm{d}s}\right)^2 \tag{3.1.6}$$

– see equation (1) and (2) in [**61**]. We remark that equation (3.1.3) is more accurate (due to the presence of the quadratic term) than equation (2.1.10) in Chapter 2.

DOI: 10.14750/ME.2016.008

This time we again assume that the corresponding elements of the second Piola-Kirchhoff stress tensor $\boldsymbol{S}$ satisfy the inequality $\sigma_\xi \gg \sigma_\eta, \sigma_\zeta$. Consequently, Hooke's law $\sigma_\xi = E(\eta,\zeta)\varepsilon_\xi$ is the constitutive equation. In the knowledge of the stresses we can determine the inner forces in the pre-buckling equilibrium configuration. Making use of Hooke's law, the kinematic equations (3.1.3), (3.1.4) and utilizing then the notations (2.1.12), (2.1.13) we get the axial force as

$$N = \int_A E\varepsilon_\xi \,\mathrm{d}A = \underbrace{\int_A E\frac{\rho_o}{\rho_o+\zeta}\,\mathrm{d}A}_{A_{eR}\simeq A_e}\varepsilon_{o\xi} + \underbrace{\int_A E\frac{\zeta\rho_o}{\rho_o+\zeta}\,\mathrm{d}A}_{Q_{eR}=-\frac{I_{e\eta}}{\rho_o}}\kappa_o + \underbrace{\int_A E\,\mathrm{d}A}_{A_e}\frac{1}{2}\psi_{o\eta}^2 =$$

$$= A_{eR}\varepsilon_{o\xi} + Q_{eR}\kappa_o + A_e\frac{1}{2}\psi_{o\eta}^2 \simeq A_e\underbrace{\left(\varepsilon_{o\xi}+\frac{1}{2}\psi_{o\eta}^2\right)}_{\varepsilon_m} - \frac{I_{e\eta}}{\rho_o}\kappa_o = A_e\varepsilon_m - \frac{I_{e\eta}}{\rho_o}\kappa_o\,. \quad (3.1.7)$$

As regards the bending moment a similar line of thought yields

$$M = \int_A E\varepsilon_\xi\zeta\,\mathrm{d}A = \int_A E\left(\frac{1}{1+\frac{\zeta}{\rho_o}}\left(\varepsilon_{o\xi}+\zeta\kappa_o\right)+\frac{1}{2}\psi_{o\eta}^2\right)\zeta\,\mathrm{d}A =$$

$$= \underbrace{\int_A E\frac{\zeta}{1+\frac{\zeta}{\rho_o}}\,\mathrm{d}A}_{Q_{eR}\simeq-\frac{I_{e\eta}}{\rho_o}}\varepsilon_{o\xi} + \underbrace{\int_A E\frac{\zeta^2}{1+\frac{\zeta}{\rho_o}}\,\mathrm{d}A}_{I_{eR}\simeq I_{e\eta}}\kappa_o + \underbrace{\int_A E\zeta\,\mathrm{d}A}_{Q_{e\eta}=0}\frac{1}{2}\psi_{o\eta}^2 =$$

$$= -\frac{I_{e\eta}}{\rho_o}\left(\frac{\mathrm{d}u_o}{\mathrm{d}s}+\frac{w_o}{\rho_o}\right) - I_{e\eta}\frac{\mathrm{d}}{\mathrm{d}s}\left(\frac{\mathrm{d}w_o}{\mathrm{d}s}-\frac{u_o}{\rho_o}\right) = -I_{e\eta}\left(\frac{\mathrm{d}^2w_o}{\mathrm{d}s^2}+\frac{w_o}{\rho_o^2}\right)\,. \quad (3.1.8)$$

In the sequel we assume the validity of the inequality $A_e\rho_o^2/I_{e\eta} \gg 1$, or which is the same that

$$\frac{A_e\rho_o^2}{I_{e\eta}} - 1 \approx \frac{A_e\rho_o^2}{I_{e\eta}} = \left(\frac{\rho_o}{i_e}\right)^2 = m\,, \quad i_e = \sqrt{\frac{I_{e\eta}}{A_e}}\,. \quad (3.1.9)$$

Here i_e is the E-weighted radius of gyration and m is a parameter of the geometry and material. In the knowledge of the previous formulae one can check – see Appendix A.1.1 for details – that

$$N = \frac{I_{e\eta}}{\rho_o^2}\left(\frac{A_e\rho_o^2}{I_{e\eta}}-1\right)\varepsilon_m - \frac{M}{\rho_o} \approx A_e\varepsilon_m - \frac{M}{\rho_o} =$$

$$= A_e\left[\frac{\mathrm{d}u_o}{\mathrm{d}s}+\frac{w_o}{\rho_o}+\frac{1}{2}\left(-\frac{\mathrm{d}w_o}{\mathrm{d}s}+u_o\right)^2\right] + \frac{I_{e\eta}}{\rho_o}\left(\frac{\mathrm{d}^2w_o}{\mathrm{d}s^2}+\frac{w_o}{\rho_o^2}\right)\,. \quad (3.1.10)$$

Contrarily, it is worth pointing out that – with our notations – the recent shallow beam model for homogeneous material ($E=$ constant) by Bradford et al. assume that

$$N = A_e\varepsilon_m = A_e\left[\frac{\mathrm{d}u_o}{\mathrm{d}s}+\frac{w_o}{\rho_o}+\frac{1}{2}\left(\frac{\mathrm{d}w_o}{\mathrm{d}s}\right)^2\right]; \qquad M = -I_{e\eta}\frac{\mathrm{d}^2w_o}{\mathrm{d}s^2}\,. \quad (3.1.11)$$

For the validity see equations (12) and (11) in [**61**]. The improvements implied to our new model are now easily noticeable.

For practical reasons it is sometimes worthy of changing derivatives with respect to the arc coordinate s to derivatives with respect to the angle coordinate φ. For the sake of brevity,

DOI: 10.14750/ME.2016.008

the following notational convention is introduced:

$$\frac{\mathrm{d}^n(\dots)}{\mathrm{d}s^n} = \frac{1}{\rho_o^n}\frac{\mathrm{d}^n(\dots)}{\mathrm{d}\varphi^n} = \frac{1}{\rho_o^n}(\dots)^{(n)} \;\; ; \quad n \in \mathbb{Z} \, . \tag{3.1.12}$$

3.1.2. General relations for the post-buckling state. First, we introduce a new notational convention. Quantities denoted by an asterisk are measured in the post-buckling equilibrium state while the change (increment) between the pre- and post-buckling equilibrium is denoted by a subscript $_b$. (The change from the initial configuration to the pre-buckling state is not denoted by any specific symbol.) Based on this rule, a similar line of thought as that applied in the previous subsection yields the increment in the kinematic relations. This means that for the rotation field and the change of curvature we have

$$\psi^*_{o\eta} = \frac{u^*_o}{\rho_o} - \frac{\mathrm{d}w^*_o}{\mathrm{d}s} = \frac{u_o + u_{ob}}{\rho_o} - \frac{\mathrm{d}(w_o + w_{ob})}{\mathrm{d}s} = \psi_{o\eta} + \psi_{o\eta\, b} \, , \quad \psi_{o\eta\, b} = \frac{u_{ob}}{\rho_o} - \frac{\mathrm{d}w_{ob}}{\mathrm{d}s} \, , \tag{3.1.13a}$$

$$\kappa^*_o = \frac{\mathrm{d}\psi^*_{o\eta}}{\mathrm{d}s} = \frac{1}{\rho_o}\frac{\mathrm{d}u^*_o}{\mathrm{d}s} - \frac{\mathrm{d}^2 w^*_o}{\mathrm{d}s^2} = \kappa_o + \kappa_{o\, b} \, , \quad \kappa_{o\, b} = \frac{1}{\rho_o}\frac{\mathrm{d}u_{ob}}{\mathrm{d}s} - \frac{\mathrm{d}^2 w_{ob}}{\mathrm{d}s^2} \, . \tag{3.1.13b}$$

According to (3.1.4) we obtain the expression of the 'exact' strain after buckling in the form

$$\begin{aligned} \varepsilon^*_\xi &= \frac{1}{1+\frac{\zeta}{\rho_o}}\left(\varepsilon^*_{o\xi} + \zeta\kappa^*_o\right) + \frac{1}{2}\left(\psi^*_{o\eta}\right)^2 = \frac{1}{1+\frac{\zeta}{\rho_o}}\left[\varepsilon_{o\xi} + \varepsilon_{o\xi\, b} + \zeta\left(\kappa_o + \kappa_{o\, b}\right)\right] + \frac{1}{2}\left(\psi_{o\eta} + \psi_{o\eta\, b}\right)^2 = \\ &= \frac{1}{1+\frac{\zeta}{\rho_o}}\left(\varepsilon_{o\xi} + \zeta\kappa_o\right) + \frac{1}{2}\left(\psi_{o\eta}\right)^2 + \frac{1}{1+\frac{\zeta}{\rho_o}}\left(\varepsilon_{o\xi\, b} + \zeta\kappa_{o\, b}\right) + \psi_{o\eta}\psi_{o\eta\, b} + \frac{1}{2}\psi^2_{o\eta\, b} = \varepsilon_\xi + \varepsilon_{\xi\, b} \end{aligned} \tag{3.1.14}$$

where

$$\varepsilon_{\xi\, b} = \frac{1}{1+\frac{\zeta}{\rho_o}}\left(\varepsilon_{o\xi\, b} + \zeta\kappa_{o\, b}\right) + \psi_{o\eta}\psi_{o\eta\, b} + \frac{1}{2}\psi^2_{o\eta\, b} \simeq \frac{1}{1+\frac{\zeta}{\rho_o}}\left(\varepsilon_{o\xi\, b} + \zeta\kappa_{o\, b}\right) + \psi_{o\eta}\psi_{o\eta\, b} \, , \tag{3.1.15a}$$

$$\varepsilon_{o\xi\, b} = \frac{\mathrm{d}u_{ob}}{\mathrm{d}s} + \frac{w_{ob}}{\rho_o} \, , \quad \varepsilon_{mb} = \varepsilon_{\xi\, b}|_{\zeta=0} = \varepsilon_{o\xi\, b} + \psi_{o\eta}\psi_{o\eta\, b} + \frac{1}{2}\psi^2_{o\eta\, b} \simeq \varepsilon_{o\xi\, b} + \psi_{o\eta}\psi_{o\eta\, b} \, . \tag{3.1.15b}$$

Notice that the quadratic term in the rotation increment is ignored since the validity of the inequality $0.5\psi^2_{o\eta\, b} \ll \psi_{o\eta}\psi_{o\eta\, b}$ is assumed. It is in accord with some earlier works, e.g. [**56**,**61**] where

$$\frac{1}{1+\frac{\zeta}{\rho_o}} = 1 \;\text{ and }\; \varepsilon_{m\, b} = \varepsilon_{o\xi\, b} + \psi_{o\eta}\psi_{o\eta\, b} \simeq \frac{\mathrm{d}u_{ob}}{\mathrm{d}s} + \frac{w_{ob}}{\rho_o} + \frac{\mathrm{d}w_o}{\mathrm{d}s}\frac{\mathrm{d}w_{ob}}{\mathrm{d}s}. \tag{3.1.16}$$

We proceed with the expressions for the inner axial force and bending moment. Recalling equations (3.1.7)-(3.1.8) valid for the pre-buckling state we can write

$$N^* = \int_A E\varepsilon^*_\xi \,\mathrm{d}A = \int_A E\left(\frac{1}{1+\frac{\zeta}{\rho_o}}\left(\varepsilon^*_{o\xi} + \zeta\kappa^*_o\right) + \frac{1}{2}\left(\psi^*_{o\eta}\right)^2\right)\mathrm{d}A = A_{eR}\varepsilon^*_{o\xi} + Q_{eR}\kappa^*_o + A_e\frac{1}{2}\left(\psi^*_{o\eta}\right)^2 \tag{3.1.17}$$

which is formally identical to (3.1.7). Substituting here the kinematic relations (3.1.15) and assuming again the validity of equations (2.1.13) we obtain

$$N^* = A_e\left(\varepsilon_{o\xi} + \frac{1}{2}\left(\psi_{o\eta}\right)^2\right) - \frac{I_{e\eta}}{\rho_o}\kappa_o + A_e\left(\varepsilon_{o\xi\, b} + \psi_{o\eta}\psi_{o\eta\, b}\right) - \frac{I_{e\eta}}{\rho_o}\kappa_{ob} = N + N_b \, . \tag{3.1.18}$$

The formula for the axial force increment is further manipulated as detailed under (A.1.2). The final nonlinear form is

$$N_b = \frac{I_{e\eta}}{\rho_o^2} m\varepsilon_{mb} + \frac{I_{e\eta}}{\rho_o^3}\left(w^{(2)}_{ob} + w_{ob}\right) \, . \tag{3.1.19}$$

DOI: 10.14750/ME.2016.008

It can be checked with ease by recalling (3.1.8) that

$$M^* = -I_{e\eta}\left(\frac{\mathrm{d}^2 w_o^*}{\mathrm{d}s^2} + \frac{w_o^*}{\rho_o^2}\right) = -I_{e\eta}\left(\frac{\mathrm{d}^2 w_o}{\mathrm{d}s^2} + \frac{w_o}{\rho_o^2}\right) \underbrace{-I_{e\eta}\left(\frac{\mathrm{d}^2 w_{ob}}{\mathrm{d}s^2} + \frac{w_{ob}}{\rho_o^2}\right)}_{M_b} = M + M_b \quad (3.1.20)$$

is the bending moment in the post-buckling equilibrium. With regard to equations (3.1.9) and (3.1.20), it follows from (3.1.19) that

$$N_b = \frac{I_{e\eta}}{\rho_o^2}\left(\frac{A_e \rho_o^2}{I_{e\eta}} - 1\right)\varepsilon_{mb} - \frac{M_b}{\rho_o} \approx A_e \varepsilon_{mb} - \frac{M_b}{\rho_o}\,. \quad (3.1.21)$$

For these increments similar observations can be made as those detailed in relation with equation (3.1.11) when comparing it to the model by Bradford et al.

3.2. Governing equations

3.2.1. Equilibrium conditions in the pre-buckling state. Figure 3.1 shows the centerline of the beam in the initial configuration (continuous line) as well as in the pre-buckling equilibrium state (dashed line) assuming symmetrical loading and support conditions. The beam is supported by rotationally restrained pins at both ends. These restraints – which are modelled as torsional springs – have a spring stiffness $(k_{\gamma\ell})[k_{\gamma r}]$ at the (left) [right] end. The loading can consist of the distributed force $\mathbf{f} = f_t\mathbf{e}_\xi + f_n\mathbf{e}_\zeta$ and the concentrated force P_ζ. The former one is directed downwards and is exerted at the crown point. The included angle of the curved member is 2ϑ. For the pre-buckling equilibrium state

$$\int_V \sigma_\xi \delta\varepsilon_\xi \,\mathrm{d}V = -P_\zeta\ \delta w_o|_{s=0} - k_{\gamma\ell}\psi_{o\eta}\delta\psi_{o\eta}|_{s(-\vartheta)} - k_{\gamma r}\psi_{o\eta}\delta\psi_{o\eta}|_{s(\vartheta)} + \int_{\mathcal{L}} (f_n\delta w_o + f_t\delta u_o)\,\mathrm{d}s \quad (3.2.1)$$

is the principle of virtual work, where the virtual (kinematically admissible) quantities are preceded by a symbol δ.

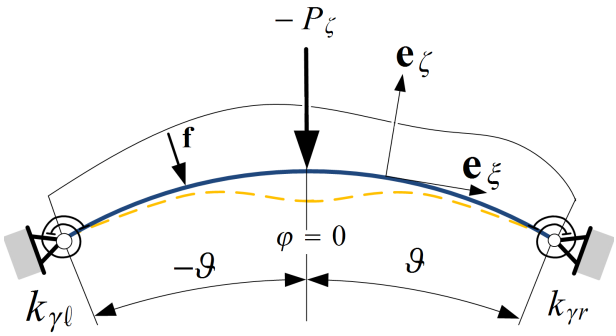

FIGURE 3.1. The investigated rotationally restrained beam.

Based on this principle one can find the equilibrium conditions, the dynamic boundary conditions (BCs) as well as the continuity and discontinuity conditions. Details are provided in Appendix A.1.2. With regard to the arbitrariness of the virtual quantities δu_o, δw_o and $\delta\psi_{o\eta}$, we have the equilibrium equations

$$\frac{\mathrm{d}N}{\mathrm{d}s} + \frac{1}{\rho_o}\left[\frac{\mathrm{d}M}{\mathrm{d}s} - \left(N + \frac{M}{\rho_o}\right)\psi_{o\eta}\right] + f_t = 0\,, \qquad \frac{\mathrm{d}}{\mathrm{d}s}\left[\frac{\mathrm{d}M}{\mathrm{d}s} - \left(N + \frac{M}{\rho_o}\right)\psi_{o\eta}\right] - \frac{N}{\rho_o} + f_n = 0\,, \quad (3.2.2)$$

the dynamic boundary conditions

$$N|_{s(\pm\vartheta)} = 0\,, \qquad \left[\frac{\mathrm{d}M}{\mathrm{d}s} - \left(N + \frac{M}{\rho_o}\right)\psi_{o\eta}\right]\Big|_{s(\pm\vartheta)} = 0\,, \quad (3.2.3a)$$

DOI: 10.14750/ME.2016.008

$$(M - k_{\gamma\ell}\psi_{o\eta})|_{s(-\vartheta)} = 0\,, \qquad (M + k_{\gamma r}\psi_{o\eta})|_{s(\vartheta)} = 0 \tag{3.2.3b}$$

and the discontinuity condition

$$\left[\frac{\mathrm{d}M}{\mathrm{d}s} - \left(N + \frac{M}{\rho_o}\right)\psi_{o\eta}\right]\Big|_{s=+0} - \left[\frac{\mathrm{d}M}{\mathrm{d}s} - \left(N + \frac{M}{\rho_o}\right)\psi_{o\eta}\right]\Big|_{s=-0} - P_\zeta = 0\,. \tag{3.2.3c}$$

The geometrical boundary conditions can assume the form

$$u_o|_{s(\pm\vartheta)} = 0\,, \quad w_o|_{s(\pm\vartheta)} = 0, \quad \psi_{o\eta}|_{s(\pm\vartheta)} = 0\,. \tag{3.2.4}$$

3.2.2. Equilibrium equations in terms of the displacements. In the sequel we focus on the stability problem of beams under a central concentrated force P_ζ. It means that the distributed load is removed. Our aim is to express the equilibrium equations in terms of the displacements. As for $(3.2.2)_1$, first, let us plug in relation (3.1.10) for the axial compressive force. Consequently, two terms vanish. What remains is

$$\frac{\mathrm{d}}{\mathrm{d}s}\left(A_e\varepsilon_m\right) - \frac{1}{\rho_o}\left(A_e\varepsilon_m\psi_{o\eta}\right) = 0\,. \tag{3.2.5}$$

It can be assumed with a good accuracy that the quadratic product $\varepsilon_m\psi_{o\eta}$ can be neglected when it is compared to the first term [**56**]. Accordingly

$$\frac{\mathrm{d}\varepsilon_m}{\mathrm{d}s} \simeq \frac{\mathrm{d}\varepsilon_{o\xi}}{\mathrm{d}s} = 0 \quad \rightarrow \quad \varepsilon_m \simeq \varepsilon_{o\xi} = \text{constant} \tag{3.2.6}$$

holds for the pre-buckling equilibrium. Hence, (depending on which theory is applied) the nonlinear/linearized strain on the centerline is constant.

Some further transformations are as well required on equation $(3.2.2)_2$. These are detailed in Appendix A.1.4. Here the final form, on which the stability investigations will be based is presented:

$$W_o^{(4)} + (2 - m\varepsilon_m)\,W_o^{(2)} + (1 - m\varepsilon_m)\,W_o = -m\varepsilon_m\,. \tag{3.2.7}$$

The new notation $W_o = w_o/\rho_o$ is referred to as the dimensionless normal displacement. For the sake of brevity, we introduce the parameter

$$\chi^2 = 1 - m\varepsilon_m. \tag{3.2.8}$$

In this way relation (3.2.7) can equivalently be rewritten as

$$W_o^{(4)} + \left(\chi^2 + 1\right)W_o^{(2)} + \chi^2 W_o = \chi^2 - 1\,. \tag{3.2.9}$$

This result is comparable with what Bradford et al. have used in their recent series of articles on stability problems of shallow arches – see, e.g. equation (14) in [**62**], which, with our notations, can be expressed as

$$W_o^{(4)} + (\chi^2 - 1)W_o^{(2)} = \chi^2 - 1\,. \tag{3.2.10}$$

The effects of our keeping the additional terms will be evaluated later in Section 3.5.

3.2.3. The principle of virtual work after the loss of stability. The principle of virtual work for the buckled configuration assumes the form

$$\int_V \sigma_\xi^*\delta\varepsilon_\xi^*\,\mathrm{d}V = -P_\zeta^*\,\delta w_o^*|_{s=0} + P_\xi^*\,\delta u_o^*|_{s=0} - \mathfrak{m}\ddot{w}_o^*\delta w_o^*|_{s=0} - \mathfrak{m}\ddot{u}_o^*\delta u_o^*|_{s=0} -$$
$$- k_{\gamma\,\ell}\psi_{o\eta}^*\delta\psi_{o\eta}^*\big|_{s(-\vartheta)} - k_{\gamma\,r}\psi_{o\eta}^*\delta\psi_{o\eta}^*\big|_{s(\vartheta)} + \int_{\mathcal{L}}\left(f_n^*\delta w_o^* + f_t^*\delta u_o^*\right)\mathrm{d}s\,, \tag{3.2.11}$$

where

$$\ddot{w}_o^* = \frac{\partial^2 w_o^*}{\partial t^2}\,, \quad \ddot{u}_o^* = \frac{\partial^2 u_o^*}{\partial t^2} \tag{3.2.12}$$

are the second time derivatives of the displacements.

DOI: 10.14750/ME.2016.008

Here it is assumed that the stability loss is a dynamical process characterized by a mass $\mathfrak{m}$ placed at the crown point of the beam (where the concentrated force acts). In other words, the effect of the mass distribution on the centerline is modelled by this concentrated mass. So far, we have made no restriction concerning the loads – they can be dead, or follower ones. However, we will assume a dead load later. Apart from these changes (3.2.11) formally coincides with (3.2.1).

Based on the detailed manipulations of Appendix A.1.3 it can be shown that the arbitrariness of the virtual quantities yields the post-buckling equations

$$\frac{\partial N_b}{\partial s}+\frac{1}{\rho_o}\frac{\partial M_b}{\partial s}-\frac{1}{\rho_o}\left(N+\frac{M}{\rho_o}\right)\psi_{o\eta\,b}-\frac{1}{\rho_o}\left(N_b+\frac{M_b}{\rho_o}\right)\psi_{o\eta\,b}+f_{tb}=0\,, \tag{3.2.13a}$$

$$\frac{\partial^2 M_b}{\partial s^2}-\frac{N_b}{\rho_o}-\frac{\partial}{\partial s}\left[\left(N+N_b+\frac{M+M_b}{\rho_o}\right)\psi_{o\eta\,b}+\left(N_b+\frac{M_b}{\rho_o}\right)\psi_{o\eta}\right]+f_{nb}=0\,. \tag{3.2.13b}$$

Moreover

$$\left[\frac{\partial M_b}{\partial s}-\left(N+N_b+\frac{M+M_b}{\rho_o}\right)\psi_{o\eta\,b}-\left(N_b+\frac{M_b}{\rho_o}\right)\psi_{o\eta}\right]\Big|_{s=-0}- \tag{3.2.14a}$$

$$-\left[\frac{\partial M_b}{\partial s}-\left(N+N_b+\frac{M+M_b}{\rho_o}\right)\psi_{o\eta\,b}-\left(N_b+\frac{M_b}{\rho_o}\right)\psi_{o\eta}\right]\Big|_{s=+0}+\mathfrak{m}\,\frac{\partial^2 w_{ob}}{\partial t^2}\Big|_{s=0}+P_{\zeta\,b}|_{s=0}=0\,,$$

$$N_b|_{s=-0}-N_b|_{s=+0}+P_{\xi\,b}+\mathfrak{m}\,\frac{\partial^2 u_{ob}}{\partial t^2}\Big|_{s=0}=0 \tag{3.2.14b}$$

are the discontinuity conditions at the crown point and

$$N_b|_{s(\pm\vartheta)}=0\,,\qquad (M_b+k_{\gamma\,r}\psi_{o\eta\,b})|_{s(\vartheta)}=0\,;\qquad (M_b-k_{\gamma\,\ell}\psi_{o\eta\,b})|_{s(-\vartheta)}=0\,,$$

$$\left[\frac{\partial M_b}{\partial s}-\left(N+N_b+\frac{M+M_b}{\rho_o}\right)\psi_{o\eta\,b}-\left(N_b+\frac{M_b}{\rho_o}\right)\psi_{o\eta}\right]\Big|_{s(\pm\vartheta)}=0 \tag{3.2.15}$$

are the dynamic boundary conditions.

Depending on the supports and loading applied, geometrical conditions such as

$$u_{ob}|_{s=-0}=u_{ob}|_{s=+0}\,,\quad w_{ob}|_{s=-0}=w_{ob}|_{s=+0}\,,\quad \psi_{o\eta\,b}|_{s=-0}=\psi_{o\eta\,b}|_{s=+0}\,, \tag{3.2.16}$$

$$u_{ob}|_{s(\pm\vartheta)}=0\,,\quad w_{ob}|_{(\pm\vartheta)}=0,\quad \psi_{o\eta\,b}|_{s(\pm\vartheta)}=0 \tag{3.2.17}$$

should be fulfilled instead of the corresponding boundary and discontinuity conditions.

3.2.4. Post-buckling equilibrium equations in terms of the displacements. Assume now – as in Subsection 3.2.2 – that there is only a dead load P_ζ exerted at the crown point of the beam and there is no concentrated mass $\mathfrak{m}$ at its point of application: $f_{nb}=f_{tb}=P_{\xi\,b}=P_{\zeta\,b}=\mathfrak{m}=0$. Observe that the structure of equilibrium equation (3.2.13a) is very similar to that of $(3.2.2)_1$. The exception is the last but one term in (3.2.13a) as it does not appear in the pre-buckling relation. However, that can be neglected since that product is quadratic in the increments. Therefore, repeating now the line of thought presented in Subsection 3.2.2 for the increments yields

$$\frac{\mathrm{d}}{\mathrm{d}s}\left(A_e\varepsilon_{mb}\right)-\underbrace{\frac{1}{\rho_o}\left(A_e\varepsilon_m\psi_{o\eta b}\right)}_{\text{it can be neglected}}=0\quad\Rightarrow\quad\frac{\mathrm{d}\varepsilon_{m\,b}}{\mathrm{d}s}\simeq\frac{\mathrm{d}\varepsilon_{o\xi\,b}}{\mathrm{d}s}=0\quad\rightarrow\quad\varepsilon_{m\,b}\simeq\varepsilon_{o\xi\,b}=\text{constant}\,. \tag{3.2.18}$$

Thus, the change in the axial strain is constant both for the nonlinear model and for the linear one.

DOI: 10.14750/ME.2016.008

Appendix A.1.5 is devoted to the detailed manipulations on equilibrium equation (3.2.13b). The resultant relation of these is

$$W_{ob}^{(4)} + (2 - m\varepsilon_m)W_{ob}^{(2)} + (1 - m\varepsilon_m)W_{ob} = -m\varepsilon_{mb} + m\varepsilon_{mb}(W_o^{(2)} + W_o) \tag{3.2.19}$$

which follows from (A.1.23). The new notation $W_{ob} = w_{ob}/\rho_o$ is the dimensionless displacement increment. Recalling (3.2.8) we have

$$W_{ob}^{(4)} + (\chi^2 + 1)W_{ob}^{(2)} + \chi^2 W_{ob} = m\varepsilon_{mb}\left[-1 + \left(W_o^{(2)} + W_o\right)\right] . \tag{3.2.20}$$

If we compare it with equation (39) in [**62**] by Bradford et al., that is

$$W_{ob}^{(4)} + (\chi^2 - 1)W_{ob}^{(2)} = m\varepsilon_{mb}\left(1 + W_o^{(2)}\right) , \tag{3.2.21}$$

the differences are easily noticeable.

3.3. Solutions for the pre-buckling state

3.3.1. General solution. In Section 3.2.2 we have derived differential equations (3.2.6) and (3.2.9), which describe the equilibrium of the beam prior to buckling. Because of the discontinuity in the shear force, the closed-form solution that satisfies the pre-buckling equilibrium is sought separately on the left [$W_{o\ell} = W_o$ if $\varphi \in [-\vartheta, 0]$] and on the right {$W_{or} = W_o$ if $\varphi \in [0, \vartheta]$} half-beam:

$$W_{or} = \frac{\chi^2 - 1}{\chi^2} + A_1 \cos\varphi + A_2 \sin\varphi - \frac{A_3}{\chi^2}\cos\chi\varphi - \frac{A_4}{\chi^2}\sin\chi\varphi , \tag{3.3.1a}$$

$$W_{o\ell} = \frac{\chi^2 - 1}{\chi^2} + B_1 \cos\varphi + B_2 \sin\varphi - \frac{B_3}{\chi^2}\cos\chi\varphi - \frac{B_4}{\chi^2}\sin\chi\varphi . \tag{3.3.1b}$$

Here A_i and B_i $(i = 1, \ldots, 4)$ are undetermined integration constants. These can be determined by using the boundary and continuity (discontinuity) conditions.

Three fundamental symmetric support arrangements will be investigated: when the beam is (a) pinned-pinned ($k_{\gamma r} = k_{\gamma \ell} = 0$), (b) fixed-fixed ($k_{\gamma r} = k_{\gamma \ell} \to \infty$) and (c) rotationally restrained by means of uniform torsional springs ($k_{\gamma r} = k_{\gamma \ell}$). The most important common property of these follows from the fact that the geometry, the loading and the supports are all symmetric in terms of φ, therefore the pre-buckling radial (dimensionless) displacement is an even function of the angle coordinate: $W_o(\varphi) = W_o(-\varphi)$. As a consequence, in what follows, it is sufficient to consider, e.g. a right half-beam model.

3.3.2. Pinned-pinned beams. As regards the boundary conditions at the crown point, the tangential displacement and the rotation are zero and there is a

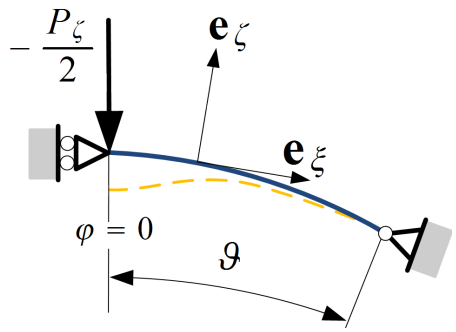

FIGURE 3.2. The simplified model of a pinned-pinned beam.

jump in the shear force with a magnitude $P_\zeta/2$. Moreover, the displacement and the bending moment are zero at the right pin-support. These boundary conditions are all gathered in Table 3.1, even in terms of the displacements.

DOI: 10.14750/ME.2016.008

TABLE 3.1. Boundary conditions for the pinned-pinned right half-beam.

Boundary conditions	
Crown point	Right end
$\psi_{o\eta}\big\|_{\varphi=+0}=0$	$W_o\big\|_{\varphi=\vartheta}=0$
$\left[-\frac{\mathrm{d}M}{\mathrm{d}s}+\frac{P_\zeta}{2}\right]_{\varphi=+0}=0$	$M\big\|_{\varphi=\vartheta}=0$

Boundary conditions in terms of W_o	
Crown point	Right end
$W_o^{(1)}\Big\|_{\varphi=+0}=0$	$W_o\big\|_{\varphi=\vartheta}=0$
$I_{e\eta}W_o^{(3)}\Big\|_{\varphi=+0}=\frac{P_\zeta}{2}$	$W_o^{(2)}\Big\|_{\varphi=\vartheta}=0$

When expressing the boundary conditions with the aid of the general solution valid for the right half-beam, we arrive at the system of linear equations

$$\begin{bmatrix} 0 & \chi & 0 & -1 \\ 0 & 0 & 0 & 1 \\ \cos\vartheta & \sin\vartheta & -\frac{1}{\chi^2}\cos\chi\vartheta & -\frac{1}{\chi^2}\sin\chi\vartheta \\ -\cos\vartheta & -\sin\vartheta & \cos\chi\vartheta & \sin\chi\vartheta \end{bmatrix} \begin{bmatrix} A_1 \\ A_2 \\ A_3 \\ A_4 \end{bmatrix} = \begin{bmatrix} 0 \\ \frac{\chi}{\chi^2-1}\frac{\hat{\mathcal{P}}}{\vartheta} \\ -\frac{\chi^2-1}{\chi^2} \\ 0 \end{bmatrix}, \quad \hat{\mathcal{P}}=\frac{P_\zeta}{2}\frac{\rho_o^2\vartheta}{I_{e\eta}}\,. \tag{3.3.2}$$

Here $\hat{\mathcal{P}}$ is a dimensionless force. Observe that the solutions

$$\begin{aligned} A_1 &= -\frac{1}{\cos\vartheta}-\frac{\tan\vartheta}{\chi^2-1}\frac{\hat{\mathcal{P}}}{\vartheta}=A_{11}+A_{12}\frac{\hat{\mathcal{P}}}{\vartheta}\,, \qquad A_2=\frac{1}{\chi^2-1}\frac{\hat{\mathcal{P}}}{\vartheta}=A_{22}\frac{\hat{\mathcal{P}}}{\vartheta}\,, \\ A_3 &= -\frac{1}{\cos\chi\vartheta}-\frac{\chi\tan\chi\vartheta}{\chi^2-1}\frac{\hat{\mathcal{P}}}{\vartheta}=A_{31}+A_{32}\frac{\hat{\mathcal{P}}}{\vartheta}\,, \quad A_4=\frac{\chi}{\chi^2-1}\frac{\hat{\mathcal{P}}}{\vartheta}=A_{42}\frac{\hat{\mathcal{P}}}{\vartheta} \end{aligned} \tag{3.3.3}$$

are decomposed into the sum of two parts depending on whether these are proportional to the loading (A_{i2}) or not (A_{i1}). Now the closed form solution for the whole beam can be constructed with the use of the function

$$H(\varphi)=\begin{cases} -1 & \varphi<0 \\ 1 & \varphi>0\,. \end{cases} \tag{3.3.4}$$

Thus,

$$\begin{aligned} W_o=\frac{\chi^2-1}{\chi^2}+A_{11}\cos\varphi-\frac{A_{31}}{\chi^2}\cos\chi\varphi+ \\ +\left(A_{12}\cos\varphi+A_{22}H\sin\varphi-\frac{A_{32}}{\chi^2}\cos\chi\varphi-\frac{A_{42}}{\chi^2}H\sin\chi\varphi\right)\frac{\hat{\mathcal{P}}}{\vartheta} \end{aligned} \tag{3.3.5}$$

is the dimensionless radial displacement. Recalling (2.1.8a) we get the rotation field

$$\begin{aligned} &\psi_{o\eta}=U_o-W_o^{(1)}\simeq -W_o^{(1)}= \\ &=D_{11}\sin\varphi+D_{31}\sin\chi\varphi+(D_{12}\sin\varphi+D_{22}\cos\varphi+D_{32}\sin\chi\varphi+D_{42}\cos\chi\varphi)\frac{\hat{\mathcal{P}}}{\vartheta}\,. \end{aligned} \tag{3.3.6a}$$

Here and in the sequel we assume that the tangential displacement has a negligible effect on the rotation field of shallow beams [**61**], [**108**]. The newly introduced nonzero constants D_{ij} $i,j\in[1,2,3,4]$ are defined by

$$D_{11}=A_{11}\,,\quad D_{12}=A_{12}\,,\quad D_{22}=-A_{22}H\,,\quad D_{31}=-\frac{A_{31}}{\chi}\,,\quad D_{32}=-\frac{A_{32}}{\chi}\,,\quad D_{42}=\frac{A_{42}H}{\chi}. \tag{3.3.6b}$$

We remark that for fixed-fixed and rotationally restrained shallow circular beams equations (3.3.5) and (3.3.6) are also valid, though the value of the constants differ.

The following line of thought is also proper for all three investigated support arrangements. As equilibrium equation (3.2.6) yields that the axial strain $(3.1.4)_1$ is constant on

DOI: 10.14750/ME.2016.008

the centerline, let us calculate the mathematical average of this quantity. According to the linear theory we thus have

$$\varepsilon_{o\xi} = \frac{1}{\vartheta}\int_0^{\vartheta} \varepsilon_{o\xi}(\varphi)\mathrm{d}\varphi = \frac{1}{\vartheta}\,U_o\big|_0^{\vartheta} + \frac{1}{\vartheta}\int_0^{\vartheta} W_o\mathrm{d}\varphi = \frac{1}{\vartheta}\int_0^{\vartheta} W_o\mathrm{d}\varphi = I_{ow} + I_{1w}\frac{\hat{\mathcal{P}}}{\vartheta}\ . \quad (3.3.7)$$

Although the above equation is linear in $\hat{\mathcal{P}}$, it is nonlinear in $\varepsilon_{o\xi}$ due to the presence of χ – see the definition under (3.2.8). We remark that the integrals I_{ow} and I_{1w} are presented in closed form in Appendix A.1.6. Equation (3.3.7) can be rearranged so that

$$I_{1w}\frac{\hat{\mathcal{P}}}{\vartheta} + I_{ow} - \varepsilon_{o\xi} = 0\ . \quad (3.3.8)$$

If we now consider the strain according to the nonlinear theory, the mathematical average of (3.1.4) is given by

$$\varepsilon_m = \frac{1}{\vartheta}\int_0^{\vartheta} \varepsilon_m(\varphi)\mathrm{d}\varphi = \frac{1}{\vartheta}\int_0^{\vartheta}\left(\varepsilon_{o\xi} + \frac{1}{2}\psi_{o\eta}^2\right)\mathrm{d}\varphi = I_{ow} + I_{1w}\frac{\hat{\mathcal{P}}}{\vartheta} + I_{o\psi} + I_{1\psi}\frac{\hat{\mathcal{P}}}{\vartheta} + I_{2\psi}\left(\frac{\hat{\mathcal{P}}}{\vartheta}\right)^2 \quad (3.3.9)$$

or which is the same

$$I_{2\psi}\left(\frac{\hat{\mathcal{P}}}{\vartheta}\right)^2 + (I_{1w} + I_{1\psi})\frac{\hat{\mathcal{P}}}{\vartheta} + (I_{ow} + I_{o\psi} - \varepsilon_m) = 0\ . \quad (3.3.10)$$

This is a more accurate quadratic relationship between the external load and the axial strain. The constants $I_{o\psi}$, $I_{1\,\psi}$ and $I_{2\psi}$ for pinned-pinned support are gathered in Appendix A.1.6.

We hereby note that the former integrals were computed numerically by using the subroutine `DQDAG` from the IMSL Library [**109**] when using a self-made Fortran 90 code to find solutions. After performing some tests, we have come to the conclusion that the accuracy of this routine turns out to be more than sufficient with its maximum error being less than 10^{-7}.

3.3.3. Fixed-fixed beams. Compared to pinned-pinned members, one boundary condition is changed at the right support of the half-beam model. This time the rotation is zero if $\varphi = \vartheta$ – we refer to Table 3.2.

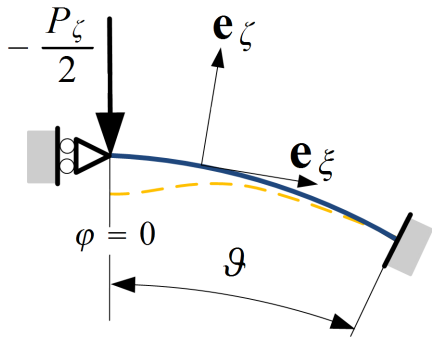

FIGURE 3.3. The simplified model of a fixed-fixed beam.

DOI: 10.14750/ME.2016.008

TABLE 3.2. Boundary conditions for the fixed-fixed right half-beam.

Boundary conditions	
Crown point	Right end
$\psi_{o\eta}\big\vert_{\varphi=+0}=0$	$W_o\big\vert_{\varphi=\vartheta}=0$
$-\frac{\mathrm{d}M}{\mathrm{d}s}\big\vert_{\varphi=+0}+\frac{P_\zeta}{2}=0$	$\psi_{o\eta}\big\vert_{\varphi=\vartheta}=0$

Boundary conditions	
Crown point	Right end
$W_o^{(1)}\big\vert_{\varphi=+0}=0$	$W_o\big\vert_{\varphi=\vartheta}=0$
$I_{e\eta}W_o^{(3)}\big\vert_{\varphi=+0}=\frac{P_\zeta}{2}$	$W_o^{(1)}\big\vert_{\varphi=\vartheta}=0$

Consequently, after recalling solution (3.3.1a) we get the equation system

$$\begin{bmatrix} 0 & \chi & 0 & -1 \\ 0 & 0 & 0 & 1 \\ \cos\vartheta & \sin\vartheta & -\frac{1}{\chi^2}\cos\chi\vartheta & -\frac{1}{\chi^2}\sin\chi\vartheta \\ -\chi\sin\vartheta & \chi\cos\vartheta & \sin\chi\vartheta & -\cos\chi\vartheta \end{bmatrix} \begin{bmatrix} A_1 \\ A_2 \\ A_3 \\ A_4 \end{bmatrix} = \begin{bmatrix} 0 \\ \hat{\mathcal{P}}\frac{1}{\vartheta}\frac{\chi}{\chi^2-1} \\ -\frac{\chi^2-1}{\chi^2} \\ 0 \end{bmatrix} \tag{3.3.11}$$

for the determination of the integration constants. From here we obtain

$$A_1=\frac{1-\chi^2}{\mathcal{D}\chi}\sin\chi\vartheta+\frac{1}{\mathcal{D}(1-\chi^2)}(\cos\vartheta\,\cos\chi\vartheta+\chi\sin\vartheta\,\sin\chi\vartheta-1)\frac{\hat{\mathcal{P}}}{\vartheta}=A_{11}+A_{12}\frac{\hat{\mathcal{P}}}{\vartheta}\,, \tag{3.3.12a}$$

$$A_2=\frac{1}{\chi^2-1}\frac{\hat{\mathcal{P}}}{\vartheta}=A_{22}\frac{\hat{\mathcal{P}}}{\vartheta}\,,\qquad A_4=\frac{\chi}{\chi^2-1}\frac{\hat{\mathcal{P}}}{\vartheta}=A_{42}\frac{\hat{\mathcal{P}}}{\vartheta}\,, \tag{3.3.12b}$$

$$A_3=\frac{1}{\mathcal{D}}\left(1-\chi^2\right)\sin\vartheta+\frac{\chi}{\mathcal{D}(1-\chi^2)}\left(\chi-\sin\vartheta\,\sin\chi\vartheta-\chi\cos\vartheta\,\cos\chi\vartheta\right)\frac{\hat{\mathcal{P}}}{\vartheta}=A_{31}+A_{32}\frac{\hat{\mathcal{P}}}{\vartheta}\,, \tag{3.3.12c}$$

where

$$\mathcal{D}=\chi\cos\vartheta\,\sin\chi\vartheta-\sin\vartheta\,\cos\chi\vartheta\,. \tag{3.3.12d}$$

It means that we can now establish the displacement and rotation fields for the whole beam in the same way as in (3.3.5), (3.3.6). On the basis of (3.3.7) and (3.3.9), calculating the mathematical average of the strain yields either

$$I_{1w}\frac{\hat{\mathcal{P}}}{\vartheta}+I_{ow}-\varepsilon_{o\xi}=0\,, \tag{3.3.13}$$

or

$$I_{2\psi}\left(\frac{\hat{\mathcal{P}}}{\vartheta}\right)^2+\left(I_{1w}+I_{1\psi}\right)\frac{\hat{\mathcal{P}}}{\vartheta}+\left(I_{ow}+I_{o\psi}-\varepsilon_m\right)=0\,. \tag{3.3.14}$$

As regards the values of the integrals I_{ow}, I_{1w} and $I_{o\psi}$, $I_{1\,\psi}$, $I_{2\psi}$, we refer the reader to Appendix A.1.6. Keep in mind however, that the constants A_1, A_2, A_3 and A_4 are now given by (3.3.12). Therefore the values of D_{ij} in (3.3.6b) also differ from those valid for pinned-pinned beams.

3.3.4. Rotationally-restrained beams. The appropriately chosen half-beam model is shown in Figure 3.4, while the boundary conditions are gathered in Table 3.3.

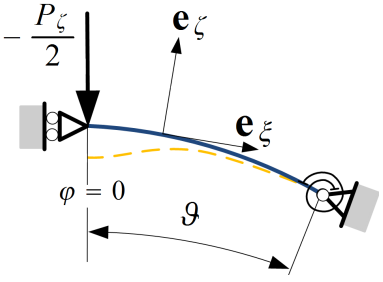

FIGURE 3.4. The simplified model of a rotationally restrained beam.

DOI: 10.14750/ME.2016.008

For the sake of brevity, it is practical to introduce the constant

$$\mathcal{S} = \frac{\rho_o k_\gamma}{I_{e\eta}}, \tag{3.3.15}$$

which is the dimensionless spring stiffness. The greater $\mathcal{S}$ is, the greater the restraining moment the springs exert on the beam.

TABLE 3.3. Boundary conditions for the rotationally restrained right half-beam.

Boundary conditions		Boundary conditions in terms of W_o	
Crown point	Right end	Crown point	Right end
$\psi_{o\eta}\big\|_{\varphi=+0} = 0$	$W_o\big\|_{\varphi=\vartheta} = 0$	$W_o^{(1)}\Big\|_{\varphi=+0} = 0$	$W_o\big\|_{\varphi=\vartheta} = 0$
$\left[-\frac{\mathrm{d}M}{\mathrm{d}s} + \frac{P_\zeta}{2}\right]_{\varphi=+0} = 0$	$[M + k_\gamma \psi_{o\,\eta}]\big\|_{\varphi=\vartheta} = 0$	$I_{e\eta} W_o^{(3)}\Big\|_{\varphi=+0} = \frac{P_\zeta}{2}$	$\left[W_o^{(2)} + \mathcal{S} W_o^{(1)}\right]\Big\|_{\varphi=\vartheta} = 0$

Here we get the following system of equations for $A_1, ..., A_4$:

$$\begin{bmatrix} \cos\vartheta & \sin\vartheta & -\frac{\cos\chi\vartheta}{\chi^2} & -\frac{\sin\chi\vartheta}{\chi^2} \\ 0 & \chi & 0 & -1 \\ -\cos\vartheta - \mathcal{S}\sin\vartheta & \mathcal{S}\cos\vartheta - \sin\vartheta & \cos\chi\vartheta + \frac{\mathcal{S}}{\chi}\sin\chi\vartheta & \sin\chi\vartheta - \frac{\mathcal{S}}{\chi}\cos\chi\vartheta \\ 0 & -1 & 0 & \chi \end{bmatrix} \begin{bmatrix} A_1 \\ A_2 \\ A_3 \\ A_4 \end{bmatrix} = \begin{bmatrix} \frac{1-\chi^2}{\chi^2} \\ 0 \\ 0 \\ \frac{\hat{\mathcal{P}}}{\vartheta} \end{bmatrix}. \tag{3.3.16}$$

Let us introduce the constant

$$\mathcal{C}_0 = \left(\chi^2 - 1\right)\cos\vartheta\cos\chi\vartheta - \mathcal{S}\left(\sin\vartheta\cos\chi\vartheta - \chi\cos\vartheta\sin\chi\vartheta\right) \tag{3.3.17}$$

thus, the solution to (3.3.16) satisfies the boundary conditions if

$$A_1 = A_{11} + \frac{\hat{\mathcal{P}}}{\vartheta}A_{12} = \frac{\left(1-\chi^2\right)\left(\chi\cos\chi\vartheta + \mathcal{S}\sin\chi\vartheta\right)}{\chi\mathcal{C}_0} + \\ + \frac{\left(1-\chi^2\right)\sin\vartheta\cos\chi\vartheta - \mathcal{S}\left(\cos\vartheta\cos\chi\vartheta + \chi\sin\vartheta\sin\chi\vartheta - 1\right)}{\left(\chi^2-1\right)\mathcal{C}_0}\frac{\hat{\mathcal{P}}}{\vartheta}, \tag{3.3.18a}$$

$$A_2 = \frac{1}{\left(\chi^2-1\right)}\frac{\hat{\mathcal{P}}}{\vartheta} = A_{22}\frac{\hat{\mathcal{P}}}{\vartheta}; \quad A_4 = \frac{\chi}{\left(\chi^2-1\right)}\frac{\hat{\mathcal{P}}}{\vartheta} = A_{42}\frac{\hat{\mathcal{P}}}{\vartheta}, \tag{3.3.18b}$$

$$A_3 = A_{31} + \frac{\hat{\mathcal{P}}}{\vartheta}A_{32} = \frac{\cos\vartheta + \mathcal{S}\sin\vartheta}{-\mathcal{C}_0} + \\ + \frac{\chi\left[\left(\chi^2-1\right)\cos\vartheta\sin\chi\vartheta - \mathcal{S}\left(\sin\vartheta\sin\chi\vartheta + \chi\cos\vartheta\cos\chi\vartheta - \chi\right)\right]}{-\left(\chi^2-1\right)\mathcal{C}_0}\frac{\hat{\mathcal{P}}}{\vartheta}. \tag{3.3.18c}$$

If $[\mathcal{S} = 0]$ $\{\mathcal{S} \to \infty\}$ we get back the results valid for [pinned-pinned (3.3.3)] and {fixed-fixed (3.3.12)} beams.

The radial displacement for the whole rotationally restrained beam is given by (3.3.5), while (3.3.6) provides the rotation field, given that the relevant A_{ij} constants are substituted. Averaging the strain again yields a formula which is formally the same as (3.3.10). The related coefficients I_{ow}, I_{1w}, $I_{o\psi}$, $I_{1\,\psi}$ and $I_{2\psi}$ are listed in Appendix A.1.6.

3.4. Possible solutions for the post-buckling state

3.4.1. General solution. After substituting the pre-buckling solution (3.3.5) into the right side of equation (3.2.20) we get

$$W_{ob}^{(4)} + (1+\chi^2)W_{ob}^{(2)} + \chi^2 W_{ob} = -m\varepsilon_{mb}\frac{1-\chi^2}{\chi^2}\left(\frac{1}{1-\chi^2} + A_3\cos\chi\varphi + A_4\sin\chi\varphi\right). \tag{3.4.1}$$

DOI: 10.14750/ME.2016.008

We remind the reader that the post-buckling axial strain on the E-weighted centerline is constant (3.2.18) and it can therefore be calculated as

$$\varepsilon_{mb} = \frac{1}{2\vartheta}\int_{-\vartheta}^{\vartheta}\left(U_{ob}^{(1)} + W_{ob} + \psi_{o\eta\,b}\psi_{o\eta}\right)\mathrm{d}\varphi = \frac{1}{2\vartheta}\,U_{ob}|_{-\vartheta}^{\vartheta} + \frac{1}{2\vartheta}\int_{-\vartheta}^{\vartheta}\left(W_{ob} + \psi_{o\eta\,b}\psi_{o\eta}\right)\mathrm{d}\varphi =$$
$$= \frac{1}{2\vartheta}\int_{-\vartheta}^{\vartheta}\left(W_{ob} + \left(U_{ob} - W_{ob}^{(1)}\right)\left(U_o - W_o^{(1)}\right)\right)\mathrm{d}\varphi \approx \frac{1}{2\vartheta}\int_{-\vartheta}^{\vartheta}\left(W_{ob} + W_{ob}^{(1)}W_o^{(1)}\right)\mathrm{d}\varphi\,. \quad (3.4.2)$$

It is clear that the rotation $\psi_{o\eta} \approx -W_o^{(1)}$ is an odd function of φ. Due to the symmetry properties of the loading and the supports, there are two basically different cases to be dealt with. If, by assumption, W_{ob} is an odd function of φ, then the above integral vanishes: ε_{mb} is equal to zero. Otherwise, when – by hypothesis – W_{ob} is an even function φ, the strain increment is a nonzero constant. We remark that these observations are naturally valid for homogeneous beams as well [**61**, **65**]. Consequently: (a) if $\varepsilon_{mb} = 0$ the differential equation that governs the problem of antisymmetric (or bifurcation) buckling is homogeneous and, according to (3.4.1), it takes the form

$$W_{ob}^{(4)} + (1+\chi^2)W_{ob}^{(2)} + \chi^2 W_{ob} = 0\,, \quad (3.4.3)$$

while (b) if $\varepsilon_{mb} = \text{constant} \neq 0$ we have to solve equation (3.2.20) (or which is the same equation (3.4.1)) keeping in mind that the buckled shape of the beam is symmetric. The latter phenomenon is called snap-through or limit-point buckling. To better understand, the two possibilities are illustrated in Figure 3.5 where a continuous line represents the centerline of the beam in the initial configuration, the dashed line is the symmetric pre-buckling shape, while the dotted line is the buckled (a) antisymmetric, (b) symmetric shape of the centerline. Although the figure in question shows rotational restraints, the shapes are valid for pinned-pinned and fixed-fixed shallow curved beams as well.

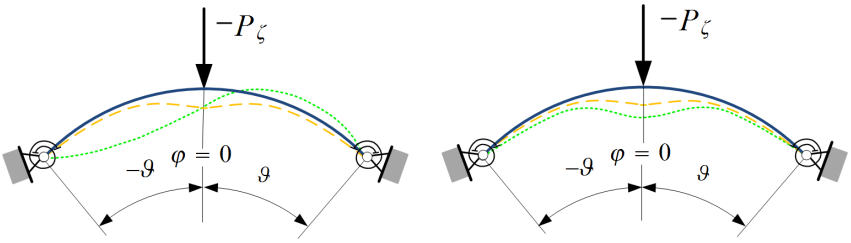

FIGURE 3.5. Possible (a) antisymmetric and (b) symmetric buckling shapes.

The general solution to the homogeneous differential equation (3.4.3) assumes the form

$$W_{ob}(\varphi) = F_1\cos\varphi + F_2\sin\varphi + F_3\sin\chi\varphi + F_4\cos\chi\varphi\,, \quad (3.4.4)$$

meanwhile the displacement field satisfying differential equation (3.4.1) is sought as

$$W_{ob}(\varphi) = C_1\cos\varphi + C_2\sin\varphi + C_3\sin\chi\varphi + C_4\cos\chi\varphi - \frac{m\varepsilon_{m\,b}}{2\chi^3}\left(\frac{2}{\chi} + A_3\varphi\sin\chi\varphi - A_4\varphi\cos\chi\varphi\right). \quad (3.4.5)$$

Here C_i and F_i are undetermined integration constants. It is important to mention that after buckling, every physical quantity is continuous through the interval $\varphi \in [-\vartheta;\vartheta]$ because there is no increment in the loading.

The newly introduced concepts, like bifurcation and limit-point buckling will further be illustrated in Subsubsection 3.5.1.3.

DOI: 10.14750/ME.2016.008

3.4.2. Pinned-pinned beams – antisymmetric buckling. The boundary conditions in terms of the displacement increments are gathered in Table 3.4.

TABLE 3.4. Boundary conditions for pinned-pinned beams when $\varepsilon_{mb} = 0$.

Boundary conditions	
Left end	Right end
$W_{ob}(\varphi)\,\vert_{\varphi=-\vartheta} = 0$	$W_{ob}(\varphi)\,\vert_{\varphi=\vartheta} = 0$
$W_{ob}^{(2)}(\varphi)\Big\vert_{\varphi=-\vartheta} = 0$	$W_{ob}^{(2)}(\varphi)\Big\vert_{\varphi=\vartheta} = 0$

After substituting the solution (3.4.4) into the former boundary conditions we arrive at the homogeneous system of linear equations:

$$\begin{bmatrix} \cos\vartheta & 0 & 0 & \cos\chi\vartheta \\ 0 & \sin\vartheta & \sin\chi\vartheta & 0 \\ \cos\vartheta & 0 & 0 & \chi^2\cos\chi\vartheta \\ 0 & \sin\vartheta & \chi^2\sin\chi\vartheta & 0 \end{bmatrix} \begin{bmatrix} F_1 \\ F_2 \\ F_3 \\ F_4 \end{bmatrix} = \begin{bmatrix} 0 \\ 0 \\ 0 \\ 0 \end{bmatrix} . \tag{3.4.6}$$

Nontrivial solution is obtained when the determinant of the coefficient matrix vanishes:

$$\mathfrak{D} = (1-\chi)^2(1+\chi)^2 \sin\chi\vartheta \cos\chi\vartheta \cos\vartheta \sin\vartheta = 0 . \tag{3.4.7}$$

Recalling the notation $\chi^2 = 1 - m\varepsilon_m$ we can come to the following conclusions: (a) if $1-\chi = 0$ then $\chi = 1$, consequently $\varepsilon_m = 0$; (b) if $1+\chi = 0$ then $\chi = -1$ and so $\varepsilon_m > 0$; (c) if $\sin\chi\vartheta = 0$ then $\chi = \pi/\vartheta$ and (d) if $\cos\chi\vartheta = 0$ then $\chi = \pi/2\vartheta$. We remark that the first two cases have no physical sense. For solution (d) we get that $W_{ob}(\varphi) = E_4\cos\frac{\pi}{2\vartheta}\varphi$ which is a contradiction as for symmetric buckled shapes $\varepsilon_{mb} \neq 0$. These thoughts mean that the lowest critical axial strain for bifurcation buckling is

$$\varepsilon_m = \frac{1}{m}\left(1-\chi^2\right) = \frac{1}{m}\left[1-\left(\frac{\mathfrak{G}(\vartheta)}{\vartheta}\right)^2\right], \qquad \text{where} \qquad \mathfrak{G}(\vartheta) = \pi . \tag{3.4.8}$$

If we now substitute solution (c) back into equation system (3.4.6) it can be checked that $F_1 = F_2 = F_4 = 0$ and consequently, it follows from (3.4.4) that

$$W_{ob}(\varphi) = F_3 \sin\frac{\pi}{\vartheta}\varphi \tag{3.4.9}$$

is the buckled antisymmetric shape of the beam with the unknown amplitude parameter F_3.

Note that if we neglect the effect of the angle of rotation on the axial strain then we shall change the notation ε_m to $\varepsilon_{o\xi}$.

3.4.3. Pinned-pinned beams – symmetric buckling. When solving differential equation (3.4.1) it is sufficient to deal with a half beam model again. Choosing the right-half beam and relying on a similar concept as introduced in Subsection 3.3.2, the boundary conditions are presented in Table 3.5.

TABLE 3.5. Boundary conditions for pinned-pinned beams when $\varepsilon_{mb} \neq 0$.

Boundary conditions	
Crown point	Right end
$W_{ob}^{(1)}(\varphi)\Big\vert_{\varphi=0} = 0$	$W_{ob}(\varphi)\,\vert_{\varphi=\vartheta} = 0$
$W_{ob}^{(3)}(\varphi)\Big\vert_{\varphi=0} = 0$	$W_{ob}^{(2)}(\varphi)\Big\vert_{\varphi=\vartheta} = 0$

DOI: 10.14750/ME.2016.008

Upon substitution of solution (3.4.5) into the boundary conditions we arrive at the inhomogeneous system of linear equations

$$\begin{bmatrix} 0 & -2\chi^3 & -2\chi^4 & 0 \\ 0 & -2\chi & -2\chi^4 & 0 \\ \cos\vartheta & \sin\vartheta & \sin\chi\vartheta & \cos\chi\vartheta \\ 2\chi^2\cos\vartheta & 2\chi^2\sin\vartheta & 2\chi^4\sin\chi\vartheta & 2\chi^4\cos\chi\vartheta \end{bmatrix} \begin{bmatrix} C_1 \\ C_2 \\ C_3 \\ C_4 \end{bmatrix} =$$

$$= m\varepsilon_{mb} \begin{bmatrix} A_4 \\ 3A_4 \\ \frac{1}{2\chi^3}\left(\frac{2}{\chi} + A_3\vartheta\sin\chi\vartheta - A_4\vartheta\cos\chi\vartheta\right) \\ A_3\left(\chi\vartheta\sin\chi\vartheta - 2\cos\chi\vartheta\right) - A_4\left(2\sin\chi\vartheta + \vartheta\chi\cos\chi\vartheta\right) \end{bmatrix} \tag{3.4.10}$$

which can be solved in closed-form – the constants C_i are presented in Appendix A.1.7. The decomposition of the resultant coefficients into two parts – one independent of $\hat{\mathcal{P}}$ and the other depending linearly on $\hat{\mathcal{P}}$ – is also carried out there in such a way that

$$C_i = \varepsilon_{mb}\left(\hat{C}_{i1} + \hat{C}_{i2}\frac{\hat{\mathcal{P}}}{\vartheta}\right) \quad , \quad i = 1, \ldots, 4\,. \tag{3.4.11}$$

The forthcoming thoughts are valid for all three support arrangements. The solution to W_{ob} for the whole beam can now be reconstructed using the previous constants – see equations (A.1.37)-(A.1.38) for further details – as

$$W_{ob} = \varepsilon_{mb}\left[\left(\hat{C}_{01} + \hat{C}_{11}\cos\varphi + \hat{C}_{41}\cos\chi\varphi + \hat{C}_{51}\varphi\sin\chi\varphi\right) + \right.$$
$$\left. + \frac{\hat{\mathcal{P}}}{\vartheta}\left(\hat{C}_{12}\cos\varphi + \hat{C}_{22}H\sin\varphi + \hat{C}_{32}H\sin\chi\varphi + \hat{C}_{42}\cos\chi\varphi + \hat{C}_{52}\varphi\sin\chi\varphi + \hat{C}_{62}H\varphi\cos\chi\varphi\right)\right]. \tag{3.4.12}$$

In the knowledge of the radial displacement we can determine the rotation increment:

$$-\psi_{o\eta\,b} \simeq W_{ob}^{(1)} = \varepsilon_{mb}\Bigg[K_{11}\sin\varphi + K_{41}\sin\chi\varphi + K_{51}\varphi\cos\chi\varphi +$$
$$+ \left(K_{12}\sin\varphi + K_{22}\cos\varphi + K_{32}\cos\chi\varphi + K_{42}\sin\chi\varphi + K_{52}\varphi\cos\chi\varphi + K_{62}\varphi\sin\chi\varphi\right)\frac{\hat{\mathcal{P}}}{\vartheta}\Bigg]\,, \tag{3.4.13}$$

where the new constants K_{ij} are defined by (A.1.41). If we neglect the effect of the tangential displacement on the angle of rotation – this assumption is the same as that the in papers [**56**, **74**] – we can rewrite equation (3.4.2) in the form

$$\varepsilon_{mb} = \frac{1}{\vartheta}\int_0^{\vartheta}\left(W_{ob} + W_o^{(1)}W_{ob}^{(1)}\right)\mathrm{d}\varphi\,. \tag{3.4.14}$$

Application of the linearized theory would result in

$$\varepsilon_{o\xi\,b} = \frac{1}{\vartheta}\int_0^{\vartheta} W_{ob}\,\mathrm{d}\varphi\,. \tag{3.4.15}$$

If we now substitute (3.3.6), (3.4.12) and (3.4.13) into equation (3.4.14), we can observe that the strain increment vanishes. Further performing the integrations we have

$$1 = \left[I_{01} + \frac{\hat{\mathcal{P}}}{\vartheta}I_{02}\right] + \left[I_{11} + \frac{\hat{\mathcal{P}}}{\vartheta}I_{12} + \left(\frac{\hat{\mathcal{P}}}{\vartheta}\right)^2 I_{13}\right]$$

DOI: 10.14750/ME.2016.008

or what is the same

$$I_{13}\left(\frac{\hat{\mathcal{P}}}{\vartheta}\right)^2+[I_{02}+I_{12}]\,\frac{\hat{\mathcal{P}}}{\vartheta}+[I_{01}+I_{11}-1]=0\;;\qquad I_{ij}\in\mathbb{R}\,. \tag{3.4.16}$$

Here the constants I_{01} and I_{02} follow from the first integral – and at the same time from the linear theory – in (3.4.14), while the coefficients I_{11}, I_{12} and I_{13} are from the second one. We can therefore remark that establishment of closed-form solutions to the integrals is again possible. Some details are gathered in Appendix A.1.8. We also remark that we have used the same IMSL subroutine as before to compute numerically the value of each integral in order to determine the critical load.

3.4.4. Fixed-fixed beams – antisymmetric buckling. Substitute solution (3.4.4) for the displacement increment W_{ob} into the boundary conditions presented in Table 3.6.

TABLE 3.6. Boundary conditions for fixed-fixed beams when $\varepsilon_{mb}=0$.

Boundary conditions	
Left support	Right support
$W_{ob}\big\vert_{\varphi=-\vartheta}=0$	$W_{ob}\big\vert_{\varphi=\vartheta}=0$
$W_{ob}^{(1)}\Big\vert_{\varphi=-\vartheta}=0$	$W_{ob}^{(1)}\Big\vert_{\varphi=\vartheta}=0$

Then nontrivial solution of the equation system

$$\begin{bmatrix}\cos\vartheta & 0 & 0 & \cos\chi\vartheta\\ 0 & \sin\vartheta & \sin\chi\vartheta & 0\\ 0 & \cos\vartheta & \chi\cos\chi\vartheta & 0\\ \sin\vartheta & 0 & 0 & \chi\sin\chi\vartheta\end{bmatrix}\begin{bmatrix}F_1\\F_2\\F_3\\F_4\end{bmatrix}=\begin{bmatrix}0\\0\\0\\0\end{bmatrix} \tag{3.4.17}$$

exists when the characteristic determinant is set to zero:

$$\mathfrak{D}=(\chi\sin\vartheta\cos\chi\vartheta-\cos\vartheta\sin\chi\vartheta)\,(\sin\vartheta\cos\chi\vartheta-\chi\cos\vartheta\sin\chi\vartheta)=0\,. \tag{3.4.18}$$

Vanishing of the first factor results in

$$\chi\tan\vartheta=\tan\chi\vartheta\;, \tag{3.4.19}$$

to which the solution can be approximated with a good accuracy by the polynomial

$$\begin{aligned}\chi\vartheta=\mathfrak{H}(\vartheta=0\ldots1.5)&=4.493\,419\,972+8.585\,048\,966\cdot10^{-3}\vartheta+3.717\,588\,695\cdot10^{-2}\vartheta^2+\\&+5.594\,338\,754\cdot10^{-2}\vartheta^3-3.056\,068\,806\cdot10^{-2}\vartheta^4+8.717\,756\,418\cdot10^{-3}\vartheta^5\;.\end{aligned} \tag{3.4.20}$$

Graphical illustration of this result is presented in Figure 3.6. It can easily be shown that an antisymmetric buckling shape is related to this solution with $F_1=F_4=0$ and $F_2=-F_3\sin\chi\vartheta/\sin\vartheta$, thus

$$W_{ob}=F_3\left(\sin\chi\varphi-\frac{\sin\chi\vartheta}{\sin\vartheta}\sin\varphi\right)\;. \tag{3.4.21}$$

DOI: 10.14750/ME.2016.008

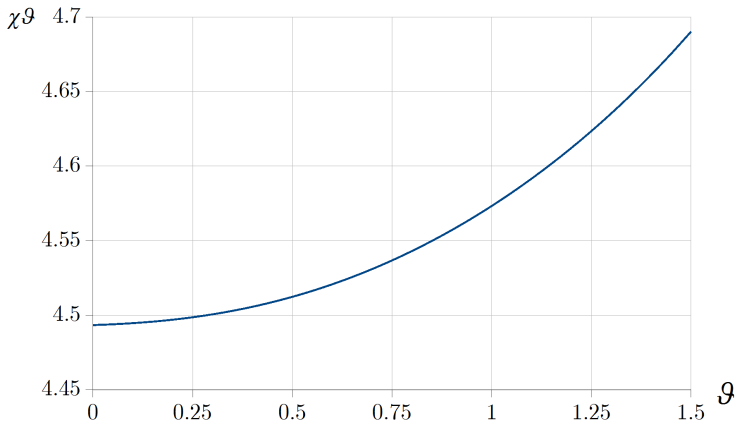

FIGURE 3.6. Antisymmetric solution for fixed-fixed beams.

Hence, the critical strain is

$$\varepsilon_m = \frac{1}{m}\left(1-\chi^2\right) = \frac{1}{m}\left[1-\left(\frac{\mathfrak{H}(\vartheta)}{\vartheta}\right)^2\right] . \tag{3.4.22}$$

If we consider the second term in (3.4.18), that is $\sin\vartheta\cos\chi\vartheta - \chi\cos\vartheta\sin\chi\vartheta = 0$ then

$$\chi\vartheta = 3.14159265 - 0.219\,240\,5286\vartheta + 1.558\,063\,614\vartheta^2 - 2.391\,954\,053\vartheta^3 + \\ + 1.895\,751\,910\vartheta^4 - 0.441\,333\,7717\vartheta^5, \quad \text{if} \quad \vartheta\in[0,1.6] \tag{3.4.23}$$

is the solution and the corresponding beam shape is of the form

$$W_{ob} = F_1\left(\cos\varphi - \frac{\sin\vartheta}{\chi\sin\chi\vartheta}\cos\chi\varphi\right) .$$

This function is symmetric in φ. So it is a contradiction.

3.4.5. Fixed-fixed beams – solution for symmetric buckling. To tackle this type of buckling – based on what has been mentioned in Subsection 3.4.3 – let us recall solution (3.4.5) which is now paired with the boundary conditions gathered in Table 3.7.

TABLE 3.7. Boundary conditions for fixed-fixed beams when $\varepsilon_{mb} \neq 0$.

Boundary conditions	
Crown point	Right end
$W_{ob}^{(1)}(\varphi)\Big\vert_{\varphi=0} = 0$	$W_{ob}(\varphi)\vert_{\varphi=\vartheta} = 0$
$W_{ob}^{(3)}(\varphi)\Big\vert_{\varphi=0} = 0$	$W_{ob}^{(1)}(\varphi)\Big\vert_{\varphi=\vartheta} = 0$

Thus, we obtain the following inhomogeneous system of linear equations:

$$\begin{bmatrix} 0 & 1 & \chi & 0 \\ 0 & 1 & \chi^3 & 0 \\ \cos\vartheta & \sin\vartheta & \sin\chi\vartheta & \cos\chi\vartheta \\ \sin\vartheta & -\cos\vartheta & -\chi\cos\chi\vartheta & \chi\sin\chi\vartheta \end{bmatrix} \begin{bmatrix} C_1 \\ C_2 \\ C_3 \\ C_4 \end{bmatrix} = \\ = m\varepsilon_{mb} \begin{bmatrix} -\frac{A_4}{2\chi^3} \\ -\frac{3A_4}{2\chi} \\ \frac{1}{2\chi^3}\left(\frac{2}{\chi} + A_3\vartheta\sin\chi\vartheta - A_4\vartheta\cos\chi\vartheta\right) \\ \frac{A_4}{2\chi^3}\left(\cos\chi\vartheta - \chi\vartheta\sin\chi\vartheta\right) - \frac{A_3}{2\chi^3}\left(\sin\chi\vartheta + \chi\vartheta\cos\chi\vartheta\right) \end{bmatrix} . \tag{3.4.24}$$

DOI: 10.14750/ME.2016.008

The solutions for C_i are presented in Appendix A.1.7. To get the load-strain relationship we have to repeat the steps detailed after equation (3.4.11).

3.4.6. Rotationally restrained beams – antisymmetric buckling. The general solution to the homogeneous equilibrium equation (3.4.3) is paired with the homogeneous BCs gathered in Table 3.8.

TABLE 3.8. Boundary conditions for rotationally restrained beams: $\varepsilon_{mb} = 0$.

Boundary conditions	
Left end	Right end
$W_{ob}\vert_{\varphi=-\vartheta} = 0$	$W_{ob}\vert_{\varphi=\vartheta} = 0$
$\left(-W_{ob}^{(2)} + \mathcal{S}W_{ob}^{(1)}\right)\Big\vert_{\varphi=-\vartheta} = 0$	$\left(W_{ob}^{(2)} + \mathcal{S}W_{ob}^{(1)}\right)\Big\vert_{\varphi=\vartheta} = 0$

Upon substitution of solution (3.4.4) into the boundary conditions we obtain

$$\begin{bmatrix} \cos\vartheta & -\sin\vartheta & -\sin\chi\vartheta & \cos\chi\vartheta \\ \cos\vartheta & \sin\vartheta & \sin\chi\vartheta & \cos\chi\vartheta \\ -\cos\vartheta - \mathcal{S}\sin\vartheta & \mathcal{S}\cos\vartheta - \sin\vartheta & \chi\left(\mathcal{S}\cos\chi\vartheta - \chi\sin\chi\vartheta\right) & -\chi\left(\chi\cos\chi\vartheta + \mathcal{S}\sin\chi\vartheta\right) \\ \cos\vartheta + \mathcal{S}\sin\vartheta & \mathcal{S}\cos\vartheta - \sin\vartheta & \chi\left(\mathcal{S}\cos\chi\vartheta - \chi\sin\chi\vartheta\right) & \chi\left(\chi\cos\chi\vartheta + \mathcal{S}\sin\chi\vartheta\right) \end{bmatrix} \begin{bmatrix} F_1 \\ F_2 \\ F_3 \\ F_4 \end{bmatrix} = \begin{bmatrix} 0 \\ 0 \\ 0 \\ 0 \end{bmatrix} \tag{3.4.25}$$

for which system the characteristic determinant is

$$\mathfrak{D} = \left[\left(\chi^2 - 1\right)\sin\vartheta\sin\chi\vartheta + \mathcal{S}\left(\cos\vartheta\sin\chi\vartheta - \chi\sin\vartheta\cos\chi\vartheta\right)\right] \cdot \\ \cdot \left[\left(\chi^2 - 1\right)\cos\vartheta\cos\chi\vartheta + \mathcal{S}\left(\chi\cos\vartheta\sin\chi\vartheta - \sin\vartheta\cos\chi\vartheta\right)\right] = 0\,. \tag{3.4.26}$$

Vanishing of the first factor results in the transcendental equation

$$\frac{\mathcal{S}\chi\tan\vartheta}{\mathcal{S} + \left(\chi^2 - 1\right)\tan\vartheta} = \tan\chi\vartheta. \tag{3.4.27}$$

Some numerical solutions for $\mathfrak{F} = \chi\vartheta$ in terms of ϑ are plotted in Figure 3.7.

Recalling (3.2.8) we get the critical strain for antisymmetric buckling:

$$\varepsilon_m = \frac{1 - \chi^2}{m} = \frac{1}{m}\left[1 - \left(\frac{\mathfrak{F}(\vartheta, \mathcal{S})}{\vartheta}\right)^2\right]. \tag{3.4.28}$$

If we now substitute solution (3.4.27) back into the boundary conditions it follows that $F_1 = F_4 = 0$ and $F_2 = -F_3\sin\chi\vartheta/\sin\vartheta$. Consequently, after recalling the general solution (3.4.4) we obtain that the shape of the beam is indeed antisymmetric:

$$W_{ob}(\varphi) = F_3\left(\sin\chi\varphi - \frac{\sin\chi\vartheta}{\sin\vartheta}\sin\varphi\right) = F_3\left(\sin\frac{\mathfrak{F}}{\vartheta}\varphi - \frac{\sin\mathfrak{F}}{\sin\vartheta}\sin\varphi\right). \tag{3.4.29}$$

DOI: 10.14750/ME.2016.008

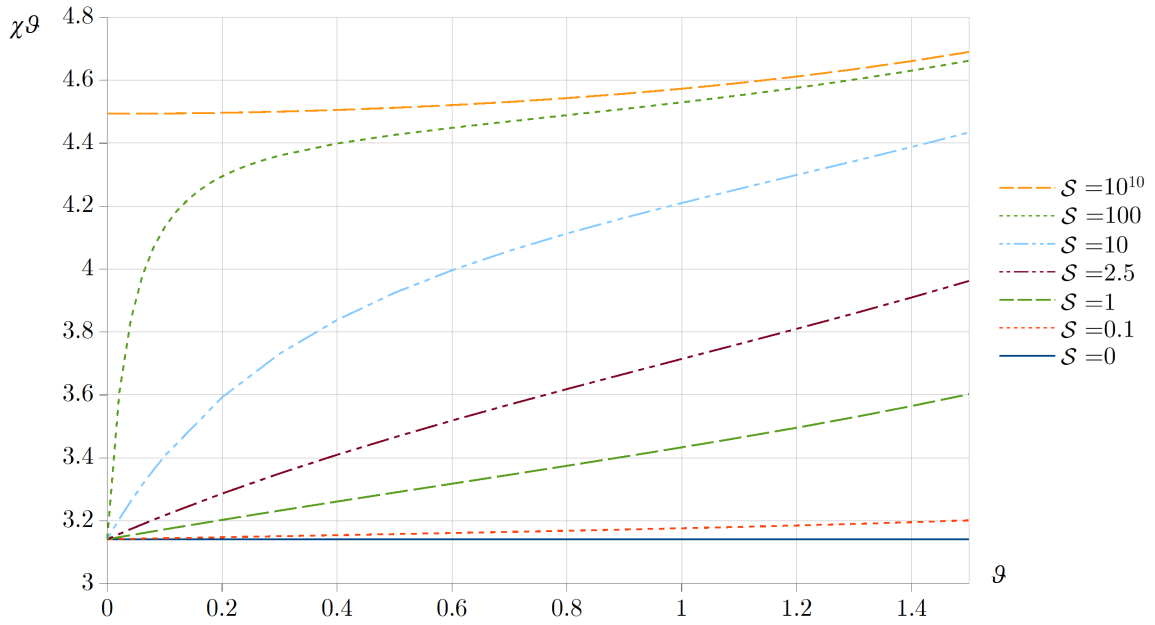

FIGURE 3.7. Some solutions to $\mathfrak{F}(\vartheta, \chi, \mathcal{S})$.

Vanishing of the second factor in (3.4.26) yields

$$\left(\chi^2 - 1\right) + \mathcal{S}\left(\chi \tan \chi\vartheta - \tan \vartheta\right) = 0\,. \tag{3.4.30}$$

After solving the above equation for $\mathfrak{J} = \chi\vartheta$, we find that a symmetric buckling shape is obtained for the radial displacement with $F_2 = F_3 = 0$ and $F_1 = F_4 \cos \chi\vartheta / \cos \vartheta$:

$$W_{ob}(\varphi) = F_4 \left(\cos \chi\varphi - \frac{\cos \chi\vartheta}{\cos \vartheta} \cos \varphi\right) = F_4 \left(\cos \frac{\mathfrak{J}}{\vartheta}\varphi - \frac{\cos \mathfrak{J}}{\cos \vartheta} \cos \varphi\right)\,. \tag{3.4.31}$$

3.4.7. Rotationally restrained beams – symmetric buckling. As the buckled shape is now symmetric the BCs collected in Table 3.9 are valid for the right half-beam.

TABLE 3.9. Boundary conditions for rotationally restrained beams: $\varepsilon_{mb} \neq 0$.

Boundary conditions	
Crown point	Right end
$W_{ob}^{(1)}\big\vert_{\varphi=0} = 0$	$W_{ob}\vert_{\varphi=\vartheta} = 0$
$W_{ob}^{(3)}\big\vert_{\varphi=0} = 0$	$W_{ob}^{(2)} + \mathcal{S} W_{ob}^{(1)}\big\vert_{\varphi=\vartheta} = 0$

Upon substitution of solution (3.4.5) into the boundary conditions, we get the equation system

$$\begin{bmatrix} \cos\vartheta & \sin\vartheta & \sin\chi\vartheta & \cos\chi\vartheta \\ -\cos\vartheta - \mathcal{S}\sin\vartheta & \mathcal{S}\cos\vartheta - \sin\vartheta & \chi\left(\mathcal{S}\cos\chi\vartheta - \chi\sin\chi\vartheta\right) & -\chi\left(\chi\cos\chi\vartheta + \mathcal{S}\sin\chi\vartheta\right) \\ 0 & 2\chi^3 & 2\chi^4 & 0 \\ 0 & 2\chi & 2\chi^4 & 0 \end{bmatrix} \begin{bmatrix} C_1 \\ C_2 \\ C_3 \\ C_4 \end{bmatrix} = m\varepsilon_{mb}$$

$$\begin{bmatrix} \frac{1}{2\chi^3}\left(\frac{2}{\chi} + A_3\vartheta\sin\chi\vartheta - A_4\vartheta\cos\chi\vartheta\right) \\ -\frac{A_3}{\chi}\left(\frac{\vartheta\sin\chi\vartheta}{2} - \frac{\cos\chi\vartheta}{\chi} - \frac{\mathcal{S}\sin\chi\vartheta}{2\chi^2} - \frac{\mathcal{S}\vartheta\cos\chi\vartheta}{2\chi}\right) - \frac{A_4}{\chi}\left(\frac{\mathcal{S}\cos\chi\vartheta}{2\chi^2} - \frac{\sin\chi\vartheta}{\chi} - \frac{\vartheta\cos\chi\vartheta}{2} - \frac{\mathcal{S}\vartheta\sin\chi\vartheta}{2\chi}\right) \\ -A_4 \\ -3A_4 \end{bmatrix}\,. \tag{3.4.32}$$

The solutions are gathered in Appendix A.1.7, just as for the other supports.

DOI: 10.14750/ME.2016.008

3.5. Computational results

Symmetrically supported shallow circular beams can buckle in an antisymmetric mode (with no strain increment) and in a symmetric mode when the length of the centerline changes. In this section the outcomes of the new nonlinear model are compared to the results derived and presented in [**56**] and [**61**] by Bradford et al. The cited authors have found that their results for shallow circular arches agree well with finite element calculations using the commercial software Abaqus and the finite element model published in [**51**]. As our new model has less neglects – we remind the reader to equations (3.2.9)-(3.2.10) and (3.2.20)-(3.2.21) –, we expect more accurate results regarding the permissible loads and a better approximation for non-shallow beams, i.e. when $\vartheta \in [0.8; 1.5]$. To facilitate the evaluations and comparisons – following the footsteps of Bradford et al. by recalling (3.1.9) – let us introduce

$$\lambda = \sqrt{\frac{A_e \rho_o^2}{I_{e\eta}}} \vartheta^2 = \sqrt{m} \vartheta^2 = \frac{\rho_o}{i_e} \vartheta^2 \,, \tag{3.5.1}$$

which is the modified slenderness ratio of the beam.

When investigating the in-plane stability of circular shallow beams, altogether, five ranges of interest can be found. The order of the ranges and its geometrical endpoints depend on the supports and the geometry. It is possible that there is

- no buckling;
- only antisymmetric buckling can happen;
- only symmetric buckling can occur;
- both symmetric and antisymmetric buckling is possible and the antisymmetric shape is the dominant;
- both symmetric and antisymmetric buckling is possible and the symmetric shape is the dominant.

Now let us overview how one can find the typical endpoints of these characteristic ranges through the example of pinned-pinned beams. This line of thought is implicitly applicable to all the other support arrangements as well. The lower limit for antisymmetric buckling can be determined from the condition that the discriminant of the quadratic polynomial (3.3.10) should be a positive number when substituting the lowest antisymmetric solution (3.4.8) for the strain (or what is the same, for χ). Thus,

$$\left[\left(I_{1w} + I_{1\psi} \right)^2 - 4 I_{2\psi} \left(I_{ow} + I_{o\psi} - \varepsilon_m \right) \right] \Big|_{\chi\vartheta = \mathfrak{G}} \geq 0 \,. \tag{3.5.2}$$

If this equation is zero we have the desired endpoint and if it is greater than zero we get the corresponding critical (buckling) load $\mathcal{P}$ directly from (3.3.10).

The lower endpoint of symmetric buckling is obtained in the following steps: (a) we set the angle coordinate to zero in (3.3.5) to get the displacement of the crown point; then (b) we substitute here equation (3.3.10) for the dimensionless load and finally (c) we take the lowest symmetric solution from (3.4.7). The condition to get the desired limit is that the displacement should be real.

In certain cases it happens that both the critical strain and the critical load $\mathcal{P}$ are equal for symmetric and antisymmetric buckling. It means that when evaluating the antisymmetric and symmetric buckling loads against the geometry we find that these two curves intersect each other. Regarding the critical behaviour of beams, this intersection point generally implies a switch between the symmetric and antisymmetric buckling modes. For a more illustrative explanation see Subsubsection 3.5.1.3. This intersection point can be found by plugging the lowest antisymmetric solution $\chi\vartheta = \pi$ – which is at the same time equal to the

DOI: 10.14750/ME.2016.008

lowest symmetric solution – into the post-buckling relationship (3.4.16). Consequently

$$\left[I_{13}\left(\frac{\mathcal{P}}{\vartheta}\right)^2+(I_{02}+I_{12})\frac{\mathcal{P}}{\vartheta}+(I_{01}+I_{11}-1)\right]\Bigg|_{m,\vartheta,\chi\vartheta=\mathfrak{G}}=0\,. \tag{3.5.3}$$

For some fixed-fixed and rotationally restrained beams we experience that there is an upper limit for antisymmetric buckling. It is found when (3.3.10) becomes zero for certain critical strains. Therefore the discriminant

$$(I_{1w}+I_{1\psi})^2-4I_{2\psi}\,(I_{ow}+I_{o\psi}-\varepsilon_m)=0 \tag{3.5.4}$$

vanishes again.

3.5.1. Pinned-pinned beams. As regards the behaviour of pinned-pinned circular beams there are four typical ranges in the following order [**61**, **110**]:

- no buckling expected;
- only symmetric (or limit point) buckling can occur;
- both symmetric and antisymmetric buckling is possible, but the previous one is the dominant;
- both symmetric and antisymmetric buckling is possible, but the former one is the dominant.

The geometrical limits for the ranges are functions of the slenderness as $\lambda=\lambda(m)$. Beams, whose slenderness ratio is sufficiently small, do not buckle. Increasing the value of λ opens the possibility of symmetric (limit point) buckling. Further raising λ yields that, theoretically, both symmetric and antisymmetric (bifurcation) buckling can occur. However, it will later be shown that meanwhile in the third typical buckling range the symmetric shape is the dominant; in the fourth one antisymmetric buckling happens first.

In Table 3.10 the typical endpoints are gathered for four magnitudes of m.

TABLE 3.10. Geometrical limits for the buckling modes – pinned-pinned beams.

m	10^3	10^4	
	$\lambda\le 3.80$	$\lambda\le 3.87$	no buckling
	$3.80<\lambda\le 7.90$	$3.87<\lambda\le 7.96$	limit point only
	$7.90<\lambda\le 9.68$	$7.96<\lambda\le 10.05$	bifurcation point after limit point
	$\lambda>9.68$	$\lambda>10.05$	bifurcation point before limit point

m	10^5	10^6	
	$\lambda\le 3.89$	$\lambda\le 3.90$	no buckling
	$3.89<\lambda\le 7.97$	$3.90<\lambda\le 7.98$	limit point only
	$7.97<\lambda\le 10.18$	$7.98<\lambda\le 10.22$	bifurcation point after limit point
	$\lambda>10.18$	$\lambda>10.22$	bifurcation point before limit point

In the forthcoming, the approximate polynomials defining the boundaries of all the notable intervals are provided and compared to the m-independent results by Bradford et al. These figures are

$$\lambda(m)=\begin{cases}3.903\,1+8.14\cdot 10^{-8}m-3.05/m^{0.5} & \text{if } m\in[10^3;10^4]\\ \dfrac{11.3\cdot 10^5}{m^2}-\dfrac{357}{m}+3.897\,471+9.1725\cdot 10^{-9}\,m-5.295\cdot 10^{-15}\,m^2 & \text{if } m\in[10^4;10^6]\\ 3.91 & \text{in } [\mathbf{61}]\,\text{p.714.}\end{cases}$$

DOI: 10.14750/ME.2016.008

These polynomials are plotted in Figure 3.8. The new model is close to the results by Bradford et al. The greatest relative difference is 2.6% when $m = 1\,000$. It has turned out that the upper limit value for the two models are only 0.01 away.

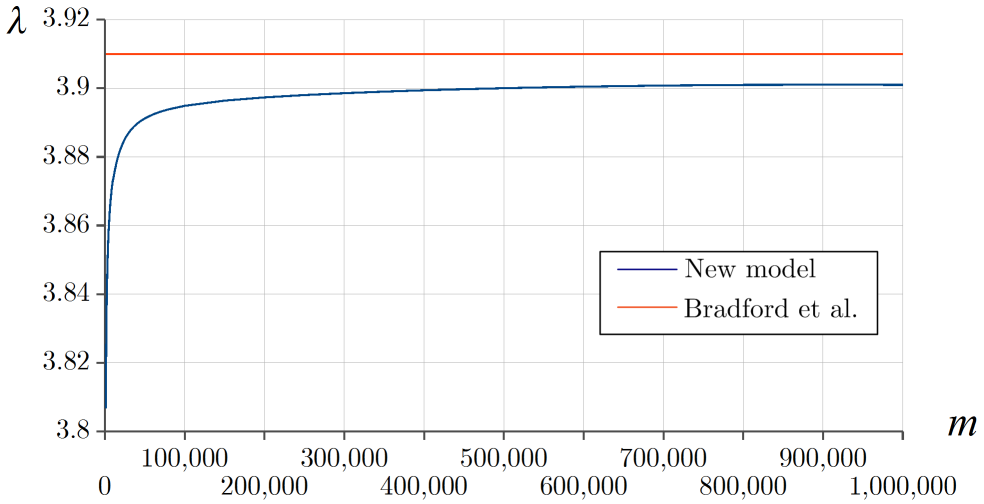

FIGURE 3.8. The lower limit for symmetric buckling – pinned-pinned beams.

Moving on now to the lower geometrical limit for antisymmetric buckling, we have

$$\lambda(m) = \begin{cases} 7.975\,6 + 5.4 \cdot 10^{-7} m - 2.15/m^{0.5} & \text{if} \quad m \in [10^3; 10^4] \\ 7.971\,4 + 1.33 \cdot 10^{-8} m - 118.14/m - 6.636 \cdot 10^{-15}\, m^2 & \text{if} \quad m \in [10^4; 10^6] \\ 7.96 & \text{in} \quad [\mathbf{61}] \text{ p. } 714. \end{cases}$$

These relationships are drawn in Figure 3.9. Accordingly, the minor differences between the models can easily be noticed.

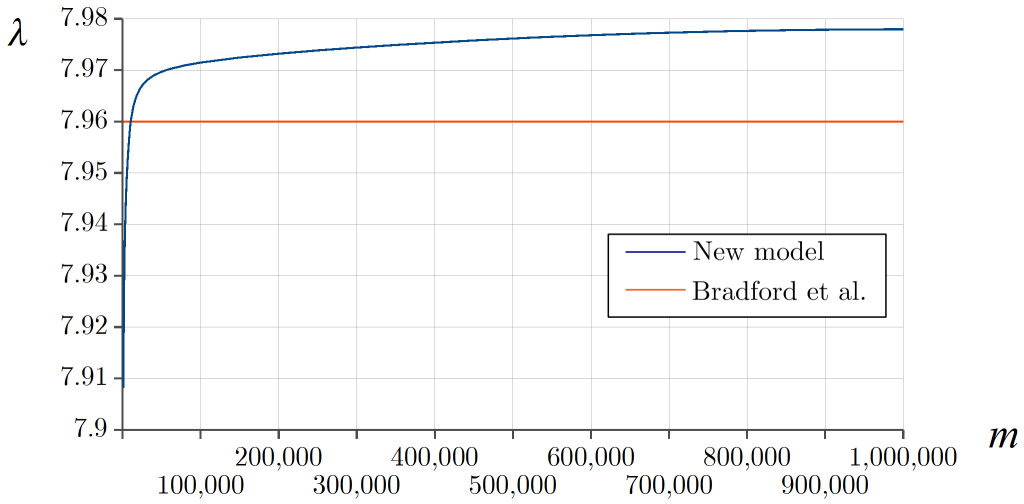

FIGURE 3.9. The lower limit for antisymmetric buckling – pinned-pinned beams.

For pinned-pinned shallow circular beams it happens that there is an intersection point of the symmetric and antisymmetric buckling curves when both the critical loads and strains

DOI: 10.14750/ME.2016.008

coincide. The equation of the fitting curve – see Figure 3.10 – is

$$\lambda(m) = \begin{cases} -271/m + 9.923 + 2.84 \cdot 10^{-5}\, m - 1.2 \cdot 10^{-9}\, m^2 & \text{if} \quad m \in [10^3; 10^4] \\ \dfrac{7.162 \cdot 10^6}{m^2} - \dfrac{2144}{m} + 10.200\,3 + 7.7 \cdot 10^{-8}\, m - 4.549 \cdot 10^{-14}\, m^2 & \text{if} \quad m \in [10^4; 10^6] \\ 9.8 & \text{in} \quad [\mathbf{61}]\,\text{p. } 714. \end{cases}$$

The limit value for our solution is $\lambda \approx 10.23$. This is again close but different by 4% from the limit for the earlier model [**61**].

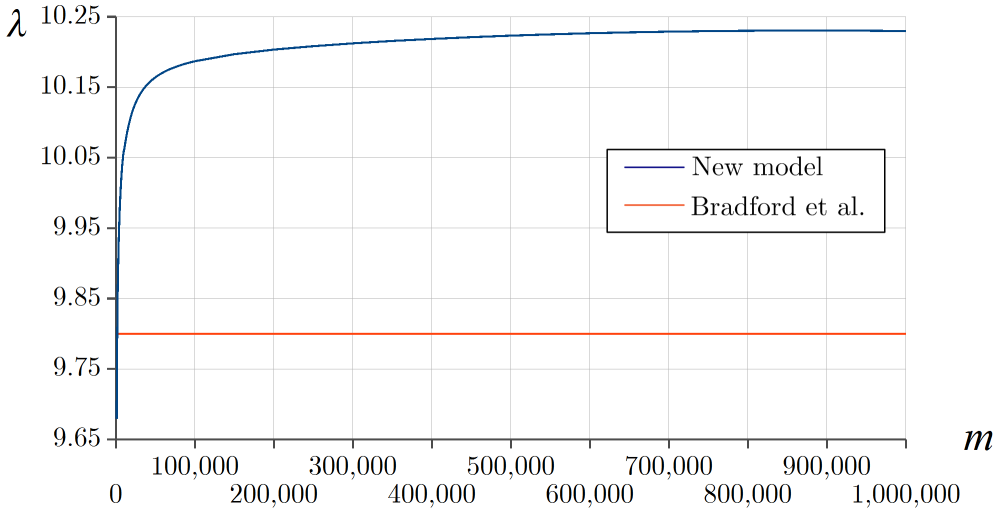

FIGURE 3.10. The intersection point – pinned-pinned beams.

3.5.1.1. *Antisymmetric bifurcation buckling.* Pinned-pinned shallow beams may buckle in an antisymmetric (bifurcation) mode with no strain increment. The loss of stability occurs when the lowest antisymmetric critical strain level, or what is the same, $\chi\vartheta = \pi$ is reached – we remind the reader to Subsection 3.4.2. Evaluating equation (3.3.10) under this condition yields the critical (dimensionless) load $\mathcal{P}$ in terms of the geometry. Computational results for four magnitudes of m are presented and compared to [**61**] in Figure 3.11.

In the surroundings of the lower limit, independently of m, the two models agree well. The figure also shows that, in both cases, the computational results tend to a certain value as the semi-vertex angle ϑ increases. These limits are rather far, though. In general, the differences in the dimensionless force between the models are slightly greater if m is smaller. In short, the new model usually returns lower permissible loads meaning that the previous one tends to overestimate the load such structural members can bear.

Comparing the models for strictly shallow members ($\vartheta \leq\sim \pi/4$), the greatest difference regarding the critical dimensionless load is $\Delta \simeq 4.9\%$ at $\vartheta = \pi/4 \simeq 0.78$, $m = 10^6$. For deeper beams, at $\vartheta = 1.15$ it is 10.5% and it can reach up to 20.5% at $\vartheta = 1.5$.

It must be mentioned that equation (59) in [**61**] is said to approximate well the critical load given that $\vartheta \geq \pi/4$. This statement is confirmed with finite element computations. Unfortunately, it is not clarified how and under what assumptions this formula was obtained. At the same time, we have plotted this relation – see the magenta dashed line in Figure 3.11. This function turns out to be dependent on the angle only. In relation to this solution, the new model yields greater critical loads between 0.78...1.23 in ϑ. After the intersection at $\vartheta \simeq 1.23$ – where the permissible loads happen to be the same – this tendency changes. At $\vartheta = 1.5$ the difference is about 16%.

DOI: 10.14750/ME.2016.008

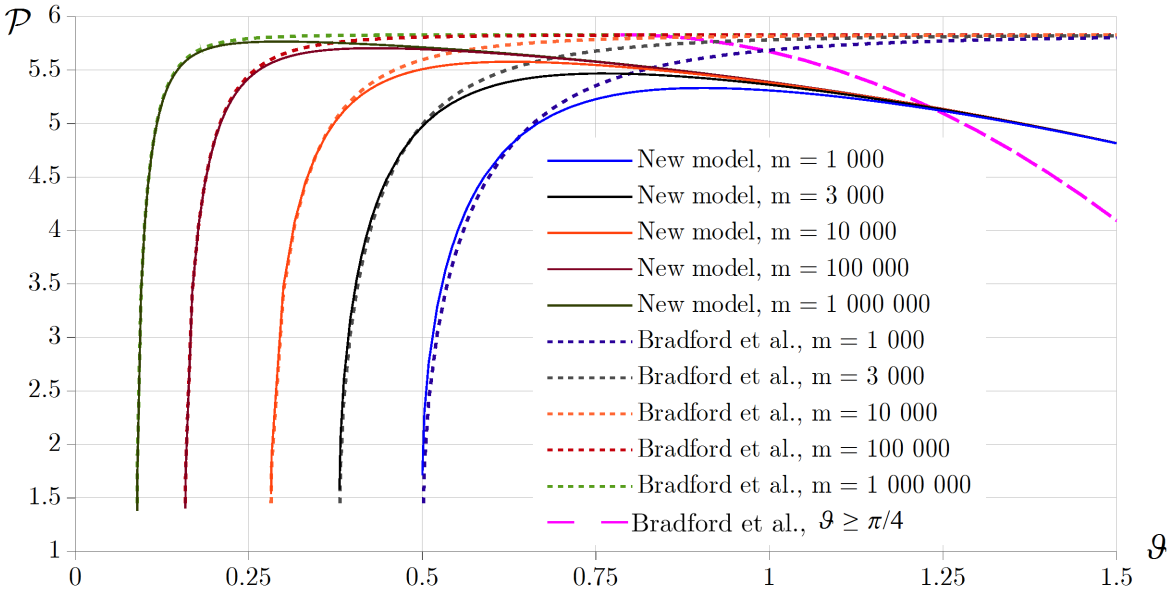

FIGURE 3.11. Antisymmetric buckling loads for pinned-pinned beams.

3.5.1.2. *Symmetric snap-through buckling.* Concerning symmetric buckling we have equation (3.3.10) which is always valid prior to buckling until the moment of the loss of stability; and equation (3.4.16). The latter one was derived assuming a symmetric buckled shape. This time there are two unknowns: the critical strain and critical load. To get these we need to solve the cited two nonlinear relations simultaneously. To tackle this mathematical problem, we have used the subroutine `DNEQNF` from the IMSL Library [**109**] under Fortran 90 programming language.

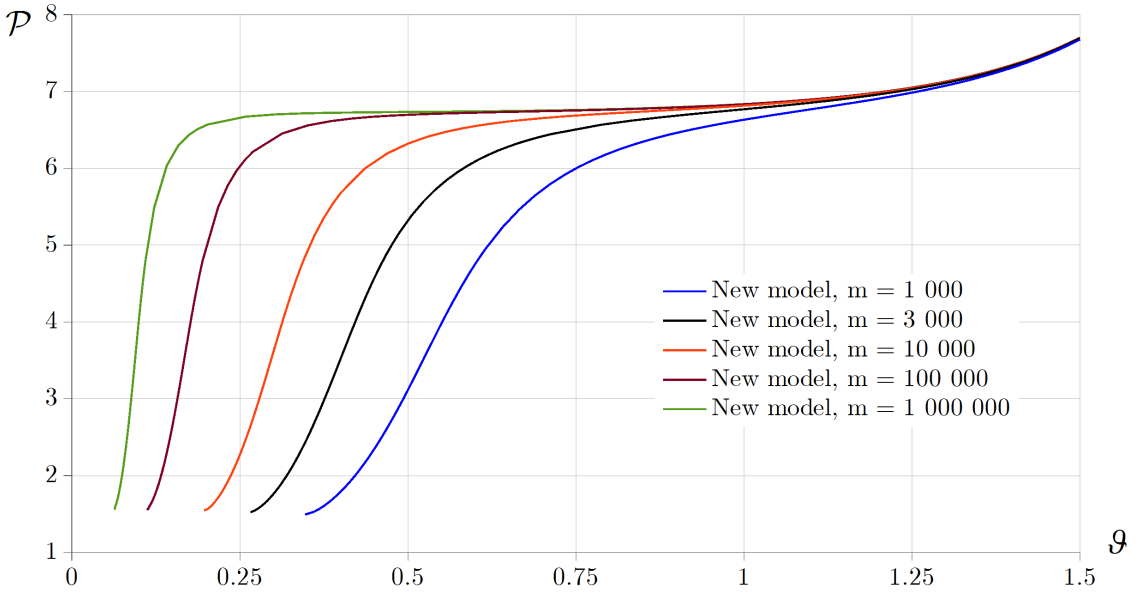

FIGURE 3.12. Symmetric buckling loads for pinned-pinned beams.

Regarding the computational results, which are provided in Figure 3.12, one can clearly see that as we increase the value of m, the corresponding curves move horizontally to the left. The curves are independent of m with a good accuracy above $\vartheta \simeq 1.25$.

DOI: 10.14750/ME.2016.008

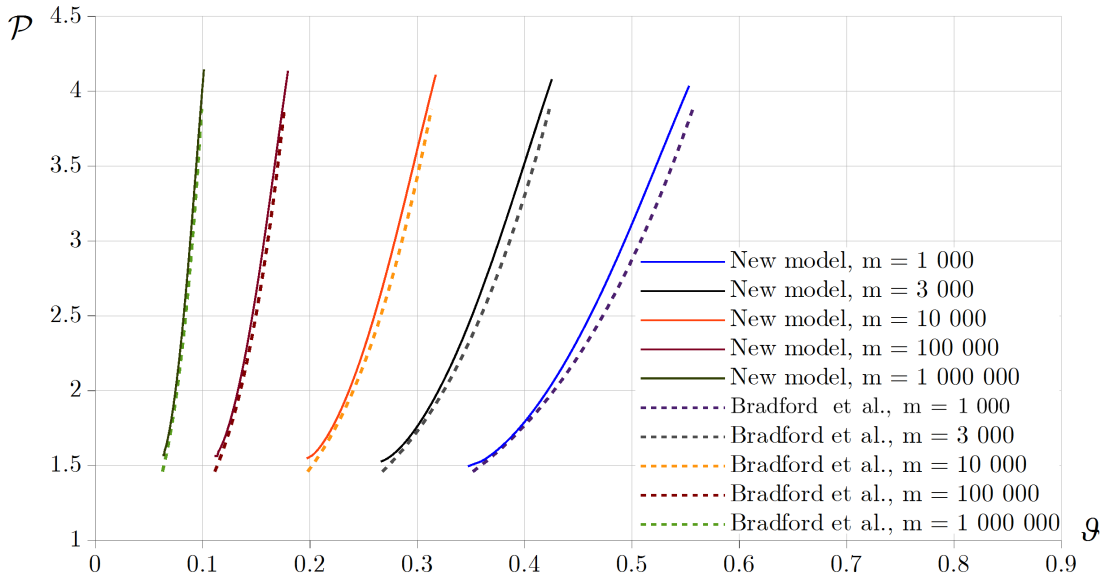

FIGURE 3.13. Symmetric buckling loads – comparison of the models.

The new model can, again, be compared to that by Bradford et al. However, results in [**61**] are only available within that range, where symmetric buckling is the dominant. The related curves are plotted between these characteristic endpoints in Figure 3.13. This time the previous model generally underestimates the permissible load. The greatest differences can be experienced around $\vartheta \in [0.5; 0.55]$, when $m = 1\,000$, that is 7 to 9%. This result is quite considerable given that the whole interval is only 0.205 wide along the abscissa.

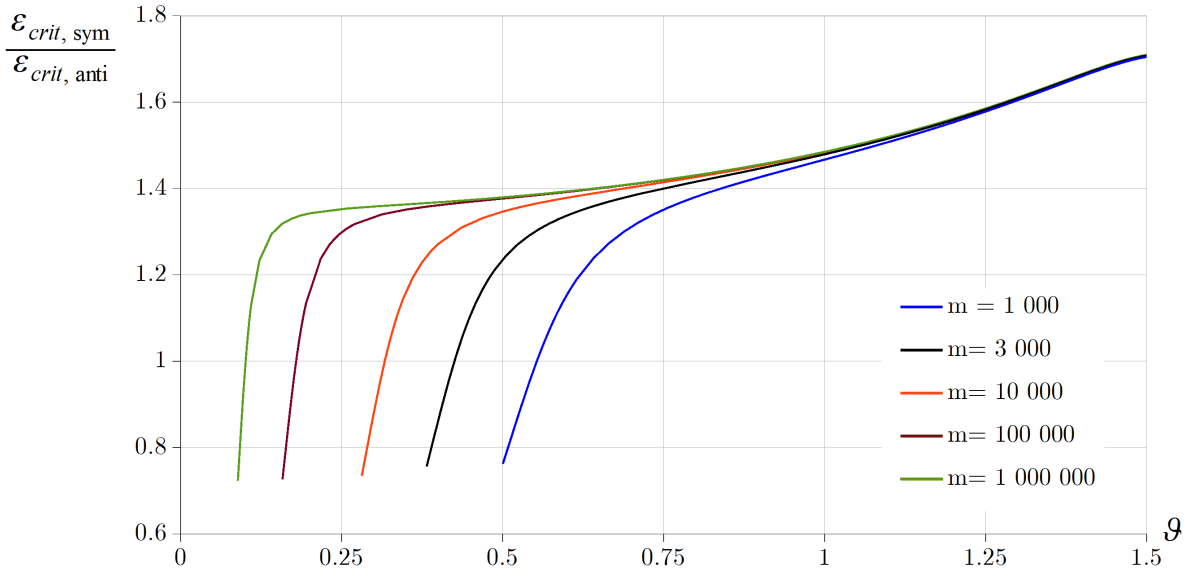

FIGURE 3.14. Critical symmetric and antisymmetric strains – pinned-pinned beams.

It is also worthy to check how the lowest critical strain for symmetric ($\varepsilon_{crit\ \mathrm{sym}}$) and antisymmetric ($\varepsilon_{crit\ \mathrm{anti}}$) buckling relates to each other – see Figure 3.14 for the details. When the rate on the ordinate reaches 1, there is a switch between the buckling modes. Prior to this, the critical strain for antisymmetric buckling is lower. After the switch, this tendency changes.

Finite element verifications. Some control finite element (FE) computations were carried out to verify the new model using the commercial finite element software Abaqus 6.7 and Adina 8.9. The tested cross-section is rectangular: the width is 0.01 $[m]$ and the height

DOI: 10.14750/ME.2016.008

is $0.005\,[m]$. Young's modulus is $2 \cdot 10^{11}\,[Pa]$. In Abaqus we have used 3-node quadratic Timoshenko beam elements ($B22$) and the Static,Riks step; while in Adina 2-node beam elements and the Collapse Analysis have been chosen. The numerical results for symmetric buckling are gathered in Table 3.11. All the geometries are picked from the range in which – according to our model – this buckling mode dominates. As it turns out, the results of the new model coincide quite well with those of Abaqus and Adina. Moreover, in this comparison these outcomes are more accurate than the results of [**61**]. The maximum difference between our model and the FE figures is only 4.3%.

TABLE 3.11. Comparison with FE calculations – pinned-pinned beams.

m	λ	$\mathcal{P}_{\text{New model}}$	$\mathcal{P}_{\text{Bradford et al.}}$	$\mathcal{P}_{\text{Abaqus}}$	$\mathcal{P}_{\text{Adina}}$
1 000	4.56	1.63	1.62	1.68	1.7
1 000	5.84	2.09	2.02	2.11	2.12
1 000	7.76	3.03	2.8	2.97	3
1 000	8.72	3.55	3.28	3.43	3.49
1 000	9.36	3.87	3.62	3.72	3.82
1 000 000	4.48	1.66	1.6	1.66	1.66
1 000 000	5.44	1.95	1.88	1.95	1.95
1 000 000	7.36	2.77	2.62	2.77	2.77
1 000 000	9.6	3.86	3.76	3.87	3.86

When trying to carry out some control calculations for antisymmetric buckling, we have found that it is possible with both software via introducing initial geometric imperfections to the model using the first (antisymmetric) buckling mode of the beams obtained from eigenvalue (and eigenshape) extraction. Regarding the magnitude of the imperfection (a number the normalized displacements of the eigenshapes are multiplied by) we have found no exact rule but only some vague recommendations in the Abaqus manual [**111**]. Neither could we find any relevant information in the related scientific articles, even though they present FE calculations – see, e.g. [**61**,**74**]. While performing some tests, we have found that the results are heavily affected by the imperfection magnitude. Since the current work is not intended to deal with the imperfection sensitivity of beams, such investigations are not included.

3.5.1.3. *Load-crown point displacement and load-strain ratios.* To better understand the behaviour of circular beams, we have drawn the four possible primary equilibrium path types through the example when m is 100 000. In Figure 3.15 for four different slendernesses, the dimensionless concentrated force $\hat{\mathcal{P}}$ is plotted against the dimensionless (vertical) displacement W_{oC} of the crown point. The former quantity is obtained upon dividing the displacement by the initial rise of the circular beam. Consequently,

$$W_{oC} = \left| \frac{W_o|_{\varphi=0}}{1-\cos\vartheta} \right| . \tag{3.5.5}$$

When $\lambda = 3.5$ ($\vartheta \simeq 0.105$), the slope of the path is always positive, so there is no buckling. When λ is 6.6 ($\vartheta \simeq 0.144$), only symmetric limit point buckling can occur, where it is indicated in the figure. At this notable point $\partial\hat{\mathcal{P}}/\partial W_{oC} = 0$. If $\lambda = 8.8$ ($\vartheta \simeq 0.166$), a bifurcation point appears but on the descending (unstable) branch of the deflection curve. Thus, the critical behaviour is still represented by the preceding limit point. Finally, if $\lambda = 11.1$ ($\vartheta \simeq 0.187$), the bifurcation point is located before the limit point, so antisymmetric buckling is expected first. When $\lambda \simeq 10.18$ ($\vartheta \simeq 0.179$) the limit- and bifurcation points in relation with the critical behaviour coincide. These four ranges are in a complete accord with Section 3.5.1, and follow each other in this same order for any investigated m. Furthermore, these results show a really good correlation with Abaqus as illustrated.

DOI: 10.14750/ME.2016.008

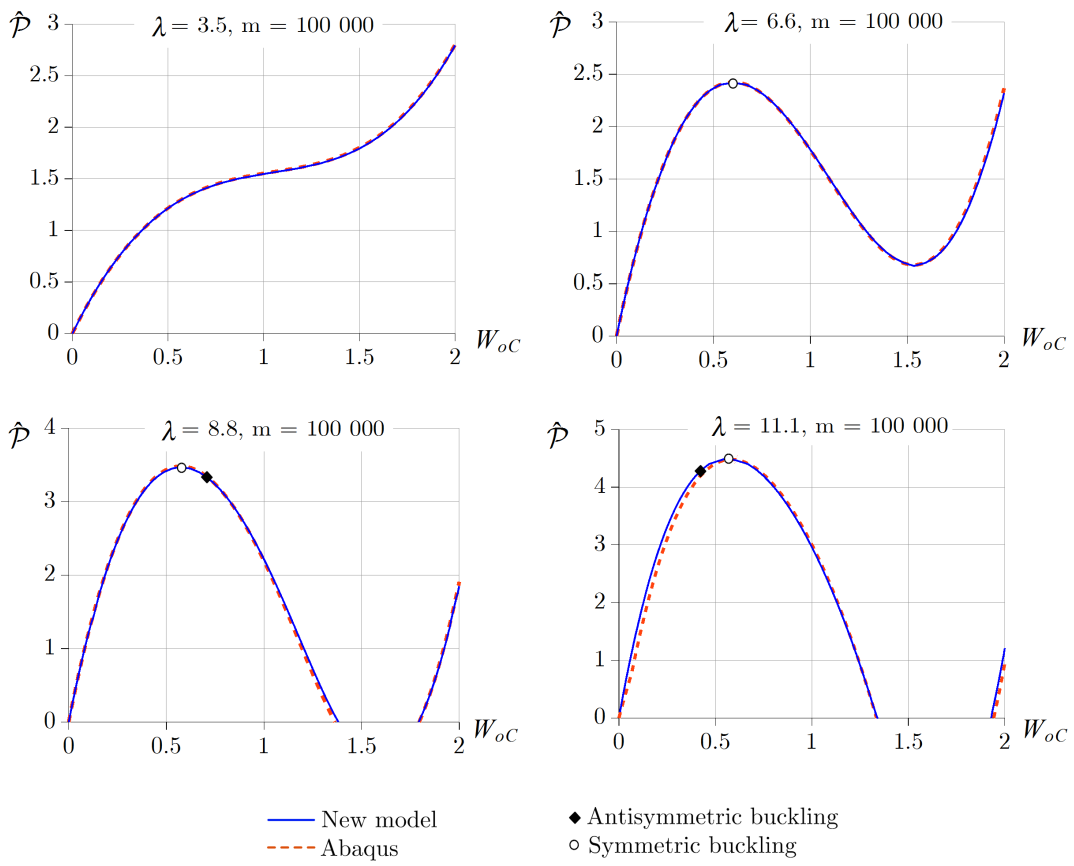

FIGURE 3.15. Load-displacement curves for pinned-pinned beams.

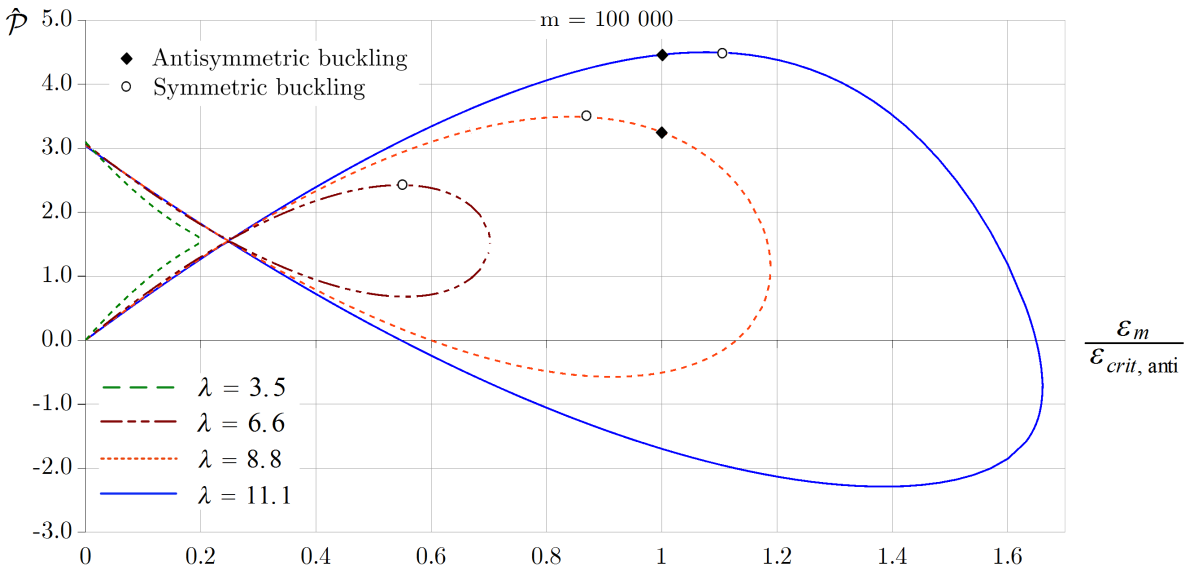

FIGURE 3.16. Dimensionless load – strain/critical strain ratio (pinned beams).

Figure 3.16 shows how the dimensionless load varies with the ratio $\varepsilon_m/\varepsilon_{crit\ \mathrm{anti}}$ for the same geometries as before. When $\lambda = 3.5$, there are two different values of $\hat{\mathcal{P}}$, which only occur once for any possible strain level. When λ is 6.6, starting from the origin we can see two points, where the tangent is zero $[\partial\hat{\mathcal{P}}/\partial(\varepsilon_m/\varepsilon_{crit\ \mathrm{anti}}) = 0]$. As indicated, symmetric snap-through buckling relates to the upper point. The critical antisymmetric strain is, obviously, not reached for these first two geometries. However, when $\lambda = 8.8$, we experience that the

DOI: 10.14750/ME.2016.008

path crosses the ratio 1 in the abscissa but before that, there is a limit point. Thus, still the former one governs. Finally, for $\lambda = 11.1$, the bifurcation point comes first and therefore an antisymmetric buckled shape is expected beforehand. It is also worth pointing out that independently of λ, one branch always starts from the origin while the other one begins around $\hat{\mathcal{P}}(\lambda) \simeq 2.9 \ldots 3.1$. At $\hat{\mathcal{P}} \simeq \pi/2$ and $\vartheta \simeq 0.248$, the related branches intersect each other.

3.5.2. Fixed-fixed beams. The behaviour of fixed-fixed beams [**112**] shows some notable differences compared to pinned-pinned members. For beams whose $m < 21\,148$ there are two ranges of interest, in which there is

- no buckling or
- symmetric buckling only.

However, beyond this limit, there are four ranges regarding the buckling behaviour. It is possible that there is

- no buckling;
- only symmetric buckling can occur;
- both symmetric and antisymmetric buckling can happen, but the previous one is the dominant;
- only symmetric buckling can occur (the bifurcation point vanishes).

So we can see that the symmetric buckling shape is the only real possibility throughout, while for pinned-pinned structural members the dominant mode was antisymmetric. The limits for each range are again functions of the slenderness as it is shown in the forthcoming. Bradford et al. [**61**] have found three ranges, when evaluating their model – the first three ranges in the previous enumeration.

The typical endpoints for four magnitudes of m are provided in Table 3.12.

TABLE 3.12. Buckling mode limits for fixed-fixed beams.

m	10^3	10^4	
	$\lambda \leq 11.61$	$\lambda \leq 11.15$	no buckling
	$\lambda > 11.61$	$\lambda > 11.15$	limit point only

m	$2.5 \cdot 10^4$	10^5	10^6	
	$\lambda \leq 11.12$	$\lambda \leq 11.06$	$\lambda \leq 11.02$	no buckling
	$11.12 < \lambda \leq 53.77$	$11.06 < \lambda \leq 42.60$	$11.02 < \lambda \leq 39.4$	limit point only
	$53.77 < \lambda \leq 86.33$	$42.60 < \lambda \leq 206.13$	$39.4 < \lambda \leq 672.15$	bifurcation p. after limit p.
	$\lambda > 86.33$	$\lambda > 206.13$	$\lambda > 672.15$	limit point only

The approximative polynomials for the range boundaries are gathered hereinafter and are compared with the previous model. The lower limit for symmetric buckling is

$$\lambda(m) = \begin{cases} \dfrac{-1.74 \cdot 10^5}{m^2} + \dfrac{608}{m} + 11.186 - 4.8 \cdot 10^{-6}\, m + 5.2 \cdot 10^{-11}\, m^2 & \text{if } m \in [10^3; 5 \cdot 10^4] \\ \dfrac{2\,530}{m} + 11.036\,3 - 8.7 \cdot 10^{-9}\, m & \text{if } m \in [5 \cdot 10^4; 10^6] \\ 11.07 & \text{in [61] p. 717.} \end{cases}$$

Overall, the two models are quite close in this respect. The maximum difference is 5.3% when $m = 1\,000$.

DOI: 10.14750/ME.2016.008

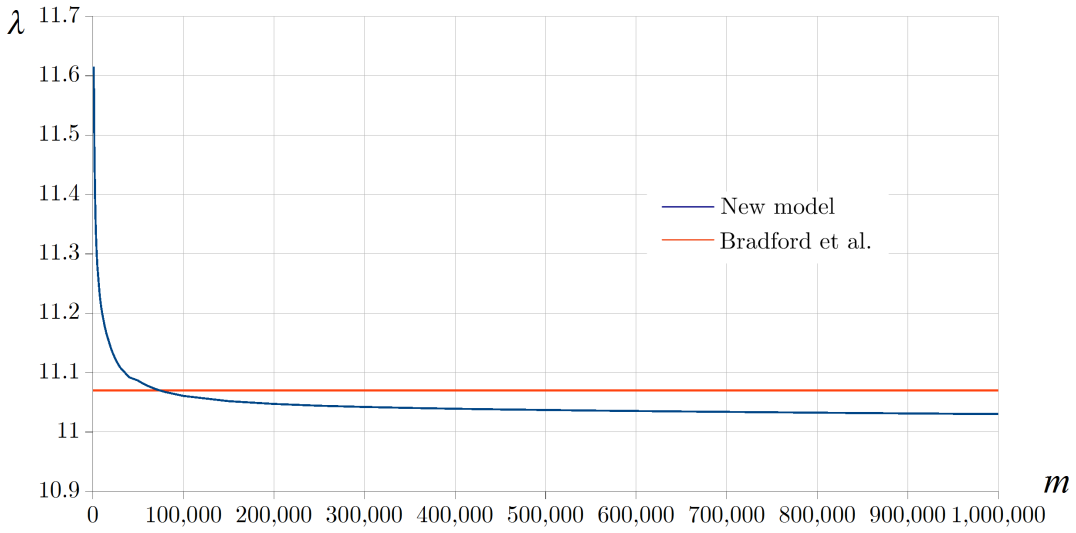

FIGURE 3.17. The lower limit for symmetric buckling – fixed-fixed beams.

As we find no upper limit for symmetric buckling as long as $\vartheta \in [0; 1.5]$, we now move on to the lower limit for antisymmetric buckling, that is

$$\lambda(m) = \begin{cases} \dfrac{2.4 \cdot 10^{44}}{m^{10}} - 0.085 \cdot m^{\frac{1}{2}} + 64.144 & \text{if} \quad m \in [21\,148; 40\,000] \\ \dfrac{314\,000}{m} + 39 + 4.6 \cdot 10^{-6}\, m & \text{if} \quad m \in [40\,000; 100\,000] \\ \dfrac{300\,000}{m} + 39.64 - 5.5 \cdot 10^{-7}\, m & \text{if} \quad m \in [100\,000; 1\,000\,000] \\ 38.15 & \text{in} \quad [\mathbf{61}] \text{ p. } 716. \end{cases}$$

Meanwhile, for Bradford et al. the result is valid for any m, in our model antisymmetric buckling is only possible when $m \geq 21\,148$. The difference to the earlier model is huge for small m-s: at the beginning it is 70% and it is still 11.2% if $m = 100\,000$. The limit values, though, are only 3.2% away. If we recall the results for pinned-pinned beams (see Figure 3.9), these numbers are considerable.

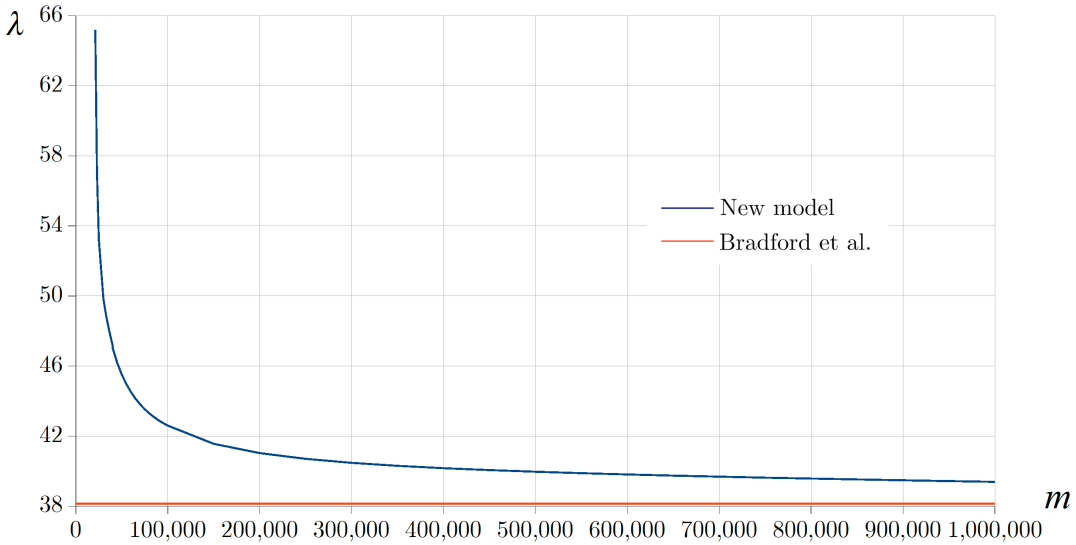

FIGURE 3.18. The lower limit for antisymmetric buckling – fixed-fixed beams.

DOI: 10.14750/ME.2016.008

Finally, the upper limit for antisymmetric buckling is approximated via the functions

$$\lambda(m) = \begin{cases} -90.3 - 2.27 \cdot 10^{-4}\, m - \dfrac{3.323 \cdot 10^{87}}{m^{20}} + 3.187\, m^{0.4} & \text{if} \quad m \in [21\,148; 10^5] \\ -10.1 - 2.628 \cdot 10^{-5} m + 0.617\, m^{0.51} & \text{if} \quad m \in [10^5; 10^6]. \end{cases}$$

Bradford et al. have not mentioned the possibility of this limit. In this model, it varies considerably with m. Altogether, we can mention that, according to the new model, no antisymmetric buckling is expected first for fixed-fixed circular beams: the symmetric shape is always the dominant. We further remark that we have found no intersection point for the symmetric and antisymmetric buckling curves.

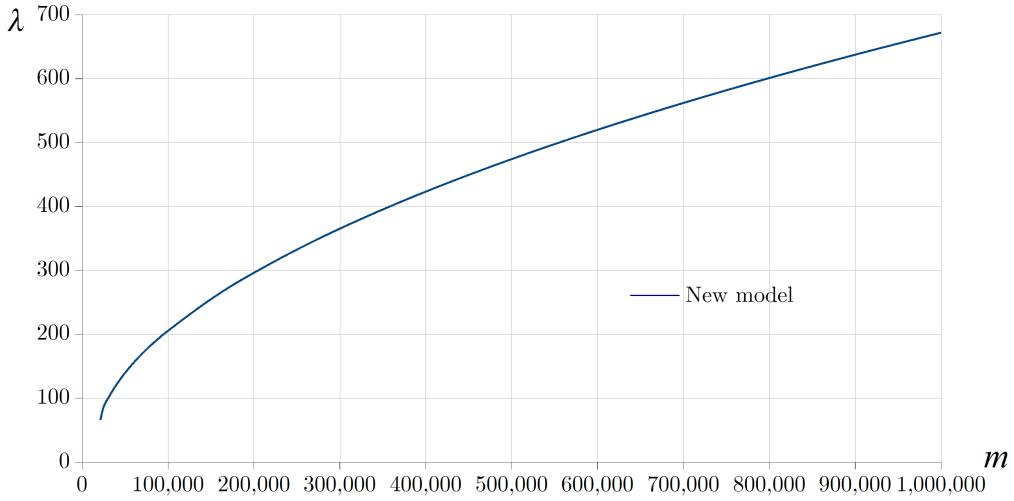

FIGURE 3.19. The upper limit for antisymmetric buckling – fixed-fixed beams.

3.5.2.1. *Antisymmetric bifurcation buckling.* Figure 3.20 reveals how the critical dimensionless load varies with the geometry when the critical strain (3.4.20) is substituted into (3.3.14). The results are compared to Figure 6 in [**61**]. Meanwhile the solution by Bradford et al. tends to a certain value ($\mathcal{P} \simeq 6.95$), our curves always have different limits which are reached after a steep decrease as ϑ increases. If both $1/m$ and ϑ are sufficiently small, the outcomes of both models seem to be rather close. However, a distinction of up to 10.3%

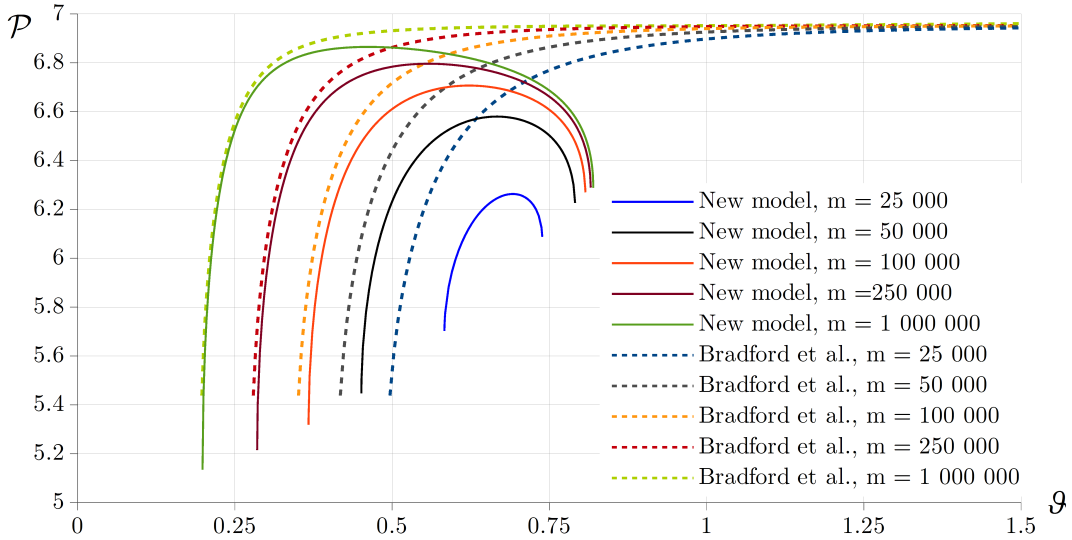

FIGURE 3.20. Antisymmetric buckling loads for fixed-fixed beams.

DOI: 10.14750/ME.2016.008

is possible in the critical dimensionless loads if, e.g. $\vartheta \simeq 0.807$ and $m = 100\,000$. When m is smaller (25 000), the differences are greater even from the lower endpoint. From our results it can clearly be seen that the (theoretical) possibility of antisymmetric bifurcation buckling is the own of shallow fixed-fixed circular beams only: around $\vartheta(m) \simeq 0.73 \ldots 0.85$ a real solution vanishes. When $m < 21\,148$ we find no real solution at all. To briefly sum up, the new model always results in lower buckling loads.

3.5.2.2. *Symmetric buckling.* To deal with the problem of symmetric buckling, we need to solve equations (3.3.14) and (3.4.16) together, when the constants for fixed-fixed beams are substituted. The numerical results are provided graphically in Figure 3.21. Unfortunately, we can only make a comparison with a restriction that $\lambda \leq 100$ since Bradford et al. have not published results beyond this limit.

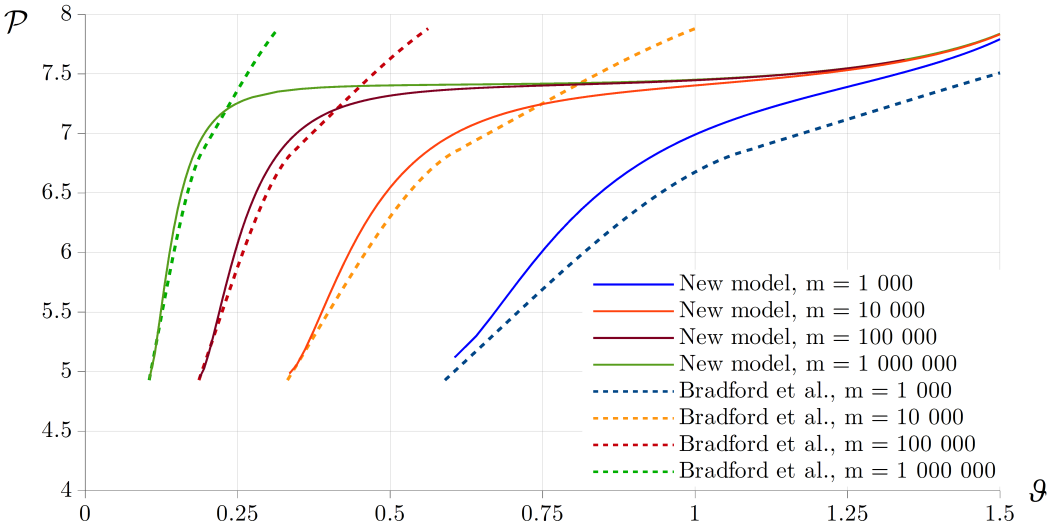

FIGURE 3.21. Symmetric buckling loads for fixed-fixed beams.

It is visible that if the angle is sufficiently great the new model yields approximately the same critical load, independently of m. It is also clear that around the lower limit

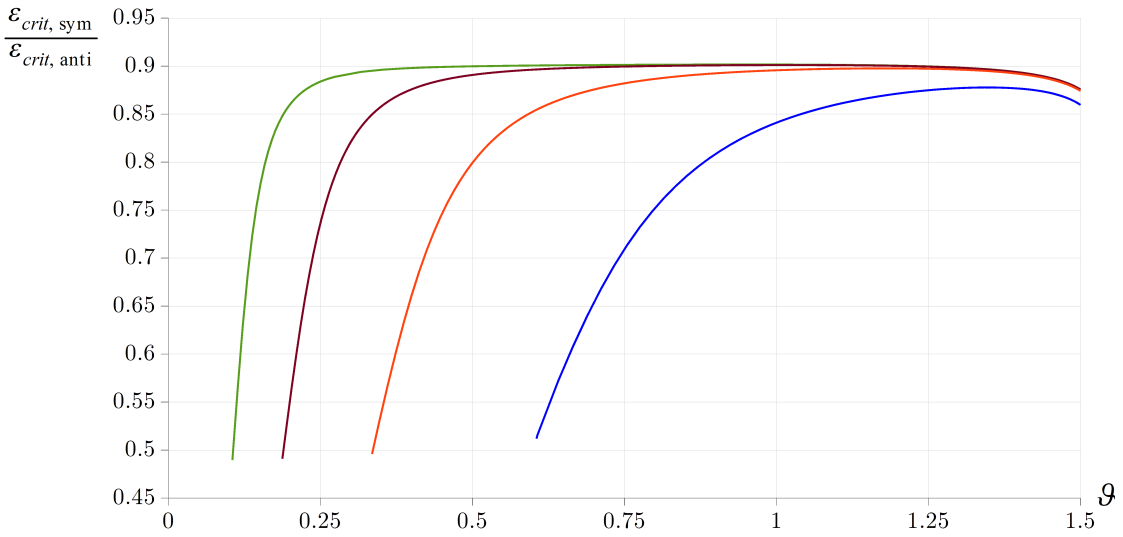

FIGURE 3.22. Critical symmetric and antisymmetric strains – fixed-fixed beams.

for symmetric buckling the two models generally predict very similar results, though the lower m is the greater the differences are. When $m = 1\,000$, the characteristics of the curves

DOI: 10.14750/ME.2016.008

by both models are very similar, otherwise there is quite a substantial distinction after a while in ϑ. The greatest difference is experienced when $m = 10^6$ and $\vartheta \simeq 0.316$, that is 7.2%. For greater central angles we would expect even greater differences. When the central angles are smaller, the model by Bradford et al. generally predicts lower critical loads than ours but then this tendency changes. The exception is $m = 1\,000$ when the new model always returns greater permissible loads in the plotted range.

When comparing the critical strains for symmetric and antisymmetric buckling in Figure 3.22, we can again confirm that symmetric buckled shape is the only possibility.

Finite element verifications. Using the same software and settings as for pinned-pinned beams, some finite element control calculations were again carried out for symmetric buckling. The results can be seen in Table 3.13. The correlation of the figures is absolutely

TABLE 3.13. Comparison with FE calculations – fixed-fixed beams.

m	λ	$\mathcal{P}_{\text{New model}}$	$\mathcal{P}_{\text{Bradford et al.}}$	$\mathcal{P}_{\text{Abaqus}}$	$\mathcal{P}_{\text{Adina}}$
1 000	13	5.30	5.17	5.09	5.35
1 000	16	5.76	5.50	5.50	5.69
1 000	23	6.53	6.15	6.29	6.70
1 000	35	7.09	6.80	6.99	7.36
1 000	44	7.29	7.00	7.29	7.62
1 000	54	7.46	7.20	7.53	7.81
1 000	63.4	7.62	7.38	7.71	7.97
1 000 000	13	5.14	5.17	5.14	5.15
1 000 000	23	6.36	6.15	6.42	6.37
1 000 000	84	7.32	7.69	7.37	7.36
1 000 000	285	7.40	n.a.	7.47	7.49
1 000 000	612	7.42	n.a.	7.6	7.59
1 000 000	1090	7.46	n.a.	7.72	7.73
1 000 000	1868	7.64	n.a.	7.98	8.00

favourable. The maximum difference compared to the Abaqus results is +4.7% and it is −4.5% for Adina. These extreme values were experienced for deep beams. It suggests that the new model is indeed appropriate to predict the critical load of fixed-fixed circular deep beams with a good accuracy as long as $\vartheta \leq 1.5$.

3.5.2.3. *Load-crown point displacement and load-strain ratio graphs.* Figure 3.23 presents the four possible primary equilibrium path types for beams with $m \geq 21\,148$ and the two characteristic modes when $m < 21\,148$. First, let us see the two common types. Beams with small λ – e.g. 9.5 – do not buckle. Increasing the slenderness ratio ($\lambda = 17.5$) results in the appearance of a limit point. Thus, symmetric snap-through buckling can occur for both picked magnitudes of m. The next two modes are relevant only when $m \geq 21\,148$. If $\lambda(m = 100\,000) = 47$, there is a bifurcation point on the descending (unstable) branch of the load-deflection curve, so still the symmetric shape governs. If $\lambda(m = 100\,000) = 210$, then the bifurcation point vanishes. What remains is a limit point. The results, regarding the first stabile branches until the first limit point show an excellent correlation with finite element results – see the dashed lines in the relevant figure.

DOI: 10.14750/ME.2016.008

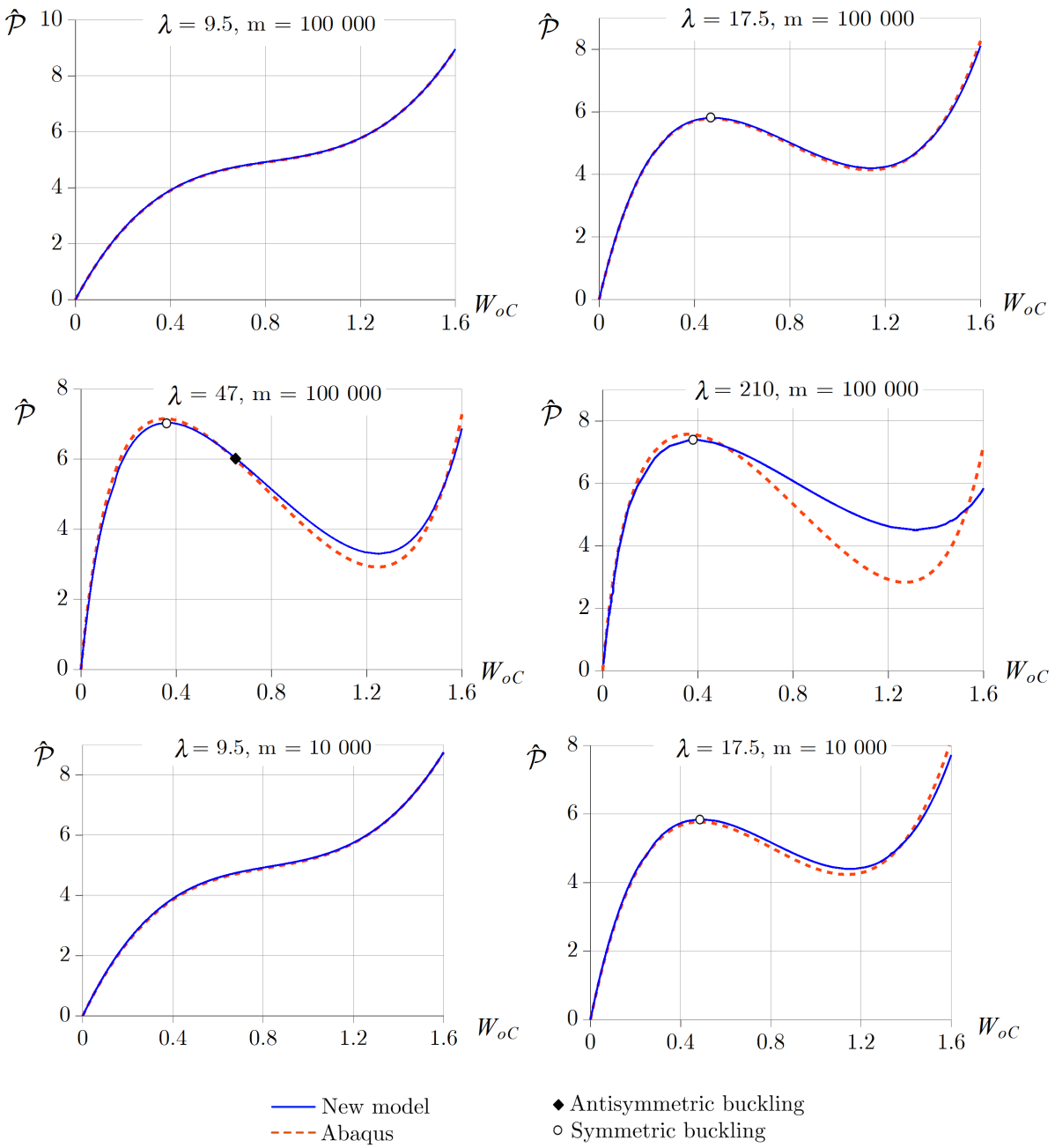

FIGURE 3.23. Load - displacement curves – fixed-fixed beams.

The typical dimensionless load - strain ratio graphs are shown separately for $m \geq 21\,148$ and $m < 21\,148$ in Figure 3.24 and 3.25, respectively. First, let $m = 100\,000$ and $\lambda = 9.5$. There are two possible values of $\hat{\mathcal{P}}$ and each occurs once. If we change λ to 17.5 the two branches have an intersection and further, on that branch starting from the origin we find a point where $\partial\hat{\mathcal{P}}/\partial(\varepsilon_m/\varepsilon_{crit\ \mathrm{anti}}) = 0$. This point relates to symmetric snap-through buckling. It is the only option as $\varepsilon_m/\varepsilon_{crit\ \mathrm{anti}}$ is always less than 1. Increasing the slenderness to 47, it can be seen that the critical antisymmetric strain is reached, i.e. antisymmetric buckling is also possible. However, this point can be found after the limit point, so still the symmetric shape is the dominant. Finally, when $\lambda = 210$, we find that the intersection point of the two branches are considerably further in the abscissa, compared to the previous curves and (partly for this reason) the bifurcation point vanishes.

DOI: 10.14750/ME.2016.008

Decreasing m to 10 000 – see Figure 3.25 – there are two characteristic types. In terms of physical sense, these coincide with the first two cases of the previous paragraph. Increasing the slenderness above 17.5 would never result in the appearance of a bifurcation point: the ratio 1 on the horizontal axis is never reached.

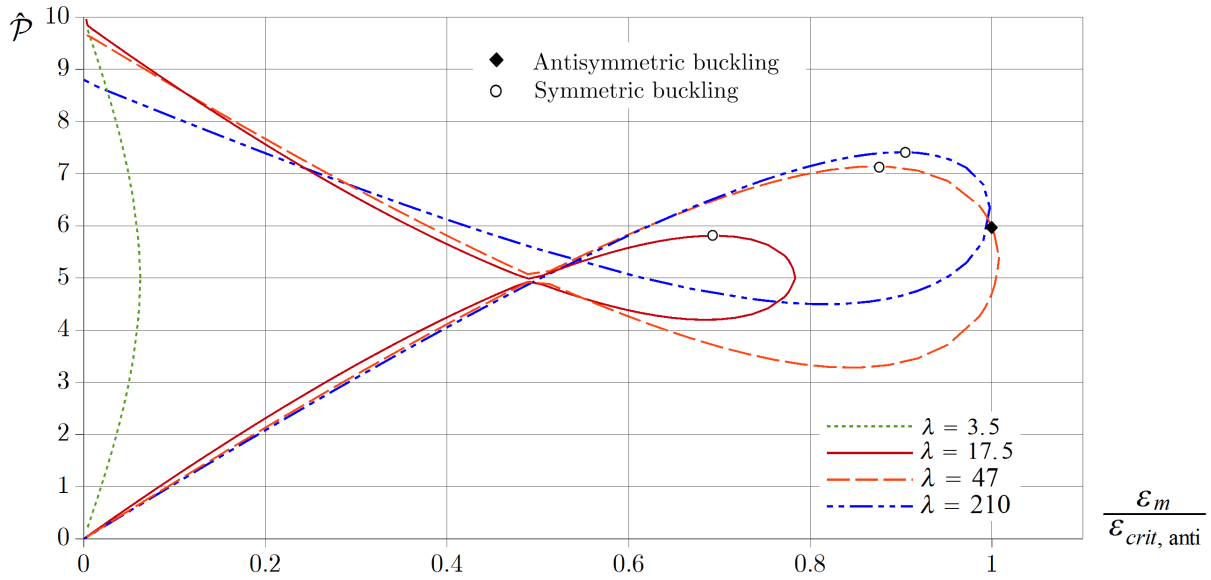

FIGURE 3.24. Dimensionless load-strain graph types, $m \geq 21\,148$.

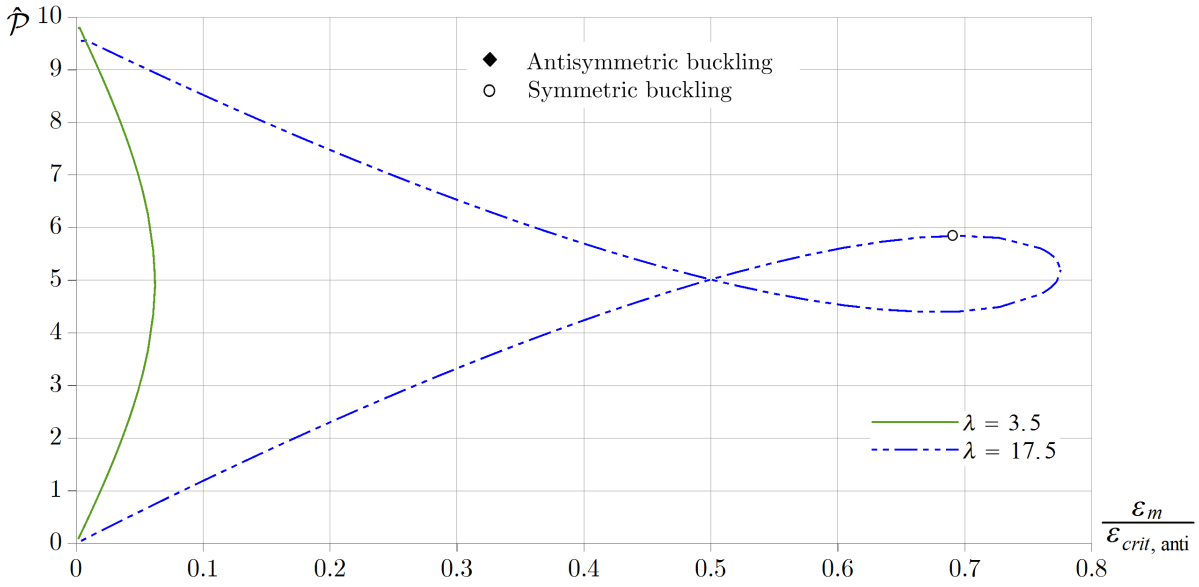

FIGURE 3.25. Dimensionless load-strain graph types, $m < 21\,148$.

We remark that λ and m have a considerable effect on where the upper branch commences on the ordinate if $\varepsilon_m = 0$. The intersection point of the branches is also a function of these quantities. However, the physically possible (lower) branches always start from the origin.

3.5.3. Rotationally restrained beams. In the present subsection beams with rotational end-restraints are investigated and evaluated [**113**]. Such beams will be compared to pinned-pinned ($\mathcal{S} = 0$) and fixed-fixed ($\mathcal{S} \to \infty$) structural members to demonstrate the effect of the dimensionless spring stiffness – see (3.3.15). We remark that the model seems to be valid for both limits: we always get back the same results as in the preceding sections.

DOI: 10.14750/ME.2016.008

Altogether, there are five intervals of interest. For certain geometries and spring stiffnesses, it is possible that there is

- no buckling;
- only symmetric buckling can occur;
- both symmetric and antisymmetric buckling is possible, but the previous one is the dominant;
- both symmetric and antisymmetric buckling is possible and the former one governs;
- symmetric buckling is the only possibility as the bifurcation point vanishes.

First, the effect of the dimensionless spring stiffness $\mathcal{S}$ on the endpoints of the typical ranges is studied. The dark red dashed lines are only added lines to the forthcoming figures with no physical meaning. Choosing m to be 1 000, Figure 3.26 shows the effects of the dimensionless spring stiffness on the buckling ranges in terms of the semi-vertex angle. The evaluation is always carried out along a visionary vertical line, i.e. assuming a fixed $\mathcal{S}$ in the forthcoming diagrams. If $\mathcal{S} = 0$, we get back the same results (buckling modes and endpoints) as for pinned-pinned beams. Thus, below $\vartheta = 0.347$, there is no buckling – such range is always denoted by (I). Then, up until $\vartheta = 0.5$, only symmetric buckling can occur (II). Even though the possibility of antisymmetric buckling appears after a further increase in ϑ, the symmetric shape is the dominant (III) as long as the intersection point of the symmetric and antisymmetric buckling curves is reached at $\vartheta = 0.553$. After that, the critical strain for antisymmetric buckling is always lower, therefore it is the governing mode (IV).

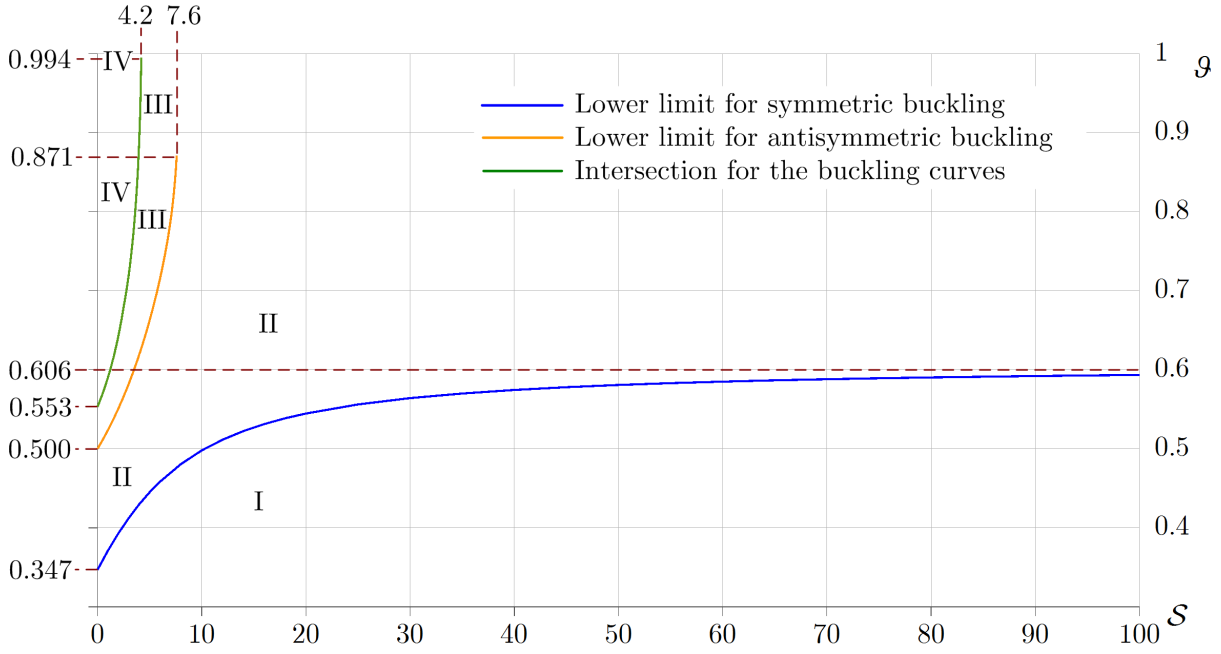

FIGURE 3.26. Typical buckling ranges in terms of $\mathcal{S}$ – $m = 1\,000$.

Apart from the range endpoints, there are no other remarkable differences as long as $\mathcal{S} \leq 4.2$. Passing this value results in the disappearance of the intersection point. It means that the antisymmetric buckling point is always located on the unstable branch of the primary equilibrium path. The next important limit is $\mathcal{S} = 7.6$ since above that, even the possibility of antisymmetric buckling vanishes. It can also be observed that as $\mathcal{S} \to \infty$, i.e. the beam is fixed, the switch between no buckling and symmetric buckling approaches to $\vartheta = 0.606$.

DOI: 10.14750/ME.2016.008

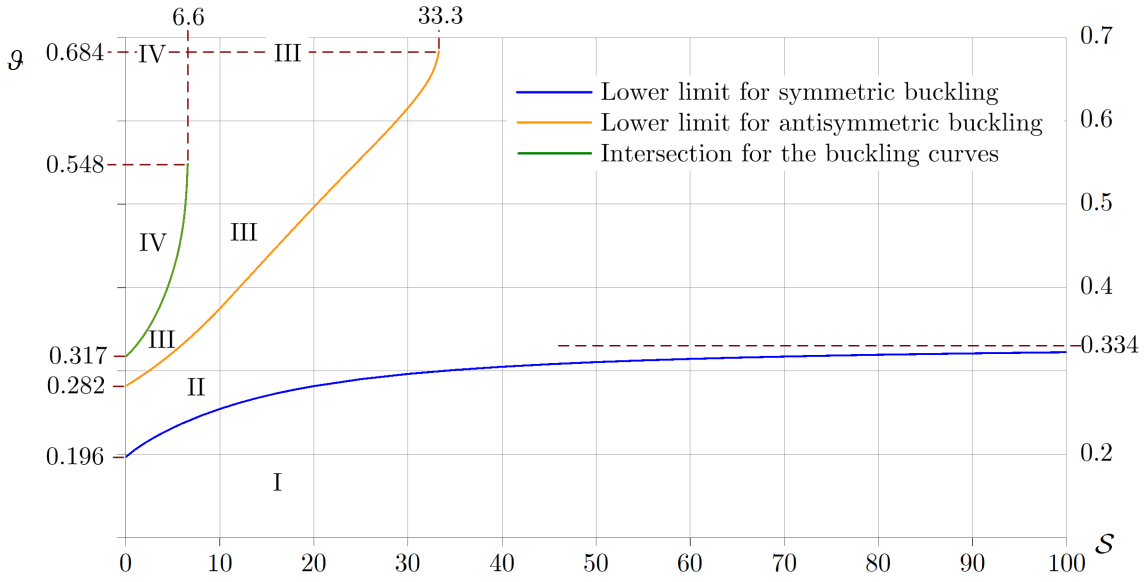

FIGURE 3.27. Typical buckling ranges in terms of $\mathcal{S}$ – $m = 10\,000$.

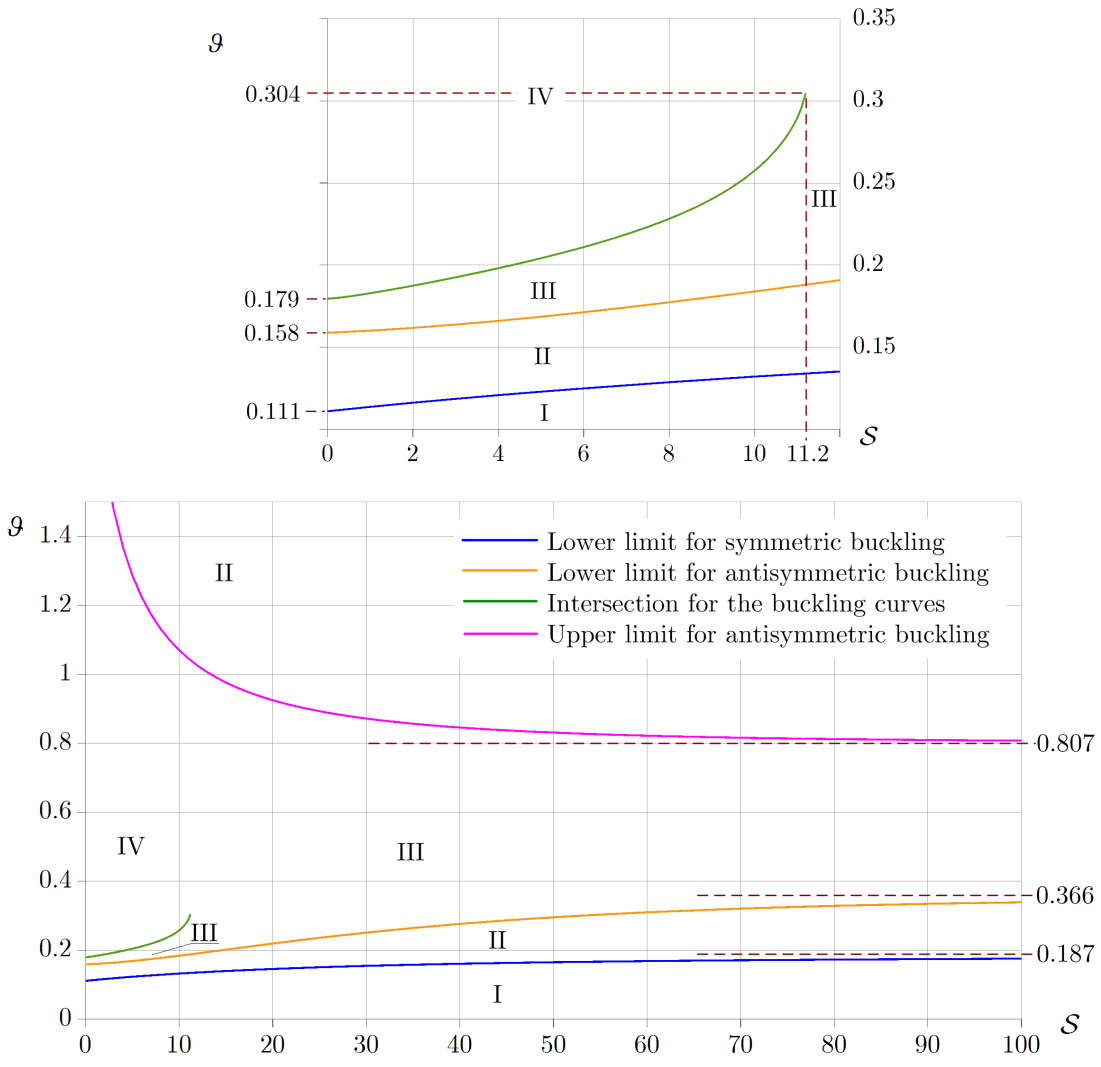

FIGURE 3.28. Typical buckling ranges in terms of $\mathcal{S}$ – $m = 100\,000$.

DOI: 10.14750/ME.2016.008

The behaviour of beams with $m = 10\,000$ is very similar to the previous description – see Figure 3.27. Now an intersection point exists until $\mathcal{S} \leq 6.6$ and a lower limit for antisymmetric buckling can be found as long as $\mathcal{S} \leq 33.3$. Consequently, these two endpoints show an increase in $\mathcal{S}$ due to an increase in m. It is also a noticeable property that increasing m yields a decrease in all the typical range endpoints expressed in ϑ.

The results are a little more complex for $m = 100\,000$ as it is revealed in Figure 3.28. This time there exists an upper limit for antisymmetric buckling above $\mathcal{S}(\vartheta < 1.5) = 2.8$. Therefore, if $\mathcal{S} \in [0; 2.8]$, given that the angle is sufficiently small, there is no buckling (I). It is followed by the range of symmetric buckling only (II). Then the possibility of antisymmetric buckling appears but only after symmetric buckling (III). After that, the antisymmetric shape governs throughout. However, between $2.8 \ldots 11.2$ in $\mathcal{S}$, after range (IV), the symmetric shape becomes again the dominant (II), since the possibility of antisymmetric buckling vanishes. After $\mathcal{S} = 11.2$, the intersection point also vanishes, so above range (I) the symmetric shape governs.

The relevant curves for $m = 1\,000\,000$ are plotted in Figure 3.29. These follow each other very similarly to $m = 100\,000$. As can be seen, an increase in m results in a slight increase in the upper limit for antisymmetric buckling and a decrease in all other limits in ϑ.

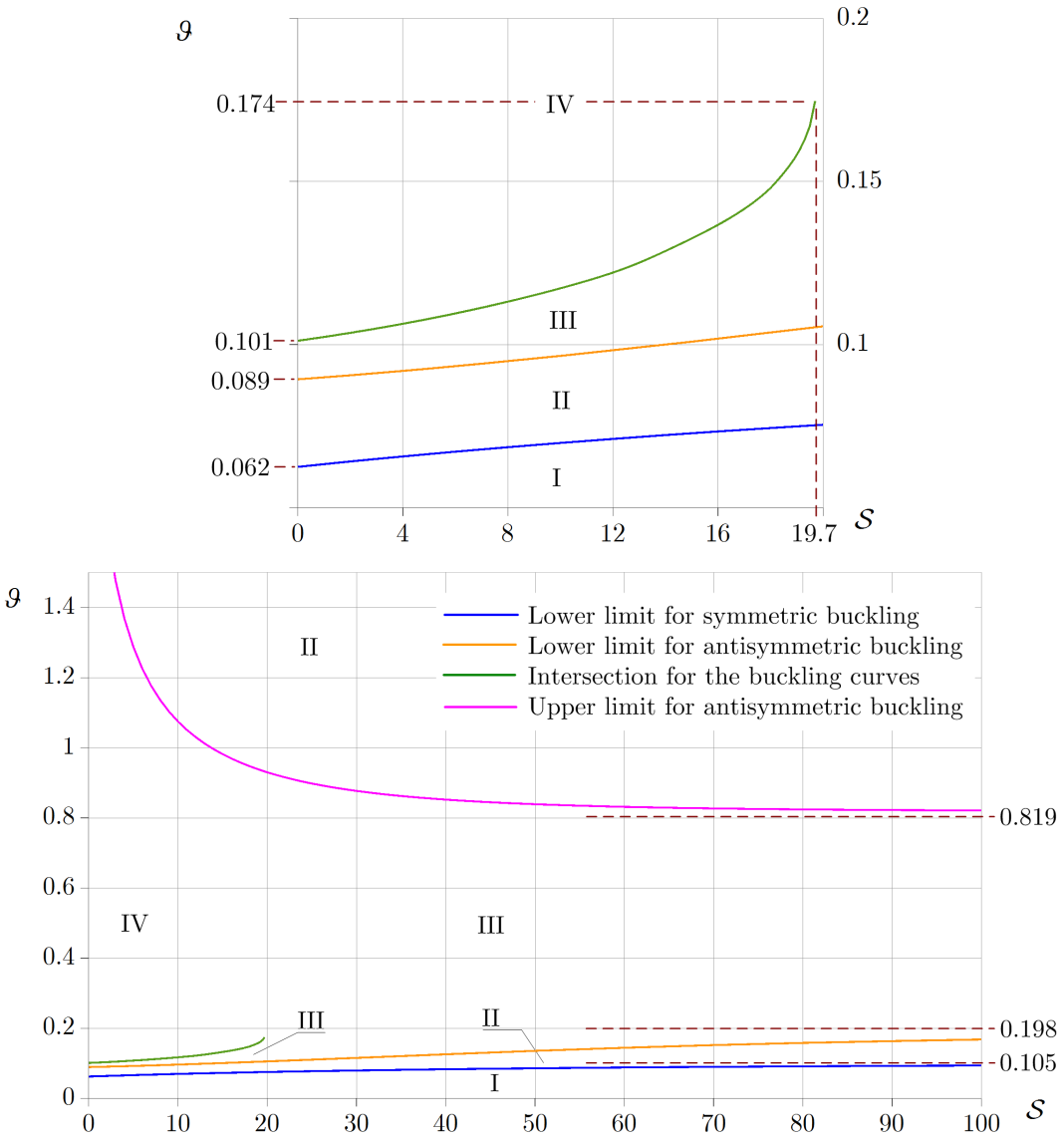

FIGURE 3.29. Typical buckling ranges in terms of $\mathcal{S}$ – $m = 1\,000\,000$.

DOI: 10.14750/ME.2016.008

3.5.3.1. *Antisymmetric and symmetric buckling.* In the sequel the governing (critical) buckling loads are drawn for four magnitudes of m as functions of the semi-vertex angle. In each of these graphs, curves are presented for $\mathcal{S} = 0$ (pinned-pinned beam); $\mathcal{S} = 10^{20}$ (fixed-fixed beam with a very good accuracy) and $\mathcal{S} = 1$ (rotationally restrained beam). When both symmetric (drawn with fine dashed lines in the corresponding figures) and antisymmetric (drawn using continuous lines) shape is possible only the dominant kind is plotted. The evaluation procedure is the same as that detailed at the very beginning of Section 3.5.

In Figure 3.30, m is chosen to be 1 000. The lower limits for symmetric buckling are $\vartheta(\mathcal{S} = 0) = 0.346$; $\vartheta(\mathcal{S} = 1) = 0.371$ and $\vartheta(\mathcal{S} = 10^{20}) = 0.606$. This buckling mode is the dominant for fixed-fixed beams throughout the whole interval. As for the other two cases, an intersection point can be found at $\vartheta(\mathcal{S} = 0) = 0.553$ and $\vartheta(\mathcal{S} = 1) = 0.590$. Therefore, beyond these points, antisymmetric buckling governs. It can be observed that increasing the value of $\mathcal{S}$ results that the lower limit for symmetric buckling and the intersection point moves right in this diagram with increasing related buckling loads. It is also clear that rotationally restrained beams can bear such loading levels, which are always between the critical loads for pinned-pinned and fixed-fixed beams. Above $\vartheta \simeq 0.7$, it is quite a notable range in $\mathcal{P}$ so account for such restraints seems inevitable.

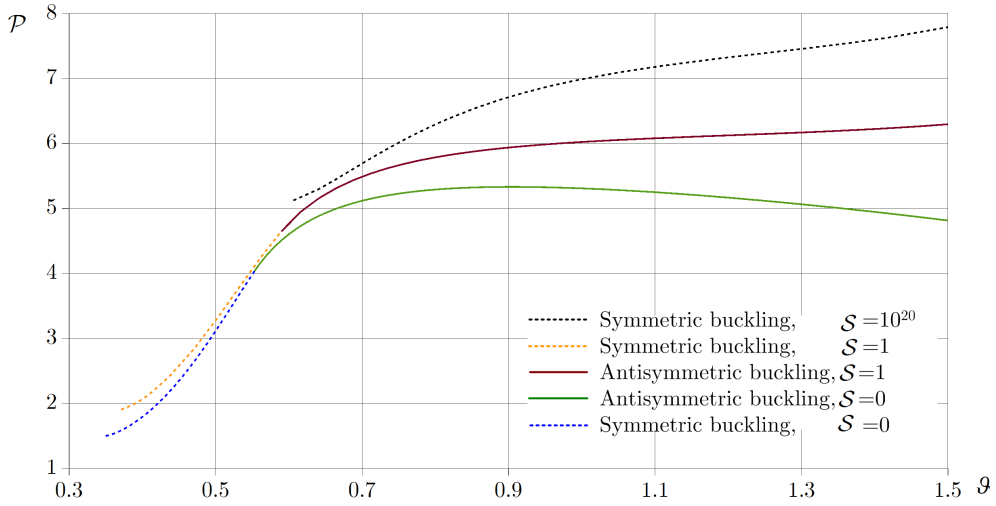

FIGURE 3.30. Buckling loads versus the semi-vertex angle when $m = 1\,000$.

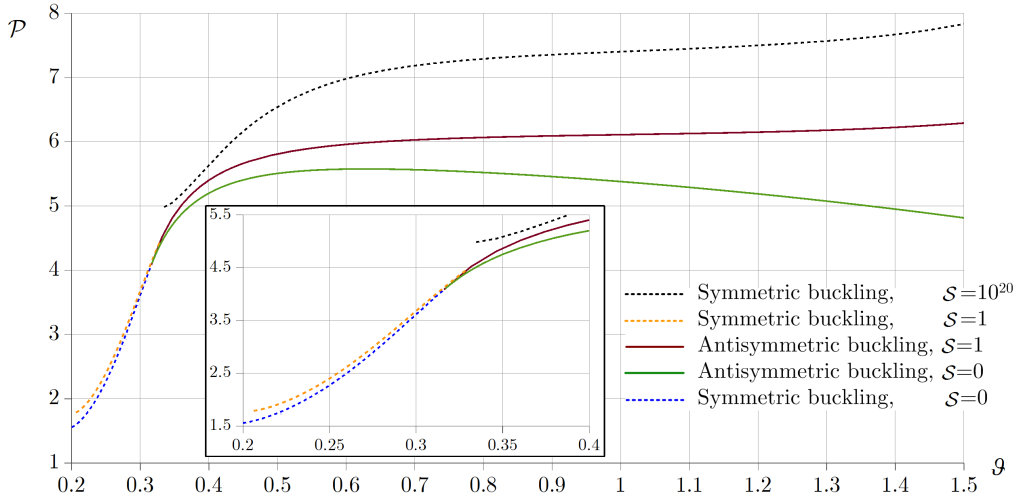

FIGURE 3.31. Buckling loads versus the semi-vertex angle when $m = 10\,000$.

DOI: 10.14750/ME.2016.008

Setting m to 10 000 yields the results shown in Figure 3.31. Now the lower endpoints of symmetric buckling are $\vartheta(\mathcal{S}=0)=0.196$; $\vartheta(\mathcal{S}=1)=0.205$ and $\vartheta(\mathcal{S}=10^{20})=0.334$. It means that an increase in m returns a decrease in this limit. The intersection point increases in the angle with the spring stiffness: $\vartheta(\mathcal{S}=0)=0.317$; $\vartheta(\mathcal{S}=1)=0.328$. It is also clear that the symmetric buckling curves of the two least stiff supports (for which $\mathcal{S}=0$ and $\mathcal{S}=1$) run quite close for smaller angles. The critical load for any $\mathcal{S}$ is generally greater this time compared to the results when $m=1\,000$.

In Figure 3.32, m is picked to be 100 000. The curves representing symmetric buckling for $\mathcal{S}=0$ and $\mathcal{S}=1$ and its endpoints almost coincide – there are hardly any noticeable differences, so they could even be treated together. The lower limit for symmetric buckling, anyway, further decreases: $\vartheta(\mathcal{S}=0)=0.111$; $\vartheta(\mathcal{S}=1)=0.113$ and $\vartheta(\mathcal{S}=10^{20})=0.187$. At the same time, the intersection point occurs at $\vartheta(\mathcal{S}=0)=0.179$; $\vartheta(\mathcal{S}=1)=0.182$. The symmetric buckling curves are again closer to each other and the lower endpoint of all the curves are closer to the origin.

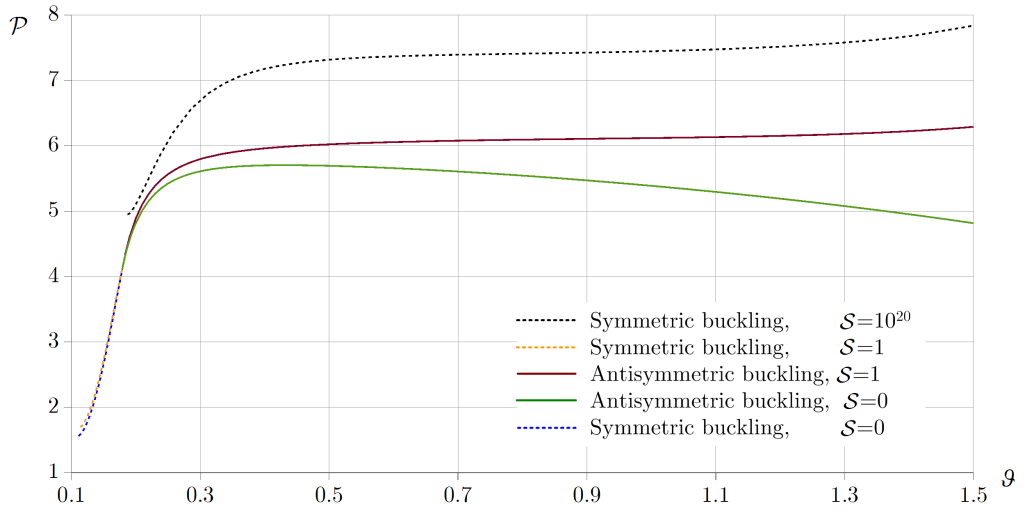

FIGURE 3.32. Buckling loads versus the semi-vertex angle when $m=100\,000$.

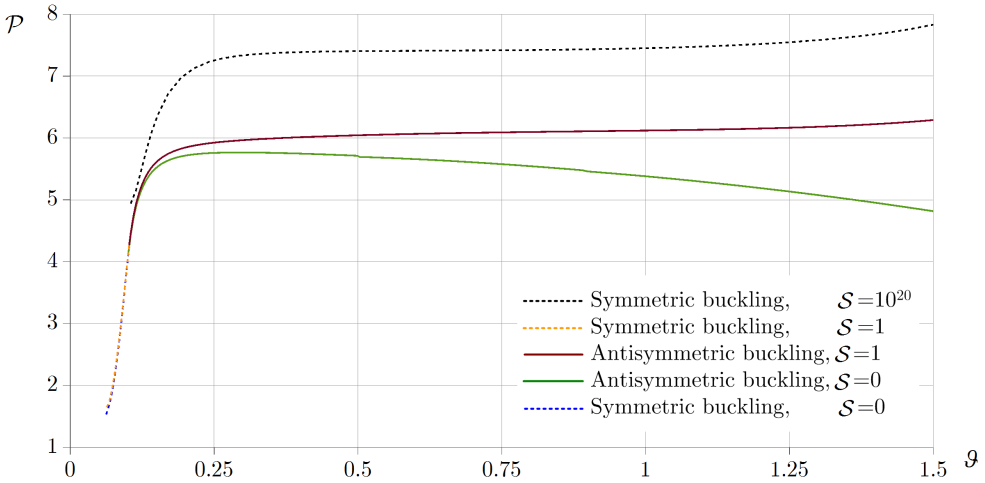

FIGURE 3.33. Buckling loads versus the semi-vertex angle when $m=1\,000\,000$.

With $m=1\,000\,000$, we find that $\vartheta(\mathcal{S}=0)=0.062$; $\vartheta(\mathcal{S}=1)=0.063$ and $\vartheta(\mathcal{S}=10^{20})=0.105$ are the lower limits for symmetric buckling and $\vartheta(\mathcal{S}=0)=0.101$; $\vartheta(\mathcal{S}=1)=0.102$ give the intersection point. Thus, again, when $\mathcal{S}$ is 0 and 1, these figures are the same with

DOI: 10.14750/ME.2016.008

a good accuracy. Generally, the differences compared to $m = 100\,000$ are not that relevant when moving from $m = 1\,000$ to $m = 10\,000$.

To sum up the outcomes, it is obvious from the former figures that the presence of the springs can have a considerable effect on the buckling load. Just to pick an illustrative example, if $m = 1\,000\,000$ and $\vartheta = 1$, the critical dimensionless load $\mathcal{P}$ can vary between 5.4 and 7.5. This interval becomes even greater, when ϑ is greater.

Finite element verifications. The results for symmetric buckling are again verified by FE computations using Abaqus and the same settings as mentioned in Subsubsection 3.5.1.1. It can be seen that the greatest differences (4.4%) are experienced when $m = 10^6$ and $\vartheta = 1.366$, so predictions for not so shallow beams seem to be really good. The new model, anyway, generally yields lower permissible loads except for when $m = 10^3$ and $\vartheta = 0.641$.

TABLE 3.14. Some control FE results regarding the symmetric buckling loads.

$\mathcal{S}$	m	ϑ	$\mathcal{P}_{\text{Abaqus}}$	$\mathcal{P}_{\text{New model}}$
$0/10/10^{20}$	10^3	0.641	4.98 / 5.03/5.09	5.23 / 5.26 / 5.29
$0/10/10^{20}$	10^3	1.052	6.78 / 6.83 / 6.99	6.70 / 6.86 / 7.09
$0/10/10^{20}$	10^3	1.416	7.48 / 7.51 / 7.71	7.36 / 7.43 / 7.62
$0/100/10^{20}$	10^6	0.289	6.75 / 7.20 / 7.38	6.69 / 7.14 / 7.32
$0/10/10^{20}$	10^6	0.782	6.98 / 7.18 / 7.52	6.76 / 6.99 / 7.42
$0/10/10^{20}$	10^6	1.366	7.58 / 7.70 / 7.98	7.26 / 7.39 / 7.64

3.5.3.2. *The primary equilibrium paths and the load-strain relationships.* On the horizontal axis in Figure 3.34, the dimensionless displacement of the crown point W_{oC} is plotted against the dimensionless load $\hat{\mathcal{P}}$ for beams with $m = 100\,000$.

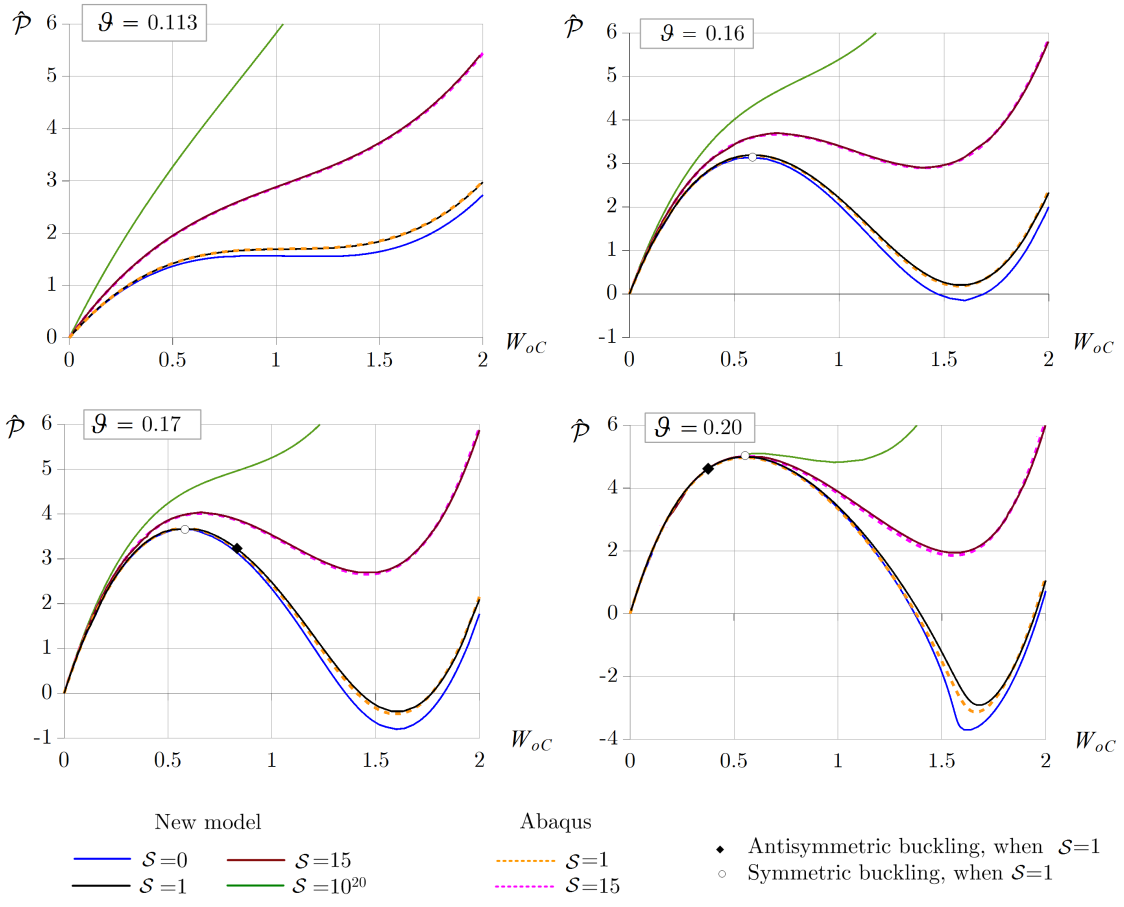

FIGURE 3.34. Dimensionless crown point displacement versus dimensionless load, $m = 100\,000$.

DOI: 10.14750/ME.2016.008

There are four central angles picked to represent the different path types of rotationally restrained beams when $\mathcal{S} = 1$ and 15. These are compared with results valid for pinned-pinned and fixed-fixed beams. Finite element computations are also provided using fine dashed lines. When $\vartheta = 0.113$, the slope is always positive and there is neither limit point nor bifurcation point for the spring supported beams. This is also true for the fixed-fixed beam with, of course, less displacement under the same load. However, for the pin-supported member there is a limit point. Increasing ϑ to 0.16 results in the appearance of a limit point for all but the fixed beam. The corresponding critical loads increase together with $\mathcal{S}$. The fixed-fixed beam still has a positive tangent throughout but its curve generally runs closer to the others up until the first limit point on the curves for the restrained beams. At $\vartheta = 0.17$, there is a bifurcation point but on the descending branch of the corresponding curve for the pinned-pinned and restrained beams. Finally, for $\vartheta = 0.2$, there is a limit point in all four curves. These points are really close to each other as well as all the whole first stable branches. This time and above this central angle, the two picked rotationally restrained and pinned-pinned beams buckle antisymmetrically first, as the bifurcation point is located on the stable branch. Meanwhile, fixed-fixed beams can still buckle symmetrically only. The Abaqus computations confirm the validity of the outcomes.

For $\mathcal{S} = 1$ the load-strain curves are drawn in Figure 3.35. When $\vartheta = 0.113$, there are two different branches to which always a different $\hat{\mathcal{P}}$ belongs. If $\vartheta = 0.16$, the branches intersect each other and a limit point also appears meaning that symmetric snap-through buckling can occur. However, the ratio $\varepsilon_m/\varepsilon_{m\,crit\,\mathrm{anti}} = 1$ is not reached. Increasing ϑ to 0.17, we experience that a bifurcation point appears after the limit point. Finally, if ϑ is equal to or greater than 0.2, the bifurcation point comes prior to the limit point: the antisymmetric buckling shape dominates for such shallow circular beams under a central load. It is also a remarkable property that every time there are two branches. The first one always starts at the origin. There is an intersection point of the two corresponding branches around $\varepsilon_m/\varepsilon_{m\,crit\,\mathrm{anti}} \approx 0.27$, where the loading level is $\hat{\mathcal{P}} \approx 1.75$.

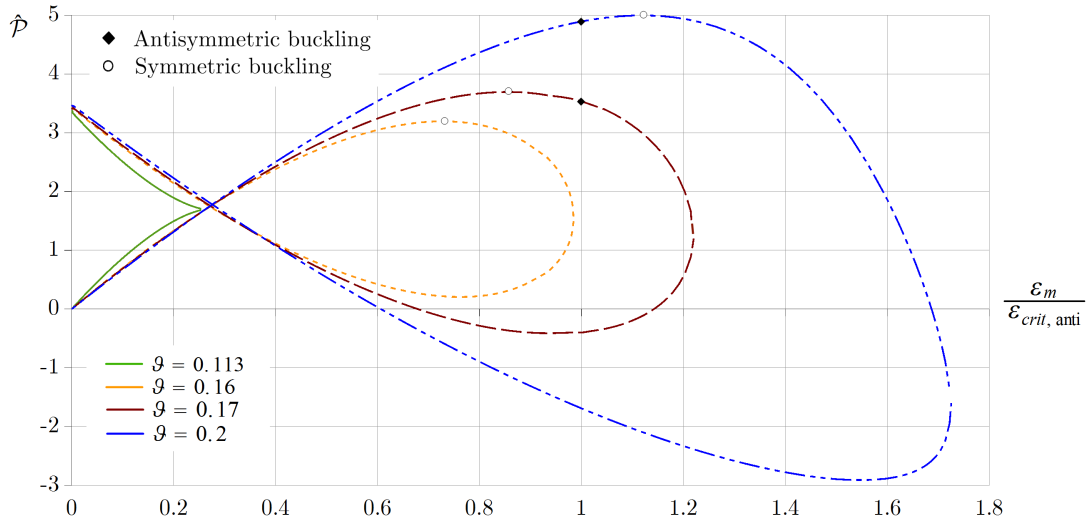

FIGURE 3.35. Typical load-strain relationships for $m = 100\,000$.

3.6. The effect of heterogeneity on the buckling load

We now demonstrate how heterogeneity can affect the buckling load of bilayered beams with rectangular cross-section, given that only the material composition is varied – the overall geometry remains unchanged. As can be seen from Figure 3.36, the upper layer has a Young's modulus E_1 and a height b_1. The height is a parameter: $b_1 \in [0, b]$. When $b_1 = 0$, the beam

DOI: 10.14750/ME.2016.008

is homogeneous with a Young's modulus E_2. In this case, the heterogeneity parameter is always denoted by m_{hom} and the radius of the E-weighted centerline is $\rho_{o\ \text{hom}}$. (If $b_1 = b$, the homogeneous cross-section has a Young's modulus E_1.) For any other (and obviously heterogeneous) distributions, in this section, we use the notations m_{het} and $\rho_{o\ \text{het}}$.

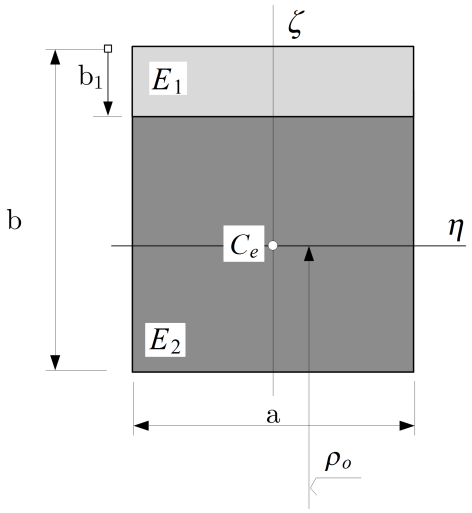

FIGURE 3.36. The investigated bilayered cross-section.

Recalling (2.1.13) and (3.1.9), we would like to find out how the ratio

$$\frac{m_{\text{het}}}{m_{\text{hom}}(b_1 = 0)} = \frac{A_e I_\eta E_2}{A E_2 I_{e\eta}} \left[\frac{\rho_{o\ \text{het}}}{\rho_{o\ \text{hom}}}\right]^2 \tag{3.6.1}$$

is related to the material distribution. It turns out that this fraction is a function of the quotients ρ_o/b, b_1/b and E_2/E_1 for this simple rectangular cross-section. The first, and otherwise dominant term on the right side of the former expression depends only on the ratios E_2/E_1 and b_1/b – see the definitions (2.1.13). Some possible solutions are plotted in Figure 3.37. On the account of heterogeneity, we can see an up to 55% difference when $E_2/E_1 = 5$. It is also clear that when $b/b_1 = 0.5$, the coherent curves intersect each other and the maxima of these are also the same. It means that the plotted ratio is obviously independent of whether the upper or the lower layer has a greater Young's modulus. The quotient E_2/E_1 only affects at what rate of b/b_1 the maximum is reached.

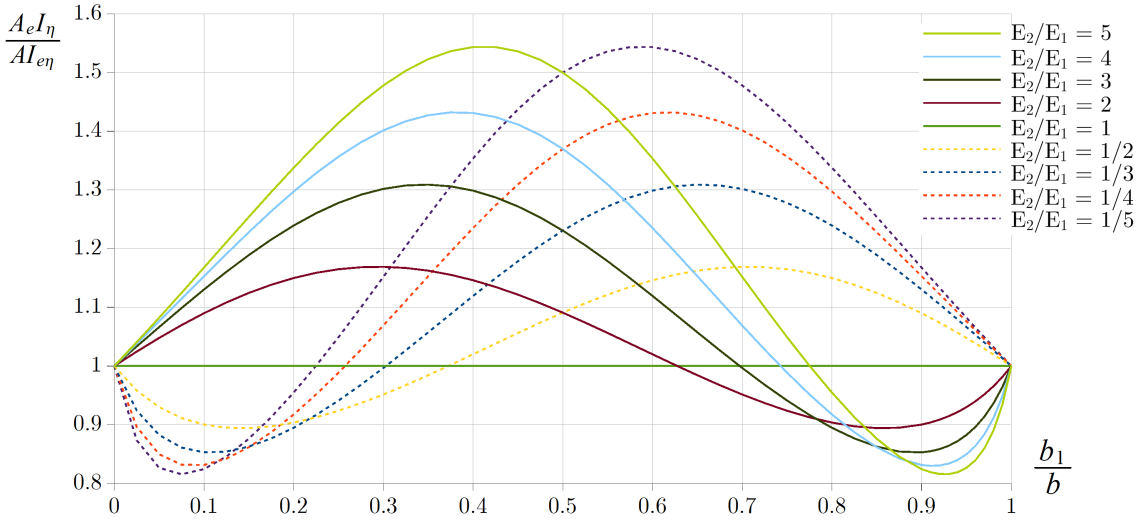

FIGURE 3.37. The first term in (3.6.1).

DOI: 10.14750/ME.2016.008

The second term in (3.6.1) further depends on the ratio $\rho_{o\,\mathrm{hom}}/b$. For the rates 10, 50 and 100, the results are plotted in Figure 3.38. It can be seen that this term has a much less considerable effect – at most $\pm 4\%$, when $\rho_{o\,\mathrm{hom}}/b = 10$. For the other two picked ratios it is always less than 1%. So for most geometries and material distributions the ratio $(\rho_{o\ \mathrm{het}}/\rho_{o\ \mathrm{hom}})^2$ can be considered to be 1 with a good accuracy.

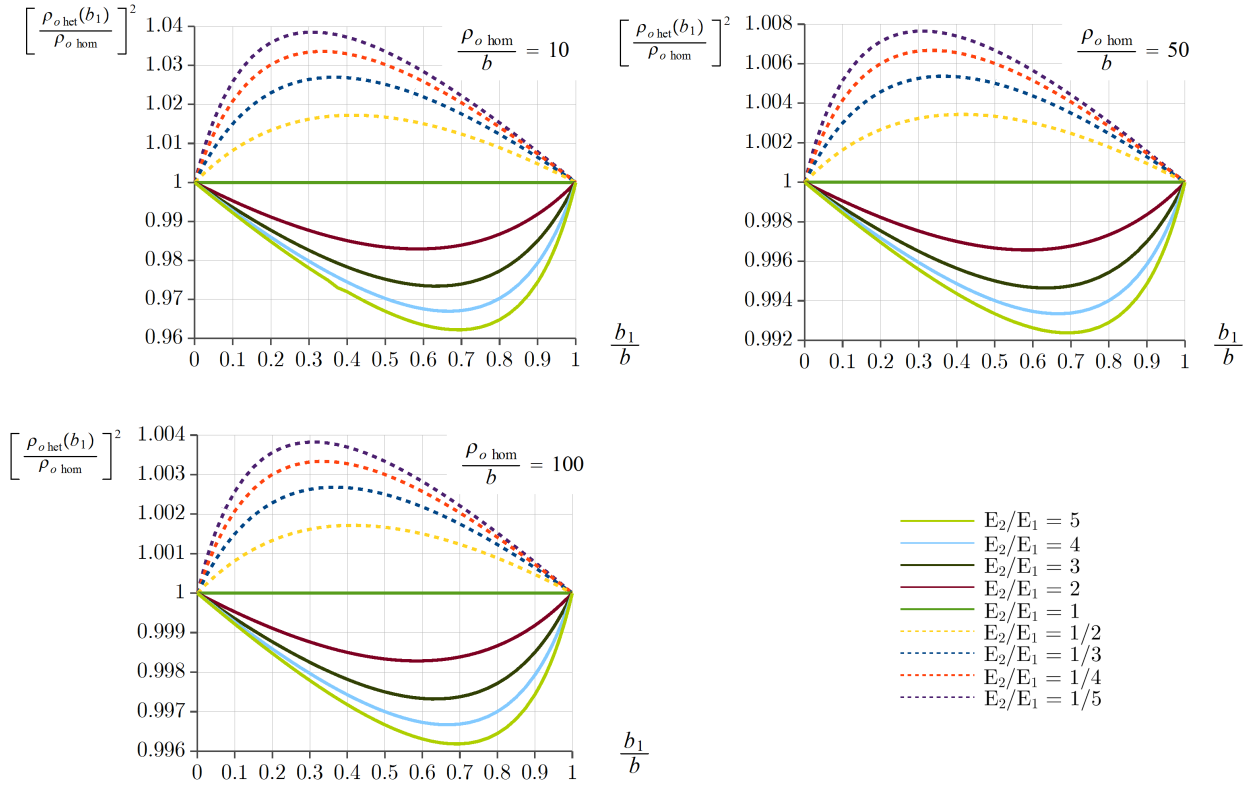

FIGURE 3.38. The second term in (3.6.1).

To sum up, the ratio $m_{\mathrm{het}}/m_{\mathrm{hom}}$ is always the product of the previous two matching figures. Here we plot this quotient for $\rho_{o\,\mathrm{hom}}/b = 10$ – see Figure 3.39.

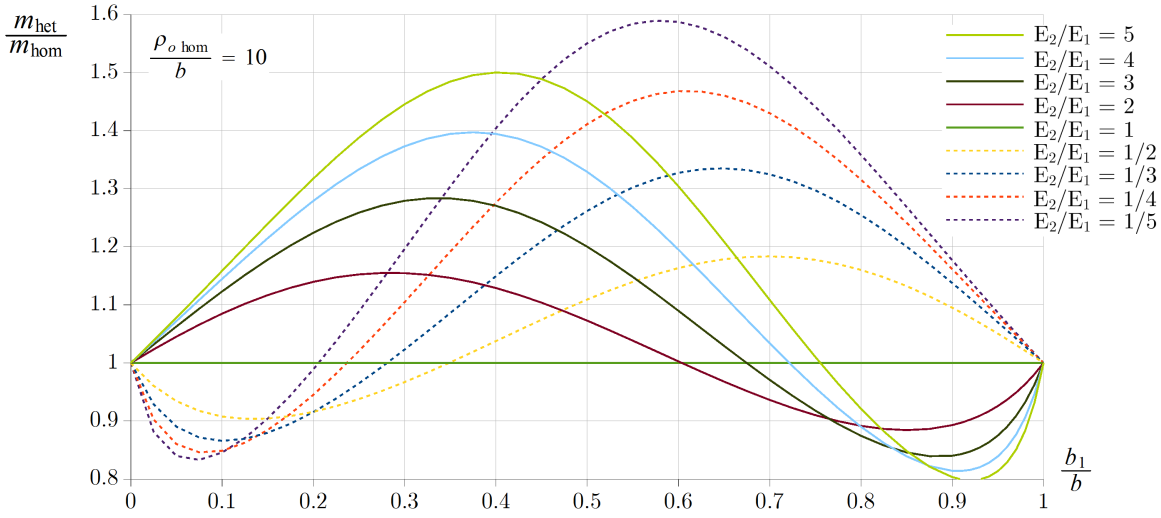

FIGURE 3.39. Variation of (3.6.1) because of the heterogeneity.

DOI: 10.14750/ME.2016.008

As it can therefore be seen, due to the heterogeneity, the maxima in the rates of m are as follows:

- $m_{\text{het}}/m_{\text{hom}} = 1.500$ at $b_1/b = 0.405$, if $E_2/E_1 = 5$;
- $m_{\text{het}}/m_{\text{hom}} = 1.397$ at $b_1/b = 0.375$, if $E_2/E_1 = 4$;
- $m_{\text{het}}/m_{\text{hom}} = 1.284$ at $b_1/b = 0.337$, if $E_2/E_1 = 3$;
- $m_{\text{het}}/m_{\text{hom}} = 1.155$ at $b_1/b = 0.285$, if $E_2/E_1 = 2$;
- $m_{\text{het}}/m_{\text{hom}} = 1.183$ at $b_1/b = 0.689$, if $E_2/E_1 = 1/2$;
- $m_{\text{het}}/m_{\text{hom}} = 1.335$ at $b_1/b = 0.646$, if $E_2/E_1 = 1/3$;
- $m_{\text{het}}/m_{\text{hom}} = 1.468$ at $b_1/b = 0.609$, if $E_2/E_1 = 1/4$;
- $m_{\text{het}}/m_{\text{hom}} = 1.589$ at $b_1/b = 0.580$, if $E_2/E_1 = 1/5$.

3.6.1. Numerical example. Let us insist on the former bilayered rectangular cross-section. We choose a pinned-pinned circular beam with $E_2/E_1 = 4$. The following m_{hom} values are tested: $1.2 \cdot 10^3$; $1.08 \cdot 10^4$; $1.0008 \cdot 10^5$; 10^6. We would like to find out how heterogeneity affects the critical load through the variation of the parameter m. Investigations are carried out until the maxima of the parameter m_{het} is reached, while gradually increasing the ratio b_1/b – see the preceding figures. All the results are shown graphically in Figure 3.40. For every picked central angle only the dominant buckling mode is evaluated. When it is a symmetric shape, the corresponding curve is fine dashed. When it is an antisymmetric shape (it is the more general thanks to the pinned supports), then the curve is continuous. Since the interval of symmetric buckling for pinned-pinned beams is quite narrow as shown in Figure 3.13, there are generally one or at most two samples picked from this range.

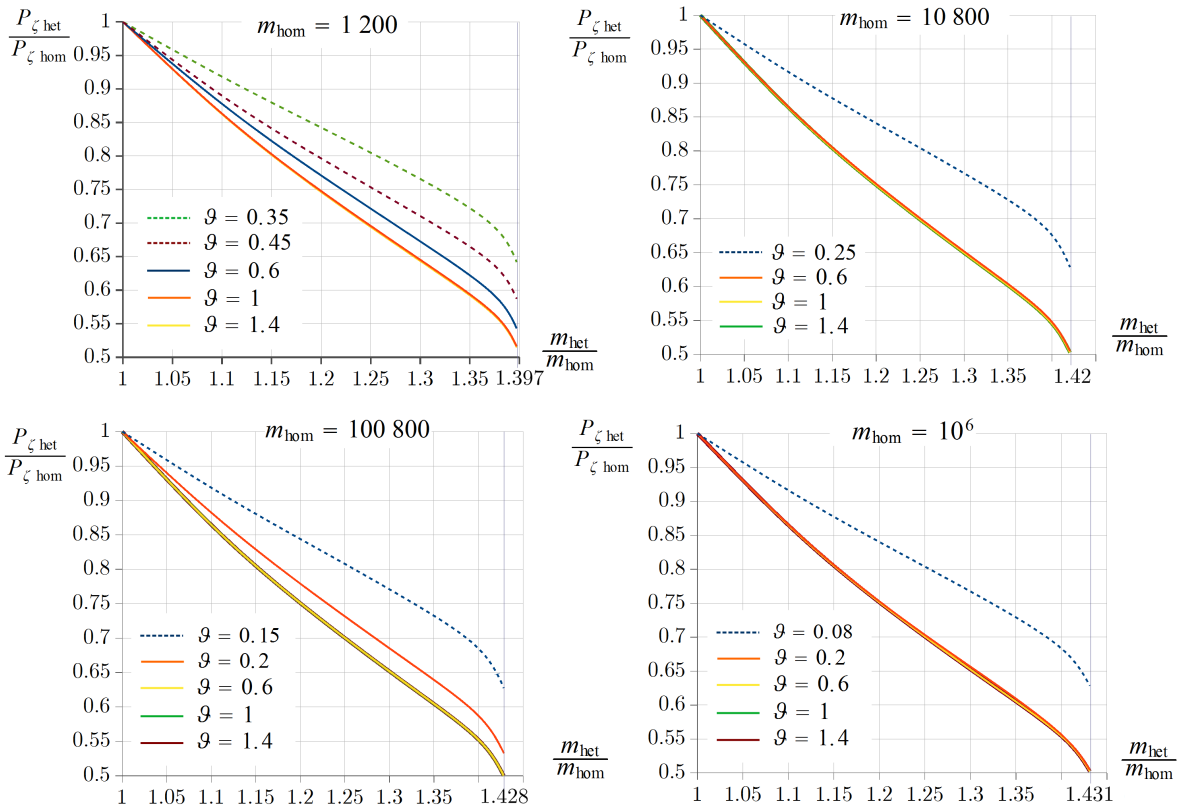

FIGURE 3.40. The effect of the heterogeneity on the critical load.

Overall, we can conclude that heterogeneity has a really massive effect on the buckling load, independently of the magnitude of the tested m-s. This can even be 50% for antisymmetric case and 41% for symmetric buckling. It is also a conclusion that, for every sample, the semi-vertex angle ϑ does not really have an impact on the plotted ratios: the related curves usually

DOI: 10.14750/ME.2016.008

coincide for the majority of the interval. We can as well observe the fact that increasing the value of m_{hom} results in a slight increase in the maxima of the ratio $m_{\text{het}}/m_{\text{hom}}$ measured along the abscissa.

3.7. Summary of the results achieved in Section 3

I have investigated the in-plane elastic static stability of circular beams with cross-sectional inhomogeneity provided that the beams are subjected to a vertical force at the crown point. The most important results are as follows:

1. I have derived a new model both for the pre-buckling radial displacements and for the post-buckling radial displacements — in the later case both for symmetric and asymmetric buckling. Cross-sectional inhomogeneity is implied in these equations via the parameter m. The equations and therefore the model I have established are more accurate than those solved by Bradford et al. [**56**, **61**] for homogeneous material.
2. Though I have neglected the effect of the tangential displacement on the angle of rotation – most papers like [**56**, **61**, **73**, **74**] also utilize this assumption – the results for the critical loads seem to be be more accurate than those published in [**56**, **61**] thanks to the less neglects. Further, the results happen to approximate well the critical behaviour of not strictly shallow circular beams.
3. Solutions are provided for (a) pinned-pinned, (b) fixed-fixed and (c) rotationally restrained beams. For each case, I have determined what characters the stability loss can have: no buckling, limit point buckling, bifurcation buckling after limit point buckling, bifurcation buckling precedes limit point buckling. The endpoints of the corresponding intervals are not constant in λ (as in the previous models) but depend on the parameter m.
4. Comparisons have been made with previous results and commercial FE computations as well. These confirm that the results of the novel model are indeed more accurate than the earlier results. For small central angles the differences are, in general, smaller than for greater central angles.
5. Cross-sectional inhomogeneity can have a significant effect on the critical load as the provided simple example shows.

DOI: 10.14750/ME.2016.008

CHAPTER 4

In-plane vibrations of loaded heterogeneous deep circular beams

4.1. Introductory remarks

In this chapter we investigate the in-plane vibrations of deep circular beams under a constant concentrated vertical load, which is exerted at the crown point. For such problem, according to the reviewed literature, there are no preceding scientific works. We aim to find out how we can account for the effect of the concentrated load. A further goal is to demonstrate the effects of heterogeneity on the frequency spectrum. The forthcoming method implies the Green function matrix and requires the application of a geometrically linear model. But contrary to the preceding stability model, the effects of the tangential displacement on the rotation field are not neglected. Since we remain within the frames of the linear theory, there is a need for some simplifications compared to the stability model of Chapter 3.

4.1.1. Equations of the static equilibrium. On the basis of the previous chapter only the most important relations are gathered here. The first one of these is that the axial

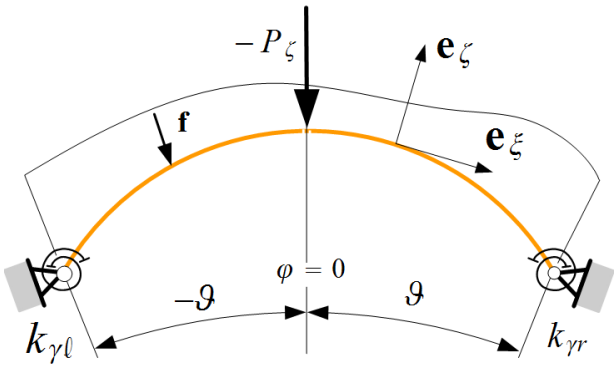

FIGURE 4.1. A circular deep beam under compression.

strain is approximated linearly, i.e. the square of the rotation field $\psi_{o\eta}^2$ is dropped compared to (3.1.3), consequently

$$\varepsilon_\xi = \frac{1}{1+\frac{\zeta}{\rho_o}}\left(\varepsilon_{o\xi}+\zeta\kappa_o\right)\ ,\quad \varepsilon_{o\xi}=\frac{\mathrm{d}u_o}{\mathrm{d}s}+\frac{w_o}{\rho_o},\quad \psi_{o\eta}=\frac{u_o}{\rho_o}-\frac{\mathrm{d}w_o}{\mathrm{d}s},\quad \kappa_o=\frac{\mathrm{d}u_o}{\rho_o\mathrm{d}s}-\frac{\mathrm{d}^2w_o}{\mathrm{d}s^2}\ . \tag{4.1.1}$$

But this time the effect of the tangential displacement on the rotations will be kept to better approximate the the behaviour of deep curved beams. The constitutive equation is unchanged meaning that Hooke's law yields

$$N=\frac{I_{e\eta}}{\rho_o^2}m\varepsilon_{o\xi}-\frac{M}{\rho_o},\qquad M=-I_{e\eta}\left(\frac{\mathrm{d}^2w_o}{\mathrm{d}s^2}+\frac{w_o}{\rho_o^2}\right)\ , \tag{4.1.2a}$$

$$N+\frac{M}{\rho_o}=\frac{I_{e\eta}}{\rho_o^2}m\varepsilon_{o\xi},\quad \text{with}\quad \tilde{m}=\frac{\mathrm{A_e}\rho_o^2}{\mathrm{I}_{e\eta}}-1\simeq\frac{\mathrm{A_e}\rho_o^2}{\mathrm{I}_{e\eta}}=m\ . \tag{4.1.2b}$$

These formulae are the same as (3.1.7), (3.1.8) and (3.1.10) given that we swap ε_m for $\varepsilon_{o\xi}$.

DOI: 10.14750/ME.2016.008

The equilibrium equations and the (dis)continuity conditions in terms of N and M – obtained from the principle of virtual work – are also unchanged and are shown under (3.2.2)-(3.2.4) for rotationally restrained beams. What comes next are the expressions of the equilibrium equations

$$\begin{aligned} &\frac{\mathrm{d}N}{\mathrm{d}s}+\frac{1}{\rho_o}\left[\frac{\mathrm{d}M}{\mathrm{d}s}-\left(N+\frac{M}{\rho_o}\right)\psi_{o\eta}\right]+f_t=0\,,\\ &\frac{\mathrm{d}}{\mathrm{d}s}\left[\frac{\mathrm{d}M}{\mathrm{d}s}-\left(N+\frac{M}{\rho_o}\right)\psi_{o\eta}\right]-\frac{N}{\rho_o}+f_n=0 \end{aligned} \tag{4.1.3}$$

in which N and M should be given in terms of the kinematic quantities using (4.1.2). In this way, from $(4.1.3)_1$ we get

$$\frac{I_{e\eta}}{\rho_o^3}m\frac{\mathrm{d}\varepsilon_{o\xi}}{\mathrm{d}\varphi}-\frac{I_{e\eta}}{\rho_o^3}m\varepsilon_{o\xi}\psi_{o\eta}+f_t=0\,, \tag{4.1.4}$$

where the product $\varepsilon_{o\xi}\psi_{o\eta}$ – being quadratic in the displacements – can be neglected when it is compared to the other terms. Thus, we find that

$$\frac{\mathrm{d}\varepsilon_{o\xi}}{\mathrm{d}\varphi}=\varepsilon_{o\xi}^{(1)}=U_o^{(2)}+W_o^{(1)}=-\frac{\rho_o^3}{mI_{e\eta}}f_t \tag{4.1.5}$$

where the following notations are applied:

$$U_o=\frac{u_o}{\rho_o}\,,\qquad W_o=\frac{w_o}{\rho_o}\,,\qquad (\ldots)^{(n)}=\frac{\mathrm{d}^n(\ldots)}{\mathrm{d}\varphi^n}\quad n\in\mathbb{Z}. \tag{4.1.6}$$

If the density of the distributed forces in the tangential direction f_t is zero, i.e. there is only a radial load on the beam, then

$$\varepsilon_{o\xi}=\text{constant}. \tag{4.1.7}$$

The manipulations on $(4.1.3)_2$ are detailed in Appendix A.2.1. The result is

$$W_o^{(4)}+\left(2-m\varepsilon_{o\xi}\right)W_o^{(2)}+\left[1+m\left(1-\varepsilon_{o\xi}\right)\right]W_o+mU_o^{(1)}=\frac{\rho_o^3}{I_{e\eta}}f_n\,. \tag{4.1.8}$$

To sum up, when the distributed forces do not vanish we arrive at the system of DEs

$$\begin{aligned} &\begin{bmatrix}0&0\\0&1\end{bmatrix}\begin{bmatrix}U_o\\W_o\end{bmatrix}^{(4)}+\begin{bmatrix}-m&0\\0&2-m\varepsilon_{o\xi}\end{bmatrix}\begin{bmatrix}U_o\\W_o\end{bmatrix}^{(2)}+\\ &\quad+\begin{bmatrix}0&-m\\m&0\end{bmatrix}\begin{bmatrix}U_o\\W_o\end{bmatrix}^{(1)}+\begin{bmatrix}0&0\\0&1+m\left(1-\varepsilon_{o\xi}\right)\end{bmatrix}\begin{bmatrix}U_o\\W_o\end{bmatrix}^{(0)}=\frac{\rho_o^3}{I_{e\eta}}\begin{bmatrix}f_t\\f_n\end{bmatrix}. \end{aligned} \tag{4.1.9}$$

If the distributed forces are equal to zero and the beam is subjected to a compressive force at the crown point then the static equilibrium is governed by

$$W_o^{(5)}+\left(1+\chi^2\right)W_o^{(3)}+\chi^2W_o^{(1)}=0, \tag{4.1.10}$$

or equivalently by

$$U_o^{(6)}+\left(1+\chi^2\right)U_o^{(4)}+\chi^2U_o^{(2)}=0, \tag{4.1.11}$$

where

$$\chi^2=1-m\varepsilon_{o\xi},\quad \text{since}\quad m\varepsilon_{o\xi}<1\,. \tag{4.1.12}$$

Here the strain is due to the concentrated force P_ζ.

It is also possible that the concentrated force is directed upwards, i.e. it causes a positive strain. There are two cases: (a) if $m\varepsilon_{o\xi}<1$ then the previous three relations hold; (b) if the former relation is not valid then χ^2 is redefined by

$$\chi^2=m\varepsilon_{o\xi}-1,\quad \text{provided that}\quad m\varepsilon_{o\xi}>1\,. \tag{4.1.13}$$

DOI: 10.14750/ME.2016.008

Thus, the static equilibrium is governed by

$$W_o^{(5)} + \left(1-\chi^2\right) W_o^{(3)} - \chi^2 W_o^{(1)} = 0, \tag{4.1.14}$$

or equivalently by

$$U_o^{(6)} + \left(1-\chi^2\right) U_o^{(4)} - \chi^2 U_o^{(2)} = 0. \tag{4.1.15}$$

4.1.2. Equations of the vibrations. In accordance with the notational conventions introduced in Subsection 3.1.2, the increments in the various quantities are still distinguished by a subscript $_b$. Now these increments are related to the time-dependent vibrations [$w_{ob} = w_{ob}(s,t)$; $u_{ob} = u_{ob}(s,t)$ – t denotes the time]. Here we gather the most important linearized formulae based on the subsection cited.

As regards the axial strain and the rotation field, recalling (3.1.14), we have

$$\varepsilon_{\xi\, b} \simeq \frac{1}{1+\frac{\zeta}{\rho_o}} \left(\varepsilon_{o\xi\, b} + \zeta \kappa_{o\, b}\right) \ , \quad \varepsilon_{o\xi\, b} = \frac{\partial u_{ob}}{\partial s} + \frac{w_{ob}}{\rho_o} \ , \tag{4.1.16a}$$

$$\psi_{o\eta\, b} = \frac{u_{ob}}{\rho_o} - \frac{\partial w_{ob}}{\partial s} \ , \quad \kappa_{o\, b} = \frac{1}{\rho_o}\frac{\partial u_{ob}}{\partial s} - \frac{\partial^2 w_{ob}}{\partial s^2}. \tag{4.1.16b}$$

Hooke's law for the increments (3.1.17)-(3.1.21) yields

$$N_b = \frac{I_{e\eta}}{\rho_o^2} m \varepsilon_{o\xi\, b} - \frac{M_b}{\rho_o} \ , \quad M_b = -I_{e\eta}\left(\frac{\partial^2 w_{ob}}{\partial s^2} + \frac{w_{ob}}{\rho_o^2}\right) \ , \quad N_b + \frac{M_b}{\rho_o} = \frac{I_{e\eta}}{\rho_o^2} m \varepsilon_{o\xi\, b}. \tag{4.1.17}$$

At the same time the equations of motion

$$\frac{\partial}{\partial s}\left(N_b + \frac{M_b}{\rho_o}\right) - \frac{1}{\rho_o}\left(N + \frac{M}{\rho_o}\right)\psi_{o\eta\, b} + f_{tb} = 0 \ , \tag{4.1.18a}$$

$$\frac{\partial^2 M_b}{\partial s^2} - \frac{N_b}{\rho_o} - \frac{\partial}{\partial s}\left[\left(N + \frac{M}{\rho_o}\right)\psi_{o\eta\, b} + \left(N_b + \frac{M_b}{\rho_o}\right)\psi_{o\eta}\right] + f_{nb} = 0 \tag{4.1.18b}$$

formally coincide with (3.2.13) given that the quadratic terms in the increments are neglected. As we are now dealing with the vibrations, the increments in the distributed forces are forces of inertia

$$f_{tb} = -\rho_a A \frac{\partial^2 u_{ob}}{\partial t^2}, \qquad f_{nb} = -\rho_a A \frac{\partial^2 w_{ob}}{\partial t^2}, \tag{4.1.19}$$

where ρ_a is the average density of the cross-section:

$$\rho_a = \frac{1}{A}\int_A \rho\left(\eta,\zeta\right) \mathrm{d}A \tag{4.1.20}$$

If we repeat the same procedure as that leading to (3.2.18) but on (4.1.18a) we have

$$\frac{I_{e\eta}}{\rho_o^2} m \frac{\mathrm{d}\varepsilon_{o\xi\, b}}{\mathrm{d}s} - \frac{1}{\rho_o}\frac{I_{e\eta}}{\rho_o^2} m \varepsilon_{o\xi} \psi_{o\eta\, b} + f_{tb} = 0 \ . \tag{4.1.21}$$

Moreover, after neglecting the second (quadratic term), we arrive at

$$-m\left(U_{ob}^{(2)} + W_{ob}^{(1)}\right) = \frac{\rho_o^3}{I_{e\eta}} f_{tb} \, . \tag{4.1.22}$$

The manipulations performed on (4.1.18b) are detailed in Appendix A.2.2. The result is

$$W_{ob}^{(4)} + \left(2 - m\varepsilon_{o\xi}\right) W_{ob}^{(2)} + \left[1 + m\left(1-\varepsilon_{o\xi}\right)\right] W_{ob} + m U_{ob}^{(1)} = \frac{\rho_o^3}{I_{e\eta}} f_{nb} \ . \tag{4.1.23}$$

Consequently, the two governing equations in matrix form are

$$\begin{bmatrix} 0 & 0 \\ 0 & 1 \end{bmatrix} \begin{bmatrix} U_{ob} \\ W_{ob} \end{bmatrix}^{(4)} + \begin{bmatrix} -m & 0 \\ 0 & 2 - m\varepsilon_{o\xi} \end{bmatrix} \begin{bmatrix} U_{ob} \\ W_{ob} \end{bmatrix}^{(2)} +$$

DOI: 10.14750/ME.2016.008

$$+\begin{bmatrix} 0 & -m \\ m & 0 \end{bmatrix}\begin{bmatrix} U_{ob} \\ W_{ob} \end{bmatrix}^{(1)}+\begin{bmatrix} 0 & 0 \\ 0 & 1+m\,(1-\varepsilon_{o\xi}) \end{bmatrix}\begin{bmatrix} U_{ob} \\ W_{ob} \end{bmatrix}^{(0)}=\frac{\rho_o^3}{I_{e\eta}}\begin{bmatrix} f_{tb} \\ f_{nb} \end{bmatrix}\,. \quad (4.1.24)$$

Under the assumption of harmonic vibrations

$$U_{ob}(\varphi,t)=\hat{U}_{ob}(\varphi)\sin\alpha t \qquad \text{and} \qquad W_{ob}(\varphi,t)=\hat{W}_{ob}(\varphi)\sin\alpha t \quad (4.1.25)$$

with $\hat{U}_{ob}$ and $\hat{W}_{ob}$ denoting the amplitudes. The corresponding relations for these latter quantities follow from (4.1.24) as

$$\underbrace{\begin{bmatrix} 0 & 0 \\ 0 & 1 \end{bmatrix}}_{\overset{4}{\mathbf{P}}}\underbrace{\begin{bmatrix} \hat{U}_{ob} \\ \hat{W}_{ob} \end{bmatrix}}_{\mathbf{y}}^{(4)}+\underbrace{\begin{bmatrix} -m & 0 \\ 0 & 2-m\varepsilon_{o\xi} \end{bmatrix}}_{\overset{2}{\mathbf{P}}}\begin{bmatrix} \hat{U}_{ob} \\ \hat{W}_{ob} \end{bmatrix}^{(2)}+$$

$$+\underbrace{\begin{bmatrix} 0 & -m \\ m & 0 \end{bmatrix}}_{\overset{1}{\mathbf{P}}}\begin{bmatrix} \hat{U}_{ob} \\ \hat{W}_{ob} \end{bmatrix}^{(1)}+\underbrace{\begin{bmatrix} 0 & 0 \\ 0 & 1+m\,(1-\varepsilon_{o\xi}) \end{bmatrix}}_{\overset{0}{\mathbf{P}}}\begin{bmatrix} \hat{U}_{ob} \\ \hat{W}_{ob} \end{bmatrix}^{(0)}=\underbrace{\Lambda\begin{bmatrix} \hat{U}_{ob} \\ \hat{W}_{ob} \end{bmatrix}}_{\mathbf{r}} \quad (4.1.26)$$

in which

$$\Lambda=\rho_a\frac{A\rho_o^3}{I_{e\eta}}\alpha^2 \quad (4.1.27)$$

is the unknown eigenvalue and α is the eigenfrequency sought. The influence of the direction and the magnitude of the concentrated load P_ζ is incorporated into this model via the strain $\varepsilon_{o\xi}$, while the heterogeneity is present through the eigenvalue $\Lambda(\rho_a, I_{e\eta})$ and the parameter $m(A_e, I_{e\eta}, \rho_o)$.

If the beam is unloaded there is no initial strain in it: $\varepsilon_{o\xi}=0$. Then we get back those equations which govern the free vibrations [**41**, **100**]:

$$\begin{bmatrix} 0 & 0 \\ 0 & 1 \end{bmatrix}\begin{bmatrix} \hat{U}_{ob} \\ \hat{W}_{ob} \end{bmatrix}^{(4)}+\begin{bmatrix} -m & 0 \\ 0 & 2 \end{bmatrix}\begin{bmatrix} \hat{U}_{ob} \\ \hat{W}_{ob} \end{bmatrix}^{(2)}+\begin{bmatrix} 0 & -m \\ m & 0 \end{bmatrix}\begin{bmatrix} \hat{U}_{ob} \\ \hat{W}_{ob} \end{bmatrix}^{(1)}+$$

$$+\begin{bmatrix} 0 & 0 \\ 0 & m+1 \end{bmatrix}\begin{bmatrix} \hat{U}_{ob} \\ \hat{W}_{ob} \end{bmatrix}^{(0)}=\Lambda\begin{bmatrix} \hat{U}_{ob} \\ \hat{W}_{ob} \end{bmatrix}\,. \quad (4.1.28)$$

Depending on the supports of the beam, the system (4.1.26) or (4.1.28) is associated with appropriate homogeneous boundary conditions so that together these constitute eigenvalue problems. The left side of these systems can briefly be rewritten in the form

$$\mathbf{K}\left[\mathbf{y}\left(\varphi\right),\varepsilon_{o\xi}\right]=\overset{4}{\mathbf{P}}\mathbf{y}^{(4)}+\overset{2}{\mathbf{P}}\mathbf{y}^{(2)}+\overset{1}{\mathbf{P}}\mathbf{y}^{(1)}+\overset{0}{\mathbf{P}}\mathbf{y}^{(0)}\,. \quad (4.1.29)$$

In the sequel, two support arrangements will be exposed to further investigations. The boundary conditions for pinned-pinned beams ($k_{\gamma\ell}=k_{\gamma r}=0$) are

$$\hat{U}_{ob}\Big|_{\pm\vartheta}=\hat{W}_{ob}\Big|_{\pm\vartheta}=\hat{W}_{ob}^{(2)}\Big|_{\pm\vartheta}=0. \quad (4.1.30a)$$

Thus, the displacements and the bending moment $(4.1.17)_2$ are all zero at both ends. For fixed-fixed members ($k_{\gamma\ell}; k_{\gamma r}\to\infty$) the third condition is related to the end-rotations $(4.1.16)_3$:

$$\hat{U}_{ob}\Big|_{\pm\vartheta}=\hat{W}_{ob}\Big|_{\pm\vartheta}=\hat{W}_{ob}^{(1)}\Big|_{\pm\vartheta}=0\,. \quad (4.1.30b)$$

4.2. Solutions to the homogeneous parts

4.2.1. The static equilibrium. As we have pointed out in Subsection 4.1.1, there are two possible cases to deal with.

DOI: 10.14750/ME.2016.008

4.2.1.1. *If* $m\varepsilon_{o\xi} < 1$. Solutions to the dimensionless displacements W_o and U_o in (4.1.10) and (4.1.11) with the integration constants T_i, $i = 1, 2, \ldots$ are sought as

$$W_o = -T_2 - T_3 \cos\varphi + T_4 \sin\varphi - \chi T_5 \cos\chi\varphi + \chi T_6 \sin\chi\varphi \,, \tag{4.2.1}$$

$$U_o = T_2\varphi - \int W_o(\varphi)\,\mathrm{d}\varphi = T_1 + \hat{T}_2\varphi + T_3 \sin\varphi + T_4 \cos\varphi + T_5 \sin\chi\varphi + T_6 \cos\chi\varphi \,. \tag{4.2.2}$$

The constant part of W_o and the linear part of U_o should satisfy the equilibrium equation (4.1.8) when $f_n = 0$. This condition provides the connection between the coefficients T_2 and $\hat{T}_2$:

$$[1 + m(1 - \varepsilon_{o\xi})]\, W_o + mU_o^{(1)} = -T_2\,[1 + m(1 - \varepsilon_{o\xi})] + m\hat{T}_2 = 0 \tag{4.2.3}$$

from where

$$\hat{T}_2 = \frac{1 + m(1 - \varepsilon_{o\xi})}{m} T_2 \,. \tag{4.2.4}$$

4.2.1.2. *If* $m\varepsilon_{o\xi} > 1$. In most cases when the concentrated force is directed upwards the general solutions of (4.1.14) and (4.1.15) are

$$W_o = -S_2 - S_3 \cos\varphi + S_4 \sin\varphi - \chi S_5 \cosh\chi\varphi - S_6\chi \sinh\chi\varphi \,, \tag{4.2.5a}$$

$$U_o = S_1 + \hat{S}_2\varphi + S_3 \sin\varphi + S_4 \cos\varphi + \chi S_5 \sinh\chi\varphi + S_6\chi \cosh\chi\varphi \,, \quad S_i \in \mathbb{R}. \tag{4.2.5b}$$

The connection between S_2 and $\hat{S}_2$ is obtained from the same condition as previously, thus

$$[1 + m(1 - \varepsilon_{o\xi})]\, W_o + mU_o^{(1)} = -\,[1 + m(1 - \varepsilon_{o\xi})]\, S_2 + m\hat{S}_2 = 0 \tag{4.2.6}$$

from which

$$\hat{S}_2 = \frac{1 + m(1 - \varepsilon_{o\xi})}{m} S_2 \,. \tag{4.2.7}$$

4.2.2. The increments. Let us determine the solutions for the homogeneous parts of equations (4.1.26):

$$\hat{U}_{ob}^{(2)} + \hat{W}_{ob}^{(1)} = 0 \,, \tag{4.2.8}$$

$$\hat{W}_{ob}^{(4)} + 2\hat{W}_{ob}^{(2)} + \hat{W}_{ob} + m\left(\hat{U}_{ob}^{(1)} + \hat{W}_{ob}\right) - m\varepsilon_{o\xi}\left(\hat{W}_{ob} + \hat{W}_{ob}^{(2)}\right) = 0 \,. \tag{4.2.9}$$

After deriving the second equation with respect to the angle coordinate we have

$$\hat{W}_{ob}^{(5)} + 2\hat{W}_{ob}^{(3)} + \hat{W}_{ob}^{(1)} + \underbrace{m\left(\hat{U}_{ob}^{(2)} + \hat{W}_{ob}^{(1)}\right)}_{=0} - m\varepsilon_{o\xi}\left(\hat{W}_{ob}^{(1)} + \hat{W}_{ob}^{(3)}\right) = 0 \,. \tag{4.2.10}$$

Substituting here now $(4.2.8)_1$ we obtain

$$\hat{W}_{ob}^{(5)} + 2\hat{W}_{ob}^{(3)} + \hat{W}_{ob}^{(1)} - m\varepsilon_{o\xi}\left(\hat{W}_{ob}^{(1)} + \hat{W}_{ob}^{(3)}\right) = -\hat{U}_{ob}^{(6)} - 2\hat{U}_{ob}^{(4)} - \hat{U}_{ob}^{(2)} + m\varepsilon_{o\xi}\left(\hat{U}_{ob}^{(2)} + \hat{U}_{ob}^{(4)}\right) = 0 \tag{4.2.11}$$

or more concisely

$$\hat{W}_{ob}^{(5)} + (2 - m\varepsilon_{o\xi})\,\hat{W}_{ob}^{(3)} + (1 - m\varepsilon_{o\xi})\,\hat{W}_{ob}^{(1)} = \hat{U}_{ob}^{(6)} + (2 - m\varepsilon_{o\xi})\,\hat{U}_{ob}^{(4)} + (1 - m\varepsilon_{o\xi})\,\hat{U}_{ob}^{(2)} = 0. \tag{4.2.12}$$

DOI: 10.14750/ME.2016.008

4.2.2.1. *Solution when* $m\varepsilon_{o\xi} < 1$. This inequality applies to all beams under compression because the strain is a negative number as the concentrated force is directed downwards. However, the inequality also holds for some beams under tension (when the force is directed upwards). Therefore, with the notation

$$\chi^2 = 1 - m\varepsilon_{o\xi} \tag{4.2.13}$$

the related differential equations assume the forms

$$\hat{W}_{ob}^{(5)} + \left(\chi^2 + 1\right)\hat{W}_{ob}^{(3)} + \chi^2\hat{W}_{ob}^{(1)} = \hat{U}_{ob}^{(6)} + \left(1 + \chi^2\right)\hat{U}_{ob}^{(4)} + \chi^2\hat{U}_{ob}^{(2)} = 0\ . \tag{4.2.14}$$

It is not too difficult to check that the solutions for the dimensionless amplitudes are

$$\hat{W}_{ob} = -J_2 - J_3\cos\varphi + J_4\sin\varphi - \chi J_5\cos\chi\varphi + \chi J_6\sin\chi\varphi\ ; \tag{4.2.15}$$

and

$$\hat{U}_{ob} = \hat{J}_2\varphi + J_1 + J_3\sin\varphi + J_4\cos\varphi + J_5\sin\chi\varphi + J_6\cos\chi\varphi \tag{4.2.16}$$

in which the constants J_2 and $\hat{J}_2$ are not independent since the corresponding solutions should satisfy both (4.2.8) and (4.2.9). The first equation is identically satisfied. As regards the second one, the linear part of $\hat{U}_{ob}$ and the constant part of $\hat{W}_{ob}$ should satisfy it, therefore it follows from the relation

$$\hat{W}_{ob} + m\left(\hat{U}_{ob}^{(1)} + \hat{W}_{ob}\right) - m\varepsilon_{o\xi}\hat{W}_{ob} = -J_2 + m\left(\hat{J}_2 - J_2\right) + m\varepsilon_{o\xi}J_2 = 0 \tag{4.2.17}$$

that

$$\hat{J}_2 = \frac{1 + m\left(1 - \varepsilon_{o\xi}\right)}{m}J_2 = \mathcal{M}J_2\ . \tag{4.2.18}$$

4.2.2.2. *Solution when* $m\varepsilon_{o\xi} > 1$. This time the beam is always in tension, because then $\varepsilon_{o\xi} > 0$. Let us now denote

$$\chi^2 = m\varepsilon_{o\xi} - 1\ . \tag{4.2.19}$$

The differential equations to deal with are

$$\hat{W}_{ob}^{(5)} + \left(1 - \chi^2\right)\hat{W}_{ob}^{(3)} - \chi^2\hat{W}_{ob}^{(1)} = \hat{U}_{ob}^{(6)} + \left(1 - \chi^2\right)\hat{U}_{ob}^{(4)} - \chi^2\hat{U}_{ob}^{(2)} = 0\ . \tag{4.2.20}$$

As it can be observed, the solutions are slightly different compared to Subsubsection 4.2.2.1:

$$\hat{W}_{ob} = -L_2 - L_3\cos\varphi + L_4\sin\varphi - \chi L_5\cosh\chi\varphi - L_6\chi\sinh\chi\varphi\ , \tag{4.2.21a}$$

$$\hat{U}_{ob} = L_1 + \hat{L}_2\varphi + L_3\sin\varphi + L_4\cos\varphi + \chi L_5\sinh\chi\varphi + L_6\chi\cosh\chi\varphi\ , \quad L_i \in \mathbb{R}. \tag{4.2.21b}$$

The connection between L_2 and $\hat{L}_2$ is obtained again from the condition that the linear part of $\hat{U}_{ob}$ and the constant part of $\hat{W}_{ob}$ should satisfy equation (4.2.9), consequently

$$\left[1 + m\left(1 - \varepsilon_{o\xi}\right)\right]\hat{W}_{ob} + m\hat{U}_{ob}^{(1)} = -\left[1 + m\left(1 - \varepsilon_{o\xi}\right)\right]L_2 + m\hat{L}_2 = 0\ . \tag{4.2.22}$$

As a result we get that

$$\hat{L}_2 = \frac{1 + m\left(1 - \varepsilon_{o\xi}\right)}{m}L_2 = \mathcal{M}L_2\ . \tag{4.2.23}$$

It turns out to be formally the same as (4.2.18).

DOI: 10.14750/ME.2016.008

4.3. The Green function matrix

The theoretical background for the solution of the eigenvalue problems in question is summarized here on the basis of [**41**]. Since the matrix $\overset{4}{\mathbf{P}}$ is non-invertible in (4.1.29), the cited system is degenerated. We are now dealing with the inhomogeneous differential equations

$$\mathbf{K}[\mathbf{y}(\varphi),\varepsilon_{o\xi}]=\sum_{\kappa=0}^{4}\overset{\kappa}{\mathbf{P}}(\varphi)\mathbf{y}^{(\kappa)}(\varphi)=\mathbf{r}(\varphi)\,,\qquad \overset{3}{\mathbf{P}}(\varphi)=\mathbf{0}, \tag{4.3.1}$$

where $\mathbf{r}(\varphi)$ is a prescribed inhomogeneity. The boundary conditions – we remind the reader to equations (4.1.30a), (4.1.30b) – are

$$\hat{U}_{ob}(-\vartheta)=0,\quad \hat{W}_{ob}(-\vartheta)=0,\quad \hat{W}^{(2)}_{ob}(-\vartheta)=0\quad|\quad \hat{U}_{ob}(\vartheta)=0,\quad \hat{W}_{ob}(\vartheta)=0,\quad \hat{W}^{(2)}_{ob}(\vartheta)=0 \tag{4.3.2}$$

and

$$\hat{U}_{ob}(-\vartheta)=0,\quad \hat{W}_{ob}(-\vartheta)=0,\quad \hat{W}^{(1)}_{ob}(-\vartheta)=0\quad|\quad \hat{U}_{ob}(\vartheta)=0,\quad \hat{W}_{ob}(\vartheta)=0,\quad \hat{W}^{(1)}_{ob}(\vartheta)=0 \tag{4.3.3}$$

for pinned-pinned and fixed-fixed beams, respectively. Equations (4.3.1)-(4.3.2) and (4.3.1)-(4.3.3) constitute two boundary value problems.

Solution to the homogeneous differential equations $\mathbf{K}[\mathbf{y}]=\mathbf{0}$ depends on the definition of χ^2. Exactly as beforehand, there are two possibilities:

$$\chi^2=\begin{cases}1-m\varepsilon_{o\xi} & \text{if} \quad m\varepsilon_{o\xi}<1\\ m\varepsilon_{o\xi}-1 & \text{if} \quad m\varepsilon_{o\xi}>1\,.\end{cases} \tag{4.3.4}$$

The solution to $\mathbf{y}$ can be expressed in the form

$$\mathbf{y}=\left[\sum_{j=1}^{4}\underset{(2\times2)}{\mathbf{Y}}{}^{j}\,\underset{(2\times2)}{\mathbf{C}}{}^{j}\right]\underset{(2\times1)}{\mathbf{e}}\,, \tag{4.3.5a}$$

where – based on (4.2.15)-(4.2.16) – the general solutions to the differential equations are

$$\mathbf{Y}_1=\begin{bmatrix}\cos\varphi & 0\\ \sin\varphi & 0\end{bmatrix},\quad \mathbf{Y}_2=\begin{bmatrix}-\sin\varphi & 0\\ \cos\varphi & 0\end{bmatrix},\quad \mathbf{Y}_3=\begin{bmatrix}\cos\chi\varphi & \mathcal{M}\varphi\\ \chi\sin\chi\varphi & -1\end{bmatrix},\quad \mathbf{Y}_4=\begin{bmatrix}-\sin\chi\varphi & 1\\ \chi\cos\chi\varphi & 0\end{bmatrix}, \tag{4.3.5b}$$

if $m\varepsilon_{o\xi}<1$. Recalling (4.2.21) it can be seen that $\mathbf{Y}_3$ and $\mathbf{Y}_4$ are different when $m\varepsilon_{o\xi}>1$, that is

$$\mathbf{Y}_3=\begin{bmatrix}\cosh\chi\varphi & \mathcal{M}\varphi\\ \chi\sinh\chi\varphi & -1\end{bmatrix},\quad \mathbf{Y}_4=\begin{bmatrix}-\sinh\chi\varphi & 1\\ \chi\cosh\chi\varphi & 0\end{bmatrix}. \tag{4.3.5c}$$

In equation (4.3.5a), $\mathbf{C}_i$ are arbitrary constant matrices and $\mathbf{e}$ is an arbitrary column matrix. Solutions to the boundary value problems (4.3.1)-(4.3.2) and (4.3.1)-(4.3.3) are sought in the form

$$\mathbf{y}(\varphi)=\int_{-\vartheta}^{\vartheta}\mathbf{G}(\varphi,\psi)\mathbf{r}(\psi)\mathrm{d}\psi\,,\quad \mathbf{G}(\varphi,\psi)=\begin{bmatrix}G_{11}(\varphi,\psi) & G_{12}(\varphi,\psi)\\ G_{21}(\varphi,\psi) & G_{22}(\varphi,\psi)\end{bmatrix}, \tag{4.3.6}$$

where $\mathbf{G}(\varphi,\psi)$ is the Green function matrix. The physical sense of this matrix is shown in Figure 4.2. When the beam, which is pre-loaded by the force P_ζ, is further loaded by a concentrated dimensionless unit force in the tangential/normal direction at ψ, the Green function matrix returns the response of the structural element, that is the dimensionless tangential/normal displacement at φ. The green and blue arrows belong together in the related figure.

DOI: 10.14750/ME.2016.008

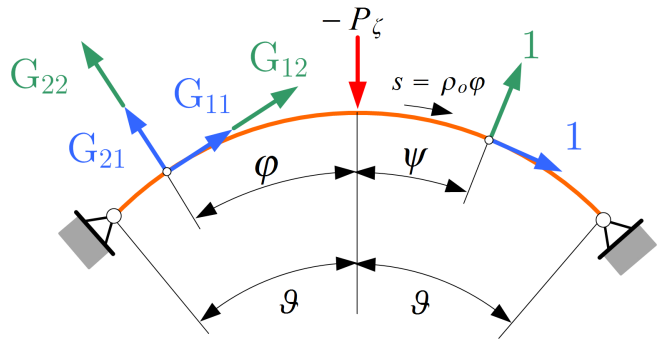

FIGURE 4.2. The physical sense of the Green function matrix.

The Green function matrix is defined by the following four properties [**41**]:

1. It is a continuous function of the angle coordinates φ and ψ in both of the triangular ranges $-\vartheta \le \varphi \le \psi \le \vartheta$ and $-\vartheta \le \psi \le \varphi \le \vartheta$.

   The functions $\{G_{11}(\varphi,\psi), G_{12}(\varphi,\psi)\}$ $[G_{21}(\varphi,\psi), G_{22}(\varphi,\psi)]$ are {2 times} [4 times] differentiable with respect to φ. Moreover, the derivatives

$$\frac{\partial^\kappa \mathbf{G}(\varphi,\psi)}{\partial\varphi^\kappa} = \mathbf{G}^{(\kappa)}(\varphi,\psi) \quad \kappa = 1,2\,; \tag{4.3.7a}$$

$$\frac{\partial^\kappa G_{2j}(\varphi,\psi)}{\partial\varphi^\kappa} = G_{2j}^{(\kappa)}(\varphi,\psi) \quad \kappa = 1,\ldots,4;\ j = 1,2 \tag{4.3.7b}$$

   are continuous in φ and ψ.

2. Let ψ be fixed in $[-\vartheta,\vartheta]$. Despite the fact that the functions and the derivatives

$$G_{11}(\varphi,\psi)\,,\ \ G_{12}^{(1)}(\varphi,\psi)\,,\ \ G_{21}^{(\kappa)}(\varphi,\psi)\ \ \kappa = 1,2,3\,;\ \ G_{22}^{(\kappa)}(\varphi,\psi)\ \ \kappa = 1,2 \tag{4.3.8a}$$

   are continuous in the whole range, the derivatives $G_{11}^{(1)}(\varphi,\psi)$ and $G_{22}^{(3)}(\varphi,\psi)$ have a jump at $\varphi = \psi$, that is

$$\lim_{\varepsilon\to 0}\left[G_{11}^{(1)}(\varphi+\varepsilon,\varphi) - G_{11}^{(1)}(\varphi-\varepsilon,\varphi)\right] = 1/\overset{2}{P}_{11}(\varphi), \tag{4.3.8b}$$

$$\lim_{\varepsilon\to 0}\left[G_{22}^{(3)}(\varphi+\varepsilon,\varphi) - G_{22}^{(3)}(\varphi-\varepsilon,\varphi)\right] = 1/\overset{4}{P}_{22}(\varphi)\,. \tag{4.3.8c}$$

3. Let $\boldsymbol{\alpha}$ denote an arbitrary constant vector. For a fixed $\psi \in [-\vartheta,\vartheta]$, the vector $\mathbf{G}(\varphi,\psi)\boldsymbol{\alpha}$ – as a function of φ ($\varphi \neq \psi$) – should satisfy the homogeneous differential equations $\mathbf{K}\left[\mathbf{G}(\varphi,\psi)\boldsymbol{\alpha}\right] = \mathbf{0}$.

4. The vector $\mathbf{G}(\varphi,\psi)\boldsymbol{\alpha}$, as a function of φ, should satisfy the boundary conditions (4.3.2) or (4.3.3).

In addition, there is one unique Green function matrix to any given boundary value problem [**41**]. If the Green function matrix exists – it is proven in [**41**] – then the vector (4.3.6) satisfies the differential equation (4.3.1) and the boundary conditions (4.3.2) or (4.3.3).

Consider now the differential equations written briefly in the form

$$\mathbf{K}[\mathbf{y}] = \Lambda\mathbf{y}\,; \tag{4.3.9}$$

where $\mathbf{K}[\mathbf{y}]$ is given by (4.1.29) and Λ is the eigenvalue sought – see (4.1.27). The ordinary differential equations (4.3.9) are associated with homogeneous boundary conditions – see (4.3.2) or (4.3.3) – and as it has already been mentioned, together they constitute boundary value problems, which are now, in fact, eigenvalue problems.

The vectors $\mathbf{a}^T(\varphi) = [a_1(\varphi)|a_2(\varphi)]$ and $\mathbf{b}^T(\varphi) = [b_1(\varphi)|b_2(\varphi)]$ are comparison vectors if they are different from zero, satisfy the boundary conditions and are differentiable as many

DOI: 10.14750/ME.2016.008

times as required. Both eigenvalue problems (4.3.9)-(4.3.2) and (4.3.9)-(4.3.3) are self-adjoint because the product

$$(\mathbf{a},\mathbf{b})_M = \int_{-\vartheta}^{\vartheta} \mathbf{a}^T\mathbf{K}\mathbf{b}\,\mathrm{d}\varphi \tag{4.3.10}$$

is commutative, i.e. $(\mathbf{a},\mathbf{b})_M = (\mathbf{b},\mathbf{a})_M$. Due to the this property the Green function matrix is cross-symmetric: $\mathbf{G}(\varphi,\psi) = \mathbf{G}^T(\psi,\varphi)$.

4.4. Numerical solution to the eigenvalue problems

Making use of (4.3.6), each of the eigenvalue problems (4.3.9)-(4.3.2) and (4.3.9)-(4.3.3) can be replaced by a homogeneous system of integral equations of the form

$$\mathbf{y}(\varphi) = \Lambda \int_{-\vartheta}^{\vartheta} \mathbf{G}(\varphi,\psi)\mathbf{y}(\psi)\mathrm{d}\psi\ . \tag{4.4.1}$$

Numerical solution to this eigenvalue problem can be sought by quadrature methods [**114**]. Consider the integral formula

$$J(\phi) = \int_{-\vartheta}^{\vartheta} \phi(\psi)\,\mathrm{d}\psi \equiv \sum_{j=0}^{n} w_j\phi(\psi_j) \qquad \psi_j \in [-\vartheta,\vartheta]\ , \tag{4.4.2}$$

where $\psi_j(\varphi)$ is a vector and the weights w_j are known. Having utilized the latter equation, we obtain from (4.4.1) that

$$\sum_{j=0}^{n} w_j\mathbf{G}(\varphi,\psi_j)\tilde{\mathbf{y}}(\psi_j) = \tilde{\iota}\tilde{\mathbf{y}}(\varphi) \qquad \tilde{\iota} = 1/\tilde{\Lambda} \qquad \psi_j \in [-\vartheta,\vartheta] \tag{4.4.3}$$

is the solution, which yields an approximate eigenvalue $\tilde{\Lambda} = 1/\tilde{\iota}$ and a corresponding approximate eigenfunction $\tilde{\mathbf{y}}(\varphi)$. After setting φ to ψ_i $(i = 0,1,2,\ldots,n)$ we have

$$\sum_{j=0}^{n} w_j\mathbf{G}(\psi_i,\psi_j)\tilde{\mathbf{y}}(\psi_j) = \tilde{\iota}\tilde{\mathbf{y}}(\psi_i) \qquad \tilde{\iota} = 1/\tilde{\Lambda} \qquad \psi_i,\psi_j \in [-\vartheta,\vartheta]\,, \tag{4.4.4}$$

or what is the same, a system in the form

$$\mathcal{G}\mathcal{D}\tilde{\mathcal{Y}} = \tilde{\iota}\tilde{\mathcal{Y}}\ , \tag{4.4.5}$$

where $\mathcal{G} = [\mathbf{G}(\psi_i,\psi_j)]$ is symmetric if the problem is self-adjoint. Further

$$\mathcal{D} = \mathrm{diag}(w_0, w_0|w_1, w_1|\ldots|w_n, w_n)$$

and $\tilde{\mathcal{Y}}^T = [\tilde{\mathbf{y}}^T(\psi_0)|\tilde{\mathbf{y}}^T(\psi_1)|\ldots|\tilde{\mathbf{y}}^T(\psi_n)]$. After solving the generalized algebraic eigenvalue problem (4.4.5) we have the approximate eigenvalues $\tilde{\Lambda}_r$ and eigenvectors $\tilde{\mathcal{Y}}_r$, while the corresponding eigenfunction is obtained from a substitution into (4.4.3):

$$\tilde{\mathbf{y}}_r(\varphi) = \tilde{\Lambda}_r \sum_{j=0}^{n} w_j\mathbf{G}(\varphi,\psi_j)\tilde{\mathbf{y}}_r(\psi_j) \qquad r = 0,1,2,\ldots,n\ . \tag{4.4.6}$$

Divide the range $[-\vartheta,\vartheta]$ into equidistant subintervals of length h and apply the integration formula to each subinterval. By repeating the line of thought leading to (4.4.6), one can readily show that the algebraic eigenvalue problem obtained has the same structure as (4.4.6).

It is also possible to consider the system of integral equations (4.4.1) as if it were a boundary integral equation and apply isoparametric approximation on the subintervals, i.e. over the elements. If this is the case, one can approximate the eigenfunction on the e-th element (on the e-th subinterval which is mapped onto the range $\gamma \in [-1,1]$ and is denoted by $\mathfrak{L}_e$) by

$$\overset{e}{\mathbf{y}} = \mathbf{N}_1(\gamma)\overset{e}{\mathbf{y}}_1 + \mathbf{N}_2(\gamma)\overset{e}{\mathbf{y}}_2 + \mathbf{N}_3(\gamma)\overset{e}{\mathbf{y}}_3\ , \tag{4.4.7}$$

DOI: 10.14750/ME.2016.008

where quadratic local approximation is assumed. Here $\mathbf{N}_i = \mathrm{diag}(N_i)$, $N_1 = 0.5\gamma(\gamma - 1)$, $N_2 = 1 - \gamma^2$, $N_3 = 0.5\gamma(\gamma + 1)$ and $\overset{e}{\mathbf{y}}_i$ is the value of the eigenfunction $\mathbf{y}(\varphi)$ at the left endpoint, the midpoint and the right endpoint of the e-th element, respectively. Upon substitution of the approximation (4.4.7) into (4.4.1) we have

$$\tilde{\mathbf{y}}(\varphi) = \tilde{\Lambda} \sum_{e=1}^{n_{be}} \int_{\mathfrak{L}_e} \mathbf{G}(\varphi,\gamma)[\mathbf{N}_1(\gamma)|\mathbf{N}_2(\gamma)|\mathbf{N}_3(\gamma)]\mathrm{d}\gamma \begin{bmatrix} \overset{e}{\mathbf{y}}_1 \\ \overset{e}{\mathbf{y}}_2 \\ \overset{e}{\mathbf{y}}_3 \end{bmatrix} , \tag{4.4.8}$$

in which, n_{be} is the number of elements (subintervals). Using equation (4.4.8) as a point of departure and repeating the line of thought leading to (4.4.5), we again find an algebraic eigenvalue problem.

4.5. Construction of the Green function matrices

4.5.1. The structure of the Green function matrix. Recalling the third property of the definition from Section 4.3, equation (4.3.6) and the general solution (4.3.5a); the Green function matrix can be expressed in the form [**41**]

$$\underbrace{\mathbf{G}(\varphi,\psi)}_{(2\times 2)} = \sum_{j=1}^{4} \mathbf{Y}_j(\varphi)\left[\mathbf{A}_j(\psi) \pm \mathbf{B}_j(\psi)\right] , \tag{4.5.1}$$

where the sign is [positive](negative) if $[\varphi \le \psi](\varphi \ge \psi)$. The matrices $\mathbf{Y}_j$, $\mathbf{A}_j$ and $\mathbf{B}_j$ are partitioned in the following way

$$\mathbf{Y}_j = \begin{bmatrix} \overset{j}{Y}_{11} & \overset{j}{Y}_{12} \\ \overset{j}{Y}_{21} & \overset{j}{Y}_{22} \end{bmatrix} = \begin{matrix} 1\,\{ \\ 1\,\{ \end{matrix} \underbrace{\begin{bmatrix} \mathbf{Y}_{j1} \\ \mathbf{Y}_{j2} \end{bmatrix}}_{(2\times 2)}, \tag{4.5.2a}$$

$$\mathbf{A}_j = \begin{bmatrix} \overset{j}{A}_{11} & \overset{j}{A}_{12} \\ \overset{j}{A}_{21} & \overset{j}{A}_{22} \end{bmatrix} = \begin{bmatrix} \underbrace{\mathbf{A}_{j1}}_{(2\times 1)} & \underbrace{\mathbf{A}_{j2}}_{(2\times 1)} \end{bmatrix}, \quad \mathbf{B}_j = \begin{bmatrix} \overset{j}{B}_{11} & \overset{j}{B}_{12} \\ \overset{j}{B}_{21} & \overset{j}{B}_{22} \end{bmatrix} = \begin{bmatrix} \underbrace{\mathbf{B}_{j1}}_{(2\times 1)} & \underbrace{\mathbf{B}_{j2}}_{(2\times 1)} \end{bmatrix}. \tag{4.5.2b}$$

Observe that $\mathbf{Y}_{j1}$, $\mathbf{Y}_{j2}$ are row matrices while $\mathbf{A}_{j1}$, $\mathbf{A}_{j2}$ and $\mathbf{B}_{j1}$, $\mathbf{B}_{j2}$ are column matrices. Keep in mind that $\mathbf{Y}_3$ and $\mathbf{Y}_4$ are different for the two cases considered, i.e. when $m\varepsilon_{o\xi} \lessgtr 1$.

4.5.2. The Green function matrix when $m\varepsilon_{o\xi} < 1$. We commence with the determination of the matrices $\mathbf{B}_j$, which can be calculated by utilizing the second property of the definition. It is related to the (dis)continuity conditions (4.3.8) in Section 4.3. Thus, there are two equation systems to be solved. The first system can be constructed by fulfilling the relations

$$\begin{bmatrix} \sum_{j=1}^{4} \mathbf{Y}_{j1}\mathbf{B}_{j1} \\ \sum_{j=1}^{4} \mathbf{Y}_{j2}\mathbf{B}_{j1} \\ \sum_{j=1}^{4} \mathbf{Y}_{j1}^{(1)}\mathbf{B}_{j1} \\ \sum_{j=1}^{4} \mathbf{Y}_{j2}^{(1)}\mathbf{B}_{j1} \\ \sum_{j=1}^{4} \mathbf{Y}_{j2}^{(2)}\mathbf{B}_{j1} \\ \sum_{j=1}^{4} \mathbf{Y}_{j2}^{(3)}\mathbf{B}_{j1} \end{bmatrix} = \begin{bmatrix} 0 \\ 0 \\ -\frac{1}{2}\left(\overset{2}{P}_{11}\right)^{-1} \\ 0 \\ 0 \\ 0 \end{bmatrix} \tag{4.5.3}$$

given that we use the angle coordinate ψ when expressing $\mathbf{Y}_j$. If we recall (4.3.1) and (4.3.5b) it can easily be seen that $\overset{2}{P}_{11} = -m$. Since $\overset{j}{Y}_{12} = \overset{j}{Y}_{22} = 0$ for $j = 1, 2$; the quantities $\overset{1}{B}_{21}$ and $\overset{2}{B}_{21}$ are set to zero.

DOI: 10.14750/ME.2016.008

The other system to be dealt with is quite similar:

$$\begin{bmatrix} \sum_{j=1}^{4} \mathbf{Y}_{j1}\mathbf{B}_{j2} \\ \sum_{j=1}^{4} \mathbf{Y}_{j2}\mathbf{B}_{j2} \\ \sum_{j=1}^{4} \mathbf{Y}_{j1}^{(1)}\mathbf{B}_{j2} \\ \sum_{j=1}^{4} \mathbf{Y}_{j2}^{(1)}\mathbf{B}_{j2} \\ \sum_{j=1}^{4} \mathbf{Y}_{j2}^{(2)}\mathbf{B}_{j2} \\ \sum_{j=1}^{4} \mathbf{Y}_{j2}^{(3)}\mathbf{B}_{j2} \end{bmatrix} = \begin{bmatrix} 0 \\ 0 \\ 0 \\ 0 \\ 0 \\ -\frac{1}{2}\left(\overset{4}{P}_{22}\right)^{-1} \end{bmatrix} . \tag{4.5.4}$$

Here $\overset{4}{P}_{22} = 1$. Since $\overset{j}{Y}_{12} = \overset{j}{Y}_{22} = 0$ for $j = 1, 2$; the quantities $\overset{1}{B}_{22}$ and $\overset{2}{B}_{22}$ are also set to zero. According to equations (4.5.3) and (4.5.4), the matrices $\mathbf{B}_j$ are independent of the boundary conditions.

For the sake of brevity, we introduce the following notational conventions for the nonzero coefficients

$$a = \overset{1}{B}_{1i},\ b = \overset{2}{B}_{1i},\ c = \overset{3}{B}_{1i},\ d = \overset{3}{B}_{2i},\ e = \overset{4}{B}_{1i},\ f = \overset{4}{B}_{2i}\ , \qquad i = 1, 2. \tag{4.5.5}$$

If $i = 1$ we have the system

$$\begin{bmatrix} \cos\psi & -\sin\psi & \cos\chi\psi & \mathcal{M}\psi & -\sin\chi\psi & 1 \\ \sin\psi & \cos\psi & \chi\sin\chi\psi & -1 & \chi\cos\chi\psi & 0 \\ -\sin\psi & -\cos\psi & -\chi\sin\chi\psi & \mathcal{M} & -\chi\cos\chi\psi & 0 \\ \cos\psi & -\sin\psi & \chi^2\cos\chi\psi & 0 & -\chi^2\sin\chi\psi & 0 \\ -\sin\psi & -\cos\psi & -\chi^3\sin\chi\psi & 0 & -\chi^3\cos\chi\psi & 0 \\ -\cos\psi & \sin\psi & -\chi^4\cos\chi\psi & 0 & \chi^4\sin\chi\psi & 0 \end{bmatrix} \begin{bmatrix} a \\ b \\ c \\ d \\ e \\ f \end{bmatrix} = \begin{bmatrix} 0 \\ 0 \\ \frac{1}{2m} \\ 0 \\ 0 \\ 0 \end{bmatrix} . \tag{4.5.6}$$

The solutions are

$$a = \overset{1}{B}_{11} = \frac{\chi^2 \sin\psi}{2\left(1-\chi^2\right)\left(1-\mathcal{M}\right)m}\ , \qquad b = \overset{2}{B}_{11} = \frac{\chi^2\cos\psi}{2\left(1-\chi^2\right)\left(1-\mathcal{M}\right)m}\ , \tag{4.5.7a}$$

$$c = \overset{3}{B}_{11} = -\frac{\sin\chi\psi}{2\chi\left(1-\chi^2\right)\left(1-\mathcal{M}\right)m}\ , \qquad d = \overset{3}{B}_{21} = -\frac{1}{2\left(1-\mathcal{M}\right)m}\ , \tag{4.5.7b}$$

$$e = \overset{4}{B}_{11} = -\frac{\cos\chi\psi}{2\chi\left(1-\chi^2\right)\left(1-\mathcal{M}\right)m}\ , \qquad f = \overset{4}{B}_{21} = \frac{\mathcal{M}\psi}{2m\left(1-\mathcal{M}\right)}\ . \tag{4.5.7c}$$

If $i = 2$, then

$$\begin{bmatrix} \cos\psi & -\sin\psi & \cos\chi\psi & \mathcal{M}\psi & -\sin\chi\psi & 1 \\ \sin\psi & \cos\psi & \chi\sin\chi\psi & -1 & \chi\cos\chi\psi & 0 \\ -\sin\psi & -\cos\psi & -\chi\sin\chi\psi & \mathcal{M} & -\chi\cos\chi\psi & 0 \\ \cos\psi & -\sin\psi & \chi^2\cos\chi\psi & 0 & -\chi^2\sin\chi\psi & 0 \\ -\sin\psi & -\cos\psi & -\chi^3\sin\chi\psi & 0 & -\chi^3\cos\chi\psi & 0 \\ -\cos\psi & \sin\psi & -\chi^4\cos\chi\psi & 0 & \chi^4\sin\chi\psi & 0 \end{bmatrix} \begin{bmatrix} a \\ b \\ c \\ d \\ e \\ f \end{bmatrix} = \begin{bmatrix} 0 \\ 0 \\ 0 \\ 0 \\ 0 \\ -\frac{1}{2} \end{bmatrix} \tag{4.5.8}$$

is the equation system for the unknowns and the solutions assume the forms

$$a = \overset{1}{B}_{12} = \frac{\cos\psi}{2\left(1-\chi^2\right)}\ , \qquad b = \overset{2}{B}_{12} = -\frac{\sin\psi}{2\left(1-\chi^2\right)}\ , \qquad c = \overset{3}{B}_{12} = -\frac{\cos\chi\psi}{2\left(1-\chi^2\right)\chi^2}\ ,$$

$$d = \overset{3}{B}_{22} = 0\ , \qquad e = \overset{4}{B}_{12} = \frac{\sin\chi\psi}{2\left(1-\chi^2\right)\chi^2}\ , \qquad f = \overset{4}{B}_{22} = \frac{1}{2\chi^2}\ . \tag{4.5.9}$$

DOI: 10.14750/ME.2016.008

4.5.2.1. *Constants for pinned-pinned supports.* We now move on to the matrices $\mathbf{A}_j$ which can be determined if we recall the fourth property of the Green function matrix. First, let $\boldsymbol{\alpha}^T = [1\,|\,0]$ and thus, set $\overset{1}{A}_{21}; \overset{2}{A}_{21}$ to zero. The latter choice is because of the structure of $\mathbf{Y}_1$ and $\mathbf{Y}_2$. The boundary conditions (4.3.2) yield the following equation system:

$$\begin{bmatrix} \sum_{j=1}^4 \mathbf{Y}_{j1}|_{\varphi=-\vartheta} & \mathbf{A}_{j1}|_{\psi} \\ \sum_{j=1}^4 \mathbf{Y}_{j1}|_{\varphi=\vartheta} & \mathbf{A}_{j1}|_{\psi} \\ \sum_{j=1}^4 \mathbf{Y}_{j2}|_{\varphi=-\vartheta} & \mathbf{A}_{j1}|_{\psi} \\ \sum_{j=1}^4 \mathbf{Y}_{j2}|_{\varphi=\vartheta} & \mathbf{A}_{j1}|_{\psi} \\ \sum_{j=1}^4 \mathbf{Y}^{(2)}_{j2}\Big|_{\varphi=-\vartheta} & \mathbf{A}_{j1}|_{\psi} \\ \sum_{j=1}^4 \mathbf{Y}^{(2)}_{j2}\Big|_{\varphi=\vartheta} & \mathbf{A}_{j1}|_{\psi} \end{bmatrix} = \begin{bmatrix} -\sum_{j=1}^4 \mathbf{Y}_{j1}|_{\varphi=-\vartheta} & \mathbf{B}_{j1}|_{\psi} \\ \sum_{j=1}^4 \mathbf{Y}_{j1}|_{\varphi=\vartheta} & \mathbf{B}_{j1}|_{\psi} \\ -\sum_{j=1}^4 \mathbf{Y}_{j2}|_{\varphi=-\vartheta} & \mathbf{B}_{j1}|_{\psi} \\ \sum_{j=1}^4 \mathbf{Y}_{j2}|_{\varphi=\vartheta} & \mathbf{B}_{j1}|_{\psi} \\ -\sum_{j=1}^4 \mathbf{Y}^{(2)}_{j2}\Big|_{\varphi=-\vartheta} & \mathbf{B}_{j1}|_{\psi} \\ \sum_{j=1}^4 \mathbf{Y}^{(2)}_{j2}\Big|_{\varphi=\vartheta} & \mathbf{B}_{j1}|_{\psi} \end{bmatrix} . \tag{4.5.10}$$

Second, let $\boldsymbol{\alpha}^T = [0\,|\,1]$ and set $\overset{1}{A}_{22}; \overset{2}{A}_{22}$ to zero for similar reasons as before. Then the boundary conditions determine that the system to be dealt with is

$$\begin{bmatrix} \sum_{j=1}^4 \mathbf{Y}_{j1}|_{\varphi=-\vartheta} & \mathbf{A}_{j2}|_{\psi} \\ \sum_{j=1}^4 \mathbf{Y}_{j1}|_{\varphi=\vartheta} & \mathbf{A}_{j2}|_{\psi} \\ \sum_{j=1}^4 \mathbf{Y}_{j2}|_{\varphi=-\vartheta} & \mathbf{A}_{j2}|_{\psi} \\ \sum_{j=1}^4 \mathbf{Y}_{j2}|_{\varphi=\vartheta} & \mathbf{A}_{j2}|_{\psi} \\ \sum_{j=1}^4 \mathbf{Y}^{(2)}_{j2}\Big|_{\varphi=-\vartheta} & \mathbf{A}_{j2}|_{\psi} \\ \sum_{j=1}^4 \mathbf{Y}^{(2)}_{j2}\Big|_{\varphi=\vartheta} & \mathbf{A}_{j2}|_{\psi} \end{bmatrix} = \begin{bmatrix} -\sum_{j=1}^4 \mathbf{Y}_{j1}|_{\varphi=-\vartheta} & \mathbf{B}_{j2}|_{\psi} \\ \sum_{j=1}^4 \mathbf{Y}_{j1}|_{\varphi=\vartheta} & \mathbf{B}_{j2}|_{\psi} \\ -\sum_{j=1}^4 \mathbf{Y}_{j2}|_{\varphi=-\vartheta} & \mathbf{B}_{j2}|_{\psi} \\ \sum_{j=1}^4 \mathbf{Y}_{j2}|_{\varphi=\vartheta} & \mathbf{B}_{j2}|_{\psi} \\ -\sum_{j=1}^4 \mathbf{Y}^{(2)}_{j2}\Big|_{\varphi=-\vartheta} & \mathbf{B}_{j2}|_{\psi} \\ \sum_{j=1}^4 \mathbf{Y}^{(2)}_{j2}\Big|_{\varphi=\vartheta} & \mathbf{B}_{j2}|_{\psi} \end{bmatrix} . \tag{4.5.11}$$

Consequently, the unknown nonzero matrix elements are

$$\overset{1}{A}_{1i}(\psi),\ \overset{2}{A}_{1i}(\psi),\ \overset{3}{A}_{1i}(\psi),\ \overset{3}{A}_{2i}(\psi),\ \overset{4}{A}_{1i}(\psi),\ \overset{4}{A}_{2i}(\psi) \qquad i=1,2; \qquad \psi \in [-\vartheta, \vartheta]\,.$$

This time both systems can be expressed simultaneously (with the zero columns removed) as

$$\begin{bmatrix} \cos\vartheta & \sin\vartheta & \cos\chi\vartheta & -\mathcal{M}\vartheta & \sin\chi\vartheta & 1 \\ \cos\vartheta & -\sin\vartheta & \cos\chi\vartheta & \mathcal{M}\vartheta & -\sin\chi\vartheta & 1 \\ -\sin\vartheta & \cos\vartheta & -\chi\sin\chi\vartheta & -1 & \chi\cos\chi\vartheta & 0 \\ \sin\vartheta & \cos\vartheta & \chi\sin\chi\vartheta & -1 & \chi\cos\chi\vartheta & 0 \\ \sin\vartheta & -\cos\vartheta & \chi^3\sin\chi\vartheta & 0 & -\chi^3\cos\chi\vartheta & 0 \\ -\sin\vartheta & -\cos\vartheta & -\chi^3\sin\chi\vartheta & 0 & -\chi^3\cos\chi\vartheta & 0 \end{bmatrix} \begin{bmatrix} \overset{1}{A}_{1i} \\ \overset{2}{A}_{1i} \\ \overset{3}{A}_{1i} \\ \overset{3}{A}_{2i} \\ \overset{4}{A}_{1i} \\ \overset{4}{A}_{2i} \end{bmatrix} =$$

$$= \begin{bmatrix} -a\cos\vartheta - b\sin\vartheta - c\cos\chi\vartheta + d\mathcal{M}\vartheta - e\sin\chi\vartheta - f \\ a\cos\vartheta - b\sin\vartheta + c\cos\chi\vartheta + d\mathcal{M}\vartheta - e\sin\chi\vartheta + f \\ a\sin\vartheta - b\cos\vartheta + c\chi\sin\chi\vartheta + d - e\chi\cos\chi\vartheta \\ a\sin\vartheta + b\cos\vartheta + c\chi\sin\chi\vartheta - d + e\chi\cos\chi\vartheta \\ -a\sin\vartheta + b\cos\vartheta - c\chi^3\sin\chi\vartheta + e\chi^3\cos\chi\vartheta \\ -a\sin\vartheta - b\cos\vartheta - c\chi^3\sin\chi\vartheta - e\chi^3\cos\chi\vartheta \end{bmatrix} . \tag{4.5.12}$$

With the constants

$$\begin{gathered} \mathcal{C}_{11} = \left(1-\chi^2\right)\sin\vartheta, \qquad \mathcal{C}_{12} = \chi\left(1-\chi^2\right)\sin\chi\vartheta\,, \\ \mathcal{D}_{11} = \cos\vartheta\sin\chi\vartheta - \chi^3\sin\vartheta\cos\chi\vartheta - \mathcal{M}\chi\vartheta\left(1-\chi^2\right)\cos\vartheta\cos\chi\vartheta \end{gathered} \tag{4.5.13}$$

DOI: 10.14750/ME.2016.008

the solutions are gathered hereinafter:

$$\overset{1}{A}_{1i} = \frac{1}{\mathcal{C}_{11}}\left[b\left(1-\chi^2\right)\cos\vartheta + d\chi^2\right] ,$$

$$\overset{2}{A}_{1i} = \frac{a\chi^3\cos\vartheta\cos\chi\vartheta - a\chi\vartheta\left(1-\chi^2\right)\mathcal{M}\sin\vartheta\cos\chi\vartheta + a\sin\vartheta\sin\chi\vartheta + c\chi^3 + \chi^3 f\cos\chi\vartheta}{\mathcal{D}_{11}} ,$$

$$\overset{3}{A}_{1i} = -\frac{1}{\mathcal{C}_{12}}\left(d - e\chi\left(1-\chi^2\right)\cos\chi\vartheta\right) ,$$

$$\overset{3}{A}_{2i} = -\frac{1}{\mathcal{D}_{11}}\left(1-\chi^2\right)\chi\left(a\cos\chi\vartheta + c\cos\vartheta + f\cos\vartheta\cos\chi\vartheta\right) ,$$

$$\overset{4}{A}_{1i} = -\frac{1}{\mathcal{D}_{11}}\left(a + c\left(1-\chi^2\right)\mathcal{M}\chi\vartheta\cos\vartheta\sin\chi\vartheta + c\left(\chi^3\sin\vartheta\sin\chi\vartheta + \cos\vartheta\cos\chi\vartheta\right) + f\cos\vartheta\right) ,$$

$$\overset{4}{A}_{2i} = -\frac{1}{\mathcal{C}_{12}\sin\vartheta}\left(b\chi\left(1-\chi^2\right)\sin\chi\vartheta - d\mathcal{M}\vartheta\chi\left(1-\chi^2\right)\sin\vartheta\sin\chi\vartheta + d\chi^3\cos\vartheta\sin\chi\vartheta - \right.$$
$$\left. - d\sin\vartheta\cos\chi\vartheta + e\chi\sin\vartheta - e\chi^3\sin\vartheta\right) . \quad (4.5.14)$$

4.5.2.2. *Constants for fixed-fixed supports.* Only the last two equations need be changed in (4.5.10) and (4.5.11) because of the different boundary conditions (4.3.3). These rows in question are now

$$\sum_{j=1}^{4}\mathbf{Y}_{j2}^{(1)}\Big|_{\varphi=-\vartheta}\mathbf{A}_{j1}\big|_{\psi} = -\sum_{j=1}^{4}\mathbf{Y}_{j2}^{(1)}\Big|_{\varphi=-\vartheta}\mathbf{B}_{j1}\big|_{\psi} , \quad (4.5.15a)$$

$$\sum_{j=1}^{4}\mathbf{Y}_{j2}^{(1)}\Big|_{\varphi=\vartheta}\mathbf{A}_{j1}\big|_{\psi} = \sum_{j=1}^{4}\mathbf{Y}_{j2}^{(1)}\Big|_{\varphi=\vartheta}\mathbf{B}_{j1}\big|_{\psi} \quad (4.5.15b)$$

and

$$\sum_{j=1}^{4}\mathbf{Y}_{j2}{}^{(1)}\Big|_{\varphi=-\vartheta}\mathbf{A}_{j2}\big|_{\psi} = -\sum_{j=1}^{4}\mathbf{Y}_{j2}{}^{(1)}\Big|_{\varphi=-\vartheta}\mathbf{B}_{j2}\big|_{\psi} , \quad (4.5.16a)$$

$$\sum_{j=1}^{4}\mathbf{Y}_{j2}{}^{(1)}\Big|_{\varphi=\vartheta}\mathbf{A}_{j2}\big|_{\psi} = \sum_{j=1}^{4}\mathbf{Y}_{j2}{}^{(1)}\Big|_{\varphi=\vartheta}\mathbf{B}_{j2}\big|_{\psi} . \quad (4.5.16b)$$

As a result, we obtain the following system:

$$\begin{bmatrix} \cos\vartheta & \sin\vartheta & \cos\chi\vartheta & -\mathcal{M}\vartheta & \sin\chi\vartheta & 1 \\ \cos\vartheta & -\sin\vartheta & \cos\chi\vartheta & \mathcal{M}\vartheta & -\sin\chi\vartheta & 1 \\ -\sin\vartheta & \cos\vartheta & -\chi\sin\chi\vartheta & -1 & \chi\cos\chi\vartheta & 0 \\ \sin\vartheta & \cos\vartheta & \chi\sin\chi\vartheta & -1 & \chi\cos\chi\vartheta & 0 \\ \cos\vartheta & \sin\vartheta & \chi^2\cos\chi\vartheta & 0 & \chi^2\sin\chi\vartheta & 0 \\ \cos\vartheta & -\sin\vartheta & \chi^2\cos\chi\vartheta & 0 & -\chi^2\sin\chi\vartheta & 0 \end{bmatrix} \begin{bmatrix} \overset{1}{A}_{1i} \\ \overset{2}{A}_{1i} \\ \overset{3}{A}_{1i} \\ \overset{3}{A}_{2i} \\ \overset{4}{A}_{1i} \\ \overset{4}{A}_{2i} \end{bmatrix} =$$

$$= \begin{bmatrix} -a\cos\vartheta - b\sin\vartheta - c\cos\chi\vartheta + d\mathcal{M}\vartheta - e\sin\chi\vartheta - f \\ a\cos\vartheta - b\sin\vartheta + c\cos\chi\vartheta + d\mathcal{M}\vartheta - e\sin\chi\vartheta + f \\ a\sin\vartheta - b\cos\vartheta + c\chi\sin\chi\vartheta + d - e\chi\cos\chi\vartheta \\ a\sin\vartheta + b\cos\vartheta + c\chi\sin\chi\vartheta - d + e\chi\cos\chi\vartheta \\ -a\cos\vartheta - b\sin\vartheta - c\chi^2\cos\chi\vartheta - e\chi^2\sin\chi\vartheta \\ a\cos\vartheta - b\sin\vartheta + c\chi^2\cos\chi\vartheta - e\chi^2\sin\chi\vartheta \end{bmatrix} . \quad (4.5.17)$$

DOI: 10.14750/ME.2016.008

Let us introduce the constants

$$\begin{gathered}\mathcal{C}_{31}=\left(1-\chi^2\right)\sin\vartheta\sin\chi\vartheta+\mathcal{M}\chi\vartheta\left(\chi\cos\vartheta\sin\chi\vartheta-\sin\vartheta\cos\chi\vartheta\right)\ ,\\ \mathcal{D}_{31}=\chi\sin\vartheta\cos\chi\vartheta-\cos\vartheta\sin\chi\vartheta\end{gathered}\tag{4.5.18}$$

with which we can simplify the solutions to (4.5.17) into these forms:

$$\begin{gathered}\overset{1}{A}_{1i}=\frac{1}{\mathcal{D}_{31}}\left[b\left(\sin\vartheta\sin\chi\vartheta+\chi\cos\vartheta\cos\chi\vartheta\right)-d\chi\cos\chi\vartheta+e\chi^2\right]\ ,\\ \overset{2}{A}_{1i}=\frac{a\mathcal{M}\chi\vartheta\left(\chi\sin\vartheta\sin\chi\vartheta+\cos\vartheta\cos\chi\vartheta\right)+\left[f\chi^2-a\left(1-\chi^2\right)\cos\vartheta\right]\sin\chi\vartheta+c\mathcal{M}\chi\vartheta\chi^2}{\mathcal{C}_{31}},\\ \overset{3}{A}_{1i}=-\frac{1}{\mathcal{D}_{31}\chi}\left[b+e\chi\left(\chi\sin\vartheta\sin\chi\vartheta+\cos\vartheta\cos\chi\vartheta\right)-d\cos\vartheta\right]\ ,\\ \overset{3}{A}_{2i}=-\frac{1}{\mathcal{C}_{31}}\left[a\left(1-\chi^2\right)\sin\chi\vartheta+c\chi\left(1-\chi^2\right)\sin\vartheta-f\chi\left(\chi\cos\vartheta\sin\chi\vartheta-\sin\vartheta\cos\chi\vartheta\right)\right]\ ,\\ \overset{4}{A}_{1i}=\frac{-1}{\mathcal{C}_{31}}\left[a\mathcal{M}\vartheta+c\mathcal{M}\chi\vartheta\left(\chi\cos\vartheta\cos\chi\vartheta+\sin\vartheta\sin\chi\vartheta\right)+c\left(1-\chi^2\right)\sin\vartheta\cos\chi\vartheta+f\sin\vartheta\right],\\ \overset{4}{A}_{2i}=\frac{1}{\mathcal{D}_{31}\chi}\left[b\left(1-\chi^2\right)\cos\chi\vartheta+d\mathcal{M}\chi\vartheta\left(\chi\sin\vartheta\cos\chi\vartheta-\cos\vartheta\sin\chi\vartheta\right)-\right.\\ \left.-d\left(1-\chi^2\right)\cos\vartheta\cos\chi\vartheta+e\chi\left(1-\chi^2\right)\cos\vartheta\right]\ .\end{gathered}\tag{4.5.19}$$

4.5.3. The Green function matrix when $m\varepsilon_{o\xi}>1$. If we repeat the line of thought leading to (4.5.6) we can easily determine the coefficients in the matrices $\mathbf{B}_j$. Obviously, we shall now use (4.3.5c) for $\mathbf{Y}_3$ and $\mathbf{Y}_4$. When $i=1$, from the system of linear equations

$$\begin{bmatrix}\cos\psi & -\sin\psi & \cosh\chi\psi & \mathcal{M}\psi & \sinh\chi\psi & 1\\ \sin\psi & \cos\psi & -\chi\sinh\chi\psi & -1 & -\chi\cosh\chi\psi & 0\\ -\sin\psi & -\cos\psi & \chi\sinh\chi\psi & \mathcal{M} & \chi\cosh\chi\psi & 0\\ \cos\psi & -\sin\psi & -\chi^2\cosh\chi\psi & 0 & -\chi^2\sinh\chi\psi & 0\\ -\sin\psi & -\cos\psi & -\chi^3\sinh\chi\psi & 0 & -\chi^3\cosh\chi\psi & 0\\ -\cos\psi & \sin\psi & -\chi^4\cosh\chi\psi & 0 & -\chi^4\sinh\chi\psi & 0\end{bmatrix}\begin{bmatrix}a\\ b\\ c\\ d\\ e\\ f\end{bmatrix}=\begin{bmatrix}0\\ 0\\ \frac{1}{2m}\\ 0\\ 0\\ 0\end{bmatrix}\tag{4.5.20}$$

we obtain the solutions

$$\begin{gathered}a=\overset{1}{B}_{11}=-\frac{\chi^2\sin\psi}{2\left(1+\chi^2\right)\left(1-\mathcal{M}\right)m}\ ,\qquad b=\overset{2}{B}_{11}=-\frac{\chi^2\cos\psi}{2\left(1+\chi^2\right)\left(1-\mathcal{M}\right)m}\ ,\\ c=\overset{3}{B}_{11}=-\frac{\sinh\chi\psi}{2\chi\left(1+\chi^2\right)\left(1-\mathcal{M}\right)m}\ ,\qquad d=\overset{3}{B}_{21}=-\frac{1}{2\left(1-\mathcal{M}\right)m}\ ,\\ e=\overset{4}{B}_{11}=\frac{\cosh\chi\psi}{2\chi\left(1+\chi^2\right)\left(1-\mathcal{M}\right)m}\ ,\qquad f=\overset{4}{B}_{21}=\frac{\mathcal{M}\psi}{2\left(1-\mathcal{M}\right)m}\ .\end{gathered}\tag{4.5.21}$$

If $i=2$

$$\begin{bmatrix}\cos\psi & -\sin\psi & \cosh\chi\psi & \mathcal{M}\psi & \sinh\chi\psi & 1\\ \sin\psi & \cos\psi & -\chi\sinh\chi\psi & -1 & -\chi\cosh\chi\psi & 0\\ -\sin\psi & -\cos\psi & \chi\sinh\chi\psi & \mathcal{M} & \chi\cosh\chi\psi & 0\\ \cos\psi & -\sin\psi & -\chi^2\cosh\chi\psi & 0 & -\chi^2\sinh\chi\psi & 0\\ -\sin\psi & -\cos\psi & -\chi^3\sinh\chi\psi & 0 & -\chi^3\cosh\chi\psi & 0\\ -\cos\psi & \sin\psi & -\chi^4\cosh\chi\psi & 0 & -\chi^4\sinh\chi\psi & 0\end{bmatrix}\begin{bmatrix}a\\ b\\ c\\ d\\ e\\ f\end{bmatrix}=\begin{bmatrix}0\\ 0\\ 0\\ 0\\ 0\\ -\frac{1}{2}\end{bmatrix}\tag{4.5.22}$$

DOI: 10.14750/ME.2016.008

is the equation system to be solved – compare it with (4.5.8) – and the solutions are

$$a=\overset{1}{B}_{12}=\frac{\cos\psi}{2\left(1+\chi^2\right)}\,,\quad b=\overset{2}{B}_{12}=-\frac{\sin\psi}{2\left(1+\chi^2\right)}\,,\qquad c=\overset{3}{B}_{12}=\frac{\cosh\chi\psi}{2\left(1+\chi^2\right)\chi^2}\,,$$
$$d=\overset{3}{B}_{22}=0\,,\qquad e=\overset{4}{B}_{12}=-\frac{\sinh\chi\psi}{2\chi^2\left(1+\chi^2\right)}\,,\qquad f=\overset{4}{B}_{22}=-\frac{1}{2\chi^2}\,. \tag{4.5.23}$$

4.5.3.1. *Constants for pinned-pinned supports.* Similarly as in Subsubsection 4.5.2.1 the boundary conditions (4.1.30a) are used to determine the constants in $\mathbf{A}_j$. With these in hand we arrive at the equation system

$$\begin{bmatrix} \cos\vartheta & \sin\vartheta & \cosh\chi\vartheta & -\mathcal{M}\vartheta & -\sinh\chi\vartheta & 1\\ \cos\vartheta & -\sin\vartheta & \cosh\chi\vartheta & \mathcal{M}\vartheta & \sinh\chi\vartheta & 1\\ -\sin\vartheta & \cos\vartheta & \chi\sinh\chi\vartheta & -1 & -\chi\cosh\chi\vartheta & 0\\ \sin\vartheta & \cos\vartheta & -\chi\sinh\chi\vartheta & -1 & -\chi\cosh\chi\vartheta & 0\\ \sin\vartheta & -\cos\vartheta & \chi^3\sinh\chi\vartheta & 0 & -\chi^3\cosh\chi\vartheta & 0\\ -\sin\vartheta & -\cos\vartheta & -\chi^3\sinh\chi\vartheta & 0 & -\chi^3\cosh\chi\vartheta & 0 \end{bmatrix} \begin{bmatrix} \overset{1}{A}_{1i}\\ \overset{2}{A}_{1i}\\ \overset{3}{A}_{1i}\\ \overset{3}{A}_{2i}\\ \overset{4}{A}_{1i}\\ \overset{4}{A}_{2i} \end{bmatrix} =$$
$$= \begin{bmatrix} -a\cos\vartheta-b\sin\vartheta-c\cosh\chi\vartheta+d\mathcal{M}\vartheta+e\sinh\chi\vartheta-f\\ a\cos\vartheta-b\sin\vartheta+c\cosh\chi\vartheta+d\mathcal{M}\vartheta+e\sinh\chi\vartheta+f\\ a\sin\vartheta-b\cos\vartheta-c\chi\sinh\chi\vartheta+d+e\chi\cosh\chi\vartheta\\ a\sin\vartheta+b\cos\vartheta-c\chi\sinh\chi\vartheta-d-e\chi\cosh\chi\vartheta\\ -a\sin\vartheta+b\cos\vartheta-c\chi^3\sinh\chi\vartheta+e\chi^3\cosh\chi\vartheta\\ -a\sin\vartheta-b\cos\vartheta-c\chi^3\sinh\chi\vartheta-e\chi^3\cosh\chi\vartheta \end{bmatrix}\,. \tag{4.5.24}$$

Making use of the notations

$$\mathcal{C}_{21}=\left(1+\chi^2\right)\sin\vartheta,\quad \mathcal{C}_{22}=\chi\left(1+\chi^2\right)\sinh\chi\vartheta\,,$$
$$\mathcal{D}_{22}=-\cos\vartheta\sinh\chi\vartheta-\chi^3\sin\vartheta\cosh\chi\vartheta+\mathcal{M}\vartheta\chi\left(1+\chi^2\right)\cos\vartheta\cosh\chi\vartheta \tag{4.5.25}$$

the solutions for $\overset{1}{A}_{1i},\ldots,\overset{4}{A}_{2i}$ are

$$\overset{1}{A}_{1i}=\frac{1}{\mathcal{C}_{21}}\left[b\left(1+\chi^2\right)\cos\vartheta-d\chi^2\right],$$
$$\overset{2}{A}_{1i}=\frac{\left(a\chi^3\cos\vartheta+a\vartheta\chi\left(1+\chi^2\right)\mathcal{M}\sin\vartheta+f\chi^3\right)\cosh\chi\vartheta-a\sin\vartheta\sinh\chi\vartheta+c\chi^3}{\mathcal{D}_{22}},$$
$$\overset{3}{A}_{1i}=\frac{1}{\mathcal{C}_{22}}\left(d+e\chi\left(1+\chi^2\right)\cosh\chi\vartheta\right)\,,$$
$$\overset{3}{A}_{2i}=\frac{\chi}{\mathcal{D}_{22}}\left(1+\chi^2\right)\left(a\cosh\chi\vartheta+c\cos\vartheta+f\cos\vartheta\cosh\chi\vartheta\right)\,,$$
$$\overset{4}{A}_{1i}=-\frac{a-c\left(1+\chi^2\right)\mathcal{M}\chi\vartheta\cos\vartheta\sinh\chi\vartheta+c\left(\chi^3\sin\vartheta\sinh\chi\vartheta+\cos\vartheta\cosh\chi\vartheta\right)+f\cos\vartheta}{\mathcal{D}_{22}}\,,$$
$$\overset{4}{A}_{2i}=-\frac{1}{\mathcal{C}_{22}\sin\vartheta}\left(b\chi\left(1+\chi^2\right)\sinh\chi\vartheta-d\mathcal{M}\vartheta\chi\left(1+\chi^2\right)\sin\vartheta\sinh\chi\vartheta-d\chi^3\cos\vartheta\sinh\chi\vartheta+\right.$$
$$\left.+d\sin\vartheta\cosh\chi\vartheta+e\chi\left(1+\chi^2\right)\sin\vartheta\right)\,. \tag{4.5.26}$$

DOI: 10.14750/ME.2016.008

4.5.3.2. *Constants for fixed-fixed supports.* For the matrices $\mathbf{A}_j$, the boundary conditions (4.1.30b) yield the equation system upon repeating the steps leading to (4.5.17). Consequently

$$\begin{bmatrix} \cos\vartheta & \sin\vartheta & \cosh\chi\vartheta & -\mathcal{M}\vartheta & -\sinh\chi\vartheta & 1 \\ \cos\vartheta & -\sin\vartheta & \cosh\chi\vartheta & \mathcal{M}\vartheta & \sinh\chi\vartheta & 1 \\ -\sin\vartheta & \cos\vartheta & \chi\sinh\chi\vartheta & -1 & -\chi\cosh\chi\vartheta & 0 \\ \sin\vartheta & \cos\vartheta & -\chi\sinh\chi\vartheta & -1 & -\chi\cosh\chi\vartheta & 0 \\ \cos\vartheta & \sin\vartheta & -\chi^2\cosh\chi\vartheta & 0 & \chi^2\sinh\chi\vartheta & 0 \\ \cos\vartheta & -\sin\vartheta & -\chi^2\cosh\chi\vartheta & 0 & -\chi^2\sinh\chi\vartheta & 0 \end{bmatrix} \begin{bmatrix} \overset{1}{A}_{1i} \\ \overset{2}{A}_{1i} \\ \overset{3}{A}_{1i} \\ \overset{3}{A}_{2i} \\ \overset{4}{A}_{1i} \\ \overset{4}{A}_{2i} \end{bmatrix} =$$

$$= \begin{bmatrix} -a\cos\vartheta - b\sin\vartheta - c\cosh\chi\vartheta + d\mathcal{M}\vartheta + e\sinh\chi\vartheta - f \\ a\cos\vartheta - b\sin\vartheta + c\cosh\chi\vartheta + d\mathcal{M}\vartheta + e\sinh\chi\vartheta + f \\ a\sin\vartheta - b\cos\vartheta - c\chi\sinh\chi\vartheta + d + e\chi\cosh\chi\vartheta \\ a\sin\vartheta + b\cos\vartheta - c\chi\sinh\chi\vartheta - d - e\chi\cosh\chi\vartheta \\ -a\cos\vartheta - b\sin\vartheta + c\chi^2\cosh\chi\vartheta - e\chi^2\sinh\chi\vartheta \\ a\cos\vartheta - b\sin\vartheta - c\chi^2\cosh\chi\vartheta - e\chi^2\sinh\chi\vartheta \end{bmatrix}, \quad (4.5.27)$$

from where with the constants

$$\begin{aligned} \mathcal{C}_{41} &= -\left(1+\chi^2\right)\sin\vartheta\sinh\chi\vartheta + \chi\mathcal{M}\vartheta\left(\chi\cos\vartheta\sinh\chi\vartheta + \sin\vartheta\cosh\chi\vartheta\right) ; \\ \mathcal{D}_{41} &= \chi\sin\vartheta\cosh\chi\vartheta - \cos\vartheta\sinh\chi\vartheta \end{aligned} \quad (4.5.28)$$

the closed form solutions are

$$\begin{aligned} \overset{1}{A}_{1i} &= \frac{1}{\mathcal{D}_{41}}\left(b\left(\sin\vartheta\sinh\chi\vartheta + \chi\cos\vartheta\cosh\chi\vartheta\right) - d\chi\cosh\chi\vartheta - \chi^2 e\right) , \\ \overset{2}{A}_{1i} &= \frac{a\mathcal{M}\vartheta\chi\left(\chi\sin\vartheta\sinh\chi\vartheta - \cos\vartheta\cosh\chi\vartheta\right) + \left[a\left(1+\chi^2\right)\cos\vartheta + f\chi^2\right]\sinh\chi\vartheta + c\mathcal{M}\vartheta\chi^3}{\mathcal{C}_{41}}, \\ \overset{3}{A}_{1i} &= \frac{1}{\mathcal{D}_{41}\chi}\left[b + e\chi\left(\chi\sin\vartheta\sinh\chi\vartheta - \cos\vartheta\cosh\chi\vartheta\right) - d\cos\vartheta\right] , \\ \overset{3}{A}_{2i} &= \frac{1}{\mathcal{C}_{41}}\left[a\left(1+\chi^2\right)\sinh\chi\vartheta + c\chi\left(1+\chi^2\right)\sin\vartheta + f\chi\left(\chi\cos\vartheta\sinh\chi\vartheta + \sin\vartheta\cosh\chi\vartheta\right)\right] , \\ \overset{4}{A}_{1i} &= -\frac{a\mathcal{M}\vartheta - c\mathcal{M}\vartheta\chi\left(\chi\cos\vartheta\cosh\chi\vartheta + \sin\vartheta\sinh\chi\vartheta\right) + \left[c\left(1+\chi^2\right)\cosh\chi\vartheta + f\right]\sin\vartheta}{\mathcal{C}_{41}}; \\ \overset{4}{A}_{2i} &= \frac{1}{\mathcal{D}_{41}\chi}\left(-b\left(1+\chi^2\right)\cosh\chi\vartheta + d\mathcal{M}\chi\vartheta\left(\chi\sin\vartheta\cosh\chi\vartheta - \cos\vartheta\sinh\chi\vartheta\right) + \right. \\ &\quad \left. + d\left(1+\chi^2\right)\cos\vartheta\cosh\chi\vartheta + e\chi\left(1+\chi^2\right)\cos\vartheta\right) . \end{aligned} \quad (4.5.29)$$

4.6. The load-strain relationships

It is vital to be aware of how the loading affects the strain on the centerline. In practise, the loading is the known quantity. However, our formulation involves the axial strain $\varepsilon_{o\xi}$ as parameter. Because the model is linear, the effects the deformations have on the equilibrium state can be neglected with a good accuracy [**41**]. We can establish the desired $\varepsilon_{o\xi} = \varepsilon_{o\xi}\left(\hat{\mathcal{P}}\right)$ relationship on the basis of the system (4.1.9) given that we set $f_n = f_t = \varepsilon_{o\xi} = 0$ in the equation cited. Solution for the dimensionless displacements are sought separately on the left and right half beam due to the discontinuity in the shear force as

$$U_o\left(\varphi = -\vartheta ... 0\right) = O_1\cos\varphi - O_2\sin\varphi + O_3\left(\varphi\cos\varphi - \sin\varphi\right) + O_4\left(m+1\right)\varphi +$$

DOI: 10.14750/ME.2016.008

$$+ O_5\left(-\cos\varphi - \varphi\sin\varphi\right) + O_6\ ,$$

$$W_o\left(\varphi = -\vartheta ... 0\right) = O_1\sin\varphi + O_2\cos\varphi + O_3\varphi\sin\varphi - O_4 m + O_5\varphi\cos\varphi\ ,$$

$$U_o\left(\varphi = 0 ... \vartheta\right) = R_1\cos\varphi - R_2\sin\varphi + R_3\left(\varphi\cos\varphi - \sin\varphi\right) + R_4\left(m+1\right)\varphi + \\ + R_5\left(-\cos\varphi - \varphi\sin\varphi\right) + R_6\ ,$$

$$W_o\left(\varphi = 0 ... \vartheta\right) = R_1\sin\varphi + R_2\cos\varphi + R_3\varphi\sin\varphi - R_4 m + R_5\varphi\cos\varphi\ , \quad O_i;\ R_i \in \mathbb{R}. \tag{4.6.1}$$

Therefore, the strain is

$$\varepsilon_{o\xi} = U_o^{(1)} + W_o = O_4 = R_4\ . \tag{4.6.2}$$

4.6.1. Pinned-pinned beams. The related differential equations (4.1.9) are associated with the boundary conditions

$$U_o|_{\pm\vartheta} = W_o|_{\pm\vartheta} = M|_{\pm\vartheta} = 0 \tag{4.6.3a}$$

and the continuity (discontinuity) conditions

$$U_o|_{\varphi=-0} = U_o|_{\varphi=+0}\ , \qquad W_o|_{\varphi=-0} = W_o|_{\varphi=+0}\ , \qquad \psi_{o\eta}|_{\varphi=-0} = \psi_{o\eta}|_{\varphi=+0}\ ,$$
$$N|_{\varphi=-0} = N|_{\varphi=+0}\ , \qquad M|_{\varphi=-0} = M|_{\varphi=+0}\ , \qquad \left.\frac{\mathrm{d}M}{\mathrm{d}s}\right|_{\varphi=+0} - \left.\frac{\mathrm{d}M}{\mathrm{d}s}\right|_{\varphi=-0} - P_\zeta = 0 \tag{4.6.3b}$$

prescribed at the crown point. Here, all physical quantities are known in terms of the displacements – see (4.1.1)-(4.1.2b). The altogether twelve conditions are detailed and the equation system is constructed in Appendix A.2.3. Based on these results, the load-strain relationship is

$$\varepsilon_{o\xi} = \frac{\hat{\mathcal{P}}}{\vartheta}\frac{\vartheta\sin^3\vartheta - 2\cos\vartheta\sin^2\vartheta + \vartheta\sin\vartheta\cos^2\vartheta + 2\cos^2\vartheta - 2\cos^3\vartheta}{m\left(\vartheta\sin^2\vartheta - 3\sin\vartheta\cos\vartheta + 3\vartheta\cos^2\vartheta\right) + 2\vartheta\cos^2\vartheta}\ . \tag{4.6.4}$$

The strain $\varepsilon_{o\xi}$ is [negative] (positive) if the dimensionless force

$$\hat{\mathcal{P}} = \frac{P_\zeta \rho_o^2 \vartheta}{2 I_{e\eta}} \tag{4.6.5}$$

is [negative] (positive).

4.6.2. Fixed-fixed beams. Following a similar line of thought as in the previous subsection, for fixed-fixed beams, the load-strain relationship is

$$\varepsilon_{o\xi} = -\frac{\hat{\mathcal{P}}}{\vartheta}\frac{\left(1-\cos\vartheta\right)\left(\sin\vartheta - \vartheta\right)}{\vartheta\left(1+m\right)\left[\vartheta + \sin\vartheta\cos\vartheta\right] - 2m\sin^2\vartheta}\ . \tag{4.6.6}$$

For the details see Appendix A.2.3.

4.7. The critical strain

The critical strain is also important to be aware of. At this value the beam under compression loses its stability. It can be obtained for a given support arrangement if we solve the eigenvalue problem defined by equations (4.1.24) with the right side set to zero (the heterogeneous beam is in static equilibrium under the action of the force exerted at the crown point – there is no load increment). The eigenvalue is $\chi^2 = 1 - m\varepsilon_{o\xi}$ because buckling can only occur when $\varepsilon_{o\xi} < 0$. The solutions happen to be the same as (4.2.15), (4.2.16) except for the hat symbols, that is

$$W_{ob} = -J_2 - J_3\cos\varphi + J_4\sin\varphi - \chi J_5\cos\chi\varphi + \chi J_6\sin\chi\varphi\ ; \tag{4.7.1}$$

$$U_{ob} = \mathcal{M} J_2\varphi + J_1 + J_3\sin\varphi + J_4\cos\varphi + J_5\sin\chi\varphi + J_6\cos\chi\varphi\ . \tag{4.7.2}$$

DOI: 10.14750/ME.2016.008

4.7.1. Pinned-pinned beams. To obtain the critical strain we shall use the solutions (4.7.1)-(4.7.2), which should be substituted into the boundary conditions

$$U_{ob}|_{\pm\vartheta} = W_{ob}|_{\pm\vartheta} = W_{ob}^{(2)}\Big|_{\pm\vartheta} = 0\,. \tag{4.7.3}$$

In this way we get the following homogeneous system of linear equations:

$$\begin{bmatrix} 1 & -\mathcal{M}\vartheta & -\sin\vartheta & \cos\vartheta & -\sin\chi\vartheta & \cos\chi\vartheta \\ 1 & \mathcal{M}\vartheta & \sin\vartheta & \cos\vartheta & \sin\chi\vartheta & \cos\chi\vartheta \\ 0 & 1 & \cos\vartheta & \sin\vartheta & \chi\cos\chi\vartheta & \chi\sin\chi\vartheta \\ 0 & 1 & \cos\vartheta & -\sin\vartheta & \chi\cos\chi\vartheta & -\chi\sin\chi\vartheta \\ 0 & 0 & \cos\vartheta & \sin\vartheta & \chi^3\cos\chi\vartheta & \chi^3\sin\chi\vartheta \\ 0 & 0 & \cos\vartheta & -\sin\vartheta & \chi^3\cos\chi\vartheta & -\chi^3\sin\chi\vartheta \end{bmatrix} \begin{bmatrix} J_1 \\ J_2 \\ J_3 \\ J_4 \\ J_5 \\ J_6 \end{bmatrix} = \begin{bmatrix} 0 \\ 0 \\ 0 \\ 0 \\ 0 \\ 0 \end{bmatrix}. \tag{4.7.4}$$

The determinant $\mathfrak{D}$ of the coefficient matrix vanishes at the nontrivial solution, therefore

$$\mathfrak{D} = 0 = \chi\,(\chi-1)\,(\chi+1)\,(\sin\vartheta\sin\chi\vartheta)\cdot \\ \cdot\left(\sin\chi\vartheta\cos\vartheta - \chi^3\cos\chi\vartheta\sin\vartheta + \chi^3\mathcal{M}\vartheta\cos\chi\vartheta\cos\vartheta - \chi\mathcal{M}\vartheta\cos\chi\vartheta\cos\vartheta\right)\,. \tag{4.7.5}$$

This condition yields five possibilities:

$$\chi = 1\,, \qquad \chi = -1\,, \qquad \chi = 0\,, \qquad \sin\chi\vartheta = 0\,, \\ \sin\chi\vartheta\cos\vartheta - \chi^3\cos\chi\vartheta\sin\vartheta - \chi^3\mathcal{M}\vartheta\cos\chi\vartheta\cos\vartheta + \chi\mathcal{M}\vartheta\cos\chi\vartheta\cos\vartheta = 0\,. \tag{4.7.6}$$

Since the critical strain is a negative number, the first three roots have no physical sense. From the fourth condition it follows that

$$\chi\vartheta = \pm j\pi\,, \qquad j = 1, 2, \dots\,,$$

which means that $\chi\vartheta = \pi$ is the lowest reasonable root. The corresponding eigenfunctions satisfy the relations $W_{ob}(\varphi) = -W_{ob}(-\varphi)$; $U_{ob}(\varphi) = U_{ob}(-\varphi)$. Consequently

$$\varepsilon_{o\xi\,\mathrm{crit}} = -\frac{1}{m}\left(\chi^2 - 1\right) = -\frac{1}{m}\left[\left(\frac{\pi}{\vartheta}\right)^2 - 1\right] \tag{4.7.7}$$

is the critical strain. This result is the same as that obtained in relation with the stability problem of shallow beams – compare it with (3.4.8).

4.7.2. Fixed-fixed beams. The critical strain can be obtained similarly as for pinned-pinned beams. For fixed-fixed structural members

$$U_{ob}|_{\pm\vartheta} = W_{ob}|_{\pm\vartheta} = W_{ob}^{(1)}\Big|_{\pm\vartheta} = 0 \tag{4.7.8}$$

are the boundary conditions, which lead to the homogeneous equation system

$$\begin{bmatrix} 0 & 1 & \cos\vartheta & -\sin\vartheta & \chi\cos\chi\vartheta & -\chi\sin\chi\vartheta \\ 0 & 1 & \cos\vartheta & \sin\vartheta & \chi\cos\chi\vartheta & \chi\sin\chi\vartheta \\ 0 & 0 & \sin\vartheta & \cos\vartheta & \chi^2\sin\chi\vartheta & \chi^2\cos\chi\vartheta \\ 0 & 0 & -\sin\vartheta & \cos\vartheta & -\chi^2\sin\chi\vartheta & \chi^2\cos\chi\vartheta \\ 1 & \mathcal{M}\vartheta & \sin\vartheta & \cos\vartheta & \sin\chi\vartheta & \cos\chi\vartheta \\ 1 & -\mathcal{M}\vartheta & -\sin\vartheta & \cos\vartheta & -\sin\chi\vartheta & \cos\chi\vartheta \end{bmatrix} \begin{bmatrix} J_1 \\ J_2 \\ J_3 \\ J_4 \\ J_5 \\ J_6 \end{bmatrix} = \begin{bmatrix} 0 \\ 0 \\ 0 \\ 0 \\ 0 \\ 0 \end{bmatrix}. \tag{4.7.9}$$

Nontrivial solutions exist if the determinant $\mathfrak{D}$ of the coefficient matrix vanishes, that is, if

$$\mathfrak{D} = 0 = -8\chi\left(-\cos\vartheta\sin\chi\vartheta + \chi\sin\vartheta\cos\chi\vartheta\right)\times \\ \times\left(-\chi^2\sin\vartheta\sin\chi\vartheta + \chi^2\mathcal{M}\vartheta\cos\vartheta\sin\chi\vartheta - \mathcal{M}\vartheta\left(\sin\vartheta\cos\chi\vartheta\right)\chi + \sin\vartheta\sin\chi\vartheta\right)\,. \tag{4.7.10}$$

Consequently, there are three possibilities:

$$\chi = 0, \qquad \chi\sin\vartheta\cos\chi\vartheta = \cos\vartheta\sin\chi\vartheta, \tag{4.7.11}$$

DOI: 10.14750/ME.2016.008

$$\sin\chi\vartheta\left(\chi^2\mathcal{M}\vartheta\cos\vartheta+\sin\vartheta\right)=\sin\vartheta\left(\mathcal{M}\vartheta\chi\cos\chi\vartheta+\chi^2\sin\chi\vartheta\right)\ . \tag{4.7.12}$$

Equation $(4.7.11)_2$ provides the lowest physically possible solution for $\chi\vartheta$. After dividing throughout by $\cos\vartheta\chi\cos\vartheta$ we get

$$\chi\tan\vartheta=\tan\chi\vartheta\ . \tag{4.7.13}$$

This equation is the same as (3.4.19) set up for the stability investigations of shallow beams. The approximative polynomials satisfying the above relation with a good accuracy are

$$\chi\vartheta=g_{\rm ff}(\vartheta=0\ldots1.5)=4.493\,419\,972+8.585\,048\,966\cdot10^{-3}\vartheta+3.717\,588\,695\cdot10^{-2}\vartheta^2+ \\ +5.594\,338\,754\cdot10^{-2}\vartheta^3-3.056\,068\,806\cdot10^{-2}\vartheta^4+8.717\,756\,418\cdot10^{-3}\vartheta^5\ , \tag{4.7.14a}$$

$$\chi\vartheta=g_{\rm ff}(\vartheta=1.5\ldots\pi)=8.267\,582\,130\ -9.756\,084\,003\,\vartheta+10.135\,036\,093\,\vartheta^2- \\ -5.340\,762\,360\,\vartheta^3+1.848\,589\,184\,\vartheta^4-0.497\,142\,450\,\vartheta^{4.5}\ . \tag{4.7.14b}$$

Figure 4.3 confirms that the approximative results (see the orange symbols) are indeed accurate enough compared to the 'exact' solution (blue continuous line).

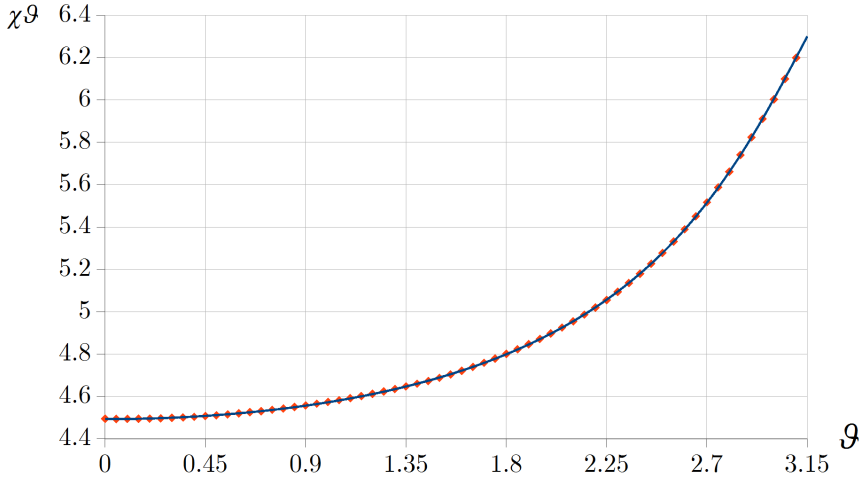

FIGURE 4.3. The solution $g_{\rm ff}(\vartheta)$ for fixed deep circular beams.

It means that the critical strain

$$\varepsilon_{o\xi\,\rm crit}=-\frac{1}{m}\left[\left(\frac{g_{\rm ff}}{\vartheta}\right)^2-1\right] \tag{4.7.15}$$

can be given in the same structure as in (3.4.22). However, this time the polynomial is valid for greater central angles as well.

4.8. Computational results

Based on the previously reviewed algorithm, a program was developed in Fortran90 language using the `DGVCRG` subroutine from the IMSL library [**109**] to compute the eigenvalues (eigenfrequencies).

To validate the model and the code, we have checked whether the solutions for the free vibrations ($|\varepsilon_{o\xi}|=|\varepsilon_{o\xi\,\rm crit}\cdot10^{-5}|\simeq0$) coincide with previous results for homogeneous beams from the literature [**41**, **100**] given that the parameter m has the same value. To do so, first, let us overview some well-known achievements. The i-th eigenfrequency for the free

DOI: 10.14750/ME.2016.008

transverse vibrations of homogeneous straight beams [**100**] is

$$\alpha_i^* = \frac{C_{i,\,\mathrm{char}}\pi^2}{\sqrt{\frac{\rho A}{I_\eta E}}\ell_b^2}\,, \tag{4.8.1}$$

where $C_{i,\,\mathrm{char}}$ denotes constants which depend on the supports and the ordinal number of the frequency sought (see Table 4.1) and moreover ℓ_b is the length of the beam. The extension of the former relation for cross-sectional inhomogeneity is [**115**]

$$\alpha_i^* = \frac{C_{i,\,\mathrm{char}}\pi^2}{\sqrt{\frac{\rho_a A}{I_{e\eta}}}\ell_b^2}\,. \tag{4.8.2}$$

TABLE 4.1. The values of $C_{i,\mathrm{char}}$ [**116**].

	$i=1$	$i=2$	$i=3$	$i=4$
Pinned-pinned beams	1	4	9	16
Fixed-fixed beams	2.266	6.243	12.23	20.25

If we recall and rearrange equations (4.1.26)-(4.1.27) with $\varepsilon_{o\xi} \simeq 0$, then

$$\alpha_i = \alpha_{i\,\mathrm{free}} = \sqrt{\frac{\Lambda_i\, I_{e\eta}}{\rho_a\, A\, \rho_o^4}} \tag{4.8.3}$$

provides the i-th natural (unloaded) frequency for curved beams. Thus, the quotient of the previous two formulae is

$$C_{i,\mathrm{char}}\frac{\alpha_i}{\alpha_i^*} = \frac{\frac{\sqrt{\Lambda_i}}{\sqrt{\frac{\rho_a\, A}{I_{e\eta}}}\rho_o^2}}{\frac{\pi^2}{\sqrt{\frac{\rho_a\, A}{I_{e\eta}}}\ell_b^2}} = \frac{\overline{\vartheta}^{\,2}\sqrt{\Lambda_i}}{\pi^2}\,. \tag{4.8.4}$$

This relation expresses the ratio of the natural frequencies of curved and straight beams with the same length ($\ell_b = \rho_o\bar{\vartheta} = \rho_o 2\vartheta$) and same material composition, i.e. it is valid not only for homogeneous materials but also for cross-sectional inhomogeneity.

Moving on now to the free longitudinal vibrations of homogeneous fixed-fixed rods, the natural frequencies assume the form [**100**]

$$\hat{\alpha}_i = \frac{K_{i\,\mathrm{char}}}{\ell_r}\sqrt{\frac{E}{\rho}}\pi\,, \tag{4.8.5}$$

where the constant $K_{i\,\mathrm{char}} = i$; $(i = 1, 2, 3, \ldots)$; ℓ_r is the length of the rod and ρ is the density of the cross-section. If we recall equation (4.8.3) for homogeneous material, we can compare this result to that valid for the free vibrations of curved beams (given that $|\varepsilon_{o\xi}| = |\varepsilon_{o\xi\,\mathrm{crit}} \cdot 10^{-5}| \simeq 0$ when calculating the eigenvalues Λ_i) in such a way that

$$K_{i\,\mathrm{char}}\frac{\alpha_{i\,\mathrm{free}}}{\hat{\alpha}_i} = \frac{1}{\sqrt{m}}\frac{\bar{\vartheta}}{\pi}\sqrt{\Lambda_i}\,. \tag{4.8.6}$$

DOI: 10.14750/ME.2016.008

4.8.1. Results for unloaded pinned-pinned beams. In Figure 4.4 the ratio (4.8.4) is plotted in terms of the central angle $\bar{\vartheta}$ of the circular beam. The following values of m were picked: 750, 1 000, 1 300, 1 750, 2 400, 3 400, 5 000, 7 500, 12 000, 20 000, 35 000, 60 000, 100 000 and 200 000.

The (comparable) outcomes are identical to those of [**41**] valid for homogeneous beams. Thus, it turns out that the ratios of the odd frequencies do not depend on m. Another important property is that there can be experienced a frequency shift: in terms of magnitude, the first/third frequency becomes the second/fourth one if the central angle is sufficiently great.

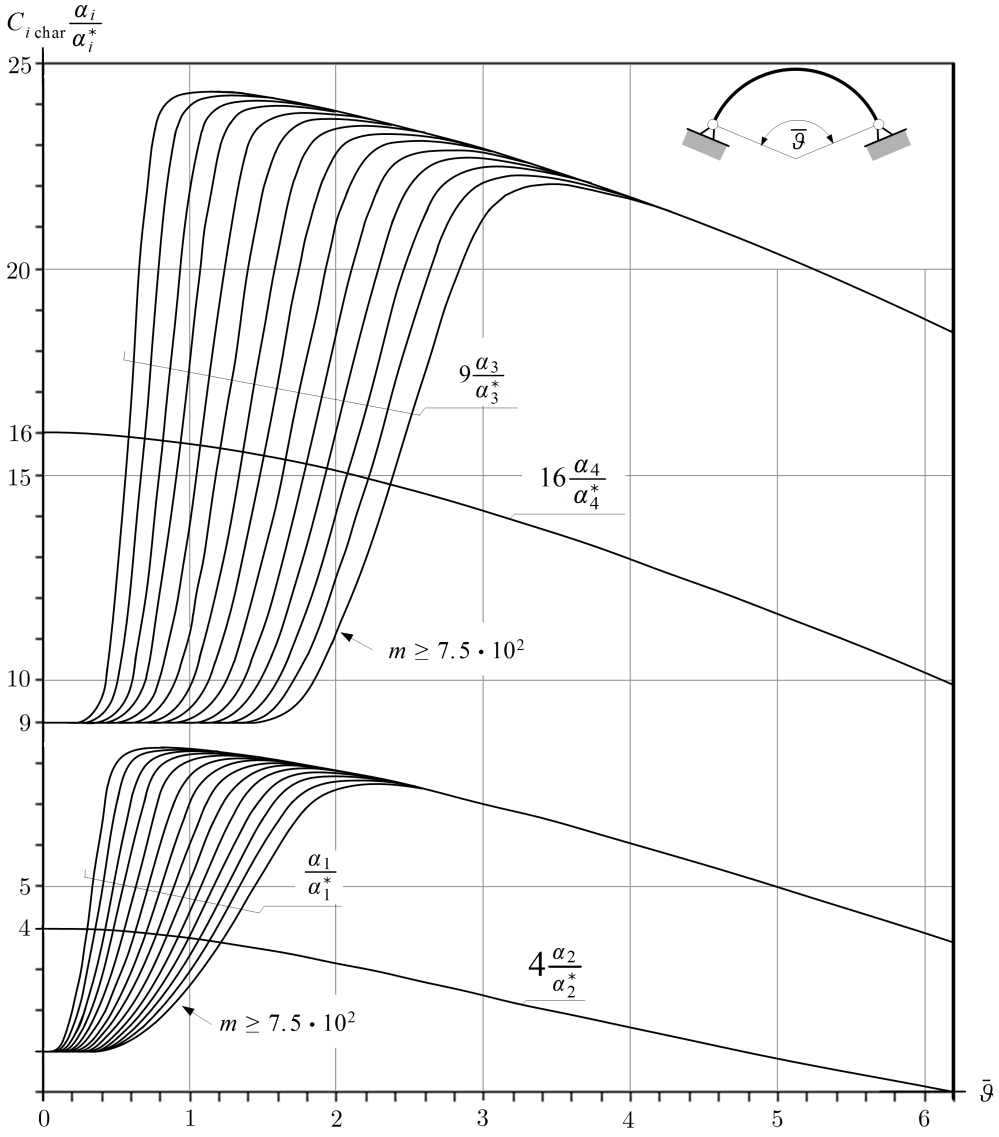

FIGURE 4.4. Vibrations of pinned-pinned circular beams when $\varepsilon_{o\xi} \simeq 0$.

A few finite element control calculations were carried out to check the results. In Abaqus 6.7 we have used the Linear Perturbation, Frequency step. The model consisted of $B22$ (3-node Timoshenko beam) elements. Further, we chose $E = 2 \cdot 10^{11}$ Pa and $\rho = 7\,800$ kg/m^3. The frequency ratios of the new model ($\alpha_{i\,\mathrm{New\,model}}$) and Abaqus ($\alpha_{i\,\mathrm{Abaqus}}$) are gathered in Tables 4.2 and 4.3. There is generally a very good agreement.

DOI: 10.14750/ME.2016.008

TABLE 4.2. FE verifications, $\rho_o/b = 10$; $m = 1\,200$.

ϑ	$\frac{\alpha_{1\text{ New model}}}{\alpha_{1\text{ Abaqus}}}$	$\frac{\alpha_{2\text{ New model}}}{\alpha_{2\text{ Abaqus}}}$	$\frac{\alpha_{3\text{ New model}}}{\alpha_{3\text{ Abaqus}}}$	$\frac{\alpha_{4\text{ New model}}}{\alpha_{4\text{ Abaqus}}}$
0.5	1.001	1.053	1.109	1.179
1	1.014	1.029	1.004	1.053
1.5	1.007	1.014	1.028	1.006
2	1.004	1.008	1.014	1.022
2.5	1.003	1.005	1.010	1.015

TABLE 4.3. FE verifications, $\rho_o/b = 30$, $m = 10\,800$.

ϑ	$\frac{\alpha_{1\text{ New model}}}{\alpha_{1\text{ Abaqus}}}$	$\frac{\alpha_{2\text{ New model}}}{\alpha_{2\text{ Abaqus}}}$	$\frac{\alpha_{3\text{ New model}}}{\alpha_{3\text{ Abaqus}}}$	$\frac{\alpha_{4\text{ New model}}}{\alpha_{4\text{ Abaqus}}}$
0.5	1.006	1.010	1.005	1.025
1	1.002	1.004	1.007	1.011
1.5	1.001	1.002	1.003	1.006
2	1.000	1.001	1.002	1.003
2.5	1.000	1.001	1.002	1.003
3	1.001	1.001	1.001	1.002

Some further comparisons with the results presented in Tables 5 and 8 in [**82**] are provided hereinafter assuming a rectangular cross-section ($A = 0.01$ m^2; $I_\eta = 8.33 \cdot 10^{-6}$ m^4) and that $E = 2 \cdot 10^{11}$ Pa, $\rho_a = 7\,800$ kg/m^3. In Table 4.4, $2\vartheta = \pi/2$ while in Table 4.5, it is $2\vartheta = \pi$.

TABLE 4.4. Comparison of the eigenfrequencies, $2\vartheta = \pi/2$, pinned supports.

m		Ref. [**117**]	Ref. [**82**] col. 1	Ref. [**82**] col. 2	Ref. [**82**] col. 5	New model
10 000	α_1	38.38	38.38	38.42	38.28	38.41
10 000	α_2	89.57	89.56	90.46	89.08	89.77
10 000	α_3	171.42	171.41	172.17	169.75	172.18
10 000	α_4	244.96	244.94	269.26	243.05	245.82
2 500	α_1	152.93	152.93	153.7	151.45	153.48
2 500	α_2	343.01	342.76	361.85	336.46	345.31
2 500	α_3	552.15	552.17	688.7	549.84	552.28
2 500	α_4	675.71	675.83	1077.01	651.82	685.38

TABLE 4.5. Comparison of the eigenfrequencies, $2\vartheta = \pi$, pinned supports.

m		Ref. [**117**]	Ref. [**82**] col. 1	Ref. [**82**] col. 2	Ref. [**82**] col. 5	New model
10 000	α_1	6.33	6.33	6.33	6.32	6.33
10 000	α_2	19.31	19.31	19.33	19.28	19.32
10 000	α_3	38.98	38.97	39.02	38.87	39.05
10 000	α_4	63.53	63.53	63.71	63.29	63.79
2 500	α_1	25.28	25.28	25.31	25.21	25.3
2 500	α_2	77.01	76.99	77.31	76.57	77.18
2 500	α_3	155.24	155.25	156.09	153.75	155.96
2 500	α_4	251.86	251.82	254.83	248.12	253.81

Tüfekçi and Arpaci [**82**] have checked their numerical results under various assumptions. In the next two tables, the notation Ref. [**82**] col. 1 denotes that the authors have accounted axial extension and rotatory inertia effects as in [**117**]. Further, Ref. [**82**] col. 2 notes that both these effects are neglected, meanwhile in the column named Ref. [**82**] col. 5, results by

DOI: 10.14750/ME.2016.008

the most accurate model are shown: not only axial and transverse shear extension effects but also rotatory inertia effects are considered. After comparing the outcomes one can conclude that the correlation, even with the model using the least neglects, is really good.

The quotient (4.8.6) is plotted in Figure 4.5 for $i = 1, 2$. According to the computational results, these ratios do not depend on the parameter m and its value are equal to 1 or 2 if the central angle is small enough.

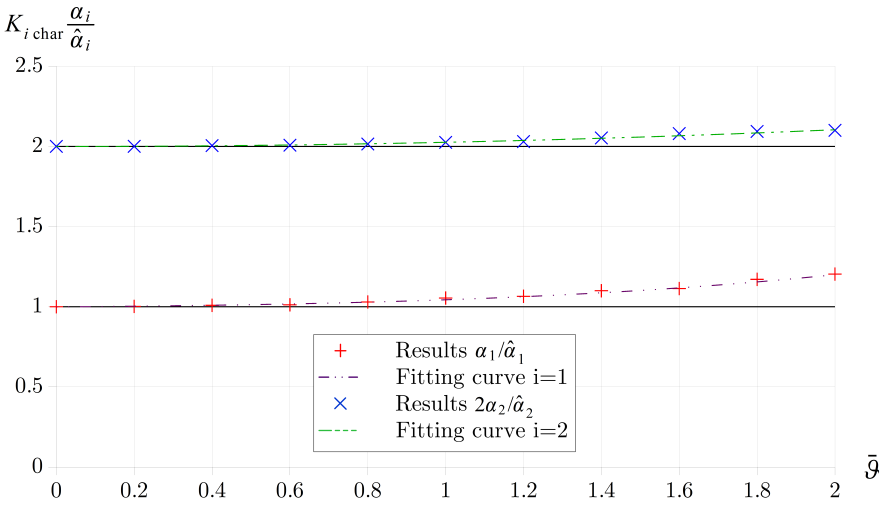

FIGURE 4.5. Results for pinned-pinned beams, when $\varepsilon_{o\xi} \simeq 0$.

4.8.2. Results for loaded pinned-pinned beams. Now the effect of the central concentrated load on the frequencies is analysed. In this subsection let α_i be the i-th natural frequency of the loaded circular beam while the unloaded (natural) frequencies are denoted by $\alpha_{i\,\mathrm{free}}$.

Figure 4.6 represents the quotient $\alpha_2^2/\alpha_{2\,\mathrm{free}}^2$ – the subscript 2 is in accord with Figure 4.4 – against the quotient $|\varepsilon_{o\xi}/\varepsilon_{o\xi\ \mathrm{crit}}|$ for beams under compression and tension. The frequencies α_2 and $\alpha_{2\,\mathrm{free}}$ are the lowest eigenfrequencies of the vibrations above the limit

$$\bar{\vartheta}(m) \simeq -0.142\,5 + 2.7 \cdot 10^{-8} m + 10\,700/m^2 + 5.04/m^{0.2}\ ,\ \ m \in [10^3; 10^6]\ . \tag{4.8.7}$$

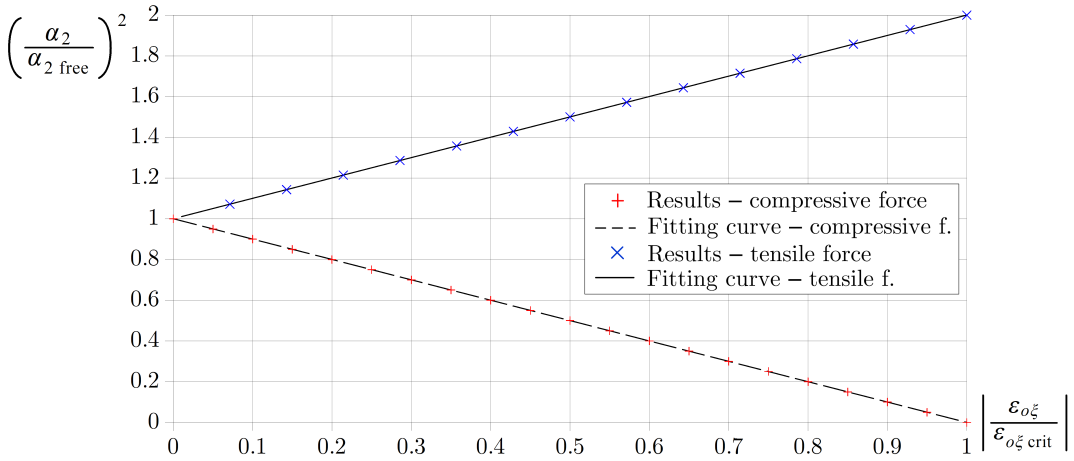

FIGURE 4.6. Results for the two loading cases of pinned-pinned beams.

The tested values of the related parameters are as follows: $m = \{10^3; 10^4; 10^5\}$; $\bar{\vartheta} = \{0.2; 0.4; 0.6; 1; 1.6; 2; 3; 4; 5; 6\}$ and $|\varepsilon_{o\xi}/\varepsilon_{o\xi\ \mathrm{crit}}| = \{10^{-5}; 0.1; 0.2; ...; 0.9; 0.99\}$. In addition to the fact that the results are independent of m and ϑ, the plotted relationships are linear

DOI: 10.14750/ME.2016.008

with a very good accuracy – i.e. the frequencies under [compression] <tension> happen to [decrease] <increase> linearly. The polynomials

$$\frac{\alpha_2^2}{\alpha_{2\,\mathrm{free}}^2} = 1.000\,46 - 1.000\,38\frac{|\varepsilon_{o\xi}|}{\varepsilon_{o\xi\,\mathrm{crit}}}\,, \quad \text{if} \quad \varepsilon_{o\xi} < 0\,, \tag{4.8.8}$$

$$\frac{\alpha_2^2}{\alpha_{2\,\mathrm{free}}^2} = 1.000\,661\,286 + 0.999\,915\,179\frac{|\varepsilon_{o\xi}|}{\varepsilon_{o\xi\,\mathrm{crit}}}\,, \quad \text{if} \quad \varepsilon_{o\xi} > 0 \tag{4.8.9}$$

fit well on these results. This achievement is basically the same as the well-known result that is valid for pinned-pinned straight beams if they are subjected to an axial force – see for instance [**86**].

4.8.3. Results for unloaded fixed-fixed beams. The quotient (4.8.4) is plotted in Figure 4.7 against the central angle. Once more, the picked values of m are 750, 1 000, 1 300, 1 750, 2 400, 3 400, 5 000, 7 500, 12 000, 20 000, 35 000, 60 000, 100 000 and 200 000. The curves run similarly as for pinned-pinned beams and the properties are also the same. The quotients are generally greater for the same parameters meaning that the fixed ends provide stiffer supports.

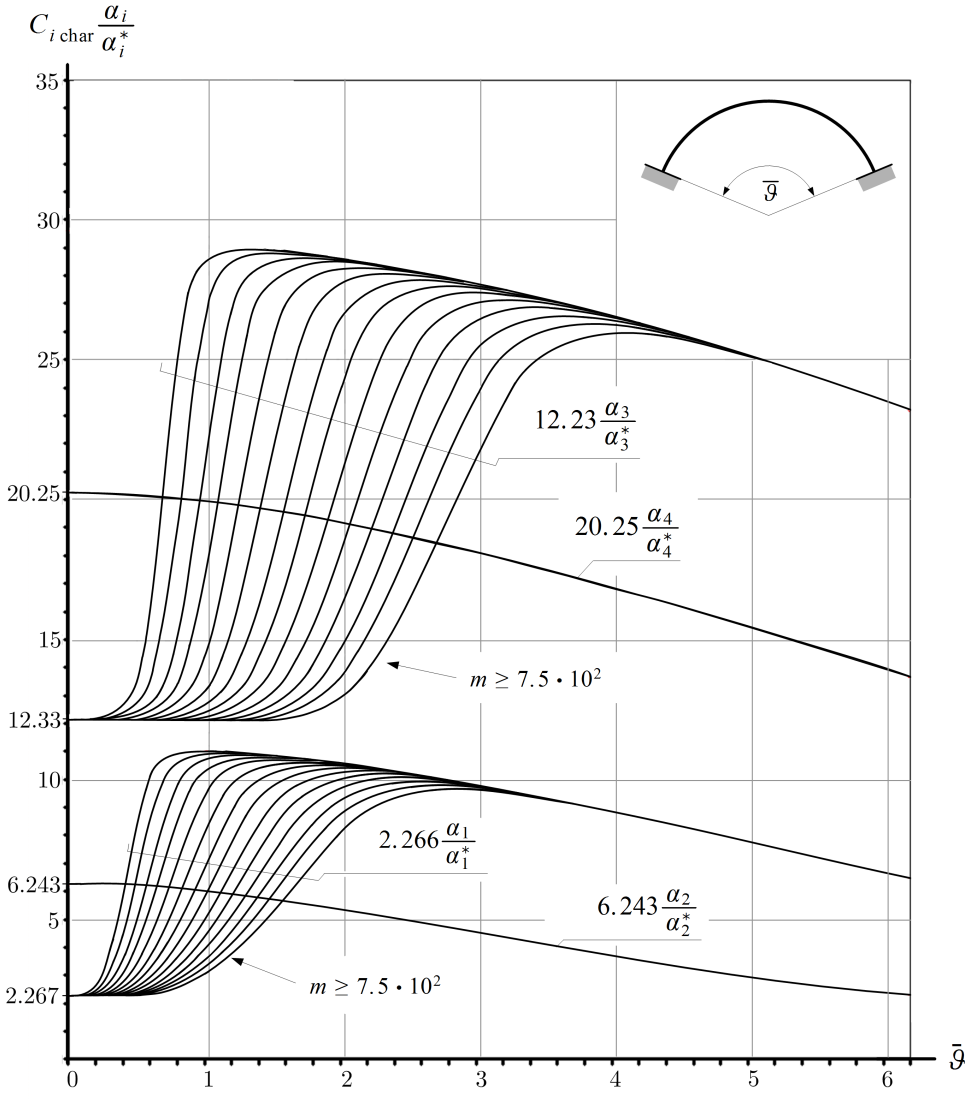

FIGURE 4.7. Results for fixed-fixed beams when $\varepsilon_{o\xi} \simeq 0$.

DOI: 10.14750/ME.2016.008

There were some experiments carried out by some kind colleagues in Romania to determine the first natural frequency of four specimens. I would like to express my gratitude to them. The method is detailed in [**118**]. The tested beams with rectangular cross-section are made of steel: $E \simeq 2 \cdot 10^{11}$ Pa. All the other parameters are gathered in Table 4.6. The measured frequencies are denoted by $\alpha_{1\,\mathrm{Meas.}}$ We can see that both the new model and Abaqus yield really close results to the experiments.

TABLE 4.6. Unloaded frequencies – comparison with measurements.

m	$\bar{\vartheta}$	A	ρ_o	$\frac{\alpha_{1\ \text{New model}}}{\alpha_{1\ \text{Meas.}}}$	$\frac{\alpha_{1\ \text{Abaqus}}}{\alpha_{1\ \text{Meas.}}}$
[−]	[°]	[mm^2]	[mm]	[−]	[−]
98 523	46	$29.7 \cdot 4.8$	434.9	1.099	1.097
84 984	43.1	$25 \cdot 5.5$	462.9	1.050	1.047
77 961	36.9	$29.5 \cdot 5$	403	1.046	1.041
281 169	31.17	$25.6 \cdot 3.1$	474.5	1.070	1.068

Some additional Abaqus computations were as well carried out. The settings were the same as mentioned in relation with pinned-pinned beams and the consequences also hold. The results are gathered in Tables 4.7 and 4.8.

TABLE 4.7. FE verifications, fixed-fixed beams, $m = 1\,200$, $\rho_o/b = 10$.

ϑ	$\frac{\alpha_{1\ \text{New model}}}{\alpha_{1\ \text{Abaqus}}}$	$\frac{\alpha_{2\ \text{New model}}}{\alpha_{2\ \text{Abaqus}}}$	$\frac{\alpha_{3\ \text{New model}}}{\alpha_{3\ \text{Abaqus}}}$	$\frac{\alpha_{4\ \text{New model}}}{\alpha_{4\ \text{Abaqus}}}$
0.5	1.019	1.115	1.193	1.314
1	1.031	1.037	1.021	1.075
1.5	1.014	1.025	1.039	1.037
2	1.008	1.015	1.022	1.032
2.5	0.971	1.010	1.015	1.022

TABLE 4.8. FE verifications, fixed-fixed beams, $m = 10\,800$, $\rho_o/b = 30$.

ϑ	$\frac{\alpha_{1\ \text{New model}}}{\alpha_{1\ \text{Abaqus}}}$	$\frac{\alpha_{2\ \text{New model}}}{\alpha_{2\ \text{Abaqus}}}$	$\frac{\alpha_{3\ \text{New model}}}{\alpha_{3\ \text{Abaqus}}}$	$\frac{\alpha_{4\ \text{New model}}}{\alpha_{4\ \text{Abaqus}}}$
0.5	1.014	1.007	1.018	1.039
1	1.004	1.006	1.010	1.014
1.5	1.002	1.003	1.006	1.009
2	1.001	1.002	1.003	1.005
2.5	1.000	1.001	1.002	1.004
3	1.000	1.001	1.002	1.004

Recalling the results gathered in Tables 1 and 4 in [**82**], we can make some additional comparisons as shown in Tables 4.9 and 4.10. All the data are the same as for pinned-pinned beams. The agreement is good yet again.

DOI: 10.14750/ME.2016.008

TABLE 4.9. Comparison of the eigenfrequencies, $2\vartheta = \pi/2$, fixed supports.

m		Ref. [**117**]	Ref. [**82**] col. 1	Ref. [**82**] col. 2	Ref. [**82**] col. 5	New model
10 000	α_1	63.07	63.06	63.16	62.62	63.1
10 000	α_2	117.22	117.19	120.76	115.85	117.5
10 000	α_3	217.13	217.08	218.41	213.28	218.2
10 000	α_4	249.26	345.21	322.26	247.96	249.8
2 500	α_1	251	251	252.66	244.24	251.89
2 500	α_2	399.68	399.65	483.04	390.09	401.16
2 500	α_3	613.25	613.33	873.64	600.7	617.25
2 500	α_4	847.24	847.07	1289.06	795.82	859.02

TABLE 4.10. Comparison of the eigenfrequencies, $2\vartheta = \pi$, fixed supports.

m		Ref. [**117**]	Ref. [**82**] col. 1	Ref. [**82**] col. 2	Ref. [**82**] col. 5	New model
10 000	α_1	12.23	12.23	12.24	12.21	12.24
10 000	α_2	26.89	26.89	26.95	26.80	26.92
10 000	α_3	49.93	49.93	50.03	49.70	50.07
10 000	α_4	76.43	76.44	76.84	75.95	76.85
2 500	α_1	48.87	48.86	48.96	48.51	48.9
2 500	α_2	106.85	106.85	107.78	105.53	107.1
2 500	α_3	198.57	198.51	200.13	194.94	199.5
2 500	α_4	299.61	299.59	307.37	292.46	302.13

The quotients (4.8.6) for $i = 1, 2$ are plotted in Figure 4.8. With a good accuracy, these ratios do not depend on the parameter m and are equal to 1 and 2, respectively if the central angle is small enough.

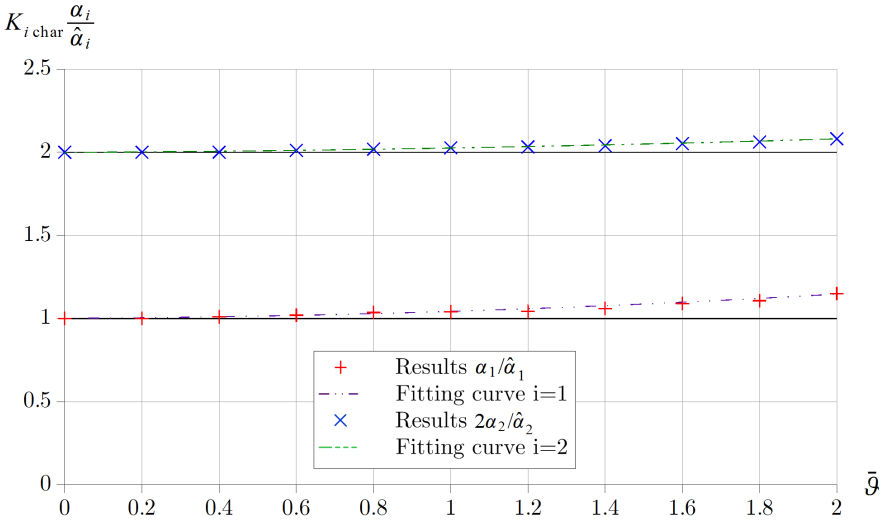

FIGURE 4.8. Comparison with vibrating rods when $\varepsilon_{o\xi} \simeq 0$.

4.8.4. Results for loaded fixed-fixed beams. When the effect of the central concentrated load is accounted – keeping the same notations as in Subsection 4.8.2 – we have found that while the numerical results for the frequency quotient $(\alpha_2/\alpha_{2\ \mathrm{free}})^2$ show some noticeable dependency on the central angle, they are insensible to the parameter m. The

DOI: 10.14750/ME.2016.008

tested values are the same as for the other support arrangement. The results are presented graphically in Figure 4.9.

We can conclude that when the beam is under compression and $\bar{\vartheta} \in [0.2; 5]$, the results are approximated with a good accuracy by the continuous black curve in the corresponding figure. The equation of that approximative polynomial is

$$\left(\frac{\alpha_2}{\alpha_{2\ \mathrm{free}}}\right)^2 = 0.999\ 354 - 0.916\ 924 \left|\frac{\varepsilon_{o\xi}}{\varepsilon_{o\xi\ \mathrm{crit}}}\right| - 0.077\ 732 \left|\frac{\varepsilon_{o\xi}}{\varepsilon_{o\xi\ \mathrm{crit}}}\right|^2 . \tag{4.8.10}$$

When $\bar{\vartheta} = 6$ we had better use

$$\left(\frac{\alpha_2}{\alpha_{2\ \mathrm{free}}}\right)^2 = 0.994\ 622 - 0.611\ 192 \left|\frac{\varepsilon_{o\xi}}{\varepsilon_{o\xi\ \mathrm{crit}}}\right| - 0.352\ 049 \left|\frac{\varepsilon_{o\xi}}{\varepsilon_{o\xi\ \mathrm{crit}}}\right|^2 . \tag{4.8.11}$$

It therefore means that the approximations are more reasonable with quadratic functions instead of linear ones.

The case of tension seems a bit more complicated as the central angle has a greater influence on the frequency quotients. The equations of the fitting curves in Figure 4.9 are

$$\left(\frac{\alpha_2}{\alpha_{2\ \mathrm{free}}}\right)^2 = 0.994\ 252 + 0.968\ 480 \left|\frac{\varepsilon_{o\xi}}{\varepsilon_{o\xi\ \mathrm{crit}}}\right| + 0.012\ 209 \left|\frac{\varepsilon_{o\xi}}{\varepsilon_{o\xi\ \mathrm{crit}}}\right|^2 , \text{ if } \bar{\vartheta} = 0.2; \tag{4.8.12}$$

$$\left(\frac{\alpha_2}{\alpha_{2\ \mathrm{free}}}\right)^2 = 0.998\ 414 + 0.971\ 007 \left|\frac{\varepsilon_{o\xi}}{\varepsilon_{o\xi\ \mathrm{crit}}}\right| - 0.058\ 161 \left|\frac{\varepsilon_{o\xi}}{\varepsilon_{o\xi\ \mathrm{crit}}}\right|^2 , \text{ if } \bar{\vartheta} = 3; \tag{4.8.13}$$

$$\left(\frac{\alpha_2}{\alpha_{2\ \mathrm{free}}}\right)^2 = 1.000\ 444 + 0.874\ 756 \left|\frac{\varepsilon_{o\xi}}{\varepsilon_{o\xi\ \mathrm{crit}}}\right| - 0.051\ 986 \left|\frac{\varepsilon_{o\xi}}{\varepsilon_{o\xi\ \mathrm{crit}}}\right|^2 , \text{ if } \bar{\vartheta} = 5; \tag{4.8.14}$$

$$\left(\frac{\alpha_2}{\alpha_{2\ \mathrm{free}}}\right)^2 = 1.000\ 926 + 0.679\ 926 \left|\frac{\varepsilon_{o\xi}}{\varepsilon_{o\xi\ \mathrm{crit}}}\right| - 0.088\ 723 \left|\frac{\varepsilon_{o\xi}}{\varepsilon_{o\xi\ \mathrm{crit}}}\right|^2 , \text{ if } \bar{\vartheta} = 6. \tag{4.8.15}$$

The frequencies α_2 and $\alpha_{2\ \mathrm{free}}$ are the lowest frequencies above the limit

$$\bar{\vartheta}(m) \simeq -0.159 + 8.874 \cdot 10^{-8}\, m - 2.99 \cdot 10^{-14}\, m^2 + 6.448/m^{0.2} , \quad m \in [7.5 \cdot 10^2; 2 \cdot 10^5] . \tag{4.8.16}$$

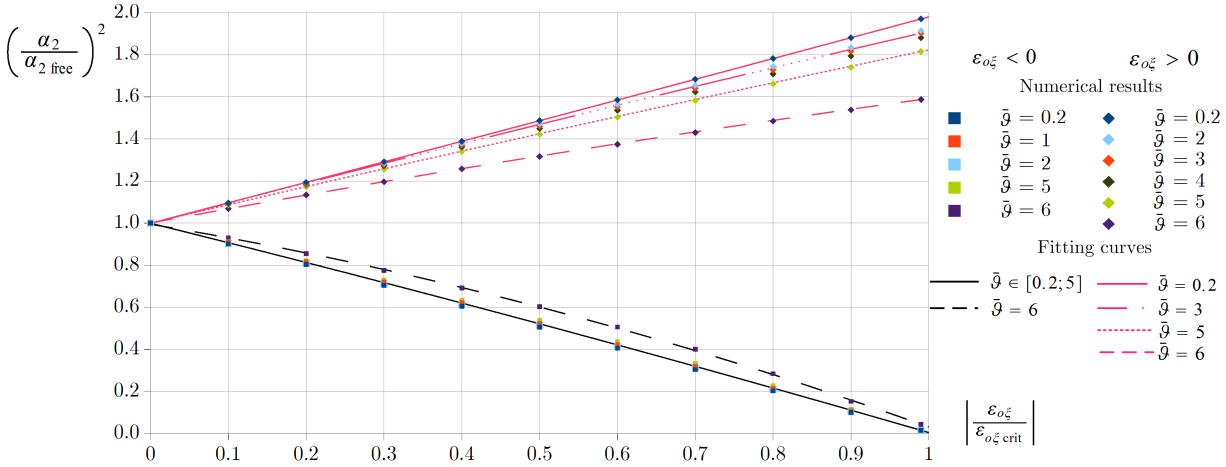

FIGURE 4.9. Results for the two loading cases of fixed-fixed beams.

DOI: 10.14750/ME.2016.008

4.8.5. The effect of heterogeneity on the frequency spectrum. Here we investigate how the frequencies can change due to the inhomogeneity. We consider a functionally graded material composition. The material properties, i. e. Young's modulus $E = E(\zeta)$ and

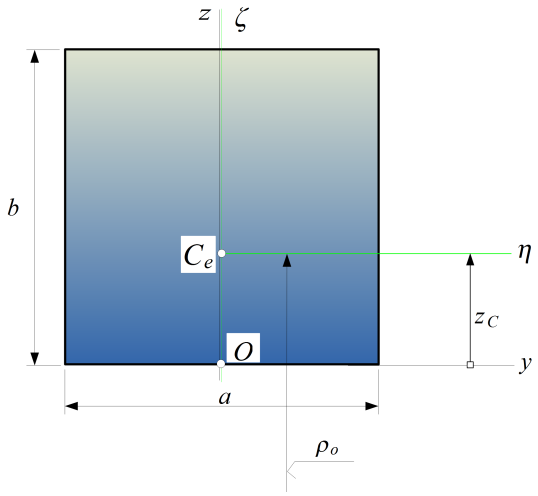

FIGURE 4.10. A functionally graded rectangular cross-section.

the density ρ are distributed along the axis z (or ζ) of the rectangular cross-section in Figure 4.10 according to a similar power law rule as in **[73, 95, 98]**:

$$E(z) = (E_m - E_c)\left(\frac{z}{b}\right)^k + E_c\,, \qquad \rho(z) = (\rho_m - \rho_c)\left(\frac{z}{b}\right)^k + \rho_c\,. \tag{4.8.17}$$

Here the subscripts $_c$ and $_m$ refer to the ceramic and metal constituents of the material and the exhibitor $k \in \mathbb{R}$. In this example we choose an aluminium oxide Al_2O_3 and aluminium constitution, therefore

$$E_c = 38{\cdot}10^4\ \text{MPa}\ ;\ \mathrm{E_m} = 7{\cdot}10^4\ \text{MPa}\ ; \rho_\mathrm{c} = 3.8{\cdot}10^{-6}\ \frac{\text{kg}}{\text{mm}^2};\ \rho_\mathrm{m} = 2.707{\cdot}10^{-6}\ \frac{\text{kg}}{\text{mm}^2}\ . \tag{4.8.18}$$

The value of the index k will be increased gradually from 0 by 0.5 until 5. If $k = 0$, the cross-section is homogeneous aluminium and the typical quantities will be distinguished by a subscript $_{\mathrm{hom}}$. Otherwise, the subscript $_{\mathrm{het}}$ is in command. (When $k \to \infty$ the whole cross-section is Al_2O_3 with a thin aluminium layer at $z = b$.) In Figures 4.11 and 4.12 we show the distribution of E and ρ along the height of the cross-section accordingly with the power law.

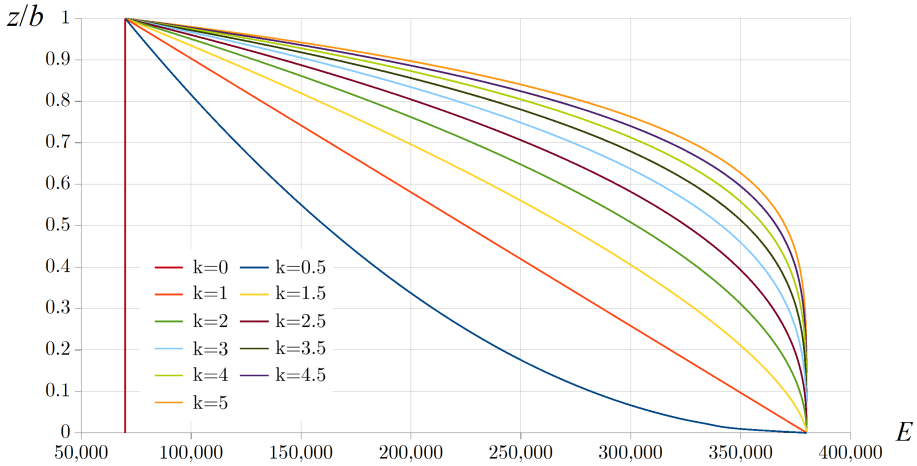

FIGURE 4.11. Variation of Young's modulus over the height of the cross-section.

DOI: 10.14750/ME.2016.008

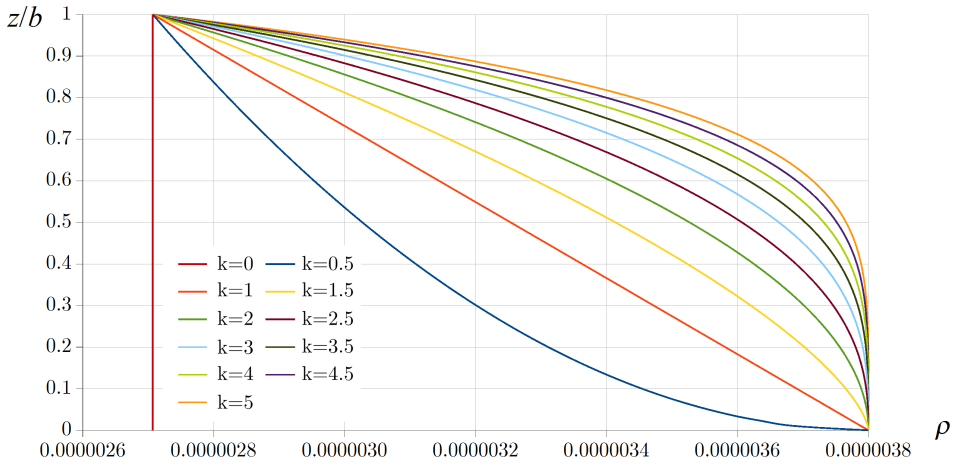

FIGURE 4.12. Variation of the density over the height of the cross-section.

Similarly as done in Section 3.6, we now plot some typical distributions along the axis z (or ζ). The parameter m consists of two parts just as in (3.6.1):

$$\frac{m_{\text{het}}}{m_{\text{hom}}(k=0)} = \frac{A_e I_\eta}{A I_{e\eta}} \left[\frac{\rho_{o\ \text{het}}}{\rho_{o\ \text{hom}}}\right]^2 . \tag{4.8.19}$$

Recalling formulae (2.1.12)-(2.1.13c), (4.8.17), (4.8.18) and Figure 4.10, the physical quantities we need for the current example assume the forms

$$E(\zeta) = (70\ 000 - 380\ 000)\left(\frac{\zeta + z_c}{b}\right)^k + 380\ 000\ , \tag{4.8.20a}$$

$$Q_{ey} = \int_A E z \mathrm{d}A = a \int_0^b \left[\left((70\ 000 - 380\ 000)\left(\frac{z}{b}\right)^k + 380\ 000\right) z\right] \mathrm{d}z\ , \tag{4.8.20b}$$

$$A_e = \int_A E \mathrm{d}A = a \int_0^b \left[(70\ 000 - 380\ 000)\left(\frac{z}{b}\right)^k + 380\ 000\right] \mathrm{d}z\ ,\ z_C = \frac{Q_{ey}}{A_e}\ , \tag{4.8.20c}$$

$$I_{e\eta} = \int_A E \zeta^2 \mathrm{d}A = a \int_{-z_c}^{(b-z_c)} \left[\left((70\ 000 - 380\ 000)\left(\frac{\zeta + z_c}{b}\right)^k + 380\ 000\right) \zeta^2\right] \mathrm{d}\zeta\ . \tag{4.8.20d}$$

The first term on the right side of (4.8.19) depends only on k as can be seen from Figure 4.13. The maximum is reached at $k = 2$, that is $\simeq 1.218$.

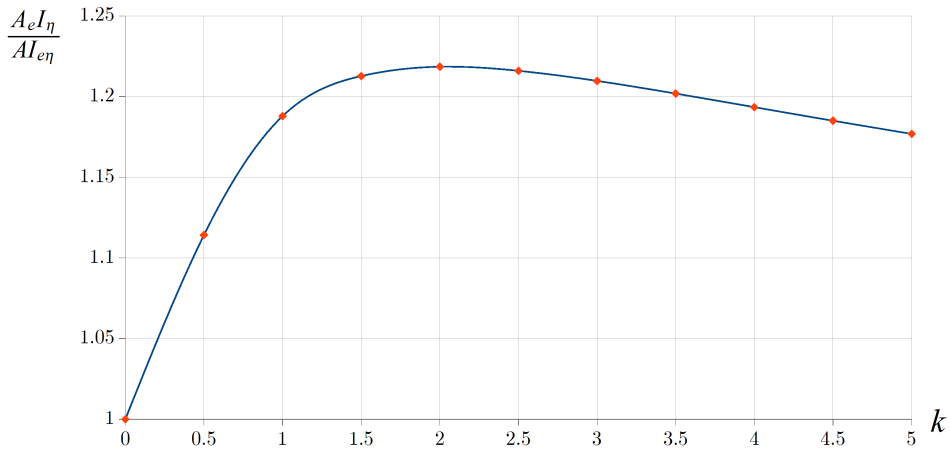

FIGURE 4.13. The first factor in (4.8.19) against k.

DOI: 10.14750/ME.2016.008

The second factor is, moreover, function of the ratio ρ_o/b. Some possible solutions with the approximative polynomials are plotted in Figure 4.14.

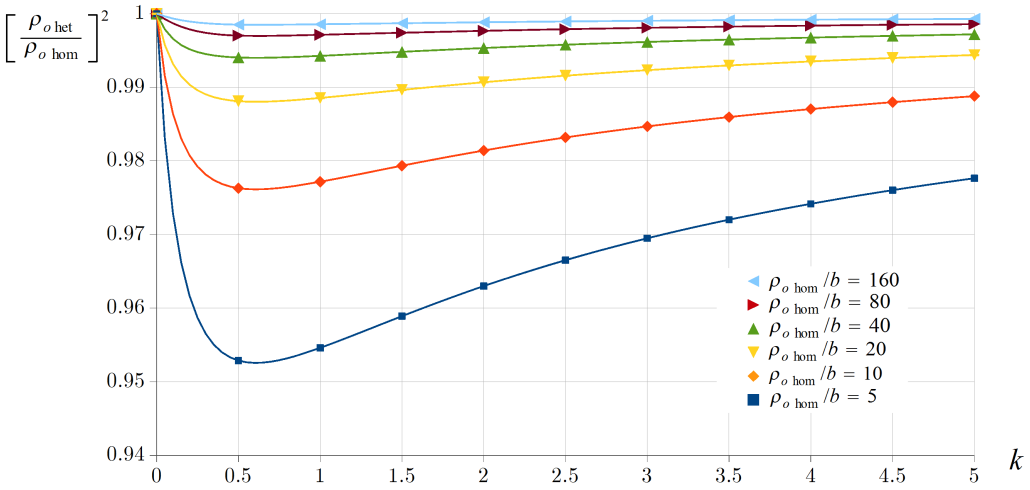

FIGURE 4.14. The second factor in (4.8.19) against k.

Therefore, the product (4.8.19) itself in terms of k and ρ_o/b is shown in Figure 4.15.

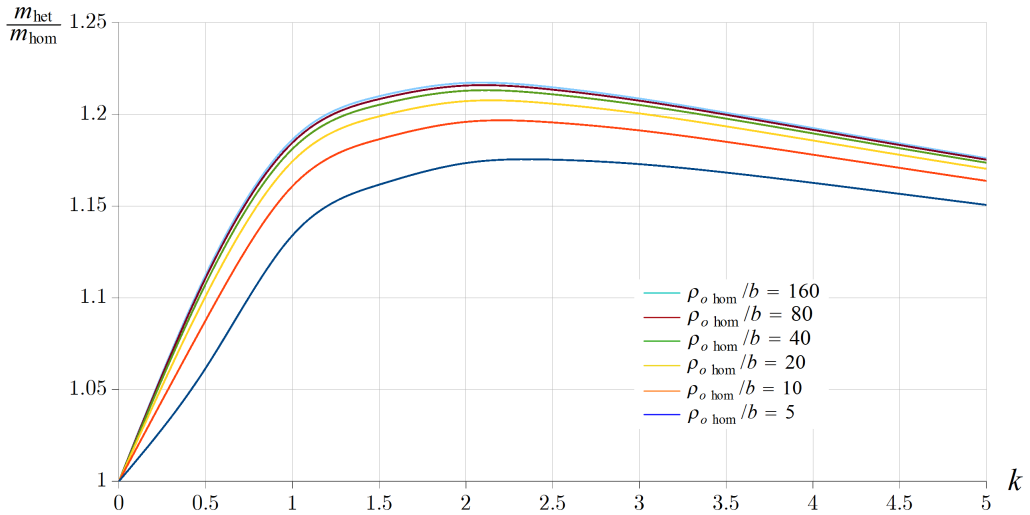

FIGURE 4.15. The parameter m (4.8.19) against k.

4.8.5.1. *Free vibrations.* Now let us see how the inhomogeneity can affect the first four natural frequencies of pinned-pinned circular beams. We choose $m_{\mathrm{hom}} = 1\,200$ and $\rho_o/b = 10$, therefore the maximum of the quotient $m_{\mathrm{het}}/m_{\mathrm{hom}}$ is $\simeq 1.196$ at $k = 2$. The picked semi-vertex angles are $\vartheta = (0.2;\ 0.4;\ 0.8;\ 1.6)$. We remind the reader to the fact that not only the parameter m but also the average density and the E-weighted moment of inertia have influence on the frequency spectrum – see equations (4.1.27) and (4.1.26). The computational results are plotted in Figure 4.16.

DOI: 10.14750/ME.2016.008

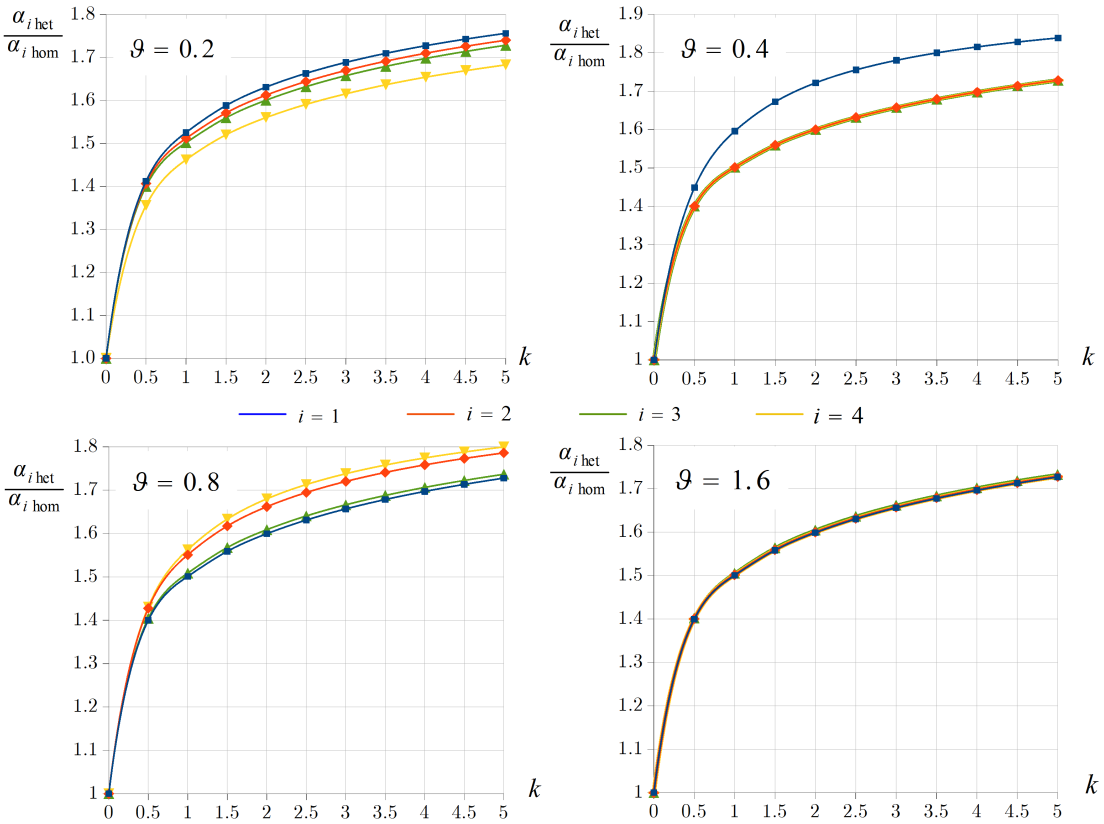

FIGURE 4.16. The change in the frequencies due to the inhomogeneity.

Generally we can conclude that there are significant differences because of the inhomogeneity. When $\vartheta = 0.2$, all four frequencies change in a similar way and in the order from the first one to the fourth one. Interestingly, when $\vartheta = 0.4$, only the second, third and fourth frequencies change almost exactly the same way. Increasing the semi-vertex angle to 0.8, we again experience a new tendency: the even frequencies are affected the mostly by the material composition. On the bottom right diagram the curves coincide with a good accuracy.

4.8.5.2. *Loaded vibrations.* Let $m_{\mathrm{hom}}(k = 0) = 10\,800$ and $\rho_o/b = 30$. $P_{\zeta\,\mathrm{ref}}$ is always the critical load of the homogeneous pinned-pinned beam – its value further depends on the central angle. We would like to briefly show how the the first four frequencies change for $k = 0.5$; 1; 2.5 and 5 given that the load is unchanged and at the same time proportional to the critical load of the homogeneous beam.

First, we investigate the case when $\vartheta = 0.2$. The quotient $P_\zeta/P_{\zeta\,\mathrm{ref}}$ is [positive] (negative) when the beam is under [compression] (tension). The beam is unloaded if this ratio is zero. The results for eight different load values in relation with the first four natural frequencies are gathered in Tables 4.11–4.14.

After observing these tables, one can conclude that the inhomogeneity affects more the frequencies under compression than in tension. The greatest influence of the load is always on the first frequency and the least is on the fourth one. It is also a common property that the corresponding frequency quotients are closest to 1 when the tensile force is the greatest. From the top to the bottom of any column, the numbers increase gradually. Both the inhomogeneity and the loading can have a huge influence on the frequencies.

DOI: 10.14750/ME.2016.008

TABLE 4.11. Results when $k = 0.5$ and $\vartheta = 0.2$.

$\frac{P_\zeta}{P_{\zeta\ \mathrm{ref}}}$	$\frac{\alpha_{1\ \mathrm{het}}\ (k=0.5)}{\alpha_{1\ \mathrm{hom}}\ (k=0)}$	$\frac{\alpha_{2\ \mathrm{het}}\ (k=0.5)}{\alpha_{2\ \mathrm{hom}}\ (k=0)}$	$\frac{\alpha_{3\ \mathrm{het}}\ (k=0.5)}{\alpha_{3\ \mathrm{hom}}\ (k=0)}$	$\frac{\alpha_{4\ \mathrm{het}}\ (k=0.5)}{\alpha_{4\ \mathrm{hom}}\ (k=0)}$
−0.8	1.238	1.230	1.308	1.347
−0.6	1.273	1.260	1.329	1.362
−0.4	1.318	1.298	1.353	1.377
−0.2	1.377	1.346	1.380	1.394
0.0	1.462	1.411	1.412	1.412
0.2	1.591	1.503	1.448	1.432
0.4	1.817	1.645	1.491	1.453
0.6	2.339	1.898	1.543	1.477
0.8	3.264	2.508	1.606	1.502

TABLE 4.12. Results when $k = 1$ and $\vartheta = 0.2$.

$\frac{P_\zeta}{P_{\zeta\ \mathrm{ref}}}$	$\frac{\alpha_{1\ \mathrm{het}}\ (k=1.0)}{\alpha_{1\ \mathrm{hom}}\ (k=0)}$	$\frac{\alpha_{2\ \mathrm{het}}\ (k=1.0)}{\alpha_{2\ \mathrm{hom}}\ (k=0)}$	$\frac{\alpha_{3\ \mathrm{het}}\ (k=1.0)}{\alpha_{3\ \mathrm{hom}}\ (k=0)}$	$\frac{\alpha_{4\ \mathrm{het}}\ (k=1.0)}{\alpha_{4\ \mathrm{hom}}\ (k=0)}$
−0.8	1.318	1.289	1.385	1.435
−0.6	1.363	1.326	1.411	1.453
−0.4	1.420	1.373	1.441	1.472
−0.2	1.497	1.433	1.474	1.492
0.0	1.604	1.512	1.513	1.515
0.2	1.766	1.624	1.557	1.539
0.4	2.046	1.796	1.609	1.566
0.6	2.681	2.097	1.672	1.594
0.8	3.782	2.813	1.749	1.625

TABLE 4.13. Results when $k = 2.5$ and $\vartheta = 0.2$.

$\frac{P_\zeta}{P_{\zeta\ \mathrm{ref}}}$	$\frac{\alpha_{1\ \mathrm{het}}\ (k=2.5)}{\alpha_{1\ \mathrm{hom}}\ (k=0)}$	$\frac{\alpha_{2\ \mathrm{het}}\ (k=2.5)}{\alpha_{2\ \mathrm{hom}}\ (k=0)}$	$\frac{\alpha_{3\ \mathrm{het}}\ (k=2.5)}{\alpha_{3\ \mathrm{hom}}\ (k=0)}$	$\frac{\alpha_{4\ \mathrm{het}}\ (k=2.5)}{\alpha_{4\ \mathrm{hom}}\ (k=0)}$
−0.8	1.402	1.364	1.484	1.545
−0.6	1.458	1.41	1.516	1.567
−0.4	1.53	1.468	1.552	1.59
−0.2	1.624	1.541	1.593	1.616
0.0	1.755	1.639	1.64	1.643
0.2	1.952	1.776	1.694	1.673
0.4	2.287	1.983	1.758	1.705
0.6	3.304	2.342	1.834	1.74
0.8	5.230	3.186	1.926	1.778

DOI: 10.14750/ME.2016.008

TABLE 4.14. Results when $k = 5$ and $\vartheta = 0.2$.

$\frac{P_\zeta}{P_{\zeta\ \mathrm{ref}}}$	$\frac{\alpha_{1\ \mathrm{het}}\ (k=5.0)}{\alpha_{1\ \mathrm{hom}}\ (k=0)}$	$\frac{\alpha_{2\ \mathrm{het}}\ (k=5.0)}{\alpha_{2\ \mathrm{hom}}\ (k=0)}$	$\frac{\alpha_{3\ \mathrm{het}}\ (k=5.0)}{\alpha_{3\ \mathrm{hom}}\ (k=0)}$	$\frac{\alpha_{4\ \mathrm{het}}\ (k=5.0)}{\alpha_{4\ \mathrm{hom}}\ (k=0)}$
−0.8	1.446	1.421	1.557	1.626
−0.6	1.509	1.474	1.594	1.651
−0.4	1.588	1.54	1.634	1.677
−0.2	1.692	1.623	1.681	1.706
0.0	1.835	1.733	1.734	1.736
0.2	2.049	1.887	1.795	1.769
0.4	2.413	2.118	1.867	1.805
0.6	4.117	2.517	1.951	1.844
0.8	7.109	3.447	2.054	1.885

Similar tendencies but with less significant differences are experienced for such semi-vertex angles when $\vartheta = 0.5$ as it turns out from Tables 4.15–4.18. Altogether, there is sill at least 22.6% distinction between the related frequencies. None of the ratios go below 1.

TABLE 4.15. Results when $k = 0.5$ and $\vartheta = 0.5$.

$\frac{P_\zeta}{P_{\zeta\ \mathrm{ref}}}$	$\frac{\alpha_{1\ \mathrm{het}}\ (k=0.5)}{\alpha_{1\ \mathrm{hom}}\ (k=0)}$	$\frac{\alpha_{2\ \mathrm{het}}\ (k=0.5)}{\alpha_{2\ \mathrm{hom}}\ (k=0)}$	$\frac{\alpha_{3\ \mathrm{het}}\ (k=0.5)}{\alpha_{3\ \mathrm{hom}}\ (k=0)}$	$\frac{\alpha_{4\ \mathrm{het}}\ (k=0.5)}{\alpha_{4\ \mathrm{hom}}\ (k=0)}$
−0.8	1.226	1.368	1.399	1.346
−0.6	1.256	1.379	1.415	1.360
−0.4	1.295	1.392	1.431	1.376
−0.2	1.344	1.409	1.446	1.393
0.0	1.411	1.431	1.462	1.411
0.2	1.505	1.459	1.475	1.431
0.4	1.650	1.494	1.488	1.453
0.6	1.908	1.539	1.500	1.477
0.8	2.528	1.596	1.512	1.503

TABLE 4.16. Results when $k = 1$ and $\vartheta = 0.5$.

$\frac{P_\zeta}{P_{\zeta\ \mathrm{ref}}}$	$\frac{\alpha_{1\ \mathrm{het}}\ (k=1.0)}{\alpha_{1\ \mathrm{hom}}\ (k=0)}$	$\frac{\alpha_{2\ \mathrm{het}}\ (k=1.0)}{\alpha_{2\ \mathrm{hom}}\ (k=0)}$	$\frac{\alpha_{3\ \mathrm{het}}\ (k=1.0)}{\alpha_{3\ \mathrm{hom}}\ (k=0)}$	$\frac{\alpha_{4\ \mathrm{het}}\ (k=1.0)}{\alpha_{4\ \mathrm{hom}}\ (k=0)}$
−0.8	1.282	1.467	1.525	1.432
−0.6	1.321	1.480	1.546	1.450
−0.4	1.369	1.497	1.565	1.469
−0.2	1.430	1.518	1.585	1.491
0.0	1.512	1.545	1.604	1.513
0.2	1.627	1.579	1.622	1.537
0.4	1.803	1.622	1.639	1.564
0.6	2.111	1.676	1.654	1.593
0.8	2.840	1.745	1.669	1.625

DOI: 10.14750/ME.2016.008

TABLE 4.17. Results when $k = 2.5$ and $\vartheta = 0.5$.

$\frac{P_\zeta}{P_{\zeta\ \mathrm{ref}}}$	$\frac{\alpha_{1\ \mathrm{het}}\ (k=2.5)}{\alpha_{1\ \mathrm{hom}}\ (k=0)}$	$\frac{\alpha_{2\ \mathrm{het}}\ (k=2.5)}{\alpha_{2\ \mathrm{hom}}\ (k=0)}$	$\frac{\alpha_{3\ \mathrm{het}}\ (k=2.5)}{\alpha_{3\ \mathrm{hom}}\ (k=0)}$	$\frac{\alpha_{4\ \mathrm{het}}\ (k=2.5)}{\alpha_{4\ \mathrm{hom}}\ (k=0)}$
−0.8	1.357	1.581	1.663	1.542
−0.6	1.405	1.598	1.685	1.564
−0.4	1.464	1.62	1.712	1.587
−0.2	1.539	1.646	1.734	1.613
0.0	1.638	1.68	1.756	1.64
0.2	1.779	1.722	1.778	1.669
0.4	1.988	1.773	1.799	1.701
0.6	2.354	1.839	1.817	1.736
0.8	3.21	1.921	1.835	1.777

TABLE 4.18. Results when $k = 5$ and $\vartheta = 0.5$.

$\frac{P_\zeta}{P_{\zeta\ \mathrm{ref}}}$	$\frac{\alpha_{1\ \mathrm{het}}\ (k=5.0)}{\alpha_{1\ \mathrm{hom}}\ (k=0)}$	$\frac{\alpha_{2\ \mathrm{het}}\ (k=5.0)}{\alpha_{2\ \mathrm{hom}}\ (k=0)}$	$\frac{\alpha_{3\ \mathrm{het}}\ (k=5.0)}{\alpha_{3\ \mathrm{hom}}\ (k=0)}$	$\frac{\alpha_{4\ \mathrm{het}}\ (k=5.0)}{\alpha_{4\ \mathrm{hom}}\ (k=0)}$
−0.8	1.416	1.657	1.735	1.624
−0.6	1.47	1.677	1.76	1.648
−0.4	1.537	1.701	1.787	1.675
−0.2	1.621	1.733	1.81	1.705
0.0	1.733	1.77	1.836	1.734
0.2	1.888	1.817	1.859	1.768
0.4	2.122	1.875	1.881	1.803
0.6	2.526	1.948	1.9	1.842
0.8	3.468	2.039	1.919	1.887

Tables 4.19–4.22 are filled with results under the assumption that $\vartheta = 1$. When $k = 0.5$, the load magnitude and direction do not have a real effect on the frequencies. In this respect the other three tables are more informative.

TABLE 4.19. Results when $k = 0.5$ and $\vartheta = 1$.

$\frac{P_\zeta}{P_{\zeta\ \mathrm{ref}}}$	$\frac{\alpha_{1\ \mathrm{het}}\ (k=0.5)}{\alpha_{1\ \mathrm{hom}}\ (k=0)}$	$\frac{\alpha_{2\ \mathrm{het}}\ (k=0.5)}{\alpha_{2\ \mathrm{hom}}\ (k=0)}$	$\frac{\alpha_{3\ \mathrm{het}}\ (k=0.5)}{\alpha_{3\ \mathrm{hom}}\ (k=0)}$	$\frac{\alpha_{4\ \mathrm{het}}\ (k=0.5)}{\alpha_{4\ \mathrm{hom}}\ (k=0)}$
−0.8	1.404	1.408	1.409	1.412
−0.6	1.405	1.408	1.409	1.412
−0.4	1.407	1.409	1.410	1.412
−0.2	1.408	1.410	1.410	1.412
0.0	1.411	1.411	1.411	1.413
0.2	1.414	1.412	1.412	1.413
0.4	1.421	1.414	1.412	1.413
0.6	1.433	1.416	1.413	1.414
0.8	1.469	1.419	1.414	1.414

DOI: 10.14750/ME.2016.008

TABLE 4.20. Results when $k = 1$ and $\vartheta = 1$.

$\frac{P_\zeta}{P_{\zeta\ \mathrm{ref}}}$	$\frac{\alpha_{1\ \mathrm{het}}\ (k=1.0)}{\alpha_{1\ \mathrm{hom}}\ (k=0)}$	$\frac{\alpha_{2\ \mathrm{het}}\ (k=1.0)}{\alpha_{2\ \mathrm{hom}}\ (k=0)}$	$\frac{\alpha_{3\ \mathrm{het}}\ (k=1.0)}{\alpha_{3\ \mathrm{hom}}\ (k=0)}$	$\frac{\alpha_{4\ \mathrm{het}}\ (k=1.0)}{\alpha_{4\ \mathrm{hom}}\ (k=0)}$
−0.8	1.168	1.330	1.401	1.443
−0.6	1.229	1.368	1.426	1.460
−0.4	1.302	1.411	1.453	1.478
−0.2	1.328	1.430	1.466	1.486
0.0	1.512	1.513	1.512	1.515
0.2	1.675	1.574	1.545	1.535
0.4	1.933	1.652	1.584	1.558
0.6	2.345	1.735	1.622	1.580
0.8	3.284	1.834	1.664	1.604

TABLE 4.21. Results when $k = 2.5$ and $\vartheta = 1$.

$\frac{P_\zeta}{P_{\zeta\ \mathrm{ref}}}$	$\frac{\alpha_{1\ \mathrm{het}}\ (k=2.5)}{\alpha_{1\ \mathrm{hom}}\ (k=0)}$	$\frac{\alpha_{2\ \mathrm{het}}\ (k=2.5)}{\alpha_{2\ \mathrm{hom}}\ (k=0)}$	$\frac{\alpha_{3\ \mathrm{het}}\ (k=2.5)}{\alpha_{3\ \mathrm{hom}}\ (k=0)}$	$\frac{\alpha_{4\ \mathrm{het}}\ (k=2.5)}{\alpha_{4\ \mathrm{hom}}\ (k=0)}$
−0.8	1.257	1.436	1.517	1.563
−0.6	1.326	1.479	1.544	1.582
−0.4	1.405	1.527	1.574	1.601
−0.2	1.507	1.59	1.605	1.622
0.0	1.639	1.639	1.639	1.643
0.2	1.819	1.707	1.676	1.665
0.4	2.085	1.791	1.714	1.688
0.6	2.533	1.878	1.757	1.713
0.8	3.554	1.987	1.803	1.738

TABLE 4.22. Results when $k = 5$ and $\vartheta = 1$.

$\frac{P_\zeta}{P_{\zeta\ \mathrm{ref}}}$	$\frac{\alpha_{1\ \mathrm{het}}\ (k=5.0)}{\alpha_{1\ \mathrm{hom}}\ (k=0)}$	$\frac{\alpha_{2\ \mathrm{het}}\ (k=5.0)}{\alpha_{2\ \mathrm{hom}}\ (k=0)}$	$\frac{\alpha_{3\ \mathrm{het}}\ (k=5.0)}{\alpha_{3\ \mathrm{hom}}\ (k=0)}$	$\frac{\alpha_{4\ \mathrm{het}}\ (k=5.0)}{\alpha_{4\ \mathrm{hom}}\ (k=0)}$
−0.8	1.324	1.516	1.602	1.651
−0.6	1.397	1.563	1.631	1.672
−0.4	1.483	1.614	1.664	1.692
−0.2	1.592	1.669	1.697	1.714
0.0	1.732	1.734	1.733	1.737
0.2	1.926	1.806	1.772	1.76
0.4	2.207	1.891	1.814	1.786
0.6	2.703	1.988	1.859	1.811
0.8	3.772	2.104	1.908	1.84

4.8.5.3. *Finite element computations.* For the forthcoming finite element computations we have used the same P_ζ loads in [N] both for the new model and for Abaqus. The tested geometry: $a = b = 10$ mm, $\rho_o/b = 30$, and the material is aluminium ($k = 0$ – see the material properties beforehand). $P_{\zeta\,\mathrm{ref}}$ denotes the critical load of the pinned-pinned beam according to (4.6.4) and (4.7.7). In Abaqus we have combined the Static, General and the Linear Perturbation, Frequency steps with $B22$ beam elements.

This comparison holds two vital basic differences we should mention. The first one is that the load-strain relationship is not known for Abaqus. The next one is the fact that the commercial software can only account for the load using a geometrically nonlinear model regarding the pre-stressing step. As a consequence, we expect more distinct results between the models as the load is increased. Despite all these remarks, some simple comparisons for $\vartheta = 0.2;\ 0.5;\ 1$ are provided in Tables 4.23–4.25.

DOI: 10.14750/ME.2016.008

TABLE 4.23. Results when $\vartheta = 0.2$.

$\frac{P_\zeta}{P_{\zeta\,\mathrm{ref}}}$	$\frac{\alpha_{1\text{ New model}}}{\alpha_{1\text{ Abaqus}}}$	$\frac{\alpha_{2\text{ New model}}}{\alpha_{2\text{ Abaqus}}}$	$\frac{\alpha_{3\text{ New model}}}{\alpha_{3\text{ Abaqus}}}$	$\frac{\alpha_{3\text{ New model}}}{\alpha_{3\text{ Abaqus}}}$
−0.8	0.815	1.132	1.136	1.321
−0.6	0.820	1.106	1.120	1.292
−0.4	0.835	1.080	1.105	1.265
−0.2	0.876	1.055	1.090	1.237
0.0	1.001	1.037	1.079	1.213
0.2	1.575	1.018	1.071	1.198
0.4	0.666	0.779	0.965	1.164

TABLE 4.24. Results when $\vartheta = 0.5$.

$\frac{P_\zeta}{P_{\zeta\,\mathrm{ref}}}$	$\frac{\alpha_{1\text{ New model}}}{\alpha_{1\text{ Abaqus}}}$	$\frac{\alpha_{2\text{ New model}}}{\alpha_{2\text{ Abaqus}}}$	$\frac{\alpha_{3\text{ New model}}}{\alpha_{3\text{ Abaqus}}}$	$\frac{\alpha_{3\text{ New model}}}{\alpha_{3\text{ Abaqus}}}$
−0.8	1.009	0.857	1.162	1.021
−0.6	1.008	0.879	1.137	1.021
−0.4	1.007	0.913	1.097	1.022
−0.2	1.006	0.956	1.054	1.023
0.0	1.006	1.010	1.004	1.025
0.2	1.008	1.083	0.947	1.029
0.4	1.013	1.186	0.881	1.036
0.6	1.031	1.347	0.804	1.047

TABLE 4.25. Results when $\vartheta = 1$.

$\frac{P_\zeta}{P_{\zeta\,\mathrm{ref}}}$	$\frac{\alpha_{1\text{ New model}}}{\alpha_{1\text{ Abaqus}}}$	$\frac{\alpha_{2\text{ New model}}}{\alpha_{2\text{ Abaqus}}}$	$\frac{\alpha_{3\text{ New model}}}{\alpha_{3\text{ Abaqus}}}$	$\frac{\alpha_{3\text{ New model}}}{\alpha_{3\text{ Abaqus}}}$
−0.8	1.218	1.084	1.063	1.059
−0.6	1.175	1.066	1.050	1.047
−0.4	1.126	1.047	1.036	1.035
−0.2	1.069	1.027	1.022	1.023
0	1.002	1.004	0.996	1.011
0.2	0.921	0.979	0.991	0.998
0.4	0.821	0.952	0.964	0.986
0.6	0.690	0.923	0.958	0.974

In general these three tables show that the models coincide really well for unloaded beams. Further, the differences are less when the force is a tensile one. The first frequencies seem to be the furthest from each other between the two models regarding the whole loading range. When the amplitude of the load is greater, the differences as well become greater as expected in advance. Altogether, the correlation is quite good between $P_\zeta/P_{\zeta\,\mathrm{ref}} \in (-0.8, \ldots, 0.4)$.

4.9. Summary of the results achieved in Section 4

I have investigated the vibrations of curved beams with cross-sectional inhomogeneity, subjected to a vertical force at the crown point. The most important results are as follows:

1. I have derived the governing equations of those boundary value problems which make it possible to determine how a radial load affects the natural frequencies. For pinned-pinned and fixed-fixed beams I have determined the Green function matrices assuming that the beam is prestressed by a central load. When computing these matrices

DOI: 10.14750/ME.2016.008

I had to take into account that the system of ordinary differential equations that govern the problem is degenerated.

2. Making use of the Green function matrices, I have reduced the self-adjoint eigenvalue problems set up for the eigenfrequencies to eigenvalue problems governed by homogeneous Fredholm integral equation systems – four homogenous Fredholm integral equation systems have been established. These integral equations can directly be used for those dead loads, which result in a constant, otherwise either negative or positive axial strain on the E-weighted centerline. I have replaced these eigenvalue problems with algebraic ones and solved them numerically.
3. It has turned out that the square of the quotient of the second loaded and unloaded natural frequencies depends almost linearly on the axial strain-critical strain ratio and is actually independent of the curved beam geometry and material inhomogeneity for pinned-pinned beams. The relations for fixed-fixed beams are more dependent on the central angle and are rather quadratic. In the knowledge of the load-strain relationship we can determine the strain due to the load, and then the natural frequencies of the loaded structure. If the strain is zero, we get back those results which are valid for the free vibrations.
4. In some cases, the numerical results are verified by commercial finite element calculations and experiments as well. According to these, it turns out that the numerical model approximates the eigenfrequencies with a good accuracy.

DOI: 10.14750/ME.2016.008

CHAPTER 5

Outline

I remark that the text in this chapter coincides more or less with the text of the Synopsis. The author's aim to provide a summary in this way is twofold. First of all, I intend to give the reader the opportunity to briefly survey the preliminaries and objectives of this work: what methodologies have been used during the solution, what results have been attained and finally, what my future research plans are. Secondly, I might be wrong but I think that it is worthy to add such a summary to the main text since the related, though, separate Synopsis will probably be preserved with less probability.

5.1. Preliminaries

As regards the preliminaries I again point out that in recent decades, curved beams have been widely used in numerous engineering applications as load carrying members. Let us just think about arch bridges, roof structures or stiffeners in the aerospace or marine industry. Scientists and designers are always being interested in the mechanical behaviour (stresses, displacements, load carrying capabilities, etc.) of such structural elements to prevent failure (e.g.: yielding, buckling, self-excited vibrations) under given loads and circumstances. Therefore, there are a number of books, articles and other scientific works delivering relevant results, see, e.g., [**8**,**13**,**22**] for calculating the stresses, [**41**,**61**,**73**] for stability problems and [**41**, **82**, **91**] as regards the issue of vibrations.

Nowadays not only homogeneous members but inhomogeneous or heterogeneous ones are also getting more and more widespread. These beams can have more advantageous properties compared to homogeneous ones, such as reduced weight; improved corrosion, fatigue and chemical resistance and higher strength. A class of nonhomogeneous material composition is the so-called cross-sectional inhomogeneity. It means that the material parameters – say, Young's modulus E or the Poisson ratio ν – have symmetric distribution with respect to the cross-sectional axis ζ. This distribution is either continuous or constant over each segment (layer). Some illustrative examples are shown in Figure 5.1. In this way it

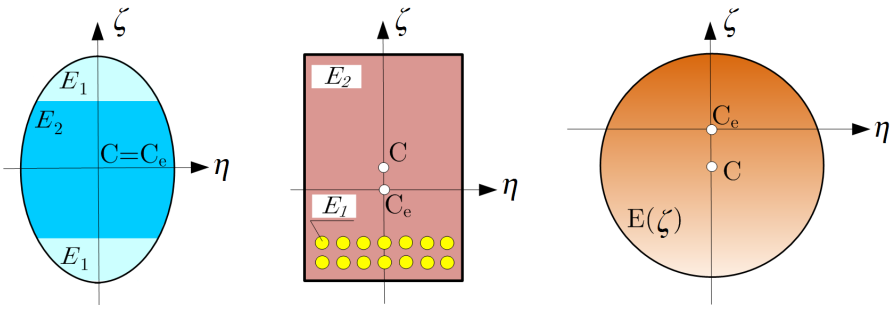

FIGURE 5.1. The concept of cross-sectional inhomogeneity.

is possible to simply model composites, multilayered or functionally graded materials. For planar, elastic, isotropic circular beams of this kind, I intend to focus on three mechanical issues: stresses, stability and vibrations.

DOI: 10.14750/ME.2016.008

5.1.1. Some mechanical issues of circular beams. As regards the mechanical behaviour of curved beams, investigations began in the 19^{th} century. The foremost load-displacement relationship was established by Bresse (1854). Winkler was the first to derive a formula for the normal stress distribution (1858) and Grashof is known for developing an equilibrium method (1878) for the calculation of the shear stresses. These results are well collected in the works [**8**, **11**].

The interest is still live, as new models for different loading cases, geometries, and even for nonhomogeneous materials are continuously being published. For instance, Ascione and Fraternali [**18**] use the finite element method to obtain solutions for the stresses in perfectly bonded layered curved beams. They assume that each layer is a Timoshenko beam. They compute interlaminar, normal and shear stresses as well. Segura and Armengaud [**19**] propose simple analytical solutions for the normal and shearing stress distributions in composites under bending loads. The normal stress distribution due to the bending moment and the axial force is hyperbolic over the cross-section. The authors have also managed to extend Bredt's formula for composite curved beams to get the shear stresses. Article [**25**] by Baksa and Ecsedi provides formulae for the stress distributions in straight beams with cross-sectional inhomogeneity under pure bending. Book [**8**] by Kozák and Szeidl also deserves mentioning as it presents how to derive the stresses in straight beams with cross-sectional inhomogeneity and also gathers formulae for the stress distributions in homogeneous curved beams. According to the literature review, it seems that curved beams with cross-sectional inhomogeneity have not yet been investigated.

Another popular topic is the buckling behaviour of beams. In 1757, Euler derived his well-known formula for the critical (buckling) load of straight bars under compression. Considering the behaviour of curved members, stability investigations began much later: around the beginning of the 19^{th} century. The early literature ignored the extensibility of the centerline – see, e.g., [**31**] by Hurlbrink. Then Chwalla and Kollbrunner [**32**] showed that account for the axial strain can notably affect the critical load. After the 1950s, work became more intensive. Szeidl in his PhD thesis [**41**] determines the critical load of circular beams under radial dead load given that the Fourier series of the load is known. Paper [**36**] by DaDeppo and Schmidt provides solution to the buckling load of deep circular beams whose loading is a vertical force. The authors have shown that quadratic terms should be accounted in the analysis.

When dealing with shallow circular beams Pi, Bradford et al. have pointed out [**51**, **61**] that account even for the pre-buckling deformations is likewise essential not to overestimate the permissible load. The authors have been intensively investigating the stability of homogeneous (shallow and deep) arches using their analytical model, which accounts for all the above mentioned properties. Nonlinearities are considered through the square of the infinitesimal rotations. The authors have evaluated their model for various loads (distributed, concentrated) and boundary conditions (pinned, fixed, elastic supports, mixed supports, etc.). Bateni et al. [**73**] use the same kinematical hypotheses as presented in [**61**] to analyse shallow arches under a concentrated load. However, their model is valid for functionally graded materials.

The vibrations of curved beams has been a field of interest as of the 1920s. Den Hartog was the first to investigate the free vibrations of such structural elements (1928). Early but still notable contributions – assuming the inextensibility of the centerline – were provided in [**76**, **78**].

Szeidl in his PhD thesis [**41**] investigates how the extensibility of the centerline can change the eigenfrequencies of the free vibrations of planar circular beams under a constant radial load. The author achieves results using the Green function matrix, with what, the related boundary value problem is transformed to a problem governed by Fredholm integral

DOI: 10.14750/ME.2016.008

equations. Kang et al. [**81**] obtain the frequencies (eigenvalues) for the in- and out-of-plane vibrations of circular Timoshenko arches given that rotatory inertia and shear deformations are accounted. Tüfekçi and Arpaci [**82**] managed to gain exact analytical solutions for the in-plane free harmonic vibrations of circular arches. The authors account for the extensibility of the centerline and also for the transverse shear and rotatory inertia effects. Kovács [**91**] deals with layered arches assuming the possibility of both perfect and even imperfect bonding between any two nearby layers.

In the reviewed literature there are some sources, which use the Green function to tackle some dynamic issues. Szeidl et al. [**100**] determine the natural frequencies of pinned and fixed circular arches using this technique. Kelemen [**101**] extends the former model. She computes the natural frequencies as functions of a constant distributed radial load. Li et al. [**103**] consider the forced vibrations of straight Timoshenko beams when these are under a time harmonic concentrated load. Damping effects at the ends are accounted.

5.2. Objectives

Based on the reviewed open literature, the main objectives of the candidate are related to cross-sectional inhomogeneity and are detailed in the forthcoming.

Objective 1: Generalization of some classical results valid for homogeneous materials. These investigations are aimed to lead to the following results:
- Generalization of two elementary relationships (valid for homogeneous curved beams) – that provide the normal stress caused by an axial force and a bending moment – for curved beams with cross-sectional inhomogeneity.
- Setting up a further formula for computing the shear stress.
- In addition, a formula for the shear correction factor is also to be derived.
- The results obtained for the stresses should be compared with those obtained by finite element computations.

Objective 2: On the basis of the literature overview, no investigations have been carried out concerning the stability problem of (shallow) circular beams under the assumption of cross-sectional inhomogeneity. Within the frames of what has been mentioned above, Objective 2 is summarized in the following items.
- I intend develop a new nonlinear model for non-strictly shallow curved beams from the principle of virtual work. It is aimed to be more accurate than those presented in [**61**, **74**] and should be applicable to cross-sectional inhomogeneity as well.
- I would like to evaluate the new model for pinned-pinned, fixed-fixed and rotationally restrained supports provided that the beam is subjected to a central load at the crown point. This would involve the determination of the critical load both for symmetric snap-through and antisymmetric bifurcation buckling.
- At the same time, the typical buckling ranges and its endpoints are also of interest.
- Comparison of the results with those available in the literature and with the Abaqus commercial finite element software should also be performed.

Objective 3: is related to the in-plane vibrations of loaded circular beams with cross-sectional inhomogeneity. I intend
- to derive those boundary value problems, which can make it clear how a radial load affects the natural frequencies of pinned-pinned and fixed-fixed beams,
- to construct the corresponding Green function matrices by taking into account that the central load at the crown point can either be compressive or tensile (four Green function matrices are to be determined),

DOI: 10.14750/ME.2016.008

– to reduce the eigenvalue problems set up for the natural frequencies (which depend on the load) to eigenvalue problems governed by homogeneous Fredholm integral equation systems (four systems should be established),
– to replace these eigenvalue problems with algebraic ones and to solve them numerically,
– to clarify how the vertical force at the crown point affects the frequencies of the vibrations (when this load is removed, I have to get back the results valid for free vibrations),
– to verify some results by Abaqus and/or experiments.

5.3. Investigations performed

While establishing the mechanical models, the validity of the following common hypotheses were considered:

– there is cross-sectional inhomogeneity,
– the displacements and deformations are sufficiently small,
– the beam models are one-dimensional,
– the (E-weighted) centerline remains in its own plane,
– the curved beam has uniform cross-section and constant initial radius,
– the cross-section is symmetric,
– the classical single-layer theory applies,
– the magnitude of the normal stress σ_ξ is much greater than that of the stress components σ_η and σ_ζ.

When deriving simple closed-form solutions for the normal stress distribution, the validity of the Euler-Bernoulli theory is assumed. Such loads that cause bending action and axial strain can be applied (with shearing effects neglected). First, an 'exact' formula is derived. Then further transformations and simplifications lead to the generalized form of the Grashof (Winkler) formula. Accordingly, the bending moment has a constant and hyperbolic effect on the normal stress distribution while the axial force causes constant stress. A further achievement is another formula for the normal stress and for the location of the neutral axis in the case of pure bending – both are dependent on the material composition.

The shear stresses are obtained by using equilibrium equations for a portion of the beam (i.e. the kinematical relations are not completely satisfied). The result is the extension of Grashof's equilibrium method for cross-sectional inhomogeneity. The advantage of this procedure is the relatively simple outcome. Moreover, a formula is proposed for the shear correction factor.

The static stability model is based on the Euler-Bernoulli hypothesis. The kinematical assumption contains a quadratic term, that is, the square of the infinitesimal rotations. Given that the investigated structural element is primarily a shallow arch, the effect of the tangential displacements on the former quantity is neglected. As the pre-buckling deformations are substantial, the change in the equilibrium state due to the deformations is accounted. The governing equilibrium equations under concentrated and distributed loads for non-uniform rotational end restraints are established using the principle of virtual work. However, solution is calculated only when there is a concentrated dead load exerted at the crown point. Due to the symmetry properties, a half-beam model is examined. The nonlinear axial strain on the centerline is constant under these conditions. In this way, a fourth-order ordinary differential equation governs the problem mathematically, which can be solved in closed-form. The former statements are valid even for the incremental quantities, which are measured after the loss of stability.

DOI: 10.14750/ME.2016.008

Semi-analytical evaluations are carried out for symmetrically supported pinned, fixed and rotationally restrained circular beams. These evaluations, on the one hand, include the determination of the pre-buckling equilibrium in terms of the material, geometry and loading. On the other hand, it is also pointed out that there are two possible buckling modes: antisymmetric bifurcation buckling with no strain increment and symmetric snap-through mode with a changing centerline length. The related critical strains and therefore the critical loads are determined in terms of the geometry. It is found that there are beams for which there is no buckling. As for the others it is also sought which of the two buckling modes dominates in terms of the geometry.

For pinned beams, mostly antisymmetric buckling can be expected. However, for fixed ones the symmetric type governs. When the spring stiffness of the supports are (equal to zero) [tend to infinity] we get back the solutions valid for (pinned) [fixed] beams. To better understand the behaviour of the members, the primary equilibrium paths are also plotted for each typical buckling range. Commercial finite element computations and comparison with the literature indicate that the results can be considered as valid for all checked supports and even for not strictly shallow arches. Simple numerical examples show that material heterogeneity can have a significant impact on the permissible loads, therefore account for this property seems inevitable.

The vibration analysis is based on linearized strains and the Euler-Bernoulli hypothesis. At the same time, the effect of the tangential displacements on the rigid body rotations are kept so that the results are applicable for deep arches as well. The natural frequencies are sought and that how a central concentrated load changes these frequencies. The equilibrium equations are derived from the principle of virtual work for a beam under concentrated and distributed loads. The strain the concentrated load causes is constant on the centerline. The pre-buckling (initial) equilibrium is governed by ordinary differential equations.

As for the dynamic part of the issue, the forces of inertia are accounted and undamped time harmonic vibrations are considered. The derivations lead to an eigenvalue problem where the square of the eigenfrequencies are proportional to these eigenvalues. Solutions are sought for those cases when the central vertical concentrated force causes compression and tension.

The Green function matrix is constructed in closed-form for both loading cases of pinned and fixed beams. The application of this technique requires linear ordinary differential equations with closed-form general solutions and self-adjoint eigenvalue problems. With the corresponding Green functions in hand, each eigenvalue problem governed by ordinary differential equations and the corresponding boundary conditions can be replaced by homogeneous Fredholm integral equations and following the procedure presented in [**41**], they can numerically be reduced to algebraic equation systems (eigenvalue problems).

When dealing with the vibrations, we must also be aware of the critical load because if this limit is reached, buckling occurs. So the critical (bifurcation) loads are also determined. Since in practise, the load is the known quantity and the model has the strain as parameter, a unique relationship between these quantities is provided.

Results are evaluated both for the free and loaded vibrations and are compared with the literature and commercial finite element software computations. Moreover, colleagues from Romania contributed with some measurements for the free vibrations of fixed beams. Thanks to their efforts it became possible to compare some numerical results also with experiments to confirm the validity of the model.

Regarding the outcomes, the quotients of the even unloaded frequencies of curved and straight beams with the same length and material only depend on the central angle and the supports, while the odd ones are also functions of the cross-sectional geometry and material distribution. It turns out that for pinned beams the quotient of the square of the

DOI: 10.14750/ME.2016.008

second loaded and unloaded frequencies (increase) [decrease] almost linearly under (tension) [compression] in terms of the strain-critical strain ratio and the central angle, geometry and material do not affect these relations. The experiences are similar but more likely quadratic and more dependent on the geometry for fixed members. The effect of the material composition on the frequencies is illustrated through simple numerical examples.

5.4. Summary of the novel results

The first objective was to provide simple formulae for calculating the stress state of heterogeneous curved beams by generalizing the formulae valid for homogeneous curved beams. These involved the expressions of the normal stress and shear stress. The shear correction factor was also determined. The most important results are gathered in

Statement 1.

1.a. I have derived an exact and two approximative relationships that provide the normal stress caused by an axial force and a bending moment in curved beams with cross-sectional inhomogeneity. The latter two are generalizations of well-known relationships valid for homogeneous curved beams. A further formula has been established for computing the shearing stress.

1.b. In addition, a formula for the shear correction factor has also been derived. The results obtained by the relationships set up for the stresses are compared with finite element computations. A good agreement is found between the different models.

As regards the corresponding publications see references {8}, {12} and {19} in Section 5.8. Though the title is the same for {12} and {19}, the former is more detailed.

Statement 2.

I have investigated the in-plane elastic static stability of circular beams with cross-sectional inhomogeneity provided that the beam is subjected to a vertical force at the crown point.

2.a. I have derived a new model both for the pre-buckling and post-buckling radial displacements - in the later case both for symmetric and antisymmetric buckling. Cross-sectional inhomogeneity is implied in these equations via the parameter m (which is a function of the E-weighted radius of gyration and the radius of curvature). The equations I have established are more accurate than those recently set up by Bradford et al. in [**56**, **61**] for homogeneous and by Bateni and Eslami [**73**] for functionally graded material. Though I neglected the effect of the tangential displacements on the angle of rotation, papers [**56**, **61**] also apply this assumption. Altogether, as the new model uses less neglects, the results for the critical load are more accurate than those published in the formerly cited works.

2.b. Solutions are provided for (a) pinned-pinned, (b) fixed-fixed and (c) rotationally restrained beams. For each case I have determined what character the stability loss can have: no buckling, limit point buckling, bifurcation buckling after limit point buckling, bifurcation buckling precedes limit point buckling. The endpoints of the corresponding intervals are not constant in the modified slenderness λ as in the previous models but further depend on the parameter m (on the E-weighted radius of gyration and the radius of curvature).

2.c. Comparisons have been made with previous results and finite element computations as well. These prove that the results obtained are applicable also for not strictly shallow beams, up until the semi-vertex angle ϑ is not greater than 1.5. For small central angles the differences between the models are, in general, smaller than for greater central angles.

DOI: 10.14750/ME.2016.008

2.d. Cross-sectional inhomogeneity can have a serious effect on the critical load. This is proven via a simple example.

As regards the corresponding publications see references {2}, {3}, {5}, {10}, {11}, {13}-{18} and {20} in Section 5.8.

Statement 3.
I have investigated the vibrations of circular beams with cross-sectional inhomogeneity, subjected to a vertical force at the crown point.

3.a. I have derived the governing equations of those boundary value problems which make it possible to determine how a radial load affects the natural frequencies. For pinned-pinned and fixed-fixed beams I have determined the Green function matrices assuming that the beam is prestressed by a central load. When computing these matrices I had to take into account that the system of ordinary differential equations that govern the problem is degenerated.

3.b. Making use of the Green function matrices, I have reduced the self-adjoint eigenvalue problems set up for the eigenfrequencies to eigenvalue problems governed by homogeneous Fredholm integral equation systems – four homogenous Fredholm integral equation systems have been established. These integral equations can directly be used for those dead loads, which result in a constant, otherwise either negative or positive axial strain on the E-weighted centerline. I have replaced these eigenvalue problems with algebraic ones and solved them numerically.

3.c. It has turned out that the square of the quotient of the second loaded and unloaded natural frequencies depends almost linearly on the axial strain-critical strain ratio and is actually independent of the curved beam geometry and material inhomogeneity for pinned-pinned beams. The relations for fixed-fixed beams are more dependent on the central angle and are rather quadratic. In the knowledge of the load-strain relationship we can determine the strain due to the load, and then the natural frequencies of the loaded structure. If the strain is zero, we get back those results which are valid for the free vibrations.

3.d. In some cases, the numerical results are verified by commercial finite element calculations and experiments as well. According to these, it turns out that the numerical model approximates the eigenfrequencies with a good accuracy.

As regards the corresponding publications see references {1}, {4}, {6}, {7}, {9}, {11} and {20} in Section 5.8.

5.5. Magyar nyelvű összefoglaló (Summary in Hungarian)

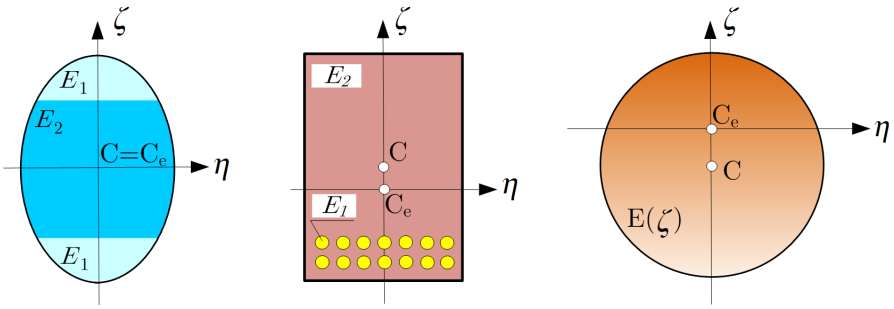

FIGURE 5.2. Néhány példa keresztmetszeti inhomogenitásra.

Napjainkban igen elterjed a görbült középvonalú rudak alkalmazása mérnöki szerkezetekben. Gondoljunk például az ívelt kialakítású hídszerkezetekre, tetőszerkezetekre, vagy például

DOI: 10.14750/ME.2016.008

repülőgépek egyes merevítő elemeire. Az ilyen rudak mechanikai viselkedésének leírásával a XIX. századtól kezdődően számos kutató foglalkozott. Az újabbnál-újabb modellek mind egyre pontosabban és általánosabban írják le ezen szerkezeti elemek viselkedését, úgy mint a feszültségek eloszlását [**8**, **13**, **25**], a rudak stabilitását [**22**, **24**, **41**], vagy épp rezgéseit [**6**,**41**,**91**,**101**,**116**]. Az előző, teljesség igénye nélkül összegyűjtött irodalmi hivatkozások mind magyar szerzők munkái.

Ma már nem csak homogén, hanem heterogén, vagy inhomogén anyagú görbe rudak legyártására is egyre gazdaságosabb lehetőség nyílik, elősegítve ezek terjedését. Az ilyen kialakítású rudak olyan előnyös tulajdonságokkal rendelkezhetnek homogén társaikkal szemben, mint például a kisebb tömeg, magasabb szilárdság, vagy a jobb korrózióállóság. Keresztmetszeti inhomogenitásnak nevezzük azt a fajta anyagi heterogenitást, amikor az anyagjellemzők, úgy, mint a rugalmassági modulusz E, vagy a Poisson tényező ν csak a keresztmetszeti koordinátáktól függenek, továbbá a keresztmetszet ζ tengelyére vonatkozóan szimmetrikus eloszlásúak. Az eloszlás lehet folytonos, vagy szakaszonként folytonos. Néhány példát szemléltet az 5.2 ábra.

A fent említett tulajdonságokkal rendelkező körívalakú rudakkal kapcsolatban a jelen dolgozat három területen ért el új eredményeket. Ezeket foglaljuk most röviden össze.

Számos modell készült, amelyek a feszültségeloszlás számítására nyújtanak viszonylag egyszerű, zárt alakú képleteket. Ugyanakkor az áttekintett irodalomban nem találtam olyan modellt, amely keresztmetszeti inhomogenitású görbe rudakban kialakuló feszültségek eloszlására irányuló, egyszerű kézi számításokra alkalmas képleteket mutatnának be. Ehhez kapcsolódóan az új eredmények:

- levezettem egy egzakt és általánosítottam ét, homogén anyagú görbe rúdra vonatkozó normálfeszültségi képletet keresztmetszeti inhomogenitás esetére, amennyiben a terhelés rúderő és/vagy hajlítónyomaték.
- Levezettem a nyírófeszültség számítására egy összefüggést egyensúlyi egyenletekből.
- A nyírási korrekciós tényezőre is felállítottam egy formulát.
- A feszültségek eloszlását az említett tulajdonságú rudakra ellenőriztem az Abaqus kereskedelmi végeselemes szoftver számításaival és jó egyezést találtam a tesztelt geometriáknál.

Keresztmetszeti inhomogenitású körívalakú síkgörbe rudak rugalmas, statikai stabilitásra vonatkozóan

- levezettem egy új modellt, ami pontosabb és általánosabb az irodalomban megtalálható, alig néhány évvel ezelőttinél [**56**, **61**].
- A modell segítségével mind az antiszimmetrikus bifurkációs, mind a szimmetrikus, átpattanás formájában bekövetkező kihajlás jellemezhető, amennyiben a terhelés a koronapontban működő függőleges irányú erő, a támaszok pedig szimmetrikusak: két végén csuklóval megtámasztott, befogott, illetve spirálrugóval megfogott rudakkal foglalkoztam.
- Meghatároztam a kritikus terhelések értékét és a jellemző kihajlási tartományokat is a geometria és a támaszok függvényében.
- Habár az érintőirányú elmozdulások hatását elhanyagoltam a szögelfordulás számításánál (lapos rudaknál ez szokásos feltevés), ennek ellenére a modell nem csak szigorúan véve lapos rudaknál közelíti jól a megengedhető terhelést. Ezt támasztják alá korábbi irodalmi eredmények és az Abaqus szoftver számításai is.

Keresztmetszeti inhomogenitású körívalakú síkgörbe rudak rezgéseivel kapcsolatban

- levezettem azokat a peremérték-feladatokat, amelyek megoldásával meghatározhatók a rúd sajátfrekvenciái.

DOI: 10.14750/ME.2016.008

- Két végén csuklóval megtámasztott, illetve befogott rudakra meghatároztam zárt alakban a Green-féle függvénymátrixokat, amelyek segítségével lehetőség nyílik megvizsgálni a koronapontban működő koncentrált terhelés frekvenciaspektrumra gyakorolt hatását.
- A Green-féle függvénymátrixok segítségével az önadjungált sajátértékfeladatokat homogén Fredholm integrálegyenlet-rendszerrel kifejezhető feladatokra vezettem vissza.
- Ezeket a sajátérték-feladatokat algebrai egyenletrendszerré alakítva megoldottam.
- Az eredmények szerint amennyiben a terhelés húzó/nyomóerő, a második terhelt frekvenciák és a szabadrezgésekhez tartozó második frekvenciák négyzetének hányadosa csuklós rudaknál igen jó közelítéssel lineárisan függ a nyúlás/kritikus nyúlás hányadostól és független a geometriától. Befogott rudaknál nagyobb a geometria befolyása erre a jellemzőre és ez a kapcsolat inkább kvadratikus.
- Amennyiben a terhelő koncentrált erő zérus, vagyis nulla a középvonal nyúlása, visszakapom a szabadrezgésekhez tartozó sajátfrekvenciákat.
- Abaqus számítások, korábbi irodalmi eredményekkel való összevetés, illetve néhány mérési eredmény igazolja az eljárást és az eredmények helyességét.

A Bíráló Bizottság által elfogadott tézisek

1. Tézis

1.a. Levezettem egy egzakt és két közelítő összefüggést a normálfeszültség számítására amennyiben a keresztmetszeti inhomogenitású görbe rúd terhelése rúderő és hajlítónyomaték. A két közelítő modell jól ismert, homogén esetre vonatkozó összefüggések általánosításai. Származtattam egy további formulát a nyírófeszültség számítására.

1.b. Ezeken felül a nyírási korrekciós tényezőre is felírtam egy összefüggést. A feszültségeloszlásokra kapott új képletek eredményeit összehasonlítottam néhány végeselemes számítással. Jó egyezés tapasztalható.

2. Tézis

Keresztmetszeti inhomogenitású síkgörbe rudak rugalmas stabilitását vizsgáltam, amennyiben a rúd terhelése koronaponti koncentrált, függőleges irányú merev erő.

2.a. Levezettem egy új modellt keresztmetszeti inhomogenitású körívalakú rudak stabilitásának vizsgálatára. Ez mind a stabilitásvesztés előtti, mind az azt követő (szimmetrikus, vagy antiszimmetrikus) egyensúlyi helyzetet pontosabban közelíti a korábbi, homogén [**56**, **61**], vagy funkcionálisan gradiens anyagra érvényes [**73**] irodalmi modelleknél. Bár elhanyagoltam a tangenciális irányú elmozdulások hatását a forgásokra – a [**56**, **61**] cikkek szintén élnek ezzel a feltevéssel – összességében az új modell kevesebb egyszerűsítést alkalmaz, következésképp a kritikus terhelésekre vonatkozó eredmények (összefüggések) pontosabbak, mint a korábbi munkák eredményei.

2.b. Kiértékeltem a modellt (a) két végén csuklóval megtámasztott; (b) két végén befogott; (c) két végén spirálrugóval megtámasztott rudakra. Meghatároztam a lehetséges stabilitási tartományokat (nincs stabilitásvesztés, szimmetrikus/antiszimmetrikus stabilitásvesztés a domináns). A jellemző tartományok határai nem állandóak a λ módosított karcsúsági tényezőben, mint a korábban is említett modelleknél, hanem függenek az m paramétertől is, tehát az E-vel súlyozott inerciasugártól és a görbületi sugártól is.

2.c. Összehasonlításokat végeztem korábbi modellekkel és végeselemes számításokkal. Ezek alapján a modell nem csak szigorúan véve lapos rudaknál közelíti jól a megengedhető terhelést, hanem egészen három radián nyílásszögig. A korábbi modellel szemben kisebbek az eltérések, ha kisebb a nyílásszög.

DOI: 10.14750/ME.2016.008

2.d. A keresztmetszeti inhomogenitásnak jelentős hatása lehet a kritikus terhelésre – ezt az állítást egyszerű számpéldával illusztráltam.

3. Tézis

Keresztmetszeti inhomogenitású görbe rudak rezgéseit is vizsgáltam, amennyiben koronaponti koncentrált, függőleges irányú erő a terhelés.

3.a. Olyan önadjungált sajátérték-feladatokat vezettem le, amelyek megoldásával meghatározható hogyan befolyásolja a sajátfrekvenciákat a radiális terhelés. Csuklós és befogott rúdra egyaránt meghatároztam a Green-féle függvénymátrixokat feltéve, hogy a rúd elő van terhelve egy koronaponti koncentrált erővel. Itt figyelembe kellett venni, hogy a közönséges differenciálegyenletek elfajulók.

3.b. A Green-féle függvénymátrixokkal az önadjungált sajátérték-feladatokat homogén Fredholm integrálegyenletekre vezettem vissza, amikből a sajátfrekvenciákat meghatároztam. Ez összesen négy, homogén Fredholm integrálegyenlet-rendszert jelent. Az integrálegyenletek minden olyan merev (konzervatív) terhelésre használhatók, amelyekre nézve állandó a középvonal menti fajlagos nyúlás – ez lehet akár pozitív, akár negatív előjelű mennyiség. A sajátérték-feladatokat algebrai egyenletrendszerrel helyettesítettem és numerikusan megoldottam.

3.c. A második terhelt és terheletlen frekvenciák négyzetének hányadosa jó közelítéssel lineárisan függ a középvonal nyúlása/kritikus nyúlás hányadostól és független a geometriától, valamint az anyagi összetételtől csuklós rudaknál. Befogott esetben ugyanakkor a kapcsolat inkább kvadratikus és a nyílásszögnek érezhető befolyása van az eredményekre. A terhelés-nyúlás kapcsolat ismeretében meghatározható az adott erőhöz tartozó nyúlás értéke és így a terhelt rúd sajátfrekvenciái. Ha zérus a nyúlás, visszakapjuk a szabadrezgésekhez tartozó frekvenciákat.

3.d. A numerikus számítási eredményeket néhány esetben végeselemes számításokkal és kísérleti eredményekkel is összevetettem. Ezek alapján a modell jól közelíti a frekvenciákat.

5.6. Possible application of the results

The results achieved can be applied to homogeneous or heterogeneous circular beams as structural elements to predict the behaviour (possible failure regarding the stresses, stability and vibrations) of the members under given circumstances. With new and improved models continuously being made, it is possible to gain more and more accurate results and thus, reduce uncertainties and save costs.

Some of the results could be harnessed in the education as nowadays nonhomogeneous materials are gradually gathering ground. Primarily, I am thinking about the simple closed-form solutions for the normal and shear stress distributions in circular beams with cross-sectional inhomogeneity. Moreover, a simplified form of the stability model could as well be included in the curriculum to broaden the student's view of the phenomenon of buckling, which is many times restricted to classical Euler column.

Moreover, the models and solutions obtained could be used for benchmark purposes to verify other models.

5.7. Future research

Based on the presented models, several additional improvements and generalizations could be made. In the simplest way, by changing the loading and/or the supports – even considering not symmetric conditions, or three-hinged beams – so that the investigations could be extended even more. Research is in progress for the vibration model when the

DOI: 10.14750/ME.2016.008

beam is pinned at the left end and is fixed at the right end and there are equal rotational end restraints.

Keeping the hypotheses of the presented stability model, an interesting question is how the buckling loads, buckling shapes and the typical ranges change if the beam is subjected to a radial or vertical load at a point, other than the crown point. The post-buckling behaviour might also be worthy of dealing with and moreover, the dynamic behaviour could also be modeled some way. It would also be desirable to develop a one-dimensional finite element model, taking finite strains and/or rotations into account when dealing with the stability problem.

But such questions could as well be arisen how to harness the experiences of presented models to tackle some issues of curved but not circular beams, out-of plane problems, bi-modular materials, to account for shear deformations, interlayer slip, etc.

It would also be satisfying to verify the results with experiments. Concerning this idea, there is an ongoing cooperation with some generous colleagues of the Transilvania University of Braşov.

5.8. Related publications by the author

Journal articles in foreign language

{1} L. Kiss and Gy. Szeidl: Vibrations of pinned-pinned heterogeneous circular beams subjected to a radial force at the crown point. *Mechanics Based Design of Structures and Machines: An International Journal*, **43**(4), 2015, 424-449.

{2} L. Kiss and Gy. Szeidl: Nonlinear in-plane stability of heterogeneous curved beams under a concentrated radial load at the crown point. *Technische Mechanik*, **35**(1), 2015, 1-30.

{3} L. Kiss and Gy. Szeidl: In-plane stability of fixed-fixed heterogeneous curved beams under a concentrated radial load at the crown point. *Technische Mechanik*, **35**(1), 2015, 31-48.

{4} L. Kiss, Gy. Szeidl, S. Vlase, B. P. Gálfi, P. Dani, I. R. Munteanu, R. D. Ionescu and J. Száva: Vibrations of fixed-fixed heterogeneous curved beams loaded by a central force at the crown point. *International Journal for Engineering Modelling*, **27**(3-4), 2014, 85-100.

{5} L. Kiss: In-plane buckling of rotationally restrained heterogeneous shallow arches subjected to a concentrated force at the crown point. *Journal of Computational and Applied Mechanics*, **9**(2), 2014, 171-199.

Journal articles in Hungarian language

{6} Kiss L. P.: Heterogén anyagú síkgörbe rúd szabadrezgéseinek sajátfrekvenciái, *GÉP*, **LXIV**(5), (2013), 16-21.

{7} Kiss L. P. And Szeidl Gy.: Tetőpontjában sugárirányú koncentrált erővel terhelt heterogén anyagú síkgörbe rúd rezgései, *Multidiszciplináris tudományok: A Miskolci Egyetem közleménye*, **3**(1-2), (2013), 67-82.

{8} Kiss L. P.: Heterogén síkgörbe rudak lehetséges mechanikai modellje, *Multidiszciplináris tudományok: A Miskolci Egyetem közleménye*, **2**(1), (2012), 61-76.

Conference papers in book

{9} Gy. Szeidl and L. Kiss (Editor: S. Vlase): *Vibrations of heterogeneous curved beams subjected to a radial force at the crown point*, Proceedings of the 5th International Conference Computational Mechanics and Virtual Engineering, COMEC 2013, 24 - 25 October 2013, Braşov, Romania, pp. 24-33. ISBN: 978-606-19-0225-5.

DOI: 10.14750/ME.2016.008

{10} Gy. Szeidl and L. Kiss (Editor: S. Vlase): *A nonlinear mechanical model for heterogeneous curved beams*, Proceedings of the 4th International Conference on Advanced Composite Materials Engineering, COMAT, 18 - 20 October 2012, Braşov, Romania, Volume 2, pp. 589-596. ISBN 0981730051.

{11} Gy. Szeidl and L. Kiss (Editor: S. Vlase): *Vibrations and stability of heterogeneous curved beams*, Proceedings of the 4th International Conference on Computational Mechanics and Virtual Engineering COMEC 2011, 20 - 22 October 2011, Braşov, Romania, pp. 471-476. ISBN 978-973-131-122-7.

{12} L. Kiss And Gy. Szeidl: *Stresses in curved beams made of heterogeneous materials*, microCAD 2011: International Scientific Conference, 31 March - 1 April 2011, Miskolc, Hungary, Section: Applied Mechanics, pp. 13-18. ISBN 978-963-661-958-9.

Conference papers on CD

{13} Gy. Szeidl and L. Kiss: *Stability analysis of pinned-pinned shallow circular beams under a central concentrated load.* microCAD 2014: International Multidisciplinary Scientific Conference, 10 - 11 April 2014, Miskolc, Hungary, Section D4: Mechanical Modelling and Finite Element Simulation, Paper 40., 8p. ISBN 978-963-358-051-6.

{14} L. Kiss: *Stability of heterogeneous curved beams: A nonlinear formulation of the problem.* microCAD 2013: International Scientific Conference, 21 - 22 March 2013, Miskolc, Hungary, Section: Applied Mechanics, Paper 7., 6p. ISBN 978-963-358-018-9.

{15} L. Kiss: *In-plane stability of heterogeneous circular arches*, 8th International Conference of PhD Students, 6 - 10 August 2012, Miskolc, Hungary, Section: Engineering Sciences, Paper 9., 8p. ISBN 978-963-661-994-7.

{16} Gy. Szeidl And L. Kiss: *Stability of heterogeneous shallow arches subjected to a concentrated dead load*, microCAD 2012: International Scientific Conference, 29 - 30 March 2013, Miskolc, Hungary, Paper 9., 8p. ISBN 978-963-661-773-8.

Conference papers in Hungarian language

{17} Kiss L., Szeidl Gy.: *Heterogén lapos görbe rudak stabilitásvizsgálata*, OGÉT 2012, 20th International Conference on Mechanical Engineering, 19 - 22 April 2012, Cluj-Napoca, Romania, pp. 234-237. ISSN 2068-1267.

Full papers that appeared in other[1] proceedings

{18} Kiss L.: Heterogén anyagú lapos görbe rudak stabilitásvizsgálata. *Diáktudomány: A Miskolci Egyetem Tudományos Diákköri Munkáiból 2011-2012.* (2012), pp. 82-88. ISSN 2062-07-21.

{19} Kiss L.: Stresses in Curved Beams Made of Heterogeneous Materials. *Diáktudomány: A Miskolci Egyetem Tudományos Diákköri Munkáiból 2010-2011.* (2011), pp. 51-56. ISSN 2062-07-21.

Conference talks

{20} Kiss L., Szeidl Gy.: Heterogén anyagú síkgörbe rudak szabadrezgéseinek és stabilitásának vizsgálata. 9th Hungarian Conference on Theoretical and Applied Mechanics. 29-31 August 2011, Miskolc.

Acknowledgements by the author concerning publications {1}, {2}, {3}, {4}, {5}, {6}, {7}, {9} and {13}: This research was supported by the **European Union and the State of Hungary**, co-financed by the **European Social Fund** in the frames of TÁMOP-4.2.4.A/2-11/1-2012-0001 'National Excellence Program'.

[1]not regularly published

DOI: 10.14750/ME.2016.008

APPENDIX A

Detailed manipulations

A.1. The long formal transformations of Chapter 3

A.1.1. Formulae for the axial force. Making use of the kinematic relation (3.1.4) and the inequality (3.1.9) we can manipulate (3.1.7) into a more favourable form:

$$N = A_e \underbrace{\left(\frac{\mathrm{d}u_o}{\mathrm{d}s} + \frac{w_o}{\rho_o} + \frac{1}{2}\psi_{o\eta}^2\right)}_{\varepsilon_m} + \frac{I_{e\eta}}{\rho_o}\frac{\mathrm{d}}{\mathrm{d}s}\left(\frac{\mathrm{d}w_o}{\mathrm{d}s} - \frac{u_o}{\rho_o}\right) =$$

$$= \frac{I_{e\eta}}{\rho_o^2}\left[\left(\frac{A_e\rho_o^2}{I_{e\eta}} - 1\right)\left(\frac{\mathrm{d}u_o}{\mathrm{d}s} + \frac{w_o}{\rho_o}\right) + \rho_o\left(\frac{\mathrm{d}^2 w_o}{\mathrm{d}s^2} + \frac{w_o}{\rho_o^2}\right)\right] + \frac{1}{2}\psi_{o\eta}^2 A_e =$$

$$= \frac{I_{e\eta}}{\rho_o^3}\left[\left(\frac{A_e\rho_o^2}{I_{e\eta}} - 1\right)\left(u_o^{(1)} + w_o\right) + w_o^{(2)} + w_o\right] + \frac{1}{2}\psi_{o\eta}^2 A_e =$$

$$= \frac{I_{e\eta}}{\rho_o^3}\left[\left(\frac{A_e\rho_o^2}{I_{e\eta}} - 1\right)\left(u_o^{(1)} + w_o\right) + w_o^{(2)} + w_o\right] + \frac{1}{2}\psi_{o\eta}^2 \underbrace{\left(\frac{A_e\rho_o^2}{I_{e\eta}} - 1 + 1\right)}_{\approx\frac{A_e\rho_o^2}{I_{e\eta}}-1}\frac{I_{e\eta}}{\rho_o^2} \simeq$$

$$\simeq \frac{I_{e\eta}}{\rho_o^2}\left(\frac{A_e\rho_o^2}{I_{e\eta}} - 1\right)\underbrace{\left(\frac{1}{\rho_o}\left(u_o^{(1)} + w_o\right) + \frac{1}{2}\psi_{o\eta}^2\right)}_{\varepsilon_m} + \underbrace{\frac{I_{e\eta}}{\rho_o^3}\left(w_o^{(2)} + w_o\right)}_{-\frac{M}{\rho_o}} \simeq A_e\varepsilon_m - \frac{M}{\rho_o}\,. \quad \text{(A.1.1)}$$

A similar line of thought for the increment in the axial force N_b results in

$$N_b = A_e\left(\varepsilon_{o\xi\,b} + \psi_{o\eta}\psi_{o\eta\,b} + \frac{1}{2}\psi_{o\eta\,b}^2\right) - \frac{I_{e\eta}}{\rho_o}\kappa_{ob} = A_e\left(\varepsilon_{o\xi\,b} + \psi_{o\eta}\psi_{o\eta\,b} + \frac{1}{2}\psi_{o\eta\,b}^2\right) + \frac{I_{e\eta}}{\rho_o^3}\left(w_{ob}^{(2)} - u_{ob}^{(1)}\right) =$$

$$= A_e\left(\varepsilon_{o\xi\,b} + \psi_{o\eta}\psi_{o\eta\,b} + \frac{1}{2}\psi_{o\eta\,b}^2\right) + \frac{I_{e\eta}}{\rho_o^3}\left(w_{ob}^{(2)} - u_{ob}^{(1)}\right) + \frac{I_{e\eta}}{\rho_o^3}w_{ob} - \frac{I_{e\eta}}{\rho_o^3}w_{ob} =$$

$$= \frac{I_{e\eta}}{\rho_o^2}\left[\left(\frac{A_e\rho_o^2}{I_{e\eta}} - 1\right)\varepsilon_{o\xi\,b} + \frac{A_e\rho_o^2}{I_{e\eta}}\left(\psi_{o\eta}\psi_{o\eta\,b} + \frac{1}{2}\psi_{o\eta\,b}^2\right)\right] + \frac{I_{e\eta}}{\rho_o^3}\left(w_{ob}^{(2)} + w_{ob}\right) \approx$$

$$\approx \frac{I_{e\eta}}{\rho_o^2}\left(\frac{A_e\rho_o^2}{I_{e\eta}} - 1\right)\left[\varepsilon_{o\xi\,b} + \left(\psi_{o\eta}\psi_{o\eta\,b} + \frac{1}{2}\psi_{o\eta\,b}^2\right)\right] + \frac{I_{e\eta}}{\rho_o^3}\left(w_{ob}^{(2)} + w_{ob}\right) =$$

$$= \frac{I_{e\eta}}{\rho_o^2}m\varepsilon_{mb} + \frac{I_{e\eta}}{\rho_o^3}\left(w_{ob}^{(2)} + w_{ob}\right)\,. \quad \text{(A.1.2)}$$

A.1.2. Transformation of the principle of virtual work – pre-buckling state. Substituting the corresponding kinematical quantities into the principle of virtual work (3.2.1) and taking the relation

$$\mathrm{d}V = \left(1 + \frac{\zeta}{\rho_o}\right)\mathrm{d}s\,\mathrm{d}A \quad \text{(A.1.3)}$$

into account, which provides the infinitesimal volume element, the left side of the principle can be rewritten as

$$\int_V \sigma_\xi\delta\varepsilon_\xi\,\mathrm{d}V = \int_{\mathcal{L}}\int_A \left(1 + \frac{\zeta}{\rho_o}\right)\sigma_\xi\left[\frac{1}{1 + \frac{\zeta}{\rho_o}}\left(\frac{\mathrm{d}\delta u_o}{\mathrm{d}s} + \frac{\delta w_o}{\rho_o} + \zeta\frac{\mathrm{d}\delta\psi_{o\eta}}{\mathrm{d}s}\right) + \psi_{o\eta}\,\delta\psi_{o\eta}\right]\mathrm{d}A\,\mathrm{d}s =$$

DOI: 10.14750/ME.2016.008

$$= \int_{\mathcal{L}} \left\{ \int_A \sigma_\xi \mathrm{d}A \left(\frac{\mathrm{d}\delta u_o}{\mathrm{d}s} + \frac{\delta w_o}{\rho_o} \right) + \int_A \zeta \sigma_\xi \mathrm{d}A \frac{\mathrm{d}\delta\psi_{o\eta}}{\mathrm{d}s} + \int_A \left(1 + \frac{\zeta}{\rho_o} \right) \sigma_\xi \, \mathrm{d}A \psi_{o\eta} \left(\frac{\delta u_o}{\rho_o} - \frac{\mathrm{d}\delta w_o}{\mathrm{d}s} \right) \right\} \mathrm{d}s =$$

$$= \int_{\mathcal{L}} \left[N \left(\frac{\mathrm{d}\delta u_o}{\mathrm{d}s} + \frac{\delta w_o}{\rho_o} \right) + M \frac{\mathrm{d}\delta\psi_{o\eta}}{\mathrm{d}s} + \left(N + \frac{M}{\rho_o} \right) \psi_{o\eta} \left(\frac{\delta u_o}{\rho_o} - \frac{\mathrm{d}\delta w_o}{\mathrm{d}s} \right) \right] \mathrm{d}s \,, \quad \text{(A.1.4)}$$

where the formulae (3.1.7)-(3.1.8) for the inner forces have also been taken into account. Applying now the integration by parts theorem and performing some arrangements we obtain the following equation:

$$\begin{aligned}
\int_V \sigma_\xi \delta\varepsilon_\xi \, \mathrm{d}V = &- \int_{\mathcal{L}} \frac{\mathrm{d}N}{\mathrm{d}s} \delta u_o \mathrm{d}s - N\delta u_o|_{s(-\vartheta)} + N\delta u_o|_{s(\vartheta)} + \int_{\mathcal{L}} \frac{N}{\rho_o} \delta w_o \mathrm{d}s - \\
&- \int_{\mathcal{L}} \frac{1}{\rho_o} \frac{\mathrm{d}M}{\mathrm{d}s} \delta u_o \mathrm{d}s - \int_{\mathcal{L}} \frac{\mathrm{d}^2 M}{\mathrm{d}s^2} \delta w_o \mathrm{d}s - \frac{\mathrm{d}M}{\mathrm{d}s} \delta w_o \Big|_{s(-\vartheta)} + \frac{\mathrm{d}M}{\mathrm{d}s} \delta w_o \Big|_{s=-0} - \frac{\mathrm{d}M}{\mathrm{d}s} \delta w_o \Big|_{s=+0} + \\
&+ \frac{\mathrm{d}M}{\mathrm{d}s} \delta w_o \Big|_{s(\vartheta)} + M\delta\psi_{o\eta}|_{s(\vartheta)} - M\delta\psi_{o\eta}|_{s(-\vartheta)} + \int_{\mathcal{L}} \frac{1}{\rho_o} \left(N + \frac{M}{\rho_o} \right) \psi_{o\eta} \delta u_o \mathrm{d}s + \\
&+ \int_{\mathcal{L}} \frac{\mathrm{d}}{\mathrm{d}s} \left[\left(N + \frac{M}{\rho_o} \right) \psi_{o\eta} \right] \delta w_o \mathrm{d}s + \left(N + \frac{M}{\rho_o} \right) \psi_{o\eta} \delta w_o \Big|_{s(-\vartheta)} - \\
&- \left(N + \frac{M}{\rho_o} \right) \psi_{o\eta} \delta w_o \Big|_{s=-0} + \left(N + \frac{M}{\rho_o} \right) \psi_{o\eta} \delta w_o \Big|_{s=+0} - \left(N + \frac{M}{\rho_o} \right) \psi_{o\eta} \delta w_o \Big|_{s(\vartheta)} \,. \quad \text{(A.1.5)}
\end{aligned}$$

Notice that $[|_{s=-0}](|_{s=+0})$ denotes the [left](right) side limit for the expression that precedes the symbol $|$. If we set (A.1.5) equal to the right side of (3.2.1) we finally get

$$\begin{aligned}
&- \int_{\mathcal{L}} \left(\frac{\mathrm{d}N}{\mathrm{d}s} + \frac{1}{\rho_o} \frac{\mathrm{d}M}{\mathrm{d}s} - \frac{1}{\rho_o} \left(N + \frac{M}{\rho_o} \right) \psi_{o\eta} + f_t \right) \delta u_o \mathrm{d}s - \\
&- \int_{\mathcal{L}} \left(\frac{\mathrm{d}^2 M}{\mathrm{d}s^2} - \frac{N}{\rho_o} - \frac{\mathrm{d}}{\mathrm{d}s} \left(N + \frac{M}{\rho_o} \right) \psi_{o\eta} + f_n \right) \delta w_o \mathrm{d}s - \\
&- \left[\frac{\mathrm{d}M}{\mathrm{d}s} - \left(N + \frac{M}{\rho_o} \right) \psi_{o\eta} \right] \delta w_o \Big|_{s(-\vartheta)} + \left[\frac{\mathrm{d}M}{\mathrm{d}s} - \left(N + \frac{M}{\rho_o} \right) \psi_{o\eta} \right] \delta w_o \Big|_{s(\vartheta)} - \\
&- \left\{ \left[\frac{\mathrm{d}M}{\mathrm{d}s} - \left(N + \frac{M}{\rho_o} \right) \psi_{o\eta} \right] \Big|_{s=+0} + \left[\frac{\mathrm{d}M}{\mathrm{d}s} - \left(N + \frac{M}{\rho_o} \right) \psi_{o\eta} \right] \Big|_{s=-0} - P_\zeta \right\} \delta w_o|_{s=0} - \\
&- N\delta u_o|_{s(-\vartheta)} + N\delta u_o|_{s(\vartheta)} + (M + k_{\gamma r}\psi_{o\eta})|_{s(\vartheta)} \, \delta\psi_{o\eta}|_{s(\vartheta)} - (M - k_{\gamma\ell}\psi_{o\eta})|_{s(-\vartheta)} \, \delta\psi_{o\eta}|_{s(-\vartheta)} = 0 \,.
\end{aligned} \quad \text{(A.1.6)}$$

A.1.3. Transformation of the principle of virtual work – post-buckling state. Expanding the quantities denoted by an asterisk in (3.2.11) and using the decompositions presented in the first paragraph of Subsection 3.1.2, we obtain

$$\begin{aligned}
\int_V (\sigma_\xi + \sigma_{\xi\, b}) \, \delta\varepsilon_{\xi b} \, \mathrm{d}V = &- (P_\zeta + P_{\zeta\, b}) \, \delta w_{o\, b}|_{s=0} + P_{\xi\, b} \, \delta u_{o\, b}|_{s=0} - \\
&- \mathfrak{m}\ddot{w}_{o\, b} \delta w_{o\, b}|_{s=0} - \mathfrak{m}\ddot{u}_{o\, b} \delta u_{o\, b}|_{s=0} - k_{\gamma\, \ell} \, (\psi_{o\eta} + \psi_{o\eta\, b}) \, \delta\psi_{o\eta\, b}|_{s(-\vartheta)} - k_{\gamma\, r} \, (\psi_{o\eta} + \psi_{o\eta\, b}) \, \delta\psi_{o\eta\, b}|_{s(\vartheta)} + \\
&+ \int_{\mathcal{L}} \left[(f_n + f_{nb}) \, \delta w_{ob} + (f_t + f_{tb}) \, \delta u_{o\, b} \right] \mathrm{d}s \,. \quad \text{(A.1.7)}
\end{aligned}$$

The kinematical quantities in the pre-buckling state are assumed to be known at this stage of the investigations. Therefore, the corresponding variations are all equal to zero. Recalling formulae (3.1.13a)-(3.1.15), for the virtual rotation and strain we can write

$$\delta\psi^*_{o\eta} = \delta\psi_{o\eta\, b} = \frac{\delta u_{ob}}{\rho_o} - \frac{\mathrm{d}\delta w_{ob}}{\mathrm{d}s} \quad \text{(A.1.8)}$$

and moreover

DOI: 10.14750/ME.2016.008

$$\delta\varepsilon^*_\xi = \delta\left(\varepsilon_\xi + \varepsilon_{\xi\,b}\right) = \delta\varepsilon_{\xi\,b} = \underbrace{\frac{1}{1+\frac{\zeta}{\rho_o}}\left(\delta\varepsilon_{o\xi\,b} + \zeta\delta\kappa_{o\,b}\right) + \psi_{o\eta}\delta\psi_{o\eta\,b}}_{\delta\varepsilon^L_{\xi\,b}} + \underbrace{\psi_{o\eta\,b}\delta\psi_{o\eta\,b}}_{\delta\varepsilon^N_{\xi\,b}} =$$

$$= \underbrace{\frac{1}{1+\frac{\zeta}{\rho_o}}\left(\frac{\partial\delta u_{o\,b}}{\partial s} + \frac{\delta w_{o\,b}}{\rho_o} + \zeta\frac{\partial\delta\psi_{o\eta\,b}}{\partial s}\right) + \psi_{o\eta}\delta\psi_{o\eta\,b}}_{\delta\varepsilon^L_{\xi\,b}} + \underbrace{\psi_{o\eta\,b}\delta\psi_{o\eta\,b}}_{\delta\varepsilon^N_{\xi\,b}}. \quad \text{(A.1.9)}$$

After substituting (3.2.1) and (A.1.9), we can rewrite the principle of virtual work (A.1.7) in the form

$$0 = -\int_V \sigma_\xi\delta\varepsilon^N_{\xi\,b}\mathrm{d}V - \int_V \sigma_{\xi\,b}\delta\varepsilon^L_{\xi\,b}\,\mathrm{d}V - \int_V \sigma_{\xi\,b}\delta\varepsilon^N_{\xi\,b}\,\mathrm{d}V - P_{\zeta\,b}\,\delta w_{o\,b}|_{s=0} + P_{\xi\,b}\,\delta u_{o\,b}|_{s=0} -$$
$$- \mathfrak{m}\ddot{w}_{ob}\delta w_{o\,b}|_{s=0} - \mathfrak{m}\ddot{u}_{ob}\delta u_{o\,b}|_{s=0} - k_{\gamma\,\ell}\psi_{o\eta\,b}\delta\psi_{o\eta\,b}|_{s(-\vartheta)} - k_{\gamma\,r}\psi_{o\eta\,b}\delta\psi_{o\eta\,b}|_{s(\vartheta)} +$$
$$+ \int_{\mathcal{L}}\left(f_{nb}\delta w_{ob} + f_{tb}\delta u_{o\,b}\right)\mathrm{d}s\,. \quad \text{(A.1.10)}$$

The first three integrals require some further manipulations which are based on the integration by parts and are detailed in the forthcoming:

$$\int_V \sigma_\xi\delta\varepsilon^N_{\xi\,b}\mathrm{d}V = \int_{\mathcal{L}}\int_A\left(1+\frac{\zeta}{\rho_o}\right)\sigma_\xi\delta\varepsilon^N_{\xi\,b}\mathrm{d}A\,\mathrm{d}s = \int_{\mathcal{L}}\left(N+\frac{M}{\rho_o}\right)\psi_{o\eta\,b}\left(\frac{\delta u_{ob}}{\rho_o} - \frac{\partial\delta w_{ob}}{\partial s}\right)\mathrm{d}s =$$
$$= \int_{\mathcal{L}}\frac{1}{\rho_o}\left(N+\frac{M}{\rho_o}\right)\psi_{o\eta\,b}\delta u_{ob}\mathrm{d}s + \int_{\mathcal{L}}\frac{\partial}{\partial s}\left[\left(N+\frac{M}{\rho_o}\right)\psi_{o\eta\,b}\right]\delta w_{ob}\mathrm{d}s +$$
$$+ \underbrace{\left[\left(N+\frac{M}{\rho_o}\right)\psi_{o\eta\,b}\Big|_{s=+0} - \left(N+\frac{M}{\rho_o}\right)\psi_{o\eta\,b}\Big|_{s=-0}\right]}_{=0}\delta w_{ob}|_{s=0} +$$
$$+ \left(N+\frac{M}{\rho_o}\right)\psi_{o\eta\,b}\delta w_{ob}\Big|_{s(-\vartheta)} - \left(N+\frac{M}{\rho_o}\right)\psi_{o\eta\,b}\delta w_{ob}\Big|_{s(\vartheta)}\,. \quad \text{(A.1.11)}$$

Furthermore

$$\int_V \sigma_{\xi\,b}\delta\varepsilon^L_{\xi\,b}\,\mathrm{d}V = \int_{\mathcal{L}}\int_A\left(1+\frac{\zeta}{\rho_o}\right)\sigma_{\xi\,b}\left[\frac{1}{1+\frac{\zeta}{\rho_o}}\left(\frac{\partial\delta u_{o\,b}}{\partial s} + \frac{\delta w_{o\,b}}{\rho_o} + \zeta\frac{\partial\delta\psi_{o\eta\,b}}{\partial s}\right) + \psi_{o\eta}\delta\psi_{o\eta\,b}\right]\mathrm{d}A\,\mathrm{d}s =$$
$$= \int_{\mathcal{L}}\Bigg\{\underbrace{\int_A\sigma_{\xi\,b}\mathrm{d}A}_{N_b}\left(\frac{\partial\delta u_{o\,b}}{\partial s} + \frac{\delta w_{o\,b}}{\rho_o}\right) + \underbrace{\int_A\zeta\sigma_{\xi\,b}\mathrm{d}A}_{M_b}\frac{\partial}{\partial s}\left(\frac{\delta u_{ob}}{\rho_o} - \frac{\partial\delta w_{ob}}{\partial s}\right) +$$
$$+ \underbrace{\int_A\left(1+\frac{\zeta}{\rho_o}\right)\sigma_{\xi\,b}\mathrm{d}A}_{N_b+\frac{M_b}{\rho_o}}\psi_{o\eta}\left(\frac{\delta u_{ob}}{\rho_o} - \frac{\partial\delta w_{ob}}{\partial s}\right)\Bigg\}\mathrm{d}s =$$
$$= -\int_{\mathcal{L}}\frac{\partial N_b}{\partial s}\delta u_{o\,b}\mathrm{d}s - N_b\delta u_{o\,b}|_{s(-\vartheta)} + \left[N_b|_{s=-0} - N_b|_{s=+0}\right]\delta u_{o\,b}|_{s=0} + N_b\delta u_{o\,b}|_{s(\vartheta)} +$$
$$+ \int_{\mathcal{L}}\frac{N_b}{\rho_o}\delta w_{o\,b}\,\mathrm{d}s - \int_{\mathcal{L}}\frac{1}{\rho_o}\frac{\partial M_b}{\partial s}\delta u_{ob}\mathrm{d}s - \int_{\mathcal{L}}\frac{\partial^2 M_b}{\partial s^2}\delta w_{ob}\mathrm{d}s + M_b\delta\psi_{o\eta\,b}|_{s(\vartheta)} - M_b\delta\psi_{o\eta\,b}|_{s(-\vartheta)} -$$
$$- \frac{\partial M_b}{\partial s}\delta w_{ob}\Big|_{s(-\vartheta)} + \underbrace{\left[\frac{\partial M_b}{\partial s}\Big|_{s=-0} - \frac{\partial M_b}{\partial s}\Big|_{s=+0}\right]}_{=0}\delta w_{ob}|_{s=0} + \frac{\partial M_b}{\partial s}\delta w_{ob}\Big|_{s(\vartheta)} +$$
$$+ \int_{\mathcal{L}}\frac{1}{\rho_o}\frac{\partial}{\partial s}\left(N_b+\frac{M_b}{\rho_o}\right)\psi_{o\eta}\delta u_{ob}\mathrm{d}s + \int_{\mathcal{L}}\frac{\partial}{\partial s}\left[\left(N_b+\frac{M_b}{\rho_o}\right)\psi_{o\eta}\right]\delta w_{ob}\mathrm{d}s +$$

DOI: 10.14750/ME.2016.008

$$+\left(N_b+\frac{M_b}{\rho_o}\right)\psi_{o\eta}\,\delta w_{ob}\Big|_{s(-\vartheta)}-\left(N_b+\frac{M_b}{\rho_o}\right)\psi_{o\eta}\delta w_{ob}\Big|_{s(\vartheta)}\,. \quad \text{(A.1.12)}$$

The third integral is formally the same as the first one if we change σ_ξ to $\sigma_{\xi\,b}$, therefore

$$\begin{aligned}\int_V\sigma_\xi\delta\varepsilon^N_{\xi\,b}\mathrm{d}V&=\int_{\mathcal{L}}\int_A\left(1+\frac{\zeta}{\rho_o}\right)\sigma_{\xi b}\delta\varepsilon^N_{\xi\,b}\mathrm{d}A\,\mathrm{d}s=\int_{\mathcal{L}}\left(N_b+\frac{M_b}{\rho_o}\right)\psi_{o\eta\,b}\left(\frac{\delta u_{ob}}{\rho_o}-\frac{\mathrm{d}\delta w_{ob}}{\mathrm{d}s}\right)\mathrm{d}s=\\&=\int_{\mathcal{L}}\frac{1}{\rho_o}\left(N_b+\frac{M_b}{\rho_o}\right)\psi_{o\eta\,b}\delta u_{ob}\mathrm{d}s+\int_{\mathcal{L}}\frac{\partial}{\partial s}\left[\left(N_b+\frac{M_b}{\rho_o}\right)\psi_{o\eta\,b}\right]\delta w_{ob}\mathrm{d}s+\\&\quad+\left[\left(N_b+\frac{M_b}{\rho_o}\right)\psi_{o\eta\,b}\Big|_{s=+0}-\left(N_b+\frac{M_b}{\rho_o}\right)\psi_{o\eta\,b}\Big|_{s=-0}\right]+\\&\quad+\left(N_b+\frac{M_b}{\rho_o}\right)\psi_{o\eta\,b}\delta w_{ob}\Big|_{s(-\vartheta)}-\left(N_b+\frac{M_b}{\rho_o}\right)\psi_{o\eta\,b}\delta w_{ob}\Big|_{s(\vartheta)}\,. \quad \text{(A.1.13)}\end{aligned}$$

As a summary of these manipulations, the principle of virtual work (A.1.7), or what is the same, equation (3.2.11) can finally be rewritten as

$$\begin{aligned}&-\int_{\mathcal{L}}\left(\frac{\partial N_b}{\partial s}-\frac{1}{\rho_o}\left(N+\frac{M}{\rho_o}\right)\psi_{o\eta\,b}+\frac{1}{\rho_o}\left[\frac{\partial M_b}{\partial s}-\left(N_b+\frac{M_b}{\rho_o}\right)\psi_{o\eta\,b}\right]+f_{tb}\right)\delta u_{o\,b}\mathrm{d}s-\\&-\int_{\mathcal{L}}\left(\frac{\partial^2 M_b}{\partial s^2}-\frac{N_b}{\rho_o}-\frac{\partial}{\partial s}\left[\left(N+N_b+\frac{M+M_b}{\rho_o}\right)\psi_{o\eta\,b}+\left(N_b+\frac{M_b}{\rho_o}\right)\psi_{o\eta}\right]+f_{nb}\right)\delta w_{ob}\mathrm{d}s-\\&\quad-\left[\frac{\partial M_b}{\partial s}-\left(N+N_b+\frac{M+M_b}{\rho_o}\right)\psi_{o\eta\,b}-\left(N_b+\frac{M_b}{\rho_o}\right)\psi_{o\eta}\right]\delta w_{ob}\Big|_{s(-\vartheta)}+\\&\quad+\left[\frac{\partial M_b}{\partial s}-\left(N+N_b+\frac{M+M_b}{\rho_o}\right)\psi_{o\eta\,b}-\left(N_b+\frac{M_b}{\rho_o}\right)\psi_{o\eta}\right]\delta w_{ob}\Big|_{s(\vartheta)}+\\&\quad+\left\{\left[\frac{\partial M_b}{\partial s}-\left(N+N_b+\frac{M+M_b}{\rho_o}\right)\psi_{o\eta\,b}-\left(N_b+\frac{M_b}{\rho_o}\right)\psi_{o\eta}\right]\Big|_{s=-0}-\right.\\&\left.-\left[\frac{\partial M_b}{\partial s}-\left(N+N_b+\frac{M+M_b}{\rho_o}\right)\psi_{o\eta\,b}-\left(N_b+\frac{M_b}{\rho_o}\right)\psi_{o\eta}\right]\Big|_{s=+0}+\mathfrak{m}\,\frac{\partial^2 w_{ob}}{\partial t^2}+P_{\zeta\,b}\Big|_{s=0}\right\}\delta w_{ob}|_{s=0}-\\&\quad-N_b\delta u_{o\,b}|_{s(-\vartheta)}+\left[N_b|_{s=-0}-N_b|_{s=+0}+P_{\xi\,b}+\mathfrak{m}\,\frac{\partial^2 u_{ob}}{\partial t^2}\Big|_{s=0}\right]\delta u_{o\,b}|_{s=0}+N_b\delta u_{o\,b}|_{s(\vartheta)}+\\&\quad+(M_b+k_{\gamma\,r}\psi_{o\eta\,b})|_\vartheta\;\delta\psi_{o\eta\,b}|_{s(\vartheta)}-(M_b-k_{\gamma\,\ell}\psi_{o\eta\,b})|_{s(-\vartheta)}\;\delta\psi_{o\eta\,b}|_{s(-\vartheta)}=0\,. \quad \text{(A.1.14)}\end{aligned}$$

A.1.4. The pre-buckling equilibrium in terms of the displacements. It follows from equation $(3.2.2)_2$ that

$$\frac{\mathrm{d}^2M}{\mathrm{d}s^2}-\psi_{o\eta}\frac{\mathrm{d}}{\mathrm{d}s}\left(N+\frac{M}{\rho_o}\right)-\left(N+\frac{M}{\rho_o}\right)\frac{\mathrm{d}\psi_{o\eta}}{\mathrm{d}s}-\frac{N}{\rho_o}=0\,. \quad \text{(A.1.15)}$$

Substitute here now equations (3.1.8) and (3.1.10) which express the inner forces as functions of the displacements. The first and third terms in (A.1.15) require no further manipulation at this point. The second one, however, vanishes – see (3.1.10) and (3.2.6). As for the fourth one, some transformations need to be performed:

$$\frac{N}{\rho_o}=\frac{A_e}{\rho_o}\varepsilon_m-\frac{M}{\rho_o^2}=\frac{I_{e\eta}}{\rho_o^3}\frac{A_e\rho_o^2}{I_{e\eta}}\varepsilon_m-\frac{M}{\rho_o^2}=\frac{I_{e\eta}}{\rho_o^3}m\varepsilon_m+\frac{I_{e\eta}}{\rho_o^4}\left(w_o^{(2)}+w_o\right)\,.$$

Consequently, the equilibrium condition (A.1.15) can now be rewritten as

$$-\frac{I_{e\eta}}{\rho_o^4}\left(w_o^{(4)}+w_o^{(2)}\right)-\frac{I_{e\eta}}{\rho_o^4}\frac{A_e\rho_o^2}{I_{e\eta}}\rho_o\varepsilon_m\psi_{o\eta}^{(1)}-\frac{I_{e\eta}}{\rho_o^3}m\varepsilon_m-\frac{I_{e\eta}}{\rho_o^4}\left(w_o^{(2)}+w_o\right)=0\,.$$

If we multiply this formula by $(-\rho_o^4/I_{e\eta})$ we get

$$\left(w_o^{(4)}+w_o^{(2)}\right)+\frac{A_e\rho_o^2}{I_{e\eta}}\rho_o\varepsilon_m\psi_{o\eta}^{(1)}+\rho_o m\varepsilon_m+\left(w_o^{(2)}+w_o\right)=$$

DOI: 10.14750/ME.2016.008

$$= \left(w_o^{(4)} + w_o^{(2)}\right) + \rho_o m \varepsilon_m \left(\psi_{o\eta}^{(1)} + 1\right) + \left(w_o^{(2)} + w_o\right) = 0\,. \quad \text{(A.1.16)}$$

If we now substitute $\psi_{o\eta}$ from (2.1.8) and $u_o^{(1)}$ from (3.1.4) into the term $\rho_o \varepsilon_m \left(1 + \psi_{o\eta}^{(1)}\right)$, we arrive at the following result:

$$\rho_o \varepsilon_m \left(1 + \psi_{o\eta}^{(1)}\right) = \rho_o \varepsilon_m \left[1 + \frac{1}{\rho_o}\left(u_o^{(1)} - w_o^{(2)}\right)\right] = \rho_o \varepsilon_m \left[1 + \frac{1}{\rho_o}\left(\rho_o \varepsilon_m - w_o - \frac{1}{2}\psi_{o\eta}^2 \rho_o - w_o^{(2)}\right)\right] \approx$$
$$\approx \rho_o \varepsilon_m \underbrace{(1 + \varepsilon_m)}_{\approx 1} - \varepsilon_m \left(w_o + w_o^{(2)}\right) \approx \rho_o \varepsilon_m - \varepsilon_m \left(w_o^{(2)} + w_o\right)\,. \quad \text{(A.1.17)}$$

Plugging it back into (A.1.16) we find that the pre-buckling displacement w_o should satisfy the differential equation

$$w_o^{(4)} + 2w_o^{(2)} + w_o - m\varepsilon_m \left(w_o^{(2)} + w_o\right) = -m\rho_o \varepsilon_m. \quad \text{(A.1.18)}$$

A.1.5. The post-buckling equilibrium in terms of the displacements. We assume there are no distributed forces. From the comparison of equations (3.1.10) and (3.2.6) as well as (3.1.21) and (3.2.18) we get that

$$\frac{\mathrm{d}}{\mathrm{d}s}\left(N + \frac{M}{\rho_o}\right) = 0\,, \qquad \frac{\mathrm{d}}{\mathrm{d}s}\left(N_b + \frac{M_b}{\rho_o}\right) = 0\,.$$

Thus, equation (3.2.13b) has the form

$$-\frac{\mathrm{d}^2 M_b}{\mathrm{d}s^2} + \frac{N_b}{\rho_o} + \underbrace{\left(N + \frac{M}{\rho_o}\right)}_{A_e \varepsilon_m} \frac{\mathrm{d}\psi_{o\eta\, b}}{\mathrm{d}s} + \underbrace{\left(N_b + \frac{M_b}{\rho_o}\right)}_{A_e \varepsilon_{mb}} \frac{\mathrm{d}\psi_{o\eta}}{\mathrm{d}s} = 0\,, \quad \text{(A.1.19)}$$

where we have neglected the quadratic terms in the increments. With regard to the last two terms, some transformations with the aid of (3.1.9) and (3.1.10) should be carried out. The first one of these is

$$A_e \varepsilon_m \frac{\mathrm{d}\psi_{o\eta\, b}}{\mathrm{d}s} + A_e \varepsilon_{mb} \frac{\mathrm{d}\psi_{o\eta}}{\mathrm{d}s} = m \frac{I_{e\eta}}{\rho_o^2}\left(\varepsilon_m \frac{\mathrm{d}\psi_{o\eta\, b}}{\mathrm{d}s} + \varepsilon_{mb} \frac{\mathrm{d}\psi_{o\eta}}{\mathrm{d}s}\right)\,. \quad \text{(A.1.20)}$$

Substitute now M_b from (3.1.20), N_b from (3.1.19) (while again utilizing (3.1.20)) into (A.1.19) and take equation (3.1.9) into account. In this way we have

$$\frac{I_{e\eta}}{\rho_o^4}\left(w_{ob}^{(4)} + w_{ob}^{(2)}\right) + \frac{I_{e\eta}}{\rho_o^4}\left(w_{ob}^{(2)} + w_{ob}\right) + m\frac{I_{e\eta}}{\rho_o^3}\varepsilon_{mb} + m\frac{I_{e\eta}}{\rho_o^3}\varepsilon_m \psi_{o\eta\, b}^{(1)} + m\frac{I_{e\eta}}{\rho_o^3}\varepsilon_{mb}\psi_{o\eta}^{(1)} = 0\,. \quad \text{(A.1.21)}$$

Let us multiply the former expression by $\rho_o^4 / I_{e\eta}$. After some minor arrangements we obtain

$$w_{ob}^{(4)} + 2w_{ob}^{(2)} + w_{ob} + m\rho_o \varepsilon_{mb}\left(1 + \psi_{o\eta}^{(1)}\right) + m\rho_o \varepsilon_m \psi_{o\eta\, b}^{(1)} = 0\,. \quad \text{(A.1.22)}$$

Now repeat the line of thought leading to (A.1.17) – by formally changing ε_m to ε_{mb} – to arrive at

$$m\rho_o \varepsilon_{mb}\left(1 + \psi_{o\eta}^{(1)}\right) \simeq m\rho_o \varepsilon_{mb}\left[1 - \frac{1}{\rho_o}\left(w_o^{(2)} + w_o\right)\right] = m\rho_o \varepsilon_{mb} - m\varepsilon_{mb}\left(w_o^{(2)} + w_o\right)\,.$$

In a similar way (with the omission of the unit) the previous procedure can be applied as well to the last term in (A.1.22):

$$m\rho_o \varepsilon_m \psi_{o\eta\, b}^{(1)} \simeq -m\varepsilon_m \left(\, w_{ob}^{(2)} + w_{ob}\right)\,.$$

Altogether

$$w_{ob}^{(4)} + (2 - m\varepsilon_m)\, w_{ob}^{(2)} + (1 - m\varepsilon_m)\, w_{ob} = -m\rho_o \varepsilon_{mb} + m\varepsilon_{mb}\left(w_o^{(2)} + w_o\right) \quad \text{(A.1.23)}$$

is the post-buckling equilibrium equation in terms of the displacements.

DOI: 10.14750/ME.2016.008

A.1.6. Computation of the pre-buckling strain. For any support arrangement substitution of W_o from (3.3.5) into (3.3.7) results in

$$\varepsilon_{o\xi} = \frac{1}{\vartheta}\int_0^{\vartheta} W_o \,\mathrm{d}\varphi = \frac{1}{\vartheta}\left[\int_0^{\vartheta}\left(\frac{\chi^2-1}{\chi^2} + A_{11}\cos\varphi - \frac{A_{31}}{\chi^2}\cos\chi\varphi\right)\mathrm{d}\varphi + \right.$$
$$\left. + \int_0^{\vartheta}\left(A_{12}\cos\varphi + A_{22}\sin\varphi - \frac{A_{32}}{\chi^2}\cos\chi\varphi - \frac{A_{42}}{\chi^2}\sin\chi\varphi\right)\right]\mathrm{d}\varphi\frac{\hat{\mathcal{P}}}{\vartheta} = I_{ow} + I_{1w}\frac{\hat{\mathcal{P}}}{\vartheta}\,,$$

where

$$I_{ow} = \frac{\chi\left(\chi^2\vartheta - \vartheta + A_{11}\chi^2\sin\vartheta\right) - A_{31}\sin\chi\vartheta}{\vartheta\chi^3}\,, \tag{A.1.24a}$$

$$I_{1w} = \frac{A_{12}\chi^3\sin\vartheta + A_{22}\chi^3\left(1-\cos\vartheta\right) - A_{32}\sin\chi\vartheta + A_{42}\left(\cos\chi\vartheta - 1\right)}{\vartheta\chi^3}\,. \tag{A.1.24b}$$

To calculate the nonlinear strain we need the square of the rotation field from (3.3.6), that is

$$\psi_{o\eta}^2 \simeq \left[D_{11}\sin\varphi + D_{31}\sin\chi\varphi + \left(D_{12}\sin\varphi + D_{22}\cos\varphi + D_{32}\sin\chi\varphi + D_{42}\cos\chi\varphi\right)\frac{\hat{\mathcal{P}}}{\vartheta}\right]^2 =$$
$$= 2\left(D_{11}\sin\varphi + D_{31}\sin\chi\varphi\right)\left(D_{12}\sin\varphi + D_{22}\cos\varphi + D_{32}\sin\chi\varphi + D_{42}\cos\chi\varphi\right)\frac{\hat{\mathcal{P}}}{\vartheta} +$$
$$+ \left(D_{11}\sin\varphi + D_{31}\sin\chi\varphi\right)^2 + \left(D_{12}\sin\varphi + D_{22}\cos\varphi + D_{32}\sin\chi\varphi + D_{42}\cos\chi\varphi\right)^2\left(\frac{\hat{\mathcal{P}}}{\vartheta}\right)^2\,. \tag{A.1.25}$$

Accordingly, we can now determine the constants in (3.3.9), which are

$$\frac{1}{\vartheta}\int_0^{\vartheta}\frac{1}{2}\psi_{o\eta}^2\left(\varphi\right)\mathrm{d}\varphi = I_{o\psi} + I_{1\psi}\frac{\hat{\mathcal{P}}}{\vartheta} + I_{2\psi}\left(\frac{\hat{\mathcal{P}}}{\vartheta}\right)^2\,. \tag{A.1.26}$$

Here

$$I_{o\psi} = \frac{1}{2\vartheta}\int_0^{\vartheta}\left(D_{11}\left(\sin\varphi\right) + D_{31}\left(\sin\chi\varphi\right)\right)^2\mathrm{d}\varphi = \frac{1}{8\vartheta\chi}\cdot$$
$$\cdot\left\{D_{11}^2\chi\left[2\vartheta - \sin 2\vartheta\right] + \frac{8D_{11}D_{31}\chi}{\left(\chi^2-1\right)}\left(\cos\vartheta\sin\chi\vartheta - \chi\sin\vartheta\cos\chi\vartheta\right) + D_{31}^2\left[2\vartheta\chi - \left(\sin 2\chi\vartheta\right)\right]\right\} \tag{A.1.27}$$

and

$$I_{1\psi} = \frac{1}{\vartheta}\int_0^{\vartheta}\left(D_{11}\sin\varphi + D_{31}\sin\chi\varphi\right)\left(D_{12}\sin\varphi + D_{22}\cos\varphi + D_{32}\sin\chi\varphi + D_{42}\cos\chi\varphi\right)\mathrm{d}\varphi =$$
$$= \frac{D_{11}D_{42}}{\vartheta\left(\chi^2-1\right)}\left(\cos\vartheta\cos\chi\vartheta + \chi\sin\vartheta\sin\chi\vartheta - 1\right) + \frac{D_{31}D_{12}}{\vartheta\left(\chi^2-1\right)}\left(\cos\vartheta\sin\chi\vartheta - \chi\sin\vartheta\cos\chi\vartheta\right) +$$
$$+ \frac{D_{31}D_{22}}{\vartheta\left(\chi^2-1\right)}\left(\chi - \chi\cos\vartheta\cos\chi\vartheta - \sin\vartheta\sin\chi\vartheta\right) +$$
$$+ \frac{D_{31}D_{32}}{2}\left(1 - \frac{\sin\chi\vartheta\cos\chi\vartheta}{\vartheta\chi}\right) + \frac{D_{11}D_{12}}{2}\left(1 - \frac{\sin\vartheta\cos\vartheta}{\vartheta}\right) +$$
$$+ \frac{D_{11}D_{22}}{2\vartheta}\sin^2\vartheta + \frac{D_{11}D_{32}}{\vartheta\left(\chi^2-1\right)}\left(\cos\vartheta\sin\chi\vartheta - \chi\sin\vartheta\cos\chi\vartheta\right) + \frac{D_{31}D_{42}}{2\vartheta\chi}\sin^2\chi\vartheta\,. \tag{A.1.28}$$

Moving on now to $I_{2\psi}$ in (A.1.26) it is worth decomposing the integrand in question into four parts:

$$I_{2\psi} = \frac{1}{2\vartheta}\int_0^{\vartheta}\left(D_{12}\sin\varphi + D_{22}\cos\varphi + D_{32}\sin\chi\varphi + D_{42}\cos\chi\varphi\right)^2\mathrm{d}\varphi =$$

DOI: 10.14750/ME.2016.008

$$= \frac{1}{2\vartheta}\int_0^{\vartheta} \left(D_{12}\sin\varphi + D_{22}\cos\varphi + D_{32}\sin\chi\varphi + D_{42}\cos\chi\varphi\right)\, D_{12}\sin\varphi\,\mathrm{d}\varphi +$$
$$+ \frac{1}{2\vartheta}\int_0^{\vartheta} \left(D_{12}\sin\varphi + D_{22}\cos\varphi + D_{32}\sin\chi\varphi + D_{42}\cos\chi\varphi\right) D_{22}\cos\varphi\,\mathrm{d}\varphi +$$
$$+ \frac{1}{2\vartheta}\int_0^{\vartheta} \left(D_{12}\sin\varphi + D_{22}\cos\varphi + D_{32}\sin\chi\varphi + D_{42}\cos\chi\varphi\right) D_{32}\sin\chi\varphi\,\mathrm{d}\varphi +$$
$$+ \frac{1}{2\vartheta}\int_0^{\vartheta} \left(D_{12}\sin\varphi + D_{22}\cos\varphi + D_{32}\sin\chi\varphi + D_{42}\cos\chi\varphi\right) D_{42}\cos\chi\varphi\,\mathrm{d}\varphi =$$
$$= I_{2\psi A} + I_{2\psi B} + I_{2\psi C} + I_{2\psi D}\,. \quad \text{(A.1.29)}$$

The first term in this sum is

$$I_{2\psi A} = \frac{1}{2\vartheta}\int_0^{\vartheta} \left(D_{12}\sin\varphi + D_{22}\cos\varphi + D_{32}\sin\chi\varphi + D_{42}\cos\chi\varphi\right)\, D_{12}\sin\varphi\,\mathrm{d}\varphi =$$
$$= \frac{D_{12}}{8\vartheta\left(1-\chi^2\right)}\left\{D_{12}\left(1-\chi^2\right)\left[2\vartheta - \sin 2\vartheta\right] + D_{22}\left(1-\chi^2\right)\left[1-\cos 2\vartheta\right] +\right.$$
$$\left. + 4D_{32}\left(\chi\sin\vartheta\cos\chi\vartheta - \cos\vartheta\sin\chi\vartheta\right) + 4D_{42}\left[1-\cos\vartheta\cos\chi\vartheta - \chi\sin\vartheta\sin\chi\vartheta\right]\right\}\,. \quad \text{(A.1.30a)}$$

The second one can briefly be expressed as

$$I_{2\psi B} = \frac{1}{2\vartheta}\int_0^{\vartheta} \left(D_{12}\sin\varphi + D_{22}\cos\varphi + D_{32}\sin\chi\varphi + D_{42}\cos\chi\varphi\right) D_{22}\cos\varphi\,\mathrm{d}\varphi =$$
$$= \frac{-D_{22}}{8\vartheta\left(\chi^2-1\right)}\left\{D_{12}\left(\chi^2-1\right)\left(\cos 2\vartheta - 1\right) - D_{22}\left(\chi^2-1\right)\left(\sin 2\vartheta + 2\vartheta\right) +\right.$$
$$+ 4D_{32}\left[\chi\left(\cos\chi\vartheta\right)\cos\vartheta + \left(\sin\chi\vartheta\right)\sin\vartheta - \chi\right] +$$
$$\left. + 4D_{42}\left[\left(\cos\chi\vartheta\right)\sin\vartheta - \chi\left(\sin\chi\vartheta\right)\cos\vartheta\right]\right\}\,. \quad \text{(A.1.30b)}$$

Moreover, for the third part, the integration yields

$$I_{2\psi C} = \frac{1}{2\vartheta}\int_0^{\vartheta} \left(D_{12}\sin\varphi + D_{22}\cos\varphi + D_{32}\sin\chi\varphi + D_{42}\cos\chi\varphi\right) D_{32}\sin\chi\varphi\,\mathrm{d}\varphi =$$
$$= \frac{D_{32}}{8\chi\vartheta\left(1-\chi^2\right)}\left\{4D_{12}\chi\left[\chi\left(\cos\chi\vartheta\right)\sin\vartheta - \left(\sin\chi\vartheta\right)\cos\vartheta\right] +\right.$$
$$+ 4D_{22}\chi\left[\left(\sin\chi\vartheta\right)\sin\vartheta + \chi\left(\cos\chi\vartheta\right)\cos\vartheta - \chi\right] +$$
$$\left. + D_{32}\left(1-\chi^2\right)\left[2\vartheta\chi - \sin 2\chi\vartheta\right] + D_{42}\left(1-\chi^2\right)\left[1-\cos 2\chi\vartheta\right]\right\} \quad \text{(A.1.30c)}$$

and finally, for the the last one we have

$$I_{2\psi D} = \frac{1}{2\vartheta}\int_0^{\vartheta} \left(D_{12}\sin\varphi + D_{22}\cos\varphi + D_{32}\sin\chi\varphi + D_{42}\cos\chi\varphi\right) D_{42}\cos\chi\varphi\,\mathrm{d}\varphi =$$
$$= \frac{D_{42}}{8\vartheta\chi\left(\chi^2-1\right)}\left\{4D_{12}\chi\left[\left(\cos\chi\vartheta\right)\cos\vartheta + \chi\left(\sin\chi\vartheta\right)\sin\vartheta - 1\right] +\right.$$
$$+ 4D_{22}\chi\left[\chi\left(\sin\chi\vartheta\right)\cos\vartheta - \left(\cos\chi\vartheta\right)\sin\vartheta\right] + 2D_{32}\left(\chi^2-1\right)\sin^2\chi\vartheta +$$
$$\left. + 2D_{42}\left(\chi^2-1\right)\left[\chi\vartheta + \left(\sin\chi\vartheta\right)\cos\chi\vartheta\right]\right\}\,. \quad \text{(A.1.30d)}$$

A.1.7. Manipulations on the displacement increment. *Pinned-pinned beams.* Considering pinned-pinned beams the solution to the equation system (3.4.10) is

$$C_1 = -m\varepsilon_{mb}\frac{-A_3\cos\chi\vartheta + A_4\left(\chi\sin\vartheta - \sin\chi\vartheta\right) - 1}{\chi^2\left(\chi^2-1\right)\cos\vartheta}\,, \quad \text{(A.1.31a)}$$

$$C_2 = m\varepsilon_{mb}\frac{A_4}{\chi\left(\chi^2-1\right)}\,, \qquad C_3 = -m\varepsilon_{mb}\frac{\left(3\chi^2-1\right)A_4}{2\chi^4\left(\chi^2-1\right)}\,, \quad \text{(A.1.31b)}$$

DOI: 10.14750/ME.2016.008

$$C_4 = -m\varepsilon_{mb}\frac{\chi\left[\vartheta\left(1-\chi^2\right)\sin\chi\vartheta + 2\chi\cos\chi\vartheta\right]A_3 + \left(1-\chi^2\right)\left[\sin\chi\vartheta - \vartheta\chi\cos\chi\vartheta\right]A_4 + 2}{2\chi^4\left(\chi^2-1\right)\cos\chi\vartheta}\,. \tag{A.1.31c}$$

It is preferable to decompose each of these coefficients into two parts: one proportional to the loading and the other not. Recalling and substituting here A_3 and A_4 for pinned-pinned beams from (3.3.3), after some arrangements, we obtain that

$$C_1 = \varepsilon_{mb}\left(m\frac{A_{31}\cos\chi\vartheta+1}{\left(\chi^2-1\right)\chi^2\cos\vartheta} + m\frac{A_{32}\cos\chi\vartheta - A_{42}\left(\chi\sin\vartheta - \sin\chi\vartheta\right)}{\left(\chi^2-1\right)\chi^2\cos\vartheta}\frac{\hat{\mathcal{P}}}{\vartheta}\right) = \varepsilon_{mb}\left(\hat{C}_{11} + \hat{C}_{12}\frac{\hat{\mathcal{P}}}{\vartheta}\right)\,, \tag{A.1.32a}$$

$$C_2 = \varepsilon_{mb}m\frac{A_{42}}{\left(\chi^2-1\right)\chi}\frac{\hat{\mathcal{P}}}{\vartheta} = \varepsilon_{mb}\hat{C}_{22}\frac{\hat{\mathcal{P}}}{\vartheta}\,, \qquad C_3 = \varepsilon_{mb}m\frac{\left(1-3\chi^2\right)A_{42}}{2\chi^4\left(\chi^2-1\right)}\frac{\hat{\mathcal{P}}}{\vartheta} = \varepsilon_{mb}\hat{C}_{32}\frac{\hat{\mathcal{P}}}{\vartheta}\,, \tag{A.1.32b}$$

$$C_4 = \varepsilon_{mb}\left(\hat{C}_{41} + \hat{C}_{42}\frac{\hat{\mathcal{P}}}{\vartheta}\right) = \varepsilon_{mb}m\frac{2 + A_{31}\left[\chi\vartheta\left(1-\chi^2\right)\sin\chi\vartheta + 2\chi^2\cos\chi\vartheta\right]}{2\chi^4\left(1-\chi^2\right)\cos\chi\vartheta} +$$
$$+\,\varepsilon_{mb}m\frac{\hat{\mathcal{P}}}{\vartheta}\frac{A_{32}\left[\chi\vartheta\left(1-\chi^2\right)\sin\chi\vartheta + 2\chi^2\cos\chi\vartheta\right] + A_{42}\left(\chi^2-1\right)\left(\chi\vartheta\cos\chi\vartheta - \sin\chi\vartheta\right)}{2\chi^4\left(1-\chi^2\right)\cos\chi\vartheta}\,, \tag{A.1.32c}$$

with the new constants defined by

$$\hat{C}_{11} = m\frac{A_{31}\cos\chi\vartheta+1}{\chi^2\left(\chi^2-1\right)\cos\vartheta}\,, \qquad \hat{C}_{12} = m\frac{A_{32}\cos\chi\vartheta - A_{42}\left(\chi\sin\vartheta - \sin\chi\vartheta\right)}{\chi^2\left(\chi^2-1\right)\cos\vartheta}\,, \tag{A.1.33a}$$

$$\hat{C}_{22} = m\frac{A_{42}}{\chi\left(\chi^2-1\right)}\,, \qquad \hat{C}_{32} = m\frac{\left(1-3\chi^2\right)A_{42}}{2\chi^4\left(\chi^2-1\right)}\,, \tag{A.1.33b}$$

$$\hat{C}_{41} = m\frac{2 + A_{31}\chi\left[\vartheta\left(1-\chi^2\right)\sin\chi\vartheta + 2\chi\cos\chi\vartheta\right]}{2\chi^4\left(1-\chi^2\right)\cos\chi\vartheta}\,, \tag{A.1.33c}$$

$$\hat{C}_{42} = m\frac{A_{32}\chi\left[\vartheta\left(1-\chi^2\right)\sin\chi\vartheta + 2\chi\cos\chi\vartheta\right] + A_{42}\left(\chi^2-1\right)\left(\chi\vartheta\cos\chi\vartheta - \sin\chi\vartheta\right)}{2\chi^4\left(1-\chi^2\right)\cos\chi\vartheta}\,. \tag{A.1.33d}$$

Fixed-fixed beams. Proceeding with the problem of fixed-fixed beams, the solution to the system (3.4.24) can preferably be expressed as

$$C_1 = -\frac{m\varepsilon_{mb}}{2\chi^3\mathcal{D}\left(1-\chi^2\right)}\left\{2\left(\chi^2-1\right)\sin\chi\vartheta + A_3\left(\chi^2-1\right)\left[\sin\chi\vartheta\,\cos\chi\vartheta + \vartheta\chi\right] +\right.$$
$$\left.+A_4\left[3\chi^2 - 2\chi^3\left(\sin\vartheta\right)\sin\chi\vartheta + \left(1-\chi^2\right)\cos^2\chi\vartheta - 2\chi^2\left(\cos\chi\vartheta\right)\cos\vartheta - 1\right]\right\}\,, \tag{A.1.34a}$$

$$C_2 = m\varepsilon_{mb}\frac{A_4}{\chi\left(\chi^2-1\right)}\,, \qquad C_3 = -m\varepsilon_{mb}A_4\frac{3\chi^2-1}{2\chi^4\left(\chi^2-1\right)}\,, \tag{A.1.34b}$$

$$C_4 = \frac{m\varepsilon_{mb}}{2\chi^4\mathcal{D}\left(1-\chi^2\right)}\left\{A_4\left[\left\{\left(1-\chi^2\right)\left[\vartheta\chi\cos\chi\vartheta - \sin\chi\vartheta\right] + 2\chi^2\left(\sin\chi\vartheta\right)\right\}\sin\vartheta +\right.\right.$$
$$\left.+\left(2\chi^3\cos\chi\vartheta - \vartheta\chi^2\left(1-\chi^2\right)\sin\chi\vartheta\right)\cos\vartheta - 2\chi^3\right] + 2\left(\chi^2-1\right)\sin\vartheta +$$
$$\left.+A_3\left(\chi^2-1\right)\left[\chi\left(\vartheta\sin\vartheta + \cos\vartheta\right)\sin\chi\vartheta + \vartheta\chi^2\cos\vartheta\cos\chi\vartheta\right]\right\}\,. \tag{A.1.34c}$$

It is practical again to decompose the constants A_i and C_i into the usual two parts. Recalling (3.3.12) we can write

$$C_1 = \varepsilon_{mb}\left(\hat{C}_{11} + \hat{C}_{12}\frac{\hat{\mathcal{P}}}{\vartheta}\right) = \varepsilon_{mb}m\frac{1}{2\chi^3\mathcal{D}}\left[2\sin\chi\vartheta + A_{31}\left(\cos\chi\vartheta\,\sin\chi\vartheta + \vartheta\chi\right)\right] -$$
$$-\,\varepsilon_{mb}m\frac{1}{2\chi^3\left(1-\chi^2\right)\mathcal{D}}\left\{A_{32}\left(\chi^2-1\right)\left[\left(\cos\chi\vartheta\right)\sin\chi\vartheta + \vartheta\chi\right] +\right.$$
$$\left.+A_{42}\left[3\chi^2 - 2\chi^3\left(\sin\vartheta\right)\sin\chi\vartheta + \left(1-\chi^2\right)\cos^2\chi\vartheta - 2\chi^2\left(\cos\chi\vartheta\right)\cos\vartheta - 1\right]\right\}\frac{\hat{\mathcal{P}}}{\vartheta}\,, \tag{A.1.35a}$$

DOI: 10.14750/ME.2016.008

$$C_2 = \varepsilon_{mb}\frac{-mA_{42}}{\chi\left(1-\chi^2\right)}\frac{\hat{\mathcal{P}}}{\vartheta} = \varepsilon_{mb}\hat{C}_{22}\frac{\hat{\mathcal{P}}}{\vartheta}\,, \qquad C_3 = \varepsilon_{mb}\frac{m\left(3\chi^2-1\right)}{2\chi^4\left(1-\chi^2\right)}A_{42}\frac{\hat{\mathcal{P}}}{\vartheta} = \varepsilon_{mb}\hat{C}_{32}\frac{\hat{\mathcal{P}}}{\vartheta}\,, \tag{A.1.35b}$$

$$\begin{aligned} C_4 = {} & \varepsilon_{mb}m\frac{1}{2\chi^4\mathcal{D}}\left\{-2\sin\vartheta - A_{31}\left[\chi\left(\vartheta\sin\vartheta+\cos\vartheta\right)\sin\chi\vartheta + \vartheta\chi^2\cos\vartheta\cos\chi\vartheta\right]\right\} + \\ & + \varepsilon_{mb}m\frac{1}{2\left(1-\chi^2\right)\chi^4\mathcal{D}}\Big\{A_{42}\left[\left[\left(1-\chi^2\right)\left(\vartheta\chi\cos\chi\vartheta-\sin\chi\vartheta\right)+2\chi^2\left(\sin\chi\vartheta\right)\right]\sin\vartheta + \right. \\ & \left. + \left(2\chi^3\cos\chi\vartheta - \vartheta\chi^2\left(1-\chi^2\right)\sin\chi\vartheta\right)\cos\vartheta - 2\chi^3\right] + \\ & + A_{32}\left(\chi^2-1\right)\left[\chi\left(\vartheta\sin\vartheta+\cos\vartheta\right)\sin\chi\vartheta + \vartheta\chi^2\cos\vartheta\cos\chi\vartheta\right]\Big\}\frac{\hat{\mathcal{P}}}{\vartheta} = \varepsilon_{mb}\left(\hat{C}_{41}+\hat{C}_{42}\frac{\hat{\mathcal{P}}}{\vartheta}\right)\,, \end{aligned} \tag{A.1.35c}$$

where the values of $\hat{C}_{ij}$ can be read off easily.

Rotationally restrained beams. The solution to the corresponding system (3.4.32) happens to be

$$\begin{aligned} C_1 = {} & \varepsilon_{mb}\left(\hat{C}_{11}+\hat{C}_{12}\frac{\hat{\mathcal{P}}}{\vartheta}\right) = \\ & = \varepsilon_{mb}\frac{m}{\chi^3\mathcal{C}_0}\left\{A_{31}\left[\chi\cos^2\chi\vartheta + 0.5\mathcal{S}\left(\vartheta\chi+\cos\chi\vartheta\sin\chi\vartheta\right)\right] + \left(\chi\cos\chi\vartheta + \mathcal{S}\sin\chi\vartheta\right)\right\} + \\ & + \varepsilon_{mb}\frac{m}{2\chi^3\left(1-\chi^2\right)\mathcal{C}_0}\Big\{A_{32}\left(1-\chi^2\right)\left[2\chi\cos^2\chi\vartheta + \mathcal{S}\left(\vartheta\chi+\cos\chi\vartheta\sin\chi\vartheta\right)\right] + \\ & + A_{42}\left[2\chi\left(1-\chi^2\right)\left(\sin\chi\vartheta-\chi\sin\vartheta\right)\cos\chi\vartheta + \right. \\ & \left. + \mathcal{S}\left(2\chi^2\cos\vartheta\cos\chi\vartheta + 2\chi^3\sin\vartheta\sin\chi\vartheta - 3\chi^2 + 1 + \left(\chi^2-1\right)\cos^2\chi\vartheta\right)\right]\Big\}\frac{\hat{\mathcal{P}}}{\vartheta}\,, \end{aligned} \tag{A.1.36a}$$

$$C_2 = \varepsilon_{mb}\hat{C}_{22}\frac{\hat{\mathcal{P}}}{\vartheta} = \varepsilon_{mb}\frac{mA_{42}}{\left(\chi^2-1\right)\chi}\frac{\hat{\mathcal{P}}}{\vartheta}\,, \quad C_3 = \varepsilon_{mb}\hat{C}_{32}\frac{\hat{\mathcal{P}}}{\vartheta} = \varepsilon_{mb}\frac{A_{42}m\left(3\chi^2-1\right)}{2\chi^4\left(1-\chi^2\right)}\frac{\hat{\mathcal{P}}}{\vartheta}\,, \tag{A.1.36b}$$

$$\begin{aligned} C_4 = {} & \varepsilon_{mb}\left(\hat{C}_{41}+\hat{C}_{42}\frac{\hat{\mathcal{P}}}{\vartheta}\right) = \varepsilon_{mb}\frac{m}{2\chi^4\left(\chi^2-1\right)\mathcal{C}_0}\left\{2\left(1-\chi^2\right)\left(\cos\vartheta+\mathcal{S}\sin\vartheta\right) + \right. \\ & \left. + A_{31}\left(\chi^2-1\right)\cos\vartheta\left[\chi\left(\vartheta\left(\chi^2-1\right)\sin\chi\vartheta - 2\chi\cos\chi\vartheta\right) - \mathcal{S}\chi\left(\left(1+\vartheta\tan\vartheta\right)\sin\chi\vartheta + \chi\vartheta\cos\chi\vartheta\right)\right]\right\} + \\ & + \varepsilon_{mb}\frac{\hat{\mathcal{P}}}{\vartheta}\frac{m}{2\chi^4\left(\chi^2-1\right)\mathcal{C}_0}\Big\{A_{32}\left(\chi^2-1\right)\cos\vartheta\left[\chi\left(\vartheta\left(\chi^2-1\right)\sin\chi\vartheta - 2\chi\cos\chi\vartheta\right) - \right. \\ & \left. - \mathcal{S}\chi\left(\left(1+\vartheta\tan\vartheta\right)\sin\chi\vartheta + \chi\vartheta\cos\chi\vartheta\right)\right] + A_{42}\left[\left(\chi^2-1\right)\left(1-\chi^2\right)\left(\vartheta\chi\cos\chi\vartheta - \sin\chi\vartheta\right)\cos\vartheta + \right. \\ & \left. + \mathcal{S}\left(2\chi^3\left(1-\cos\vartheta\cos\chi\vartheta\right) + \left(\chi^2-1\right)\vartheta\chi\left[\sin\vartheta\cos\chi\vartheta - \chi\cos\vartheta\sin\chi\vartheta\right] + \left(1-3\chi^2\right)\sin\vartheta\sin\chi\vartheta\right)\right]\Big\}\,. \end{aligned} \tag{A.1.36c}$$

It can be checked that if $[\mathcal{S}=0]$ $\{\mathcal{S}\to\infty\}$ we get back the results valid for [pinned-pinned] and {fixed-fixed} beams.

The displacement and rotation after buckling. From now on what is written is valid for all support arrangements. To be able to rewrite the solution W_{ob} in a favourable form, the particular solution W_{obp} in (3.4.5) is manipulated so that

$$\begin{aligned} W_{obp} = {} & -\varepsilon_{mb}\frac{m}{2\chi^3}\left(\frac{2}{\chi}+A_3\varphi\sin\chi\varphi - A_4\varphi\cos\chi\varphi\right) = \\ & = \varepsilon_{mb}\left[-\frac{m}{\chi^4} - \frac{A_{31}m}{2\chi^3}\varphi\sin\chi\varphi + \left(-\frac{A_{32}m}{2\chi^3}\varphi\sin\chi\varphi + \frac{A_{42}m}{2\chi^3}\varphi\cos\chi\varphi\right)\frac{\hat{\mathcal{P}}}{\vartheta}\right] = \\ & = \varepsilon_{mb}\left[\hat{C}_{01} + \hat{C}_{51}\varphi\sin\chi\varphi + \left(\hat{C}_{52}\varphi\sin\chi\varphi + \hat{C}_{62}\varphi\cos\chi\varphi\right)\frac{\hat{\mathcal{P}}}{\vartheta}\right]\,, \end{aligned} \tag{A.1.37a}$$

DOI: 10.14750/ME.2016.008

where

$$\hat{C}_{01} = -\frac{m}{\chi^4}\,, \qquad \hat{C}_{51} = -\frac{A_{31}m}{2\chi^3}\,, \qquad \hat{C}_{52} = -\frac{A_{32}m}{2\chi^3}\,, \qquad \hat{C}_{62} = \frac{A_{42}m}{2\chi^3}\,. \tag{A.1.37b}$$

Altogether, the solution for the whole beam is sought as

$$W_{ob} = C_1\cos\varphi + C_2 H\sin\varphi + C_3 H\sin\chi\varphi + C_4\cos\chi\varphi - \varepsilon_{mb}\frac{m}{2\chi^3}\left(\frac{2}{\chi} + A_3\varphi\sin\chi\varphi - A_4 H\varphi\cos\chi\varphi\right)$$

or more practically, the displacement field is

$$W_{ob} = \varepsilon_{mb}\left[\hat{C}_{01} + \hat{C}_{11}\cos\varphi + \hat{C}_{41}\cos\chi\varphi + \hat{C}_{51}\varphi\sin\chi\varphi + \right.$$
$$\left. + \left(\hat{C}_{12}\cos\varphi + \hat{C}_{22}H\sin\varphi + \hat{C}_{32}H\sin\chi\varphi + \hat{C}_{42}\cos\chi\varphi + \hat{C}_{52}\varphi\sin\chi\varphi + \hat{C}_{62}H\varphi\cos\chi\varphi\right)\frac{\hat{\mathcal{P}}}{\vartheta}\right]\,. \tag{A.1.38}$$

As regards the expression of the rotation, it is the derivative of the former relation, therefore

$$-\psi_{o\eta b} \simeq W_{ob}^{(1)} = \varepsilon_{mb}\left[-\hat{C}_{11}\sin\varphi + \left(\hat{C}_{51} - \hat{C}_{41}\chi\right)\sin\chi\varphi + \hat{C}_{51}\chi\varphi\cos\chi\varphi + \right.$$
$$+ \left(-\hat{C}_{12}\sin\varphi + \hat{C}_{22}H\cos\varphi + \left(\hat{C}_{32}\chi + \hat{C}_{62}\right)H\cos\chi\varphi + \left(\hat{C}_{52} - \hat{C}_{42}\chi\right)\sin\chi\varphi + \right.$$
$$\left.\left. + \hat{C}_{52}\chi\varphi\cos\chi\varphi - \hat{C}_{62}H\chi\varphi\sin\chi\varphi\right)\frac{\hat{\mathcal{P}}}{\vartheta}\right] \tag{A.1.39}$$

or what is the same

$$-\psi_{o\eta b} \simeq W_{ob}^{(1)} = \varepsilon_{mb}\left[K_{11}\sin\varphi + K_{41}\sin\chi\varphi + K_{51}\varphi\cos\chi\varphi + \right.$$
$$+ \left(K_{12}\sin\varphi + K_{22}\cos\varphi + K_{32}\cos\chi\varphi + K_{42}\sin\chi\varphi + \right.$$
$$\left.\left. + K_{52}\varphi\cos\chi\varphi + K_{62}\varphi\sin\chi\varphi\right)\frac{\hat{\mathcal{P}}}{\vartheta}\right]\,, \tag{A.1.40}$$

with

$$K_{11} = -\hat{C}_{11}\,, \qquad K_{41} = \hat{C}_{51} - \hat{C}_{41}\chi\,, \qquad K_{51} = \hat{C}_{51}\chi\,, \qquad K_{12} = -\hat{C}_{12}\,, \qquad K_{22} = \hat{C}_{22}H\,,$$
$$K_{32} = \hat{C}_{32}H\chi + \hat{C}_{62}H\,, \qquad K_{42} = \hat{C}_{52} - \hat{C}_{42}\chi\,, \qquad K_{52} = \hat{C}_{52}\chi\,, \qquad K_{62} = -\hat{C}_{62}\chi H\,. \tag{A.1.41}$$

A.1.8. The averaged strain increment. We aim to detail the integrals I_{01}, I_{02}, I_{11}, I_{12}, I_{13} introduced in Subsection 3.4.3 under (3.4.16). Recalling the formula for the averaged axial strain we have two terms to deal with:

$$\frac{1}{\vartheta}\int_0^{\vartheta} W_{ob}\mathrm{d}\varphi = \varepsilon_{mb}\left[I_{02}\frac{\hat{\mathcal{P}}}{\vartheta} + I_{01}\right]\,; \tag{A.1.42a}$$

$$\frac{1}{\vartheta}\int_0^{\vartheta} W_{ob}^{(1)}W_o^{(1)}\mathrm{d}\varphi = \varepsilon_{mb}\left[I_{13}\left(\frac{\hat{\mathcal{P}}}{\vartheta}\right)^2 + \frac{\hat{\mathcal{P}}}{\vartheta}I_{12} + I_{11}\right]\,. \tag{A.1.42b}$$

Starting with the first one let us integrate that part of the displacement increment which does not contain the loading $\hat{\mathcal{P}}$. Therefore, it follows that

$$I_{01} = \frac{1}{\vartheta}\int_0^{\vartheta}\left(\hat{C}_{01} + \hat{C}_{11}\cos\varphi + \hat{C}_{41}\cos\chi\varphi + \hat{C}_{51}\varphi\sin\chi\varphi\right)\mathrm{d}\varphi =$$
$$= \frac{1}{\chi^2\vartheta}\left[\chi^2\left(\hat{C}_{01}\vartheta + \hat{C}_{11}\sin\vartheta\right) + \hat{C}_{41}\chi\sin\chi\vartheta + \hat{C}_{51}\left(\sin\chi\vartheta - \chi\vartheta\cos\chi\vartheta\right)\right]\,. \tag{A.1.43a}$$

Integrating the remainder of the displacement increment yields

DOI: 10.14750/ME.2016.008

$$I_{02}=\frac{1}{\vartheta}\int_0^{\vartheta}\left(\hat{C}_{12}\cos\varphi+\hat{C}_{22}\sin\varphi+\hat{C}_{32}\sin\chi\varphi+\hat{C}_{42}\cos\chi\varphi+\hat{C}_{52}\varphi\sin\chi\varphi+\hat{C}_{62}\varphi\cos\chi\varphi\right)\mathrm{d}\varphi=$$
$$=\frac{1}{\chi^2\vartheta}\left[\chi^2\left(\hat{C}_{12}\sin\vartheta+(1-\cos\vartheta)\,\hat{C}_{22}\right)+\hat{C}_{52}\sin\chi\vartheta+(\cos\chi\vartheta-1)\,\hat{C}_{62}+\right.$$
$$\left.+\chi\left((1-\cos\chi\vartheta)\,\hat{C}_{32}+\hat{C}_{42}\sin\chi\vartheta-\hat{C}_{52}\vartheta\cos\chi\vartheta+\hat{C}_{62}\vartheta\sin\chi\vartheta\right)\right]\ . \quad \text{(A.1.43b)}$$

Observe that I_{01} and I_{02} are the only integrals that appear when the linearized theory is considered. In this way we get the

$$I_{02}\frac{\hat{\mathcal{P}}}{\vartheta}+I_{01}=1 \quad \text{(A.1.44)}$$

linear relation for $\hat{\mathcal{P}}$.

As for the second integral in (A.1.42) let us recall formulae (3.4.13) and (3.3.6a) providing the rotations and then separate the terms depending on the power of $\hat{\mathcal{P}}/\vartheta$:

$$\frac{1}{\vartheta}\int_0^{\vartheta}\psi_{o\eta}\psi_{o\eta\,b}\mathrm{d}\varphi\approx\frac{1}{\vartheta}\int_0^{\vartheta}\left(-W_o^{(1)}\right)\left(-W_{ob}^{(1)}\right)\mathrm{d}\varphi=$$
$$=-\varepsilon_{mb}\frac{1}{\vartheta}\int_0^{\vartheta}\left[(K_{11}\sin\varphi+K_{41}\sin\chi\varphi+K_{51}\,\varphi\cos\chi\varphi)+\right.$$
$$\left.+\frac{\hat{\mathcal{P}}}{\vartheta}\left(K_{12}\sin\varphi+K_{22}\cos\varphi+K_{32}\cos\chi\varphi+K_{42}\sin\chi\varphi+K_{52}\varphi\cos\chi\varphi+K_{62}\varphi\sin\chi\varphi\right)\right]\cdot$$
$$\cdot\left[D_{11}\sin\varphi+D_{31}\sin\chi\varphi+\left(D_{12}\sin\varphi+D_{22}\cos\varphi+D_{32}\sin\chi\varphi+D_{42}\cos\chi\varphi\right)\frac{\hat{\mathcal{P}}}{\vartheta}\right]\mathrm{d}\varphi=$$
$$=-\varepsilon_{mb}\frac{1}{\vartheta}\int_0^{\vartheta}\left[\left(K_{11}\sin\varphi+K_{41}\sin\chi\varphi+K_{51}\,\varphi\cos\chi\varphi\right)\left(D_{11}\sin\varphi+D_{31}\sin\chi\varphi\right)+\right.$$
$$+\left(K_{11}\sin\varphi+K_{41}\sin\chi\varphi+K_{51}\,\varphi\cos\chi\varphi\right)\left(D_{12}\sin\varphi+D_{22}\cos\varphi+D_{32}\sin\chi\varphi+D_{42}\cos\chi\varphi\right)\frac{\hat{\mathcal{P}}}{\vartheta}+$$
$$+\left(K_{12}\sin\varphi+K_{22}\cos\varphi+K_{32}\cos\chi\varphi+K_{42}\sin\chi\varphi+K_{52}\varphi\cos\chi\varphi+K_{62}\varphi\sin\chi\varphi\right)\cdot$$
$$\cdot\left(D_{11}\sin\varphi+D_{31}\sin\chi\varphi\right)\frac{\hat{\mathcal{P}}}{\vartheta}+$$
$$+\left(K_{12}\sin\varphi+K_{22}\cos\varphi+K_{32}\cos\chi\varphi+K_{42}\sin\chi\varphi+K_{52}\varphi\cos\chi\varphi+K_{62}\varphi\sin\chi\varphi\right)\cdot$$
$$\left.\cdot\left(D_{12}\sin\varphi+D_{22}\cos\varphi+D_{32}\sin\chi\varphi+D_{42}\cos\chi\varphi\right)\left(\frac{\hat{\mathcal{P}}}{\vartheta}\right)^2\right]\mathrm{d}\varphi\ ,$$

in which

$$I_{11}=-\frac{1}{\vartheta}\int_0^{\vartheta}\left(K_{11}\sin\varphi+K_{41}\sin\chi\varphi+K_{51}\,\varphi\cos\chi\varphi\right)\left(D_{11}\sin\varphi+D_{31}\sin\chi\varphi\right)\mathrm{d}\varphi\ , \quad \text{(A.1.45a)}$$

$$I_{12}=-\frac{1}{\vartheta}\int_0^{\vartheta}\left(D_{11}\sin\varphi+D_{31}\sin\chi\varphi\right)\cdot$$
$$\cdot\left(K_{12}\sin\varphi+K_{22}\cos\varphi+K_{32}\cos\chi\varphi+K_{42}\sin\chi\varphi+K_{52}\varphi\cos\chi\varphi+K_{62}\varphi\sin\chi\varphi\right)\mathrm{d}\varphi-$$
$$-\frac{1}{\vartheta}\int_0^{\vartheta}\left(K_{11}\sin\varphi+K_{41}\sin\chi\varphi+K_{51}\,\varphi\cos\chi\varphi\right)\left(D_{12}\sin\varphi+D_{22}\cos\varphi+D_{32}\sin\chi\varphi+D_{42}\cos\chi\varphi\right)\mathrm{d}\varphi, \quad \text{(A.1.45b)}$$

$$I_{13}=-\frac{1}{\vartheta}\int_0^{\vartheta}\left(D_{12}\sin\varphi+D_{22}\cos\varphi+D_{32}\sin\chi\varphi+D_{42}\cos\chi\varphi\right)\cdot$$
$$\cdot\left(K_{12}\sin\varphi+K_{22}\cos\varphi+K_{32}\cos\chi\varphi+K_{42}\sin\chi\varphi+K_{52}\varphi\cos\chi\varphi+K_{62}\varphi\sin\chi\varphi\right)\mathrm{d}\varphi\ . \quad \text{(A.1.45c)}$$

DOI: 10.14750/ME.2016.008

Construction of closed-form solutions to these is feasible. However, it is not worth dealing with these since – as it turns out – the applied Fortran subroutine and other tested mathematical softwares like Maple 16 or Scientific Work Place 5.5 can cope with these integrals easily and accurately enough.

A.2. Some additional transformations for Chapter 4

A.2.1. The static equilibrium. Substitution of (4.1.2) into $(4.1.3)_2$ yields

$$-I_{e\eta}\frac{\mathrm{d}^2}{\mathrm{d}s^2}\left(\frac{\mathrm{d}^2 w_o}{\mathrm{d}s^2}+\frac{w_o}{\rho_o^2}\right)-\frac{I_{e\eta}}{\rho_o^2}\left(\frac{\mathrm{d}^2 w_o}{\mathrm{d}s^2}+\frac{w_o}{\rho_o^2}\right)-\frac{I_{e\eta}}{\rho_o^3}m\varepsilon_{o\xi}-\frac{I_{e\eta}}{\rho_o^2}m\varepsilon_{o\xi}\frac{\mathrm{d}}{\mathrm{d}s}\psi_{o\eta}+f_n=0 \quad \text{(A.2.1)}$$

which, after some arrangements, leads to

$$w_o^{(4)}+2w_o^{(2)}+w_o+\rho_o m\varepsilon_{o\xi}+\rho_o m\varepsilon_{o\xi}\psi_{o\eta}^{(1)}=\frac{\rho_o^4}{I_{e\eta}}f_n \quad \text{(A.2.2)}$$

or equivalently to

$$W_o^{(4)}+2W_o^{(2)}+W_o+m\varepsilon_{o\xi}\left(1+U_o^{(1)}-W_o^{(2)}\right)=\frac{\rho_o^3}{I_{e\eta}}f_n\,. \quad \text{(A.2.3)}$$

If the distributed force f_n is zero then

$$W_o^{(4)}+2W_o^{(2)}+W_o+m\left(U_o^{(1)}+W_o\right)+m\varepsilon_{o\xi}\left(U_o^{(1)}-W_o^{(2)}\right)=0\,. \quad \text{(A.2.4)}$$

Equation (A.2.3) can be rewritten using $(4.1.1)_2$

$$\varepsilon_{o\xi}=U_o^{(1)}+W_o \quad \rightarrow \quad U_o^{(1)}=\varepsilon_{o\xi}-W_o, \quad \text{(A.2.5)}$$

thus

$$\begin{aligned} W_o^{(4)}+2W_o^{(2)}+W_o+m\varepsilon_{o\xi}+m\varepsilon_{o\xi}\left(\varepsilon_{o\xi}-W_o-W_o^{(2)}\right) &= \frac{\rho_o^3}{I_{e\eta}}f_n\,, \\ W_o^{(4)}+2W_o^{(2)}+W_o+m\varepsilon_{o\xi}\left(1+\varepsilon_{o\xi}\right)-m\varepsilon_{o\xi}\left(W_o+W_o^{(2)}\right) &= \frac{\rho_o^3}{I_{e\eta}}f_n\,. \end{aligned} \quad \text{(A.2.6)}$$

If we assume that $1+\varepsilon_{o\xi}\approx 1$ then finally we have

$$\begin{aligned} W_o^{(4)}+2W_o^{(2)}+W_o+m\left(U_o^{(1)}+W_o\right)-m\varepsilon_{o\xi}\left(W_o+W_o^{(2)}\right) &= \frac{\rho_o^3}{I_{e\eta}}f_n\,, \\ W_o^{(4)}+\left(2-m\varepsilon_{o\xi}\right)W_o^{(2)}+\left[1+m\left(1-\varepsilon_{o\xi}\right)\right]W_o+mU_o^{(1)} &= \frac{\rho_o^3}{I_{e\eta}}f_n\,. \end{aligned} \quad \text{(A.2.7)}$$

Equilibrium equations (4.1.5) and (A.2.7) are now gathered in matrix form:

$$\begin{aligned} &\begin{bmatrix} 0 & 0 \\ 0 & 1 \end{bmatrix}\begin{bmatrix} U_o \\ W_o \end{bmatrix}^{(4)}+\begin{bmatrix} -m & 0 \\ 0 & 2-m\varepsilon_{o\xi} \end{bmatrix}\begin{bmatrix} U_o \\ W_o \end{bmatrix}^{(2)}+ \\ &\quad+\begin{bmatrix} 0 & -m \\ m & 0 \end{bmatrix}\begin{bmatrix} U_o \\ W_o \end{bmatrix}^{(1)}+\begin{bmatrix} 0 & 0 \\ 0 & 1+m\left(1-\varepsilon_{o\xi}\right) \end{bmatrix}\begin{bmatrix} U_o \\ W_o \end{bmatrix}^{(0)}=\frac{\rho_o^3}{I_{e\eta}}\begin{bmatrix} f_t \\ f_n \end{bmatrix}. \end{aligned} \quad \text{(A.2.8)}$$

When the distributed forces are zero we can utilize

$$U_o^{(2)}+W_o^{(1)}=\varepsilon_{o\xi}^{(1)}=0 \quad \rightarrow \quad U_o^{(2)}=-W_o^{(1)} \quad \text{(A.2.9)}$$

on the first derivative of (A.2.4). As a consequence, we can eliminate either U_o

$$\begin{aligned} &W_o^{(5)}+2W_o^{(3)}+W_o^{(1)}+m\varepsilon_{o\xi}\left(U_o^{(2)}-W_o^{(3)}\right)=W_o^{(5)}+2W_o^{(3)}+W_o^{(1)}-m\varepsilon_{o\xi}\left(W_o^{(1)}+W_o^{(3)}\right)= \\ &\quad W_o^{(5)}+\left(2-m\varepsilon_{o\xi}\right)W_o^{(3)}+\left(1-m\varepsilon_{o\xi}\right)W_o^{(1)}=W_o^{(5)}+\left(1+\chi^2\right)W_o^{(3)}+\chi^2 W_o^{(1)}=0 \end{aligned} \quad \text{(A.2.10)}$$

or W_o

$$U_o^{(6)}+\left(1+\chi^2\right)U_o^{(4)}+\chi^2 U_o^{(2)}=0, \quad \text{(A.2.11)}$$

DOI: 10.14750/ME.2016.008

given that

$$\chi^2 = 1 - m\varepsilon_{o\xi}, \quad \text{if} \quad \mathrm{m}\varepsilon_{o\xi} < 1\,. \tag{A.2.12}$$

A.2.2. Equations of the vibrations. Substituting relations (4.1.17) into $(4.1.18)_2$, after some arrangements we get

$$\left(w_{ob}^{(4)} + w_{ob}^{(2)}\right) + \left(w_{ob}^{(2)} + w_{ob}\right) + m\rho_o\varepsilon_{o\xi\,b}\,\psi_{o\eta\,b}^{(1)} + m\rho_o\left(\varepsilon_{o\xi\,b} - \underbrace{(\varepsilon_{o\xi\,b}\psi_{o\eta})^{(1)}}_{\text{quadratic term}}\right) = \frac{\rho_o^4}{I_{e\eta}} f_{nb}\,, \tag{A.2.13}$$

where the underset quadratic term can be neglected with a good accuracy. Some further manipulations are need to be carried out in the latter formula taking into account that (a) $\psi_{o\eta\,b}^{(1)} = u_{ob}^{(1)}/\rho_o - w_{ob}^{(2)}/\rho_o$ and (b) $u_{ob}^{(1)} = \rho_o\varepsilon_{o\xi\,b} - w_{ob}$, therefore

$$\left(w_{ob}^{(4)} + w_{ob}^{(2)}\right) + \left(w_{ob}^{(2)} + w_{ob}\right) + m\varepsilon_{o\xi}\left(\rho_o\varepsilon_{o\xi\,b} - w_{ob} - w_{ob}^{(2)}\right) + m\rho_o\varepsilon_{o\xi\,b} = \frac{\rho_o^4}{I_{e\eta}} f_{nb}\,, \tag{A.2.14}$$

or what is the same

$$\left(w_{ob}^{(4)} + w_{ob}^{(2)}\right) + \left(w_{ob}^{(2)} + w_{ob}\right) - m\varepsilon_{o\xi}\left(w_{ob} + w_{ob}^{(2)}\right) + m\rho_o\varepsilon_{o\xi\,b}\,(1 + \varepsilon_{o\xi}) = \frac{\rho_o^4}{I_{e\eta}} f_{nb}\,. \tag{A.2.15}$$

Here we can apply the inequality $\varepsilon_{o\xi\,b} \gg \varepsilon_{\xi\,b}\varepsilon_{o\xi}$, thus

$$\left(w_{ob}^{(4)} + w_{ob}^{(2)}\right) + \left(w_{ob}^{(2)} + w_{ob}\right) + m\rho_o\varepsilon_{o\xi\,b} - m\varepsilon_{o\xi}\left(w_{ob} + w_{ob}^{(2)}\right) = \frac{\rho_o^4}{I_{e\eta}} f_{nb}\,. \tag{A.2.16}$$

Introducing the dimensionless displacements leads to

$$\left(W_{ob}^{(4)} + W_{ob}^{(2)}\right) + \left(W_{ob}^{(2)} + W_{ob}\right) + m\left(U_{ob}^{(1)} + W_{ob}\right) - m\varepsilon_{o\xi}\left(W_{ob} + W_{ob}^{(2)}\right) = \frac{\rho_o^3}{I_{e\eta}} f_{nb}\,. \tag{A.2.17}$$

So the governing equations in terms of the dimensionless displacement increments are

$$-m\left(U_{ob}^{(2)} + W_{ob}^{(1)}\right) = \frac{\rho_o^3}{I_{e\eta}} f_{tb}\,, \tag{A.2.18}$$

$$W_{ob}^{(4)} + (2 - m\varepsilon_{o\xi})\,W_{ob}^{(2)} + [1 + m\,(1 - \varepsilon_{o\xi})]\,W_{ob} + mU_{ob}^{(1)} = \frac{\rho_o^3}{I_{e\eta}} f_{nb}\,. \tag{A.2.19}$$

We repeat these relations in matrix form:

$$\begin{bmatrix} 0 & 0 \\ 0 & 1 \end{bmatrix} \begin{bmatrix} U_{ob} \\ W_{ob} \end{bmatrix}^{(4)} + \begin{bmatrix} -m & 0 \\ 0 & 2 - m\varepsilon_{o\xi} \end{bmatrix} \begin{bmatrix} U_{ob} \\ W_{ob} \end{bmatrix}^{(2)} + \\ + \begin{bmatrix} 0 & -m \\ m & 0 \end{bmatrix} \begin{bmatrix} U_{ob} \\ W_{ob} \end{bmatrix}^{(1)} + \begin{bmatrix} 0 & 0 \\ 0 & 1 + m\,(1 - \varepsilon_{o\xi}) \end{bmatrix} \begin{bmatrix} U_{ob} \\ W_{ob} \end{bmatrix}^{(0)} = \frac{\rho_o^3}{I_{e\eta}} \begin{bmatrix} f_{tb} \\ f_{nb} \end{bmatrix}\,. \tag{A.2.20}$$

A.2.3. The load-strain relationship. Substituting the solution (4.6.1) into (4.6.3b) yields

$$\begin{aligned} O_1 - O_5 + O_6 - R_1 + R_5 - R_6 &= 0, \\ O_2 - O_4 m - R_2 + R_4 m &= 0, \\ O_1 + O_5 - R_1 - R_5 &= 0, \\ -O_2 + O_4\,(m + 1) + R_2 - R_4\,(m + 1) &= 0, \\ -O_2 + 2O_3 + R_2 - 2R_3 &= 0, \\ -O_1 - 3O_5 + R_1 + 3R_5 - \frac{(\rho_o)^2\,P_\zeta}{I_{e\eta}} &= 0, \end{aligned} \tag{A.2.21}$$

which are indeed the (dis)continuity conditions and are independent of the supports.

For pinned-pinned beams the boundary conditions (4.6.3a) are

$$O_1\cos\vartheta + O_2\sin\vartheta + O_3\,(-\vartheta\cos\vartheta + \sin\vartheta) - O_4\,(m + 1)\,\vartheta + O_5\,(-\cos\vartheta - \vartheta\sin\vartheta) + O_6 = 0,$$
$$O_1\sin\vartheta + O_2\cos\vartheta + O_3\,(2\cos\vartheta - \vartheta\sin\vartheta) - O_5\,(-2\sin\vartheta - \vartheta\cos\vartheta) = 0,$$

DOI: 10.14750/ME.2016.008

$$
\begin{gathered}
-O_1 \sin\vartheta + O_2 \cos\vartheta + O_3\vartheta \sin\vartheta - O_4 m - O_5\vartheta \cos\vartheta = 0, \\
R_1 \cos\vartheta - R_2 \sin\vartheta + R_3 (\vartheta \cos\vartheta - \sin\vartheta) + R_4 (m+1)\vartheta + R_5 (-\cos\vartheta - \vartheta \sin\vartheta) + R_6 = 0, \\
-R_1 \sin\vartheta - R_2 \cos\vartheta + R_3 (2\cos\vartheta - \vartheta \sin\vartheta) - R_5 (2\sin\vartheta + \vartheta \cos\vartheta) = 0, \\
R_1 \sin\vartheta + R_2 \cos\vartheta + R_3\vartheta \sin\vartheta - R_4 m + R_5\vartheta \cos\vartheta = 0. \qquad \text{(A.2.22)}
\end{gathered}
$$

For fixed-fixed beams they are slightly different:

$$
\begin{gathered}
O_1 \cos\vartheta + O_2 \sin\vartheta + O_3 (-\vartheta \cos\vartheta + \sin\vartheta) - O_4 (m+1)\vartheta + O_5 (-\cos\vartheta - \vartheta \sin\vartheta) + O_6 = 0, \\
O_1 \cos\vartheta + O_2 \sin\vartheta + O_3 (-\sin\vartheta - \vartheta \cos\vartheta) + O_5 (\cos\vartheta - \vartheta \sin\vartheta) = 0, \\
-O_1 \sin\vartheta + O_2 \cos\vartheta + O_3\vartheta \sin\vartheta - O_4 m - O_5\vartheta \cos\vartheta = 0, \\
R_1 \cos\vartheta - R_2 \sin\vartheta + R_3 (\vartheta \cos\vartheta - \sin\vartheta) + R_4 (m+1)\vartheta + R_5 (-\cos\vartheta - \vartheta \sin\vartheta) + R_6 = 0, \\
R_1 \cos\vartheta - R_2 \sin\vartheta + R_3 (\sin\vartheta + \vartheta \cos\vartheta) + R_5 (\cos\vartheta - \vartheta \sin\vartheta) = 0, \\
R_1 \sin\vartheta + R_2 \cos\vartheta + R_3\vartheta \sin\vartheta - R_4 m + R_5\vartheta \cos\vartheta = 0\ . \qquad \text{(A.2.23)}
\end{gathered}
$$

DOI: 10.14750/ME.2016.008

A.2.3.1. *The equation system for pinned-pinned beams in Subsection 4.6.1.*

$$
\begin{bmatrix}
\cos\vartheta & \sin\vartheta & -\vartheta\cos\vartheta+\sin\vartheta & -(m+1)\,\vartheta & -\cos\vartheta-\vartheta\sin\vartheta & 1 & 0 & 0 & 0 & 0 & 0 & 0 \\
\sin\vartheta & \cos\vartheta & 2\cos\vartheta-\vartheta\sin\vartheta & 0 & -\left(-2\sin\vartheta-\vartheta\cos\vartheta\right) & 0 & 0 & 0 & 0 & 0 & 0 & 0 \\
-\sin\vartheta & \cos\vartheta & \vartheta\sin\vartheta & -m & -\vartheta\cos\vartheta & 0 & 0 & 0 & -1 & 0 & 0 & 0 \\
1 & 0 & 0 & 0 & -1 & 1 & 0 & 0 & 0 & 0 & 0 & 0 \\
0 & 1 & 0 & -m & 0 & 0 & 0 & 0 & 0 & 0 & 0 & 0 \\
1 & 0 & 0 & 0 & 1 & 0 & 0 & 0 & 0 & 0 & 0 & 0 \\
0 & -1 & 0 & m+1 & 0 & 0 & 0 & 0 & 0 & 0 & 0 & 0 \\
0 & -1 & 2 & 0 & 0 & 0 & 0 & 0 & 0 & 0 & 0 & 0 \\
-1 & 0 & 0 & 0 & -3 & 0 & 0 & 0 & 0 & 0 & 0 & 0 \\
0 & 0 & 0 & 0 & 0 & 0 & 0 & 0 & 0 & 0 & 0 & 0 \\
0 & 0 & 0 & 0 & 0 & 0 & 0 & 0 & 0 & 0 & 0 & 0 \\
0 & 0 & 0 & 0 & 0 & 0 & 0 & 0 & 0 & 0 & 0 & 0
\end{bmatrix}
\begin{bmatrix} O_1 \\ O_2 \\ O_3 \\ O_4 \\ O_5 \\ O_6 \\ R_1 \\ R_2 \\ R_3 \\ R_4 \\ R_5 \\ R_6 \end{bmatrix}
=
\begin{bmatrix} 0 \\ 0 \\ 0 \\ 0 \\ 0 \\ 0 \\ 0 \\ 0 \\ +\frac{(\rho_o)^2 P_\zeta}{I_{e\eta}} \\ 0 \\ 0 \\ 0 \end{bmatrix}
\tag{A.2.24}
$$

DOI: 10.14750/ME.2016.008

A.2.3.2. *The equation system for fixed-fixed beams in Subsection 4.6.2.*

$$
\begin{bmatrix}
\cos\vartheta & \sin\vartheta & -\vartheta\cos\vartheta+\sin\vartheta & -(m+1)\,\vartheta & -\cos\vartheta-\vartheta\sin\vartheta & 1 \\
\cos\vartheta & \sin\vartheta & -\sin\vartheta-\vartheta\cos\vartheta & 0 & \cos\vartheta-\vartheta\sin\vartheta & 0 \\
-\sin\vartheta & \cos\vartheta & \vartheta\sin\vartheta & -m & -\vartheta\cos\vartheta & 0 \\
1 & 0 & 0 & 0 & -1 & 1 \\
0 & 1 & 0 & -m & 0 & 0 \\
1 & 0 & 0 & 0 & 1 & 0 \\
0 & -1 & 0 & m+1 & 0 & 0 \\
0 & -1 & 2 & 0 & 0 & 0 \\
-1 & 0 & 0 & 0 & -3 & 0 \\
0 & 0 & 0 & 0 & 0 & 0 \\
0 & 0 & 0 & 0 & 0 & 0 \\
0 & 0 & 0 & 0 & 0 & 0
\end{bmatrix}
\begin{bmatrix}
0 & 0 & 0 & 0 & 0 & 0 \\
0 & 0 & 0 & 0 & 0 & 0 \\
0 & 0 & 0 & 0 & 0 & 0 \\
-1 & 0 & 0 & 0 & 1 & -1 \\
0 & -1 & 0 & m & 0 & 0 \\
-1 & 0 & 0 & 0 & -1 & 0 \\
0 & 1 & 0 & -(m+1) & 0 & 0 \\
0 & 1 & -2 & 0 & 0 & 0 \\
1 & 0 & 0 & 0 & 3 & 0 \\
\cos\vartheta & -\sin\vartheta & \vartheta\cos\vartheta-\sin\vartheta & (m+1)\,\vartheta & -\cos\vartheta-\vartheta\sin\vartheta & 1 \\
\cos\vartheta & -\sin\vartheta & \sin\vartheta+\vartheta\cos\vartheta & 0 & \cos\vartheta-\vartheta\sin\vartheta & 0 \\
\sin\vartheta & \cos\vartheta & \vartheta\sin\vartheta & -m & \vartheta\cos\vartheta & 0
\end{bmatrix}
\begin{bmatrix} O_1 \\ O_2 \\ O_3 \\ O_4 \\ O_5 \\ O_6 \\ R_1 \\ R_2 \\ R_3 \\ R_4 \\ R_5 \\ R_6 \end{bmatrix}
=
\begin{bmatrix} 0 \\ 0 \\ 0 \\ 0 \\ 0 \\ 0 \\ 0 \\ 0 \\ +\frac{(\rho_o)^2 P_\zeta}{I_{e\eta}} \\ 0 \\ 0 \\ 0 \end{bmatrix}
\tag{A.2.25}
$$

DOI: 10.14750/ME.2016.008

List of Figures

DOI: 10.14750/ME.2016.008

DOI: 10.14750/ME.2016.008

List of Tables

DOI: 10.14750/ME.2016.008

DOI: 10.14750/ME.2016.008

Bibliography

1. J. A. C. Bresse. *Recherches analytiques sûr la flexion et la résistance des pièces courbes.* Mallet-Bachelier and Carilian-Goeury at Vr Dalmont, Paris, 1854.
2. E. Winkler. Formänderung und Festigkeit gekrümmter Körper, insbesondere der Ringe. *Civiling*, 4:232–246, 1858.
3. F. Grashof. *Theorie der Elastizität und Festigkeit mit Bezug auf ihre Anwendungen in der Technik.* Verlag von Rudolph Gaertner, 2nd revised and enlarged edition, 1878.
4. A. E. H. Love. *A treatise on the mathematical theory of elasticity I. and II.* Cambridge: University Press, 1892 and 1893.
5. A. E. H. Love. *A treatise on the mathematical theory of elasticity.* Cambridge: University Press, Second edition, 1906.
6. S. Márkus and T. Nánási. Vibration of curved beams. *The Shock and Vibration Digest*, 13(4):3–14, 1981.
7. P. Chidamparam and A. W. Leissa. Vibrations of planar curved beams, rings and arches. *Applied Mechanis Review, ASME*, 46(9):467–483, 1993.
8. I. Kozák and Gy. Szeidl. *Chapters from the Strength of Materials.* Miskolci Egyetem, 2012. (in Hungarian).
9. B. Király (editor). *Szilárdságtan II., Nehézipari Műszaki Egyetem.* Tankönyvkiadó, Budapest, 1978. (in Hungarian).
10. A. P. Boresi, R. J. Smith, and O. M. Sidebottom. *Advanced mechanics of materials.* John Wiley & Sons, Inc., 1993.
11. F. P. Beer and E. R. Johnston. *Mechanics of Materials.* Mc Graw Hill, Metric edition, 1987.
12. Á. Muttnyánszky. *Strength of Materials (in Hungarian).* Műszaki Könyvkiadó, Budapest, 1981.
13. B. Csizmadia and E. Nándori. *Engineering Mechanics: Strength of Materials.* Nemzeti Tankönyvkiadó, 2002. (in Hungarian).
14. L. Damkilde. *Stress and stiffness analysis of beam-sections.* Department of Structural Engineering and Materials, Technical University of Denmark, 2000. (Lecture note).
15. U. Saravanan. *Advanced Solid Mechanics.* Department of Civil Engineering, Indian Institute of Technology Madras, 2013. (Lecture note).
16. S. Timoshenko. *History of strength of materials.* Dover, 1963.
17. G. Tolf. Stresses in a curved laminated beam. *Fibre Science and Technology*, 19:243–267, 1983.
18. L. Ascione and F. Fraternali. A penalty model for the analysis of curved composite beams. *Computers & Structures*, 45(5-6):985–999, 1991.
19. J. M. Segura and G. Armengaud. Analytical formulation of stresses in curved composite beams. *Archive of Applied Mechanics*, 68:206–213, 1998.
20. S. Venkatarman and B. V. Sankar. Analysis of sandwich beams with functionally graded core. In *A Collection of Technical Papers: 42nd AIAA/ASME/ASCE/AHS/ASC Structures, Structural Dynamics and Materials Conference and Exhibit*, volume 4. American Institute of Aeronautics and Astronautics, April 2001. ISBN 978-1563474774.
21. Y. Aimin. Solutions of the integral equations for shearing stresses in two-material curved beams. *Mechanics Research Communications*, 31:137–146, 2003.
22. I. Ecsedi and K. Dluhi. A linear model for the static and dynamic analysis of non-homogeneous curved beams. *Applied Mathematical Modelling*, 29:1211–1231, 2005.
23. T. H. Daouadji, A. H. Henni, A. Tounsi, and A. B. E. Abbes. Elasticity solution of a cantilever functionally graded beam. *Applied Composite Materials*, 20:1–15, 2013.
24. I. Ecsedi and Á. J. Lengyel. Curved composite beam with interlayer slip loaded by radial load. *Curved and Layered Structures*, 2:50–58, 2015.
25. A. Baksa and I. Ecsedi. A note on the pure bending of nonhomogenous prismatic bars. *International Journal of Mechanical Engineering Education*, 37(2):118–129, 2009.
26. L. Euler. *Sûr la force des colonnes.* Memoires de V Academie de Barlin, 1759.

DOI: 10.14750/ME.2016.008

27. L. A. Godoy. *Theory of elastic stability: Analysis and sensitivity*. Taylor & Francis, 1999.
28. C. M. Wang, C. Y. Wang, and J. N. Reddy. *Exact solutions for buckling of structural members*. CRC Press, 2005.
29. Z. Bazant and L. Cedolin. *Stability of structures*. World Scientific, 2010.
30. I. A. Karnovsky. *Theory of Arched Structures*. Springer, 2012.
31. E. Hurlbrink. Berechnung von rohrenartigen Kärpern, die unter ausserem Drucke stehen. *Schiffbau*, 9(14):517–523, 1907-1908.
32. E. Chwalla and C. F. Kollbrunner. Beiträge zum Knickproblen des Boganträgers und des Rahmens. *Sthalbau*, 11(10):73–78, May 1938.
33. S. P. Timoshenko and J. M. Gere. *Theory of Elastic Stability*. Engineering Sociaties Monograps. McGraw-Hill, 2^{nd} edition, 1961.
34. V. V. Bolotin. *The Dynamic Stability of Elastic Systems*. Holden-Day INC., 1964.
35. H. L. Schreyer and E. F. Masur. Buckling of shallow arches. *Journal of Engineering Mechanics Divison, ASCE*, 92(EM4):1–19, 1965.
36. D. A. DaDeppo and R. Schmidt. Sidesway buckling of deep crcular arches under a concentrated load. *Journal of Applied Mechanics,ASME*, 36(6):325–327, June 1969.
37. D. A. DaDeppo and R. Schmidt. Large deflections and stability of hingeless circular arches under interacting loads. *Journal of Applied Mechanics, ASME*, 41(4):989–994, December 1974.
38. C. L. Dym. Buckling and postbuckling behaviour of steep compressible arches. *International Journal of Solids and Structures*, 9(1):129, January 1973.
39. C. L. Dym. Bifurcation analyses for shallow arches. *Journal of the Engineering Mechanics Division, ASCE*, 99(EM2):287, April 1973.
40. C. L. Dym. *Stability Theory and Its Applications to Structural Mechanics*. Dover, 1974, 2002.
41. Gy. Szeidl. *Effect of Change in Length on the Natural Frequencies and Stability of Circular Beams*. PhD thesis, Department of Mechanics, University of Miskolc, Hungary, 1975. (in Hungarian).
42. P. A. A. Laura and M. J. Maurizi. Recent research on vibrations of arch-type structures. *The Shock and Vibration Digest*, 19(1):6–9, 1987.
43. A. K. Noor and J. M. Peters. Mixed model and reduced/selective integration displacment models for nonlinear analysis of curved beams. *International Journal of Numerical Methods in Engineering*, 17(4):615–631, 1981.
44. P. R. Calboun and D. A. DaDeppo. Nonlinear finite element analysis of clamped arches. *Journal of Structural Engineering, ASCE*, 109(3):599–612, 1983.
45. Z. M. Elias and K. L. Chen. Nonlinear shallow curved beam finite element. *Journal of Engineering Mechanics, ASCE*, 114(6):1076–1087, 1988.
46. R. K. Wen and B. Suhendro. Nonlinear curved beam element for arch structures. *Journal of Structural Engineering, ASCE*, 117(11):3496–3515, 1991.
47. D. J. Dawe. Curved finite elements for the analysis of shallow and deep arches. *Computers & Structures*, 4:559–580, 1974.
48. D. J. Dawe. Numerical studies using circular arch finite elements. *Computers & Structures*, 4:729–740, 1974.
49. A. F. D. Loula, L. P. Franca, J. R. Hughes, and I. Miranda. Stability, convergence and accuracy of a new finite element method for the circular arch problem. *Computer Methods in Applied Mechanics and Engineering*, 63:281–303, 1987.
50. F. G. Flores and L. A. Godoy. Elastic postbuckling analysis via finite element and perturbation techniques. part 1: Formulation. *International Journal for Numerical Methods in Engineering*, 33:1775–1794, 1992.
51. Y.-L. Pi and N. S. Trahair. Non-linear buckling and postbuckling of elastic arches. *Engineering Structures*, 20(7):571–579, 1998.
52. A. N. Palazotto, L. N. B. Gummadi, and J. C. Bailey. Finite element analysis of arches undergoing large rotations – I: Theoretical comparison. *Finite Elements in Analysis and Design*, 24:213–235, 1997.
53. A. N. Palazotto, L. N. B. Gummadi, and J. C. Bailey. Finite element analysis of arches undergoing large rotations – II: Classification. *Finite Elements in Analysis and Design*, 27:237–252, 1997.
54. B. Szabó and Gy. Királyfalvi. Linear models of buckling and stress stiffening. *Computer Methods in Applied Mechanics*, 171(1-2):43–59, 1999.
55. S. Rajasekaran. Static, stability and free vibration analysis of arches using a new differential transformation-based element. *International Journal of Mechanical Sciences*, 77:82–97, 2013.

DOI: 10.14750/ME.2016.008

56. Y.-L. Pi, M. A. Bradford, and F. Tin-Loi. Non-linear in-plane buckling of rotationally restrained shallow arches under a central concentrated load. *International Journal of Non-Linear Mechanics*, 43:1–17, 2008.
57. Y.-L. Pi and M. A. Bradford. Nonlinear analysis and buckling of shallow arches with unequal rotational end restraints. *Engineering Structures*, 46:615–630, 2013.
58. R. Plaut. Buckling of shallow arches with supports that stiffen when compressed. *Journal of Engineering Mechanics*, 116:973–976, 1990.
59. Y. Yang and G. s. Tong. In-plane elastic buckling of steel circular arches with horizontal spring support. *Engineering Mechanics*, 28(3):9–16, 2011.
60. Y.-L. Pi, M. A. Bradford, and F. Tin-Loi. Nonlinear analysis and buckling of elastically supported circular shallow arches. *International Journal of Solids and Structures*, 44:2401–2425, 2007.
61. M. A. Bradford, B. Uy, and Y.-L. Pi. In-plane elastic stability of arches under a central concentrated load. *Journal of Engineering Mechanics*, 128(7):710–719, 2002.
62. Y.-L. Pi, M. A. Bradford, and B. Uy. In-plane stability of arches. *International Journal of Solids and Structures*, 39:105–125, 2002.
63. Y.-L. Pi and M. A. Bradford. Non-linear in-plane postbuckling of arches with rotational end restraints under uniform loading. *International Journal of Non-Linear Mechanics*, 44:975–989, 2009.
64. Y.-L. Pi and M. A. Bradford. Effects of prebuckling analyses on determining buckling loads of pin-ended circular arches. *Mechanics Research Communications*, 37:545–553, 2010.
65. Y.-L. Pi and M. A. Bradford. Dynamic buckling of shallow pin ended arches under a sudden central concentrated load. *Journal of Sound and Vibration*, 317:898–917, 2008.
66. Y.-L. Pi and M. A. Bradford. Nonlinear dynamic buckling of shallow circular arches under a sudden uniform radial load. *Journal of Sound and Vibration*, 331:4199–4217, 2012.
67. Y.-L. Pi and M. A. Bradford. Nonlinear dynamic buckling of pinned-fixed shallow arches under a sudden central concentrated load. *Nonlinear Dynamics*, 73:1289–1306, 2013.
68. H. Shafiee, M. H. Naei, and M. R. Eslami. In-plane and out-of-plane buckling of arches made of FGM. *International Journal of Mechanical Sciences*, 48:907–915, 2006.
69. D. Kim and R. A. Chaudhuri. Postbuckling behaviour of symmetrically laminated thin shallow circular arches. *Composite Structures*, 87:101–108, 2008.
70. X. Song, S. R. Li, and Y. G. Zhao. Buckling behavior of FGM elastic arches subjected to uniformly distributed radial follow load. *Advanced Materials Research*, 239-242:422–427, 2011.
71. T. P. Vo and H.-T. Thai. Vibration and buckling of composite beams using refined shear deformation theory. *International Journal of Mechanical Sciences*, 62:67–76, 2012.
72. F. Fraternali, S. Spadea, and L. Ascione. Buckling behavior of curved composite beams with different elastic response in tension and compression. *Composite Structures*, 100:280–289, 2013.
73. M. Bateni and M. R. Eslami. Non-linear in-plane stability analysis of FGM circular shallow arches under central concentrated force. *International Journal of Non-Linear Mechanics*, 60:58–69, 2014.
74. Y.-L. Pi and M. A. Bradford. Non-linear in-plane analysis and buckling of pinned-fixed shallow arches subjected to a central concentrated load. *International Journal of Non-Linear Mechanics*, 47:118–131, 2012.
75. J. P. Den Hartog. Vibration of frames of electrical machines. *Transactions of the American Society of Mechanical Engineers, Journal of Applied Mechanics*, 50:1–6, 1928.
76. E. Volterra and J. D. Morrel. Lowest natural frequency of elastic arc for vibrations outside the plane of initial curvature. *Journal of Applied Mechanics*, 12:624–627, 1961.
77. E. Volterra and J. D. Morrel. On the fundamental frequencies of curved beams. *Bulletin of the Polytechnic Institute of Jassy*, 7(11):1–2, 1961.
78. S. Timoshenko. *Vibration problems in engineering*. D. Van Nonstrand, 1955.
79. K. Federhoffer. *Dynamik das Bogenträgers und Kreisringes*. Wien Springer Verlag, 1950.
80. M. S. Qatu and A. A. Elsharkawy. Vibration of laminated composite arches with deep curvature and arbitrary boundaries. *Computers & Structures*, 47(2):305–311, 1993.
81. K. Kang, C. W. Bert, and A. G. Striz. Vibration analysis of shear deformable circular arches by the differential quadrature method. *Journal of Sound and Vibration*, 181(2):353–360, 1995.
82. E. Tüfekçi and A. Arpaci. Exact solution of in-plane vibrations of circular arches with account taken of axial extension, transverse shear and rotatory inertia affects. *Journal of Sound and Vibration*, 209(5):845–856, 1997.
83. A. Krishnan and Y. J. Suresh. A simple cubic linear element for static and free vibration analyses of curved beams. *Computers & Structures*, 68:473–489, 1998.

DOI: 10.14750/ME.2016.008

84. C. S. Huang, K. Y. Nieh, and M. C. Yang. In plane free vibration and stability of loaded and shear-deformable circular arches. *International Journal of Solids and Structures*, 40:5865–5886, 2003.
85. B. Kanga, C. H. Riedelb, and C. A. Tanc. Free vibration analysis of planar curved beams by wave propagation. *Journal of Sound and Vibration*, 260:19–44, 2003.
86. R. Lawther. On the straightness of eigenvalue interactions. *Computational Mechanics*, 37:362–368, 2005.
87. H. Ozturk. In-plane free vibration of a pre-stressed curved beam obtained from a large deflected cantilever beam. *Finite Elements in Analysis and Design*, 47:229–236, 2011.
88. F. F. Çalım. Forced vibration of curved beams on two-parameter elastic foundation. *Applied Mathematical Modelling*, 36:964–973, 2012.
89. M. Hajianmaleki and M. S. Qatu. Static and vibration analyses of thick, generally laminated deep curved beams with different boundary conditions. *Composites Part B: Engineering*, 43:1767–1775, 2012.
90. M. Hajianmaleki and M. S. Qatu. Vibrations of straight and curved composite beams: A review. *Composite Structures*, 100:218–232, 2013.
91. B. Kovács. Vibration analysis of layered curved arch. *Journal of Sound and Vibration*, 332:4223–4240, 2013.
92. J. S. Wu, F. T. Lin, and H. J. Shaw. Free in-plane vibration analysis of a curved beam (arch) with arbitrary various concentrated elements. *Applied Mathematical Modelling*, 37:7588–7610, 2012.
93. L. Juna, R. Guangweia, P. Jina, L. Xiaobina, and W. Weiguoa. Free vibration analysis of a laminated shallow curved beam based on trigonometric shear deformation theory. *Mechanics Based Design of Structures and Machines*, 42(1):111–129, 2014.
94. L. Juna and H. Hongxinga. Variationally consistent higher-order analysis of harmonic vibrations of laminated beams. *Mechanics Based Design of Structures and Machines*, 37(3):299–326, 2009.
95. N. Ziane, S. A. Meftah, H. A. Belhadj, A. Tounsi, and E. A. A. Bedia. Free vibration analysis of thin and thick-walled FGM box beams. *International Journal of Mechanical Sciences*, 66:273–282, 2013.
96. D. S. Mashat, E. Carrera, A. M. Zenkour, S. A. A. Khateeb, and M. Filippi. Free vibration of FGM layered beams by various theories and finite elements. *Composites: Part B*, 59:269–278, 2014.
97. J. Murin, M. Aminbaghai, and V. Kutis. Exact solution of the bending vibration problem of FGM beams with variation of material properties. *Enginnering Structures*, 32:1631–1640, 2010.
98. K. K. Pradhan and S. Chakraverty. Free vibration of Euler and Timoshenko functionally graded beams by Rayleigh-Ritz method. *Composites: Part B*, 51:175–184, 2013.
99. A. Yousefi and A. Rastgoo. Free vibration of functionally graded spatial curved beams. *Composite Structures*, 93:3048–3056, 2011.
100. Gy. Szeidl, K. Kelemen, and Á. Szeidl. Natural frequencies of a circular arch – computations by the use of Green functions. *Publications of the University of Miskolc, Series D. Natural Sciences, Mathematics*, 38:117–132, 1998.
101. K. Kelemen. Vibrations of circular arches subjected to hydrostatic follower loads – computations by the use of the Green functions. *Journal of Computational and Applied Mechanics*, 1(2):167–178, 2000.
102. M. Abu-Hilal. Forced vibration of Euler-Bernoulli beams by means of dynamic Green functions. *Journal of Sound and Vibration*, 267:191–207, 2003.
103. X. Y. Li, X. Zhao, and Y. H. Li. Green's functions of the forced vibration of Timoshenko beams with damping effect. *Journal of Sound and Vibration*, 333:1781–1795, 2014.
104. G. G. G. Lueschen and L. A. Bergman. Green's functions for uniform Timoshenko beams. *Journal of Sound and Vibration*, 194(1):93–102, 1996.
105. M. A. Foda and Z. Abduljabbar. A dynamic Green function formulation for the response of a beam structure to a moving mass. *Journal of Sound and Vibration*, 210(3):295–306, 1997.
106. B. Mehri, A. Davar, and O. Rahmani. Dynamic Green function solution of beams under a moving load with different boundary conditions. *Scientia Iranica, Transaction B: Mechanical Engineering*, 16(3):273–279, 2009.
107. S. Kukla and I. Zamojska. Frequency analysis of axially loaded stepped beams by Green's function method. *Journal of Sound and Vibration*, 300:1034–1041, 2007.
108. Y. Chen and J. Feng. Elastic stability of shallow pin-ended parabolic arches subjected to step loads. *Journal of Central South University of Technology*, 17:156–162, 2010.
109. Visual Numerics International Ltd. *IMSL Computational Technology Toolkit, Math Library Volumes 1 and 2.* Visual Numerics, 23 Datchet Road, SLOUGH, Berkshire SL3 7LL, UNITED KINGDOM, 1997.
110. L. Kiss and Gy. Szeidl. Vibrations of pinned-pinned heterogeneous circular beams subjected to a radial force at the crown point. *Mechanics Based Design of Structures and Machines*, 43(4):424–449, 2015. (In the press).
111. *Abaqus Online Documentation: Version 6.7.*, 2007.

DOI: 10.14750/ME.2016.008

112. L. Kiss and Gy. Szeidl. In-plane stability of fixed-fixed heterogeneous curved beams under a concentrated radial load at the crown point. *Technische Mechanik*, 35(1):31–48, 2015.
113. L. Kiss. In-plane buckling of rotationally restrained heterogeneous shallow arches subjected to a concentrated force at the crown point. *Journal of Computational and Applied Mechanics*, 9(2):171–199, 2014.
114. C. T. H. Baker. *The Numerical Treatment of Integral Equations – Monographs on Numerical Analysis edited by L. Fox and J. Walsh*. Clarendon Press, Oxford, 1977.
115. L. P. Kiss. Solutions to some problems of heterogeneous curved beams (in Hungarian). MSc thesis, Department of Mechanics, University of Miskolc, 2011.
116. Á. Bosznay. *Műszaki rezgéstan*. Műszaki Könyvkiadó, 1962.
117. J. A. Wolf. Natural frequencies of circular arches. *Transactions of the American Society of Civil Engineers, Journal of the Structural Division*, 97:2337–2349, 1971.
118. L. Kiss, Gy. Szeidl, S. Vlase, B. P. Gálfi, P. Dani, I. R. Munteanu, R. D. Ionescu, and J. Száva. Vibrations of fixed-fixed heterogeneous curved beams loaded by a central force at the crown point. *International Journal for Engineering Modelling*, 27(3-4):85–100, 2014.